Study of ^{14}O as a Test of the Unitarity of the CKM Matrix and the CVC Hypothesis

by

Jason Timothy Burke

B.Sc. Honours (Concordia University) 1998

M.A. (University of California Berkeley) 2002

A dissertation submitted in partial satisfaction of the

requirements for the degree of

Doctor of Philosophy

in

Physics

in the

GRADUATE DIVISION

of the

UNIVERSITY OF CALIFORNIA, BERKELEY

Committee in charge:

Professor Stuart J. Freedman, Chair

Professor Eugene D. Commins

Professor Joseph Cerny

Spring 2004

The dissertation of Jason Timothy Burke is approved:

-
Chair Date

-
Date

-
Date

University of California, Berkeley

Spring 2004

Study of ^{14}O as a Test of the Unitarity of the CKM matrix and the CVC Hypothesis

Copyright 2004

by

Jason Timothy Burke

Abstract

Study of ^{14}O as a Test of the Unitarity of the CKM Matrix and the CVC Hypothesis

by

Jason Timothy Burke

Doctor of Philosophy in Physics

University of California, Berkeley

Professor Stuart J. Freedman, Chair

The study of superallowed beta decay in nuclei, in conjunction with other experiments, provide a test of the unitarity of the quark mixing matrix or CKM matrix. Non-unitarity of the CKM matrix could imply the existence of a fourth generation of quarks, right handed currents in the weak interaction, and/or new exotic fermions.

Advances in radioactive beam techniques allow the creation of nearly pure samples of nuclei for beta decay studies. The subject of this thesis is the development of a radioactive beam of ^{14}O and the study of the ^{14}O half-life and branching ratio. The radioactive beam is produced by ionizing $^{12}C^{14}O$ radioactive gas and then accelerating with an ECR ion source. The ^{14}O nucleus decays via superallowed beta decay with a branching ratio > 99%. The low Z of ^{14}O is important for calculating reliable corrections to the beta decay that generally increase in with Z. The > 99% branching ratio can be

established with modest precision on the complementary branching ratio.

When this work began the experimentally determined CKM matrix was non-unitary by 2.5 standard deviations. Recent studies of Kaon, Hyperon, and B meson decays have been used to determine V_{us} and V_{ub} matrix elements. In this work the half-life and branching ratio of ^{14}O are measured and used to establish V_{ud}. The unitarity of the CKM matrix is then assessed. The half-life of ^{14}O was determined to be 70.683 ± 0.015 s and the Gamow-Teller branching ratio was found to be 0.643 ± 0.020 %. Using these results the value of V_{ud} is 0.9738 ± 0.0005. Incorporating the new values for V_{us} of 0.2272 ± 0.0030 and V_{ub} of 0.0035 ± 0.0015 the squared sum of the first row of the CKM matrix is 0.9999 ± 0.0017 which is consistent with unitarity.

To my beautiful wife Sheril,

my future daughter Kelly Lynn Harumi,

my parents Robert and Sigrid Burke,

and my special assistant Scout

for their love and support during my years as a student.

Table of Contents

List of Figures.....v

List of Tables.....ix

1 Introduction.....1
1.1 The CKM matrix elements.....3
1.1.1 Vus Matrix Element.....3
1.1.1.1 E865 Experiment at BNL.....4
1.1.1.2 KLOE Experiment at DAϕNE.....4
1.1.1.3 Hyperon Decay Re-Analyzed.....5
1.1.2 Vub Matrix Element.....7
1.1.3 Vud Coupling Constant.....8
1.2 Ft-values.....8
1.3 Fermi Transitions in Beta Decay.....12
1.3.1 Electron Capture.....12
1.3.2 Charge Correction.....14
1.3.3 Outer Radiative Correction.....14
1.3.4 Inner Radiative Correction.....15
1.3.5 Summary of Correction Terms.....17
1.4 O-14 Q-value.....18
1.5 O-14 Branching Ratio.....21
1.6 O-14 Half-Life.....22

2 Target Designs for Production of O-14 Radioactive Beams.....26
2.1 Carbon Targets for O-14 Production.....30
2.2 Indirectly Heated Carbon Fiber.....34
2.3 Reticulated Vitreous Carbon.....37
2.4 RVC and Solid Carbon Heat Shields.....41
2.5 Carbon Aerogel.....42

3 Electron Cyclotron Resonance Ion Source Performance.....47
3.1 Multiple-CUSP Ion Source.....48
3.1.1 Antenna Lifetime.....50
3.1.2 Ionization Efficiency.....50
3.2 IRIS Electron Cyclotron Resonance Ion Source.....51

3.2.1 IRIS Plasma Chamber....52
3.2.2 Solenoid Magnetic Field....53
3.2.3 Sextupole Magnetic Field....55
3.2.4 Microwave Power Source....56
3.2.5 Stable Gas Injection Manifold....58
3.2.6 Ionization Efficiency and Support Gases....58
3.2.7 Gas Hold-Up Time....60
3.3 Ion Beam Extraction....65
3.4 Radiation Shielding....70
3.5 Analyzing Magnet....71

4 The O-14 Half-Life Experiment....72
4.1 Fitting Data....72
4.2 Previous Experiments....75
4.3 Deadtime....79
4.3.1 Extending Deadtime Distributions....81
4.3.2 Non-Extending Deadtime Distributions....82
4.3.3 Effective Deadtime....83
4.3.4 Data Readout Deadtime....85
4.4 Gamma-Ray Detector Design....85
4.5 Beta Particle Detector Design....88
4.6 Photomultiplier Tube....90
4.6.1 Photomultiplier Tube Afterpulsing....91
4.7 Signal Processing Electronics....94
4.8 Data Acquisition Timing....97
4.9 Monte Carlo Simulations....99
4.10 O-14 Source Enclosure....102
4.11 Radiation Shielding....104
4.12 Sensitivity to Gamma Ray Backgrounds....106
4.13 Calibrated Frequency Standard....106
4.14 Deadtime Measurement....107
4.14.1 Calibration of the TDC....108
4.14.2 Calibration of the Deadtime....113
4.15 Beta Detector Systematics Effects....116
4.15.1 90Sr Sealed Source for Stability Tests....116
4.15.2 High Voltage Supply Temperature Stability....117
4.15.3 High Voltage Power Supply Voltage Stability....121
4.15.4 PMT Temperature Stability....122
4.15.5 Discriminator Voltage Stability....124
4.15.6 Deadtime Uncertainty....126
4.15.7 PMT Noise....128
4.15.8 Gain Shift versus Count Rate....129
4.15.9 Summary of Systematic Effects on Half-life....130

4.16 Contamination by Other Half-Life Components.....132
4.17 Implantation of 14O.....136
4.18 Fitting Data.....138
4.19 Half-life Results.....140
4.20 Impact on Physics.....153

5 The Branching Ratio Experiment.....158
5.1 Previous Experiments.....158
5.1.1 Comment on Sidhu and Gerhart Branching Ratio Experiment.....160
5.2 The O-14 Beta Spectrum.....161
5.2.1 The Allowed Fermi Beta Spectrum.....162
5.2.2 The Allowed Gamow-Teller Beta Spectrum.....166
5.3 O-14 Source for the Branching Ratio Experiment.....169
5.4 The Beta Spectrometer.....170
5.4.1 The Spectrometer Magnetic Field Profile.....171
5.4.2 Magnetic Field Stability.....174
5.5 Multiple Wire Proportional Chamber.....174
5.5.1 Mechanical Construction of the MWPC.....175
5.5.2 Argon Ethane Fill Gas.....176
5.5.3 Pre-Amplifier Electronics.....177
5.5.4 Discriminator Electronics 179
5.5.5 Data Acquisition Electronics.....182
5.6 The Anti-Coincidence Active Collimator.....185
5.7 The Coincidence Beta Paddle.....189
5.8 Characterization of the MWPC.....193
5.8.1 High Voltage Conditioning of the MWPC.....193
5.8.2 Intrinsic Electronic Noise.....194
5.8.3 The Plateau Curve.....196
5.8.4 The Cosmic Ray Muon Background Rate.....197
5.8.5 The 14O Source Background.....199
5.8.6 The Beam Line Background.....201
5.9 Monte Carlo Simulations 202
5.9.1 Finite Source Spectrum.....203
5.9.2 Collimator Aperture Effect.....204
5.10 Data Analysis.....205
5.10.1 Weighted Background Subtraction.....206
5.11.1 Multiplicity Effect on the Branching Ratio.....208
5.11.2 MWPC Offset Uncertainty.....209
5.11.3 Shape Factor Uncertainty.....210
5.11.4 Gaussian Wire Reponse Uncertainty.....211
5.11.5 Fringe Field Shift Uncertainty.....213
5.11.6 Collimator Scattering Uncertainty.....214
5.11.7 Uncertainty Due to the Magnetic Field Drift.....216

5.11.8 Summary of Systematic and Statistical Uncertainties.....217
5.13 Final Result and Impact on Physics.....218

Conclusions.....220

Bibliography.....221

List of Figures

Figure 1.1 Summary of recent Vus measurements.....7
Figure 1.2 Fermi function values for N-14 nucleus.....10
Figure 1.3 Radiative corrections of order Zα2 for beta decay.....15
Figure 1.4 Inner radiative processes in nuclear beta decay.....16
Figure 1.5 O-14 level diagram.....17
Figure 1.6 Current status of uncertainties for Fermi decays.....18
Figure 1.7 Summary of Q-values.....20
Figure 1.8 Summary of branching ratio of 14O to 14N 3.94 MeV state.....22
Figure 1.9 O-14 experimental half-life values.....25
Figure 2.1 Overview of the 88-inch Cyclotron.....28
Figure 2.2 Vacuum diagram of the target, transfer line, and IRIS ECR.....28
Figure 2.3 Cross-section data for 14O, 11C, and 13N.....31
Figure 2.4 Target chamber shown with electrical feed through.....33
Figure 2.5 Electrical and cooling water schematic of target.....34
Figure 2.6 Tantalum filament with carbon fiber target.....35
Figure 2.7 Tantalum target temperature versus power.....36
Figure 2.8 Transmission electron micrograph of RVC material.....37
Figure 2.9 RVC target temperature as a function of applied power.....38
Figure 2.10 Assembled RVC target with heat shields installed.....39

Figure 2.11 RVC target release rate as a function of target temperature.....40
Figure 2.12 Target design two carbon heat shields are shown.....41
Figure 2.13 Target three design mounted on flange for insertion into target chamber.….42
Figure 2.14 Scanning electron microscope photo of carbon aerogel.....43
Figure 2.15 Aerogel target temperature as a function of applied power.....44
Figure 3.1 Schematic of CUSP source mounted on the test stand.....49
Figure 3.2 IRIS ECR injection side at left and extraction side on the right.....52
Figure 3.3 Schematic overview of the IRIS ECR plasma chamber.....53
Figure 3.4 IRIS ECR showing the two solenoid pancakes at right.....54
Figure 3.5 Electrical schematic for solenoid magnetic power.....55
Figure 3.6 Plasma confined radially by the sextupole magnetic field.....56
Figure 3.7 Magnetic field gradient in NdFeB sextupole.....56
Figure 3.8 Schematic of RF Level Controller.....57
Figure 3.9 Schematic of the stable support gas injection manifold.....58
Figure 3.10 Schematic diagram of the IRIS ECR settings.....60
Figure 3.11 Stable oxygen hold-up time measured in IRIS.....61
Figure 3.12 Transfer line gas hold-up time.....62
Figure 3.13 Cold trap gas hold-up time.....63
Figure 3.14 Schematic of ion extraction optics.....66
Figure 3.15 Einzel lens used to focus the beam after extraction.....66
Figure 3.16 The puller used to accelerate the ions from the plasma.....67
Figure 3.17 Beam extraction shape dependence on plasma conditions.....70
Figure 4.1 Chi-square minimization versus maximum likelihood minimization from a simulation.....74
Figure 4.2 NaI gamma ray spectrum of O-14 decay from Clark [46].....78
Figure 4.3 Summing effect on 14O half-life.....79
Figure 4.4 Extending and non-extending discriminator diagrams.....81
Figure 4.5 Half-life effect of the first deadtime on the second deadtime.....84
Figure 4.6 BaF2 fluorescence spectrum.....86
Figure 4.7 BaF2 crystal from M.S.U. with pen shown for scale.....87
Figure 4.8 Schematic of beta detector.....89
Figure 4.9 Typical beta particle spectrum from 14O source during the experiment.....90
Figure 4.10 Photomultiplier pulse shape and timing.....91
Figure 4.11 Afterpulsing electronic circuit.....92
Figure 4.12 TDC spectrum with afterpulsing occurring at 300 ns.....94

Figure 4.13 Schematic of data acquisition electronics.....95
Figure 4.14 Timing diagram of LeCroy 4434 scaler recovery time.....96
Figure 4.15 Data acquisition readout time structure.....98
Figure 4.16 Acquisition deadtime readout time structure.....99
Figure 4.17 Effect of rate dependent gain shift on half-life.....102
Figure 4.18 Scale drawing of the beta detectors located around the 14O source.....103
Figure 4.19 Scintillators mounted on PMTs in plastic enclosure.....104
Figure 4.20 Mylar vacuum window mounted on beam line.....104
Figure 4.21 Photograph of lead shielding surrounding the beta detectors.....105
Figure 4.22 TDC calibration data.....109
Figure 4.23 TDC calibration electronics.....110
Figure 4.24 TDC calibration timing diagram.....111
Figure 4.25 Typical TDC data points.....112
Figure 4.26 Deadtime calibration electronics.....113
Figure 4.27 Deadtime calibration timing diagram.....114
Figure 4.28 Sr-90 decay scheme.....117
Figure 4.29 Temperature effect on high voltage supply.....118
Figure 4.30 Temperature of high voltage supplies versus time.....119
Figure 4.31 Systematic offset due to temperature change of high voltage supply.....120
Figure 4.32 High voltage variation effect on half-life.....122
Figure 4.33 Temperature of PMTs used for the half-life experiment.....124
Figure 4.34 Discriminator response versus discriminator voltage.....126
Figure 4.35 Half-life offset due to deadtime offset.....127
Figure 4.36 Detector spectra at 10 kHz to 100 kHz rate.....130
Figure 4.37 Summary of systematic uncertainty as a function of rate.....131
Figure 4.38 Observation chamber for the half-life experiment.....133
Figure 4.39 Half-life offset due to unaccounted contaminants.....135
Figure 4.40 Ion implantation profile from SRIM 2003 software.....137
Figure 4.41 Monte Carlo simulated data fit with Minuit.....139
Figure 4.42 Detector B summed data with fit.....141
Figure 4.43 Detector C summed data with fit.....142
Figure 4.44 Detector D summed data with fit.....143
Figure 4.45 Summed Half-life results.....145
Figure 4.46 Detector B half-life results plotted with average.....146
Figure 4.47 Detector C half-life results plotted with average.....147

Figure 4.48 Detector D half-life results plotted with average.....148
Figure 4.49 Summary of individual runs.....149
Figure 4.50 Summary plot of half-life measurements.....152
Figure 4.51 Summary of Ft-values.....156
Figure 5.1 O-14 decay scheme.....162
Figure 5.2 Fermi function for 14O beta decay.....163
Figure 5.3 Order alpha radiative correction term for the Fermi branch.....165
Figure 5.4 Fermi spectrum with correction terms.....165
Figure 5.5 Order alpha radiative correction term for the branch.....168
Figure 5.6 Gamow-Teller spectrum with correction terms.....168
Figure 5.7 Schematic diagram of the spectrometer, source, and wire chamber.....171
Figure 5.8 Magnetic fringe field of the spectrometer.....172
Figure 5.11 Schematic of MWPC sense and high voltage planes.....176
Figure 5.13 Schematic layout of the vertical sense plane and supporting electronics.....178
Figure 5.14 pre-amplifier electronics overview.....179
Figure 5.15 Sixteen channel preamplifier board for MWPC.....179
Figure 5.17 32 channel MWPC discriminator board.....181
Figure 5.18 MWPC data acquisition electronics.....184
Figure 5.19 Schematic of the active collimator (side view).....186
Figure 5.20 ADC spectrum anti-coincidence collimator detector A.....186
Figure 5.21 ADC spectrum anti-coincidence collimator detector B.....187
Figure 5.23 TDC spectrum of the anti-coincdence collimator detector A.....188
Figure 5.24 TDC spectrum of the anti-coincdence collimator detector B.....189
Figure 5.25 Coincidence paddle ADC histogram.....190
Figure 5.26 Coincidence paddle TDC histogram.....191
Figure 5.27 Coincidence efficiency for vertical wire 7 in the center.....192
Figure 5.28 Coincidence efficiency for vertical wire 3 at the edge.....192
Figure 5.29 Electronic noise rate as a function of the discriminator threshold.....195
Figure 5.31 Cosmic ray background spectrum.....199
Figure 5.32 Background due to the 14O source.....201
Figure 5.33 The background due to O-14 in the beam line.....202
Figure 5.34 Momentum offset due to finite source distribution.....204
Figure 5.35 Momentum spread due to finite collimator size.....205
Figure 5.37 Effect of the offset uncertainty on the branching ratio.....210
Figure 5.38 The shape factor effect on the branching ratio.....211

Figure 5.39 The wire hit gaussian distribution versus MWPC wire number.....212
Figure 5.40 Effect of momentum spread on branching ratio.....213
Figure 5.41 Dependence of the branching ratio on the fringe field.....214
Figure 5.42 Beta spectrum with active collimator scattered events.....215
Figure 5.43 Branching ratio shift due to the magnetic field drift.....216
Figure 5.44 Beta spectrum with fit to determine branching ratio.....218
Figure 5.45 Summary of Gamow-Teller branching ratio measurements.....219

List of Tables

Table 1.2 Summary of Hyperon decays studied.....6
Table 1.3 Summary of Q-value measurements.....20
Table 1.4 Summary of N-14 G-T (1+ → 0+) branching ratio results.....22
Table 1.5 Summary of all published O-14 half-life measurements.....25
Table 3.1 Summary of hold-up times and efficiencies for O-14 beam production.....67
Table 4.1 Summary of nuclear reaction products.....77
Table 4.2 Statistical uncertainty as a function of initial rate.....78
Table 4.3 Summary of scintillation material and decay times.....90
Table 4.4 Calibration data for the Hewlett Packard frequency counters.....109
Table 4.5 TDC calibration times.....110

Table 4.6 Summary of deadtime for each channel.....117
Table 4.7 Summary of temperature effects of high voltage power supply.....121
Table 4.8 Summary of high voltage temperature effect on half-life.....122
Table 4.9 Summary of voltage variation effect on half-life.....124
Table 4.10 Photomultiplier tube temperature stability.....125
Table 4.11 Summary of background uncertainty effect on half-life.....131
Table 4.12 Summary of systematic uncertainty as a function of initial rate.....133
Table 4.13 Summary of contaminant effects on half-life.....137
Table 4.14 Summary of Monte Carlo results for maximum likelihood fit.....141
Table 4.15 Detector B results from analysis of 27 runs summed together and fit.....146
Table 4.16 Detector C results from analysis of 27 runs summed together and fit.....146
Table 4.17 Detector D results from analysis of 27 runs summed together and fit.....146
Table 4.18 Detector B results from analysis of 27 individual runs.....148
Table 4.19 Detector C results from analysis of 27 individual runs.....149
Table 4.20 Detector D results from analysis of 27 individual runs.....150
Table 4.21 Summary of half-life values for detectors B, C, and D summed runs.....152
Table 4.22 Summary of half-life values for detectors B, C, and D individual runs.....152
Table 4.23 Summary of half-life values for detectors B and C for summed runs.....152
Table 4.24 Summary of half-life values for detectors B and C for individual runs.....153
Table 4.25 Summary of half-life values for detectors B and D for summed runs.....153
Table 4.26 Summary of half-life for detectors B and D for individual runs.....153
Table 4.27 Summary of modern 14O half-life results.....155
Table 4.28 Summary of ft-values for 14O.....156
Table 4.29 Summary of ft-values of Fermi transitions.....157
Table 4.30 Summary of CKM parameters and unitarity.....159
Table 5.1 Summary of previous branching ratio measurements.....162
Table 5.2 Summary of beta endpoint energies and branching ratios.....164
Table 5.3 Summary of data cuts used for analysis.....208
Table 5.4 Summary of acquisition times and background rates.....210
Table 5.5 Summary of statistical and systematic uncertainties.....219
Table 5.6 Summary of Gamow-Teller branching ratio.....221

Chapter 1

1 Introduction

The electroweak Standard Model unifies electromagnetism and the weak force. Forces arise from the exchange particles: the photon, the W^+ vector boson, the W^- vector boson, and the Z^0 vector boson. The helicity of the particles is refered to as left or right handed. There are six left handed quarks arranged into three generations,

$$\begin{pmatrix} u \\ d \end{pmatrix}_L \quad \begin{pmatrix} c \\ s \end{pmatrix}_L \quad \begin{pmatrix} t \\ b \end{pmatrix}_L$$

where u is up, d is down, c is charm, s is strange, t is top, b is bottom. There are likewise six right handed quarks u_r, c_r, t_r, d_r, s_r, and b_r. The leptons are arranged in generations similar to the quark generations,

$$\begin{pmatrix} e \\ \nu_e \end{pmatrix}_L \quad \begin{pmatrix} \mu \\ \nu_\mu \end{pmatrix}_L \quad \begin{pmatrix} \tau \\ \nu_\tau \end{pmatrix}_L$$

where e is the electron, μ is the muon, τ is the tau particle, ν_e is the electron neutrino, ν_υ is the muon neutrino, and ν_τ is the tau neutrino. There are also the right handed leptons e_r, μ_r, and τ_r. Only left handed quarks and leptons participate in the charge current weak

interaction. The left handed $W^{\pm}$ bosons only couple to other left handed particles. The left handed quarks must appear in generations in order to correctly cancel the anomalies in the theory [1].

The Standard Model does not explain the masses of the quarks, nor does it limit the number of generations to three. The decay width of the Z^0 particle provides a test of the number of generations of quarks and leptons. The partial decay width of the Z^o particle decaying to 3 fermion families is predicted by the Standard Model to be 2.4961 ± 0.0012 GeV. This agrees with the experimentally determined value of 2.4952 ± 0.0023 GeV [2]. Another way to establish the number of quark generations is to study the quark mixing matrix.

The mass eigenstates of quarks are not the weak interaction eigenstates. Cabibbo included a mixing angle (θ) in the weak current to explain strangeness changing hyperon beta decays [3]. This theory was later extended to a 3x3 matrix by Kobayashi and Maskawa [4]. The mass eigenstates are mixed in weak interaction processes by a hypothesized three by three matrix now called the Cabibbo-Kobayashi-Maskawa (CKM) matrix,

$$\begin{pmatrix} d' \\ s' \\ b' \end{pmatrix} = \begin{pmatrix} V_{ud} & V_{us} & V_{ub} \\ V_{cd} & V_{cs} & V_{cb} \\ V_{td} & V_{ts} & V_{tb} \end{pmatrix} \begin{pmatrix} d \\ s \\ b \end{pmatrix} \quad .$$

The CKM matrix is a unitary transformation from the mass eigenstates (d,s,b) to the weak interaction eigenstates (d',s',b'). The unitarity condition requires among other things that the sum of the modulus of the elements of any row must equal one. Looking at the first

row, where the up quark couples to the down, strange, and bottom quarks, then the following equation is a test of unitarity,

$$|V_{ud}|^2+|V_{us}|^2+|V_{ub}|^2=1 \quad . \tag{1.1}$$

The matrix elements can be determined by performing experiments that isolate these particular matrix elements.

Apparent failure of the CKM unitarity appears in various extensions of the Standard Model. One possible explanation of non-unitarity results from extra Z bosons that affect the radiative corrections to electroweak processes [5]. The proposed extra Z bosons are massize (100 GeV to 10 TeV) neutral particles that would be associated with extra U(1) gauge symmetries. Couplings to exotic fermions, that are not accounted for in the current Standard Model, have also been proposed [6]. Some of the exotic fermions proposed are mirror fermions, vector doublets, or vector singlets. Mirror fermions consist of a left handed singlet fermion and right handed doublet fermions. The proposed vector doublet fermions form left and right handed doublets. The vector singlets are left and right handed singlet fermions. These new fermions lead to a redefinition of the electroweak interactions. If right handed currents are present in the electroweak interaction they could lead to a non-unitarity of the CKM matrix [7].

1.1 The CKM matrix elements

The CKM matrix elements are determined from elementary particle beta decay and nuclear beta decay. The following sections review the current status of the CKM

matrix elements that contribute to equation 1.2.

1.1.1 V_{us} Matrix Element

The V_{us} matrix element can be determined by examining Kaon and Hyperon decay. The currently accepted PDG [8] value of V_{us} is 0.2196 ± 0.0026. Recently three new results have been published, two disagree by several standard deviations from the currently accepted value. The results of the PDG, E865 experiment, KLOE experiment, and Hyperon re-analysis are summarized in Table 1.1 and plotted in Figure 1.1.

1.1.1.1 E865 Experiment at BNL

Recently the $K^+ \rightarrow \pi^o e^+ \nu$ or K_{e3} branching ratio was remeasured by the E865 experiment at Brookhaven National Laboratory [9]. The branching ratio was measured relative to $K^+ \rightarrow \pi^+\pi^0$, $K^+ \rightarrow \pi^0\mu^+\nu_\mu$, and $K^+ \rightarrow \pi^+\pi^0\pi^0$ decays. The experiment observed 70000 K_{e3} decays during a one week run. The branching ratio was found to be 5.13 ± 0.10 %. This branching ratio differs by 2.3 σ from the PDG [8] value of 4.87 ± 0.06 %. The V_{us} value determined from this branching ratio is 0.2272 ± 0.0030. This value of V_{us} is larger by 2.5 sigma from the currently accepted PDG value.

1.1.1.2 KLOE Experiment at DAϕNE

The KLOE detector is located at the DAϕNE e^+e^- collider in Frascati, Italy [10].

The KLOE detector is a cylindrical drift chamber surrounded by a lead scintillating calorimeter. The facility is also referred to as the Frascati ϕ factory. The e^+e^- beam creates ϕ mesons almost at rest in the center of the detector. Approximately half of the ϕ mesons decay to charged kaons and ≈34% of the time they decay to neutral kaons. The goals of the KLOE experiment are to measure the branching ratio of four decays $K^{\pm}_{e3}$, $K^{\pm}_{\mu 3}$, K^{0}_{e3}, and $K^{0}_{\mu 3}$. They will also measure the momentum dependence of the vector form factor $f_{\pm,0}$ (t) as well as the lifetimes of the K_L and $K^{\pm}$. These results will allow the collaboration to calculate four independent values of V_{us}. The KLOE collaboration has released two preliminary results from their measurements of Kaon decays. The KLOE results achieve the same precision as the PDG averaged values. The KLOE collaboration finds a V_{us} value of 0.2111 ± 0.0040 from K^0_{e3} decay and 0.2132 ± 0.0032 from $K^0_{\mu 3}$ decay. The weighted average of these two results V_{us} as 0.2118 ± 0.0030. Note that the results quoted by the KLOE collaboration are for $|f^+(0)V_{us}|$. These values were divided by the theoretically determined value of the vector form factor 0.9874 ± 0.0084 [11] to obtain the V_{us} term. The value of V_{us} is lower by 2.6 sigma from the currently accepted PDG value.

1.1.1.3 Hyperon Decay Re-Analyzed

Recently Cabibbo, Swallow, and Winston [12] have analyzed the PDG [13] data from semileptonic Hyperon decays to determine V_{us}. This analysis uses the measured ratio of the axial vector form factor (g_1) to the vector form factor (f_1), the decay rate of the

particle, and the theoretically determined value of (f_1) to determine V_{us}. This method avoids the uncertainty associated with calculating the axial vector form factor which is subject to SU(3) symmetry breaking. The vector form factor is not subject to first order SU(3) symmetry breaking corrections [14]. Ignoring second class currents the rate (Γ) is proportional to V_{us} as follows

$$\Gamma \propto V_{us}^2 [f_1^2 + 3 g_1^2] \quad . \tag{1.2}$$

The Hyperon decays studied are summarized in Table 1.2. The value of V_{us} is 0.2250 ± 0.0027. This result is greater by 2.0 sigma from the PDG accepted value.

Research Group	***Vus value***
Particle Data Group [8]	0.2196 ± 0.0026
E865 experiment [9]	0.2272 ± 0.0030
KLOE experiment [10]	0.2118 ± 0.0030
Hyperon decay [12]	0.2250 ± 0.0027

Table 1.1 Summary of V_{us} values

Decay Process	***Rate*** ***(μsec^{-1})***	***g_1/f_1***	***V_{us}***
$\Lambda \rightarrow \pi\ e^-\ \bar{\nu}$	3.161 ± 0.58	0.718 ± 0.15	0.2224 ± 0.0034
$\Sigma^- \rightarrow \pi\ e^-\ \bar{\nu}$	6.88 ± 0.24	-0.340 ± 0.17	0.2282 ± 0.0049
$\Xi^- \rightarrow \pi\ e^-\ \bar{\nu}$	3.44 ± 0.19	0.25 ± 0.05	0.2367 ± 0.0099
$\Xi^o \rightarrow \pi\ e^-\ \bar{\nu}$	0.876 ± 0.71	1.32 +0.22 /-0.18	0.209 ± 0.027
Total	-	-	0.2250 ± 0.0027

Table 1.2 Summary of Hyperon decays studied.

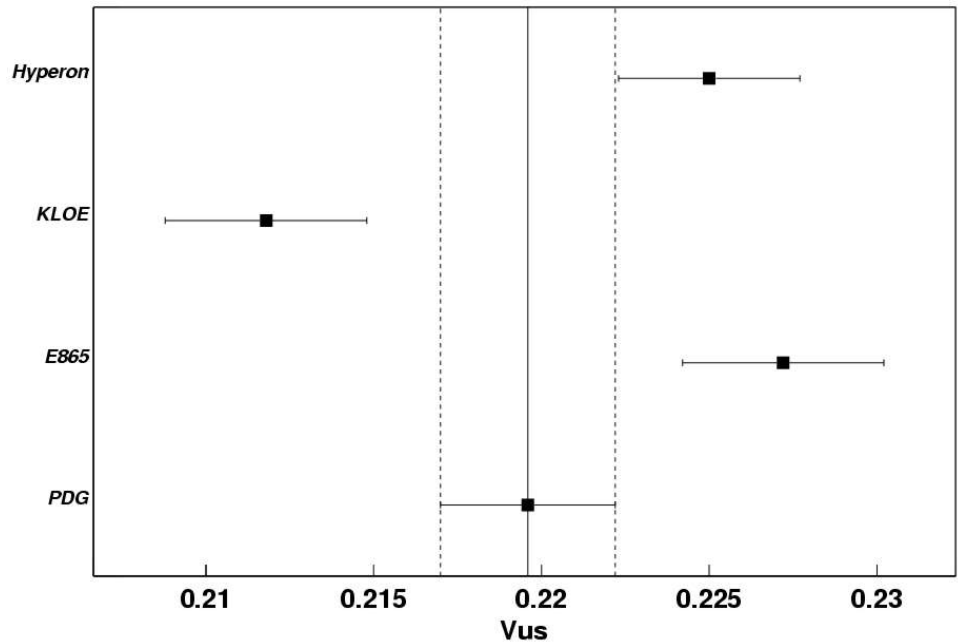

Figure 1.1 Summary of recent V_{us} measurements. The solid line indicates the currently accepted value of V_{us} from reference [8] with the dashed lines on either side representing the 1 sigma uncertainty in the value.

1.1.2 V_{ub} Matrix Element

The V_{ub} element is determined by observing the decay of $b \rightarrow u\, l\, \nu$. The source of b quarks are B mesons $(b\bar{b})$ created at the Υ(4S) resonance. The backgrounds from the B meson decays must be subtracted to determine the V_{ub} element [8]. The currently accepted value of V_{ub} is 0.0035 ± 0.0015 [8]. The V_{ub} element is not significant in the unitarity test. V_{ub} squared gives 1.225 x 10^{-5} as compared to V_{us} squared 4.822 x 10^{-2} which is 3 orders of magnitude larger. The uncertainty in this term will not affect the

unitarity condition at the current levels of precision in measurements of V_{us} and V_{ud}.

1.1.3 V_{ud} Coupling Constant

The V_{ud} element is obtained by high precision measurements of the lifetime of Fermi beta decay transitions and neutron decay experiments. The V_{ud} value obtained from purely superallowed Fermi type transitions is 0.9740 ± 0.0010 [8]. Note that the PDG [8] has doubled the uncertainty on the V_{ud} value obtained from the superallowed beta decays. The V_{ud} value from neutron decay is currently 0.9725 ± 0.0013 [8]. Results obtained from neutron decay must take into account the axial vector current present in the interaction as well as the vector current. The unweighted average of these two results is V_{ud} 0.9734 ± 0.0008 [8].

Using the recommended PDG values for the V_{ud}, V_{us}, and V_{ub} we can check the unitarity of the CKM matrix by squaring and summing these values to see if they equal 1. With $V_{ud} = 0.9734$, $V_{us} = 0.2196$, and $V_{ub} = 0.0035$ we find

$$|V_{ud}|^2 + |V_{us}|^2 + |V_{ub}|^2 = 0.9957 \pm 0.0019 \quad . \tag{1.3}$$

The current result differs by 2 sigma from unitarity. Using a gaussian probability distribution around the squared and summed CKM elements, the CKM matrix is non-unitary at the 91% confidence level. This indicates the possibility of new physics beyond the Standard Model (as mentioned in section 1.0) or an error has been made in one or more of the experiments.

1.2 Ft-values

The ft-value of an allowed transition can be used to determine beta decay coupling constants. The ft-value is the product of the statistical rate function, f, and the partial half-life, t, of a particular beta decay. The statistical rate function depends on the endpoint energy of the decay and the Fermi function, F(E, Z),

$$f \equiv f(E,Z) = \int_{m_e c^2}^{E_o} F(E,Z)\, p\, E (E_o - E)^2 dE \quad . \tag{1.4}$$

Here E is the total energy of the beta particle, p is its momentum, E_o is the total energy available for the decay (Q-value), and Z is the number of protons in the daughter nucleus. The Fermi function, F(E, Z), accounts for the effect that the Coulomb field of the daughter nucleus has on the beta particle. Figure 1.2 shows the Fermi function values for the Z = 7 nucleus as calculated by Behrens and Janecke [15]. The Fermi function is given by the following formula

$$F(E,Z) \approx \left(4(2pR)^{2\gamma-2} e^{pm\frac{\pi\alpha Z E}{p}}\right) \frac{\left|\Gamma(\gamma\, pm\, i \frac{\alpha Z E}{p})\right|^2}{(\Gamma(2\gamma+1))^2} \left(\frac{1+\gamma}{2}\right) \quad , \tag{1.5}$$

where

$$\gamma = (1-\alpha^2 Z^2)^{1/2} \quad . \tag{1.6}$$

The Fermi function depends on the proton number (Z), the nuclear radius (R), the total energy of the beta (E), the fine structure constant (α), Γ(x) is the Gamma function of x, and the momentum of the beta (p).

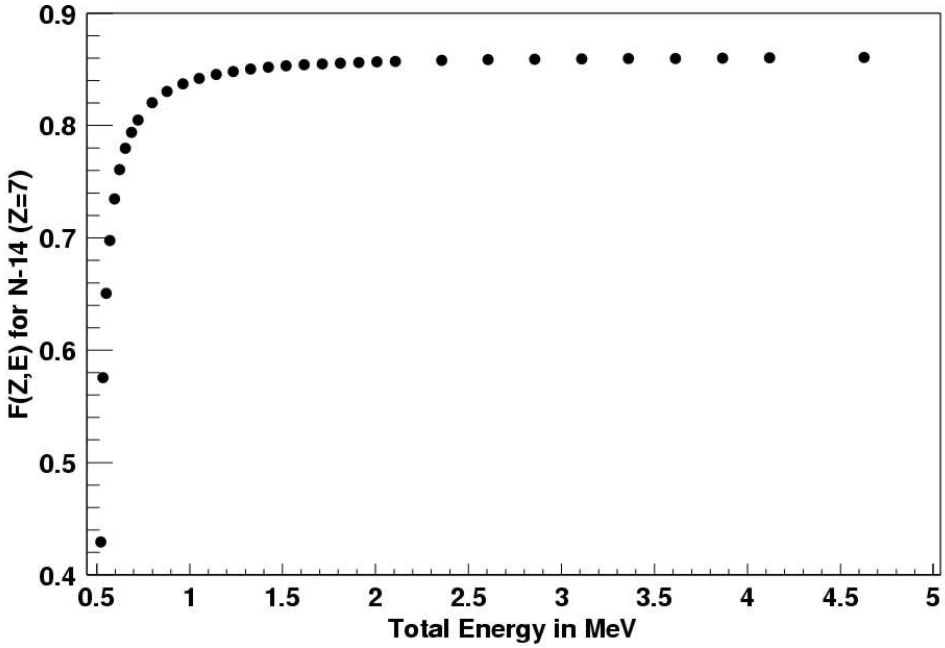

Figure 1.2 Fermi function values for N-14 nucleus.

The ft-value is proportional to the beta decay rate probability per second multiplied by the nuclear matrix elements. The beta decay probability per second is given by

$$P = K\left(G_V^2\left|\int 1\right|^2 + G_A^2\left|\int \sigma\right|^2\right) \quad . \tag{1.7}$$

Where P is the decay probability per second, K is a constant that depends on the units used, G_V is the effective vector coupling constant, $\int 1$ is the vector matrix element, G_A is the effective axial vector coupling constant, and σ is the axial vector matrix element. Only the vector matrix element contributes to Fermi beta decays. The total number of neutrons and protons in the nucleus does change and a new operator is introduced: isospin. The isospin raising operator transforms neutrons into protons and the lowering operator transforms protons into neutrons as discussed in Morita [16]. The vector matrix

element simplifies to become

$$\left|\int 1\right|^2 = \delta_{T_f T_i}\left[T_i(T_i+1) - T_{iz}T_{fz}\right] \quad . \tag{1.8}$$

Here T_i is the isospin quantum number, T_{iz} is z-component of isospin in the initial state, and T_{fz} is the z-component of isospin in the final state. In this formalism protons and neutrons are part of an isodoublet t = ½ with protons represented by t_z = +½ and neutrons by t_z = -½. Consider the ^{14}O nucleus which has 8 protons and 6 neutrons and an isospin of T_z = 8(½) + 6(-½) = 1. This nucleus decays to ^{14}N which has 7 protons and 7 neutrons and an isospin of T_z = 7(½) + 7(-½) = 0. This superallowed Fermi decay has T_i = 1, T_{iz} = 1, T_f = 1, and T_{fz} = 0. These values are used to calculate the vector matrix element

$$\left|\int 1\right|^2 = \delta_{11}\left[1(1+1) - (1)(0)\right] = 2 \quad . \tag{1.9}$$

The Fermi matrix element squared is 2 for all superallowed Fermi transitions with T = 1.

The decay probability per second is inversely proportional to the mean life,

$$P = \frac{1}{\tau} = \frac{\ln(2)}{t_{1/2}} \quad . \tag{1.10}$$

Here τ is the mean life time and $t_{1/2}$ is the half-life of the parent nucleus. Combining equations 1.4, 1.5 and 1.8 we obtain the relationship between the ft-value, G_V, and the matrix element as

$$f(E_o)t = f(E_o)\left(\frac{t_{1/2}}{BR}\right) = \frac{h\pi^2 \ln(2)}{m_e c^2 G_V^2 \left|\int 1\right|^2} \quad . \tag{1.11}$$

The branching ratio (BR) is the superallowed branching ratio. The partial half-life of the superallowed branch is determined by dividing the total half-life by the superallowed branching ratio.

1.3 Fermi Transitions in Beta Decay

Fermi transitions in nuclei can be used to calculate the largest element in the CKM matrix, V_{ud}, when combined with results from pure lepton decay. The V_{ud} component is obtained by dividing the effective vector coupling constant from nuclear beta decay by the effective vector coupling constant from pure lepton decay which does not contain the V_{ud} term,

$$|V_{ud}|^2 = \frac{G_V^2}{G_\mu^2} \quad . \tag{1.12}$$

G_V can be determined from the relationship between the ft-value and the nuclear matrix element for a given Fermi decay as outlined in section 1.3. The left hand side of equation 1.9 only depends on experimentally determined numbers specifically the endpoint energy, half-life, and branching ratio which are discussed in the following sections. There are several correction terms that are needed to account for radiative effects and nuclear isospin breaking. The ft-value with correction terms becomes

$$f(E_o)\left(\frac{t_{1/2}}{BR}\right)(1+\delta_R)(1+EC) = \frac{h\pi^2 \ln(2)}{G_V^2(1+\Delta_\beta)\left|M_{fi}\right|^2(1-\delta_C)} \quad . \tag{1.13}$$

The new terms are: EC the electron capture probability, δ_C the charge correction, Δ_β the inner radiative correction, and δ_R the outer radiative correction. These terms are defined in the following sections.

1.3.1 Electron Capture

Electron capture competes with beta decay. The electron capture can be estimated from the approximate formula given by Morita [17] as

$$\frac{P_K}{P_{add}} = 60\pi\left(\frac{\alpha Z}{E_o}\right)^3 \quad . \tag{1.14}$$

Here P_K is the K-shell electron capture probability, P_+ is the beta decay probability, α is the fine structure constant, Z is the proton number of the radioactive isotope, and E_o is the endpoint energy of the beta decay in units of electron mass, 0.511 MeV. Using ^{14}O beta decay as an example, the formula yields a ratio of 0.000406 for K-shell electron capture relative to beta decay. The probability of L-shell electron capture, P_L, is proportional to the probability of K-shell electron capture reduced by the orbital electron wave function overlap with the nucleus. The formula given by Morita [18] states $P_L \approx 0.125\ P_K$ which gives a value for $P_L = 0.0000508$. The approximate EC probability from K-shell and L-shell orbital electrons is $P_K + P_L = 0.046$ %. This approximation does not concern itself with the Coulomb field of the nucleus and screening effects due to other orbital electrons. These effects were computed and tabulated by Bambynek et al. [19] and used by Hardy [20] to compute the EC probability for ^{14}O, EC = 0.087 %. The approximation of Morita is within a factor of 2 of the more detailed analysis and provides an estimate of the size of the effect. The EC probability varies in magnitude from nucleus to nucleus: the EC probability in ^{14}O is 0.087 % and is 0.104 % in ^{54}Co. In general the EC correction term is smaller for lower Z nuclei. The calculated EC probability has a claimed uncertainty of approximately 5 parts in 100 in reference 20. For ^{14}O the EC probability is 0.087 ±

0.0044 %. With an ^{14}O half-life of 70.600 seconds the EC probability increases the partial half-life by 0.061 ± 0.003 seconds and is a significant correction to the half-life.

1.3.2 Charge Correction

The Coulomb force in the nucleus leads to two types of charge dependent correction terms: an isospin nonconserving force and a shift in the overlap of the radial nuclear wave functions.. The first term, δ_{C1}, is due to the breakdown of the isospin symmetry in the initial and final nuclear states due to the Coulomb force in the nucleus. In one approach the isospin nonconserving interaction is included in determining the nulcear wave functions from the shell model. The wave functions are then used to determine the nuclear matrix element M_F. Hardy [21] and Ormand [22] have calculated the size of this effect using a shell model calculation. The magnitude of this effect in ^{14}O is 0.005 % as listed in Table 6 by Hardy [20]. Note that there is no uncertainty given for δ_{C1} in the literature. The second term, $\delta_{C2,}$ is the result of the distortion of the radial overlap of the initial and final nuclear states. The Coulomb repulsion between the protons in the nucleus causes a radial wave function mismatch between the initial and final state nucleus [20]. The magnitude of the δ_{C2} correction term in ^{14}O is calculated to be 0.23 ± 0.08 %. The uncertainty arises from the uncertainty associated with the nuclear charge radius. The total charge correction term, δ_C, due to the charge dependent effects is 0.24 ± 0.08 % for ^{14}O decay [20].

1.3.3 Outer Radiative Correction

The outer radiative correction term is the result of photon exchange between the proton and the positron. Sirlin and Zucchini have calculated the leading order terms of order $Z\alpha^2$ which can be seen in Figure 1.3 [23]. The outer radiative corrections are vary from nucleus to nucleus due to the dependence on Z as found in the conclusion of Sirlin

$$\delta_R(Z\alpha^2) = Z\alpha^2\left(\ln\left(\frac{m_p}{m_e}\right) - \ln(2E_o) + C + \cdots\right) \quad . \tag{1.15}$$

Here Z is the proton number of the nucleus, α is the fine structure constant, m_P is the proton mass, m_e is the positron mass, E_o is the ratio of the positron energy to the positron rest mass, and C is a derived constant. In general as the Z of the nucleus increases so does the correction term. For ^{14}O this correction term is calculated by Sirlin to be 0.21 %.

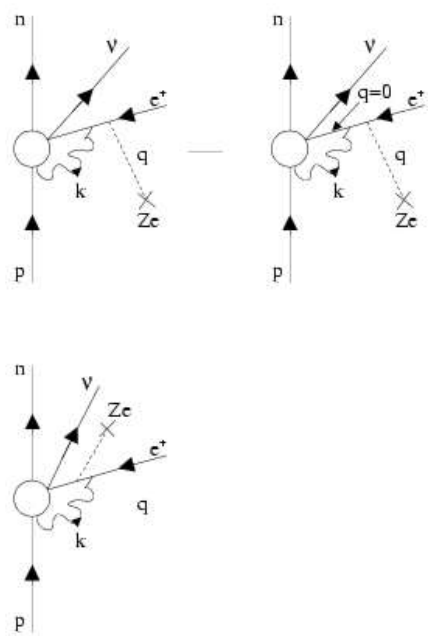

Figure 1.3 Radiative corrections of order $Z\alpha^2$ for beta decay. In the upper diagram, the diagram on the left is subtracted from the diagram on the right with q = 0.

1.3.4 Inner Radiative Correction

The inner radiative correction term depends only on the electroweak theory used to describe the quark interactions with the exchange particles. The inner radiative term does not dependent on the nucleus or its nuclear structure. The inner radiative terms are the result of virtual Z, Higgs, and photon exchanges between the vertex and the W^+ propagator as shown in Figure 1.4 [24].

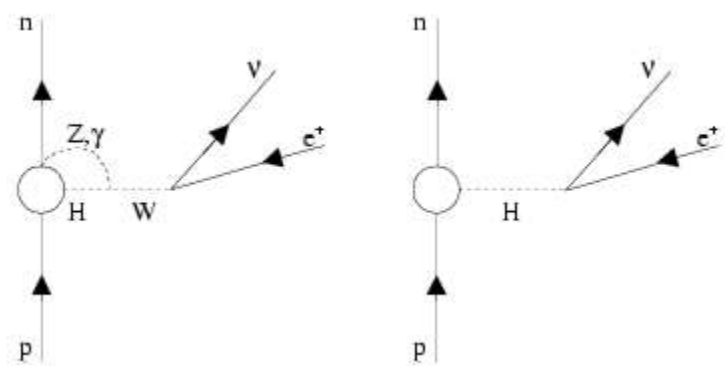

Figure 1.4 Inner radiative processes in nuclear beta decay.

The actual value computed by Sirlin is the difference between the inner radiative correction terms for muon decay and nuclear beta decay [24]. The resulting formula is

$$\Delta_B - \Delta_\mu = \frac{\alpha}{2\pi}\left[4\ln\left(\frac{m_Z}{m_P}\right) + \ln\left(\frac{m_P}{m_A}\right) + 2C + A_g + \cdots\right] \quad . \tag{1.16}$$

Here Δ_β is the inner radiative correction for nuclear beta decay, Δ_μ is the inner radiative correction for muon beta decay, m_Z is the Z boson mass, m_P is the proton mass, m_A is an energy cutoff mass between 400 MeV $\leq m_A \leq$ 1600 MeV. The model dependent constant, C, has a range between $0 \leq C \leq 0.885$. Finally the term A_g is estimated to be -0.34 and is the result of small quantum chromodynamic (QCD) corrections. Marciano and Sirlin [25] evaluated equation 1.14 and find

$$\Delta_B - \Delta_\mu = 0.0237 \pm 0.0018 \quad . \tag{1.17}$$

The V_{ud} element of the CKM matrix is now given by the following relation

$$V_{ud}^2 = \frac{G_V^2}{G_\mu^2(1+\Delta_B-\Delta_\mu)} \quad , \tag{1.18}$$

which takes into account the inner radiative terms of the muon and nuclear beta decay.

1.3.5 Summary of Correction Terms

In general, the correction terms associated with beta decay can be computed with better accuracy and precision for low Z nuclei. With this in mind, a good candidate for study is the ^{14}O isotope with Z of 8 and a branching ratio of approximately 99.3% to the superallowed Fermi transition shown in Figure 1.5. The oxygen isotope, ^{14}O is the focus of the work done for this thesis. There are eight other isotopes that have been used to determine G_V. Figure 1.6 summarizes the available Fermi transition isotopes that exist and their current measurement uncertainties.

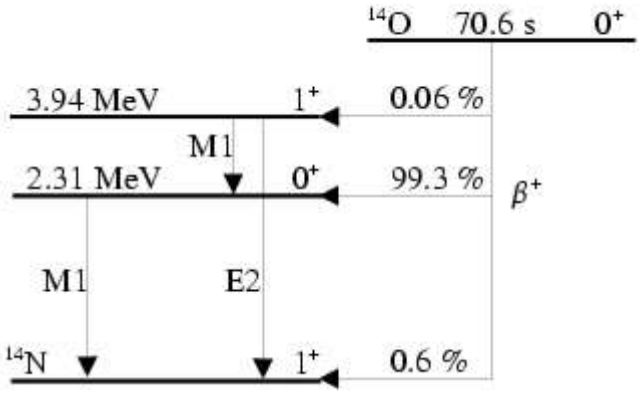

Figure 1.5 O-14 level diagram.

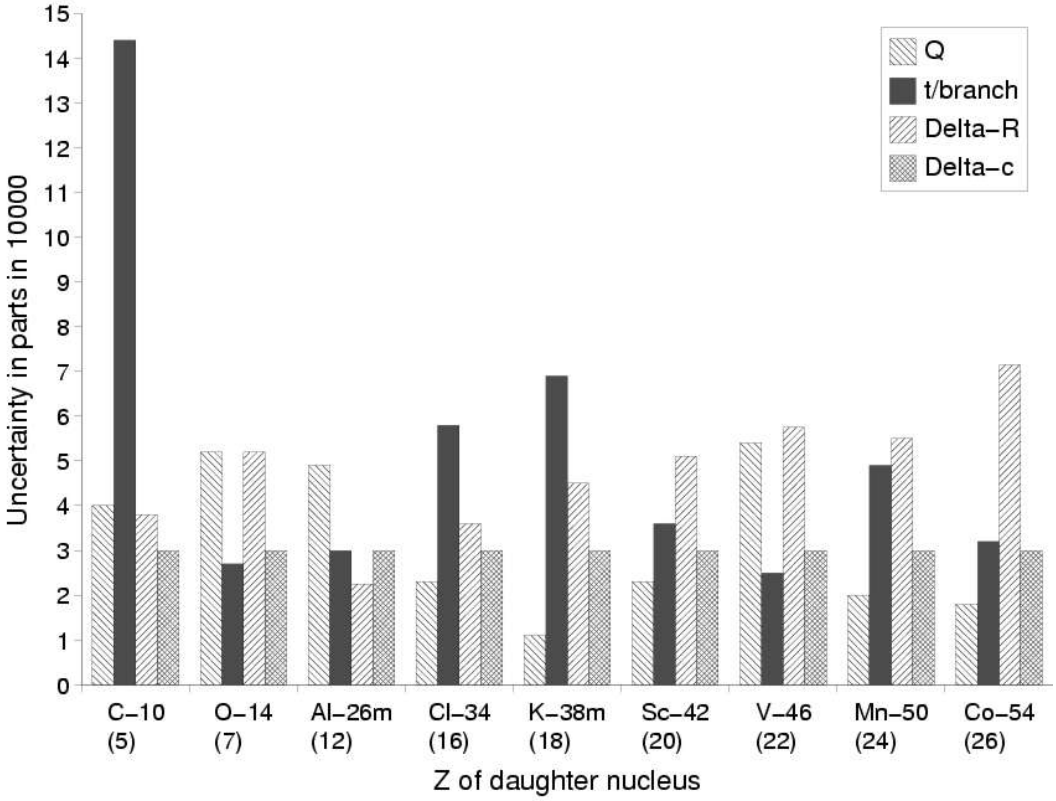

Figure 1.6 Current status of uncertainties for Fermi decays.

1.4 O-14 Q-value

The Q-value is the total rest mass difference between the particles initial and final state involved in a decay. It can be determined by measuring the mass of the initial and final nuclei or by direct excitation of the daughter nucleus. Modern mass measurements can be performed in ion traps specifically designed to measure masses to high precision. Once the masses are known the Q-value is calculated taking into account the mass of created positrons

$$(A,Z)\rightarrow(A,Z-1)+\beta^{add}+\nu_e \qquad Q=(M_Z^A-M_{Z-1}^A)c^2-2m_ec^2 \quad , \tag{1.19}$$

or electrons as the case may be,

$$(A,Z)\rightarrow(A,Z+1)+\beta^{sub}+\overline{\nu_e} \quad , \qquad Q=(M_Z^A-M_{Z+1}^A)c^2 \quad . \tag{1.20}$$

Here M is the atomic mass of the nucleus indicated by A and Z, A is the number of protons and neutrons in the nucleus and Z is the number of protons. The term $2m_ec^2$ in equation 1.16 accounts for the loss of two electron masses due to the beta decay and the orbital electron which is no longer bound to the atom. Also note that the neutrino is assumed to be massless.

Another method is to induce the nuclear reaction as a function of energy. This can be done by varying the energy of an accelerated beam incident on a fixed target as done by Tolich et al. [28]. In the Tolich experiment a proton beam, of known energy, bombarded a ^{14}N target. The ^{14}N target is composed of a gold foil attached to a cold foot whose temperature was between 9 ^{o}K and 10 ^{o}K. The ^{14}N gas solidified on the surface of the 99.995 % pure gold foil. The 2.31 MeV gamma ray from ^{14}O decay was measured as

a function of beam energy. The ten yield curves, each consisting of approximately 27 data points, were then fit to determine the ^{14}O Q-value. The Q-value of ^{14}O has been measured several times with various nuclear rections. The results, methods, and reactions used are summarized in Table 1.3 and plotted in Figure 1.7.

Experiment Year and Reference	***Experimental Method***	***Reaction***	***Q-Value and Uncertainty***
1961 [29]	Excitation threshold	$^{12}C(^{3}He,n)^{14}O$	***2830.6 ± 0.6***
1962 [*30*]	Excitation threshold	$^{12}C(^{3}He,n)^{14}O$ / $^{12}C(^{3}He,p)^{14}N^{*}$	***2832.3 ± 0.6***
1970 [31]	Excitation threshold	$^{12}C(^{3}He,n)^{14}O$	***2832.8 ± 0.5***
1977 [32]	Excitation threshold	$^{14}N(p,n)^{14}O$	***2830.7 ± 0.4***
1977 [33]	Time of Flight	$^{14}N(^{3}He,t)^{14}O$	***2829.9 ± 0.8***
1981 [34]	Excitation threshold	$^{14}N(p,n)^{14}O$	***2830.31 ± 0.08***
2003 [28]	Excitation threshold	$^{14}N(p,n)^{14}O$	***2831.53 ± 0.17***
Currently Accepted Average [27]			***2831.47 ± 0.14***

Table 1.3 Summary of Q-value measurements. Note that the 1981 value was withdrawn after publication and is not included in the weighted average.

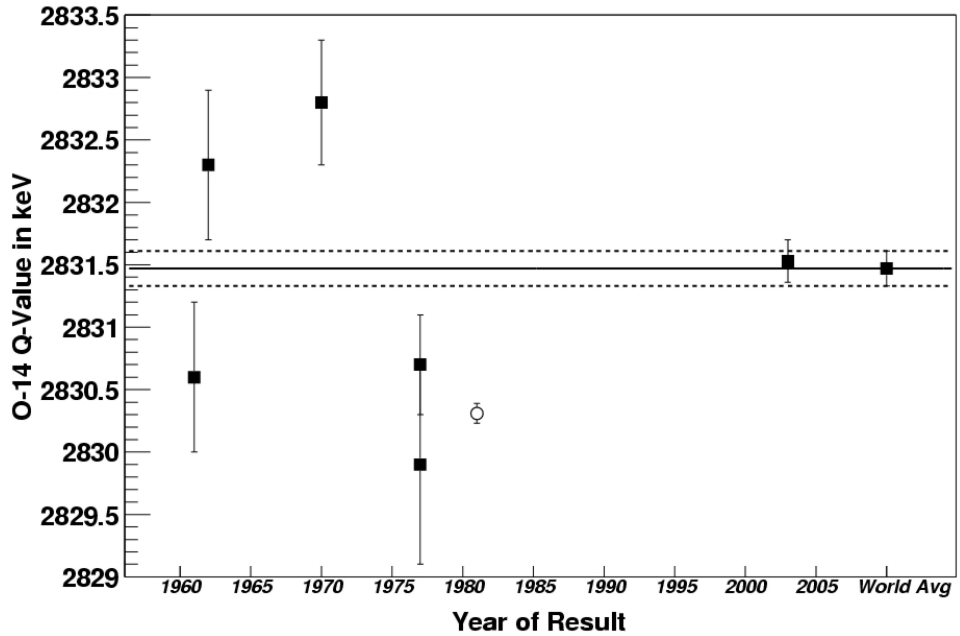

Figure 1.7 Summary of Q-values. The world average result is projected across the plot with dashed lines indicating the 1 sigma uncertainty. The retracted Q-value is indicated by an open circle.

1.5 O-14 Branching Ratio

The branching ratio is simply the relative number of decays that follow the superallowed path as opposed to another final state. In ^{14}O there are three possible transitions as can be seen in Figure 1.5. The relative strengths of each branch are due to the energy difference, the spin, and parity of the initial and final state. The branching ratio is used to determine the partial half-life of the superallowed decay of ^{14}O:

$$t_{Superallowed} = t\left(0^{add} \rightarrow 0^{add}\right) = \frac{t_{1/2}(total)}{B.R.} \quad . \tag{1.21}$$

There are two Gamow-Teller branches in the beta decay of ^{14}O. The larger (0.6 % branch)

Gamow-Teller branching ratio was measured by Sidhu and Gerhart in 1966 [35]. They found the Gamow-Teller branching ratio to the ground state to be 0.61 ± 0.01%. The weaker Gamow-Teller branching ratio (0.06 %) to the 2nd excited state of ^{14}N has been measured three times and is summarized in Table 1.4 and plotted in Figure 1.8. The previous branching ratio experiments and results, as well as this research, are discussed in detail in chapter 5.

Experiment Year and Reference	***Branching Ratio (%)***	***Uncertainty (%)***
1969 [36]	0.0620	0.0070
1980 [37]	0.0577	0.0043
1981 [38]	0.0528	0.0023
Average Value	0.0545	0.0021

Table 1.4 Summary of N-14 G-T ($1^+ \rightarrow 0^+$) branching ratio results.

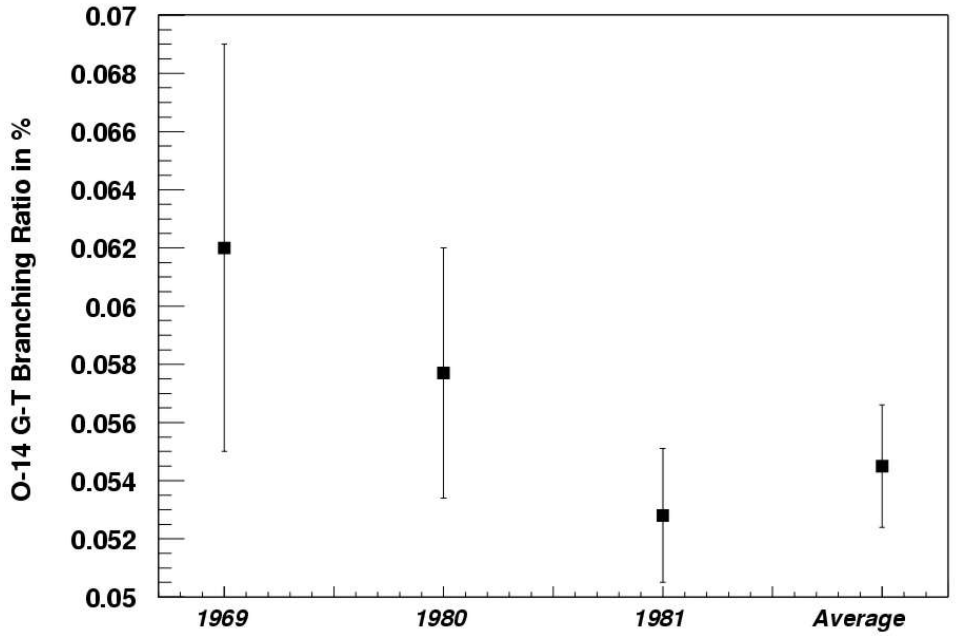

Figure 1.8 Summary of branching ratio of ^{14}O to ^{14}N 3.94 MeV state.

1.6 O-14 Half-Life

The ^{14}O half-life has been measured thirteen times over the past 55 years. The results of the previous half-life measurements are listed in Table 1.5 and plotted in Figure 1.9. In order to improve the uncertainty on G_v the half-life obtained must have a relative uncertainty on the order of 10^{-4} or 0.0007 seconds. In the past, it was not fully appreciated that the choice of statistical technique can systematically bias the final result at the required precision. Experiments performed in the 1960s were analyzed using chi-square minimization which is only justified if the data follow gaussian statistics. In other cases experimenters failed to measure the pile-up effects that are present during the experiment which systematically shifts the final half-life.

In general these experiments measured the ^{14}O half-life by observing the 2.3 MeV

gamma-ray from the decay of $^{14}N^{*} \rightarrow {}^{14}N + \gamma(2.3\ \text{MeV})$. In the experiments various forms of carbon targets were bombarded with a ^{3}He beam to create ^{14}O. After bombardment the target was moved to a counting area where gamma-ray detectors were located. Unfortunately, only three of these results has a precision better than 7×10^{-4}. Note that Clark incorporated the 1971 data sets into the results that were published in 1973, hence the results are not independent.

For various reasons Hardy [20] rejects certain experiments and includes others in calculating a "best value" for the ^{14}O half-life. Only five of these thirteen results are currently used to determine the world average and are summarized in Table 1.6. When these results are combined together the chi-square obtained is 3.150 for 4 degrees of freedom which corresponds to a 53.3% confidence level. The previous ^{14}O half-life experiments and results as well as the results of this research are discussed in detail in chapter 4.

Year of Experiment	*Half-life (seconds)*	*Uncertainty (seconds)*	*Detection Method*	*Nuclear Reaction*	*Target Type*
1949 [39]	76.500	2.000	beta particle	$^{14}N(p,n)^{14}O$	gas
1954 [40]	72.100	0.400	unknown	unknown	unknown
1960 [41]	71.100	0.100	2.3 MeV γ-ray	$^{12}C(^{3}He,n)^{14}O$	solid
1961 [42]	70.910	0.040	2.3 MeV γ-ray	$^{14}N(p,n)^{14}O$	gas
1962 [43]	71.000	0.130	2.3 MeV γ-ray	$^{12}C(^{3}He,n)^{14}O$	Solid
1963 [44]	71.300	0.100	beta particle	$^{12}C(^{3}He,n)^{14}O$	solid
1971 [45]	70.580	0.035	2.3 MeV γ-ray	$^{12}C(^{3}He,n)^{14}O$ $^{14}N(p,n)^{14}O$	solid gas
1972 [46]	70.480	0.150	2.3 MeV γ-ray	$^{12}C(^{3}He,n)^{14}O$	solid
1972 [47]	70.320	0.120	unknown	unknown	unknown
1973 [48]	70.588	0.028	2.3 MeV γ-ray	$^{12}C(^{3}He,n)^{14}O$ $^{14}N(p,n)^{14}O$	solid gas
1974 [49]	70.430	0.180	2.3 MeV γ-ray	$^{14}N(p,n)^{14}O$	solid
1978 [50]	70.613	0.025	2.3 MeV γ-ray	$^{12}C(^{3}He,n)^{14}O$	solid
1978 [51]	70.684	0.077	2.3 MeV γ-ray	$^{12}C(^{3}He,n)^{14}O$	solid
2001 [52]	70.560	0.049	2.3 MeV γ-ray	$^{12}C(^{3}He,n)^{14}O$	Separated implanted source
Average from 1961 Clark to 2001 Gaelens = 70.590 ± 0.015 seconds					

Table 1.5 Summary of all published O-14 half-life measurements.

Year and Reference	*Half-life*	*Uncertainty*
1972 [46]	70.480	0.150
1973 [48]	70.588	0.028
1974 [49]	70.430	0.180

Year and Reference	*Half-life*	*Uncertainty*
1978 [50]	70.613	0.025
1978 [51]	70.684	0.077
Total	70.603	0.018

Table 1.6 O-14 Half-lives used for world average from reference [20].

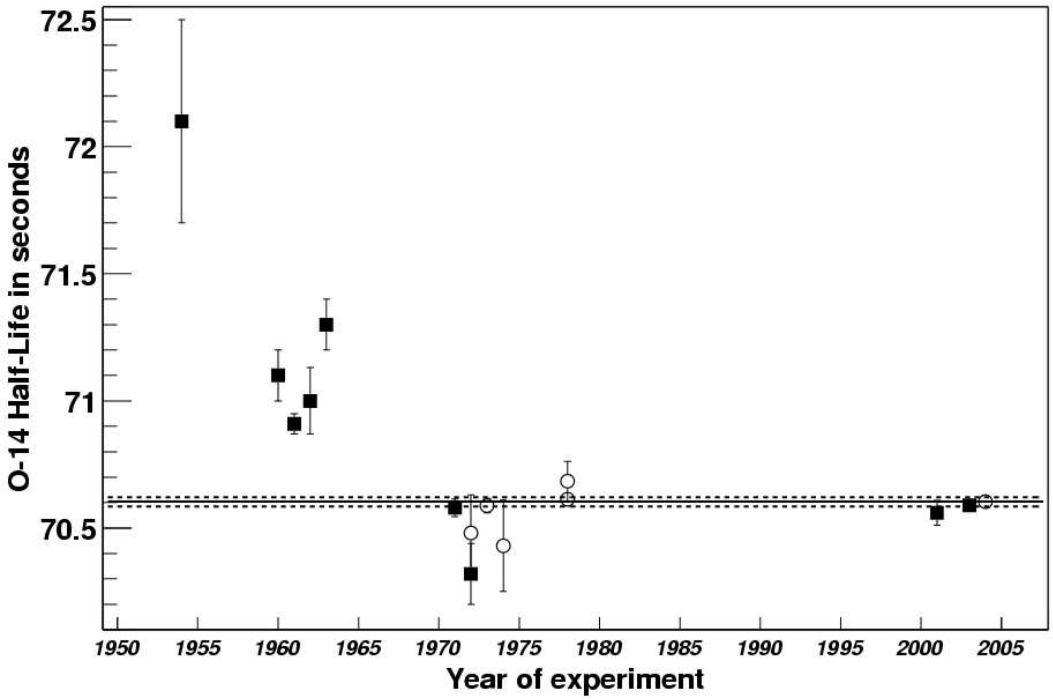

Figure 1.9 O-14 experimental half-life values. Round open markers indicate half-lives included in Hardy [20] compilation of half-life.

Chapter 2

2 Target Designs for Production of O-14 Radioactive Beams

In order to measure the ^{14}O half-life an implanted source of the isotope is desirable. Due to the short half-life (≈ 70.6 seconds) the isotope must be made by a nuclear reaction and measured almost immediately. To this end, an ISOL based radioactive beam test stand was developed at the LBNL 88-Inch Cyclotron. ISOL is an acronym for Isotope Separation On-Line and refers to the separation of short lived isotopes using various chemical, thermal, and electromagnetic based mass separators. The system consists of a high temperature production target, associated vacuum hardware for gas transport, and the ion source test stand which is used to ionize and mass separate the isotope of interest.

Atomic beam techniques, pioneered by Commins [53], were used as early as 1961 at the 60" Cyclotron on the University of California Berkeley campus and then the 88" Cyclotron for the study of ^{19}Ne decay. The most extensive study of this technique was done at CERN in what is now called ISOLDE. The ISOLDE group has been producing various isotopes using a proton beam since 1973. The goals of this group have been to

precisely measure the mass of the isotopes produced, to make isotopes for medical imaging, and improving trapping techniques for various applications. There are currently more than a dozen ISOL-type radioactive beam facilities around the world producing beams for a host of experiments.

The basic concept of the ISOL technique is that a primary beam bombards a fixed target which creates a limited number of isotopes. The target is heated to increase the diffusion rate of radioactive gases. The released gases are transported via molecular flow through a vacuum system which connects the target to an ion source. Upon entering the ion source the radioactive gas is dissociated if necessary and ionized. The ions are accelerated by a high voltage source and focused to form an ion beam. The ion beam passes through a mass analyzing system to select out one mass over charge, M/Q, species. The mass selected beam is focused onto a foil (in this case beryllium) to form an implanted source for experimentation. Figure 2.1 shows the layout of the experiment at the 88-Inch Cyclotron, including the target location in Cave 0, and vacuum transport line connecting the target to the ion source. A detailed schematic of the vacuum system is shown in Figure 2.2.

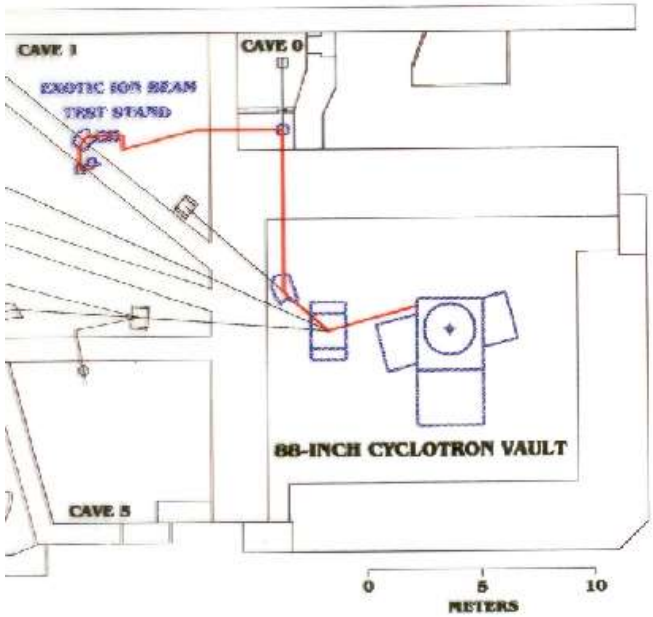

Figure 2.1 Overview of the 88-inch Cyclotron

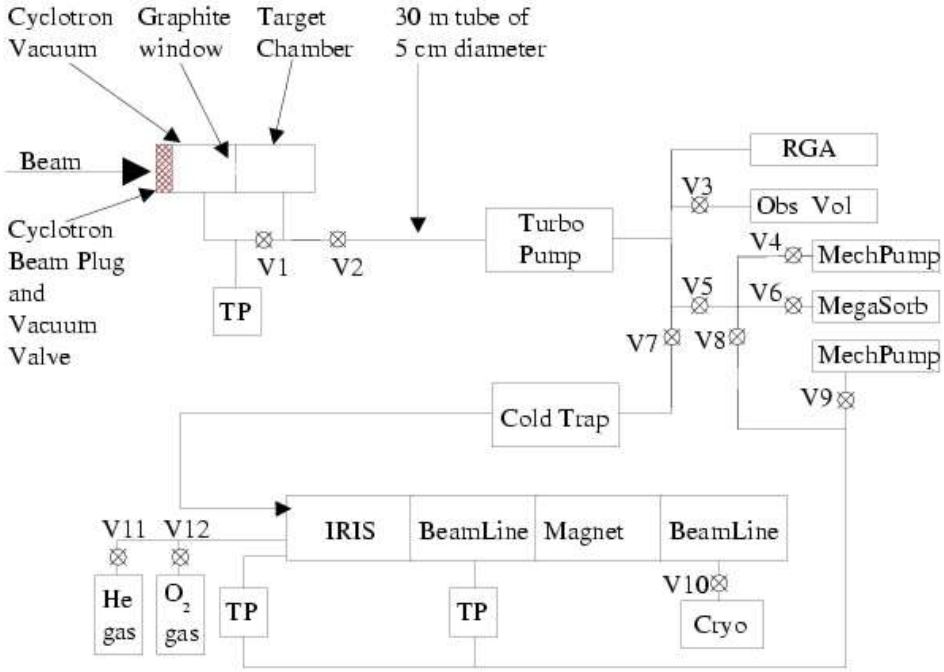

Figure 2.2 Vacuum diagram of the target, transfer line, and IRIS ECR.

The vacuum system is three separate sections interconnected in various ways. The three sections of the system are the target chamber and cyclotron vacuum, the transfer line, and the IRIS ECR and beam line. The target chamber can be isolated by closing valve V2 and opening V1 for pumping through the turbo molecular pump (TP). This configuration allows the target to be conditioned without contaminating the rest of the system. With V2, V3, V6, V7, V8 closed and valve V4 open the the transfer line can be evacuated independently of the ECR and the target. A typical pressure in the transfer line is 10^{-8} Torr (measured at the inlet of the turbomolecular pump) when the transfer line is isolated. The ECR is run in standby mode prior to an experiment with V7 and V8 closed and V9 open to the mechanical foreline pump (MechPump). The stable support gas injection is controlled by valves V11 and V12.

During an experiment the entire vacuum system, aside from the cyclotron vacuum which is isolated, is backed by the MegaSorb foreline pump. The MegaSorb is a cryogenic zeolite adsorption pump with a capacity of 1.5 million Torr-liters. The pump consists of four cylindrical stainless steel vacuum canisters which contain a zeolite compound. The cylinders are immersed in a 60 liter dewar filled with liquid nitrogen at 77 ^{o}K. In the event of a power failure the MegaSorb pump is self-contained and does not release any of the contained activity. If the power fails and no further liquid nitrogen is available, the MegaSorb takes more than 24 hours to start its warming cycle. This corresponds to 72 half-lives of the longest lived isotope which is ^{11}C with a half-life of 20.39 m. In 72 half-lives the ^{11}C activity decays by 22 orders of magnitude which essentially undetectable.

2.1 Carbon Targets for O-14 Production

This experiment used the reaction, $^{12}C(^{3}He,n)^{14}O$, with a 20 MeV $^{3}He^{1+}$ beam incident on a solid natural carbon target. Natural carbon is composed of 99% ^{12}C and 1% ^{13}C. The ^{3}He beam also produces ^{11}C, ^{13}N, ^{15}O, and ^{7}Be via the reactions $^{12}C(^{3}He,\alpha)^{11}C$, $^{12}C(^{3}He,d)^{13}N$, $^{13}C(^{3}He,n)^{15}O$, and $^{12}C(^{3}He,2\alpha)^{7}Be$. Cross section data was obtained from the evaluated nuclear data files located at the National Nuclear Data Center at Brookhaven National Laboratory. Figure 2.3 shows the cross section of the above reactions. Thick target yield is the integral of the cross section up to the beam energy. Thick target yields for these reactions are 2×10^{8} $^{14}O/p\mu A$, 2×10^{9} $^{11}C/p\mu A$, 5×10^{8} $^{13}N/p\mu A$, and 10^{5} $^{7}Be/p\mu A$. The thick target yield is the product of the cross section integrated over the energy of the incident particle. Range of the beam, in a "thick target", is less than the physical target thickness. ^{7}Be does not diffuse out of the target and has a half-life of 53 days. This isotope is only a concern with respect to post-experiment contamination. ^{15}O production rate was estimated by comparing the measured total differential cross section of ^{14}O to ^{15}O found in reference [54]. The total differential cross section for ^{14}O was found to be 73 mb/sr and 124 mb/sr for ^{15}O. An ^{15}O production rate with a target containing 1% ^{13}C is inferred to be $(0.01)x(124/73)x(2x10^{8}\ ^{14}O/p\mu A)$ which yields 3.4×10^{6} $^{15}O/p\mu A$.

Another nuclear reaction with a large cross-section that produces ^{14}O is $^{14}N(p,n)^{14}O$. This reaction requires a nitrogen gas target. Separation of the ^{14}O from the ^{14}N would

require processing of the entire gas volume. The ECR ion source, discussed in chapter 3, cannot tolerate the gas loads that would be present due to this type of target. A nitrogen gas target was not pursued for this reason.

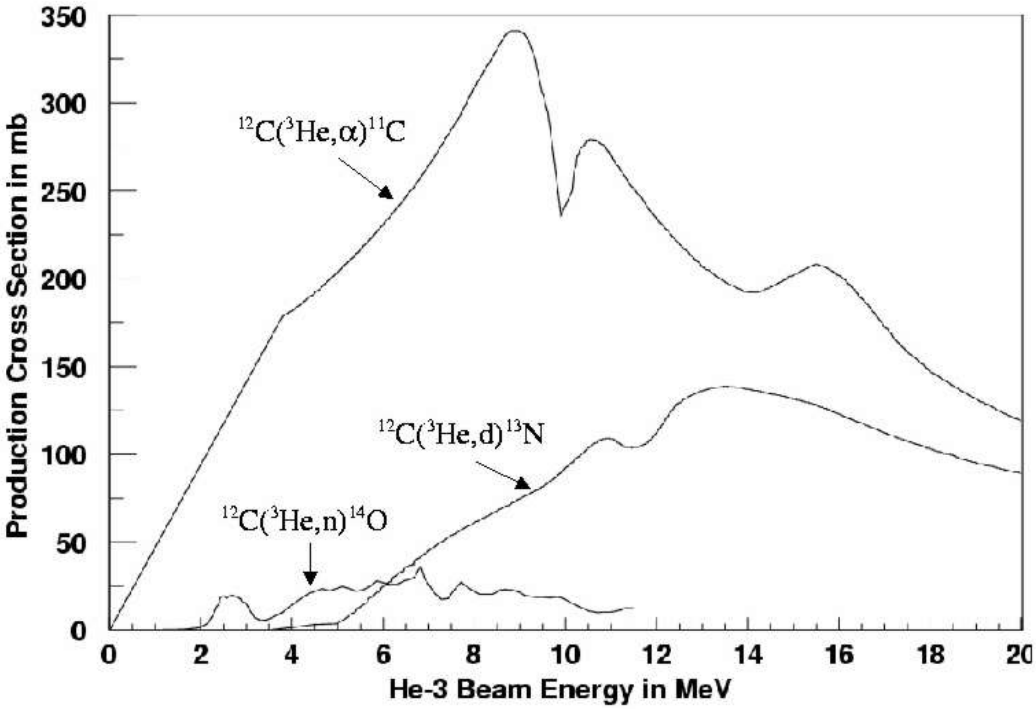

Figure 2.3 Cross-section data for ^{14}O, ^{11}C, and ^{13}N. The data shown here were obtained from the National Nuclear Data Center located at Brookhaven National Laboratory.

This ^{14}O production reaction allows the target to be made of solid carbon. Carbon can be made in a variety of forms; sheets, fiber mats, solid graphite, foams, and more recently aerogel. The ^{14}O formed in the target by the nuclear reaction recoils and stops in the surrounding carbon. In the carbon lattice $^{12}C^{14}O$ or $^{12}C^{14}O^{16}O$ forms and begins to diffuse out of the bulk of the target as a gas. The diffusion rate of the ^{14}O into the vacuum system is the limiting factor in the release efficiency of the ^{14}O. To increase the diffusion

rate the target is heated to a couple of thousand degrees Kelvin. This was demonstrated by the Louvain-La-Neuve group using the reaction $^{12}C(^{3}He,n)^{14}O$ in 1994 [55].

The diffusion of CO molecules out of the target is a complicated process. The CO molecule is initially formed in the microscopic carbon structure of the material. In reticulated vitreous carbon the microscopic structure has interweaving filament structure with filament diameters of hundreds of micrometers. The density of the carbon in these filaments is on the order of the solid carbon density (2.265 g/cm^3). The CO molecule diffuses through the solid carbon to the surface of the filament. The molecule begins diffusing through the volume between the larger filament structure until it finally reaches the exterior surface of the target. From the exterior surface of the target the molecules travel via molecular flow up the transfer line and pass through the turbomolecular pump.

One way to decrease the diffusion time is to reduce the distance the CO molecules travel through the solid carbon microstructure. Carbon aerogel material has a "mother of pearl" filament structure with diameters on the order of a few hundred nanometers. The molecules travel approximately a 1000 times shorter distance to the surface of the microscopic structure. The molecules diffuse through the volume between filaments until they reach the exterior surface as described above. The drawback to this structure is the reduced mean free path due to the density of the smaller filaments. Decreasing the diffusion time of the CO molecules increases the efficiency of the target. In the end experiment shows that carbon aerogel has a better release efficiency than reticulated vitreous carbon by a factor of 5. These targets and materials are discussed in the following sections of this chapter.

The dominant heat loss mechanism for the target at these temperatures is radiative. The loss rate can be calculated using the blackbody radiative equation,

$$P = A \sigma T^4 \quad , \tag{2.1}$$

where P is the power radiated in Watts, A is the area of the radiating surface in meters squared, σ is the Stefan-Boltzmann constant, and T is absolute temperature in Kelvin. A typical target with dimensions 3 cm x 3 cm x 0.5 cm has an area of approximately 25 cm^2. At a temperature of 2000 ^oC the power radiated is ≈3800 watts. The chamber in which the target resides must be actively cooled. Figure 2.4 is a photograph of the vacuum chamber used to house the target, wrapped with copper cooling coils.

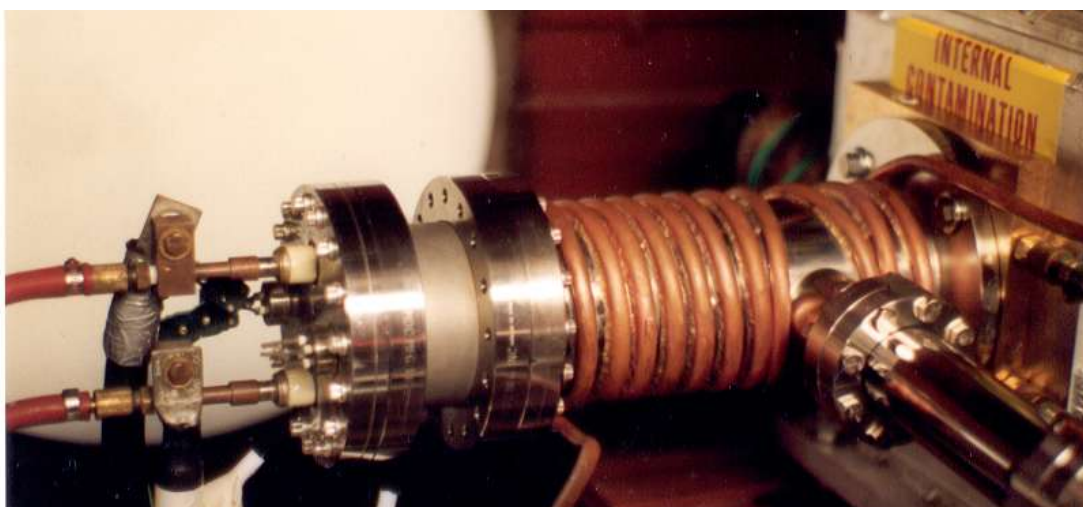

Figure 2.4 Target chamber shown with electrical feed through

The target was heated by passing electrical current directly across it, illustrated in Figure 2.5. This required connecting both sides of the target to a water cooled electrical leads. The leads were thermally isolated from the target with graphite standoffs. The

electrical contact was ensured by bolting the target edges in place under compression using a small amount of graphite fiber. The graphite fiber ensured that the target could expand laterally avoiding mechanical stresses associated with heating and

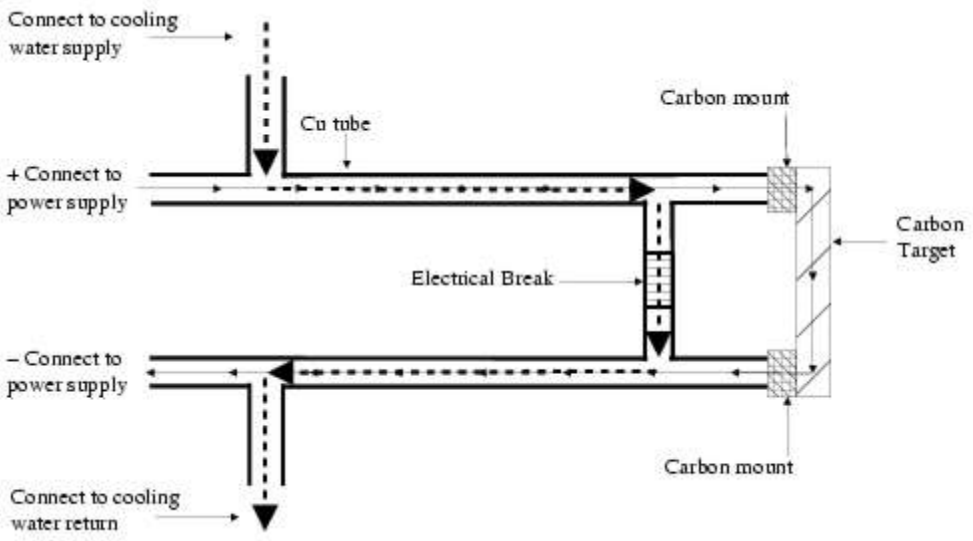

Figure 2.5 Electrical and cooling water schematic of target

cooling. The electrical leads were connected to a variable direct current power supply. The power supply, an ESS model 40V-250A, is a low voltage high current supply. The power supply was interlocked to the cooling water supply shutting off automatically if the water flow is interrupted. Four designs were tested before until the final material and target configuration was established.

2.2 Indirectly Heated Carbon Fiber

The first target design used the same basic indirect heating technique as the sodium atom trapping experiment at the 88-Inch Cyclotron [56]. A piece of carbon fiber mat 0.64 cm thick was placed in a tantalum filament, see Figure 2.6.

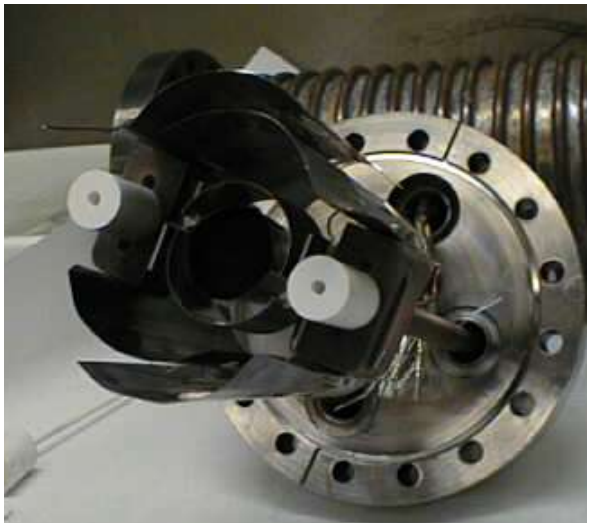

Figure 2.6 Tantalum filament with carbon fiber target

The tantalum was connected to the copper electrical vacuum feed through. The electrical leads were connected to a 10 V 500 A EMI power supply. The resistance of the tantalum filament ranges between 0.004 ohms when cool to 0.007 ohms when hot. The temperature of the carbon was determined by observing the blackbody radiation using an optical pyrometer to within ± 100 degrees Celsius. Figure 2.7 below shows the target temperature versus power curve.

Two experimental runs were performed using the carbon mat as a target. The ^{14}O rate was measured using a germanium detector. The detector was set to monitor the 2.31 MeV peak from ^{14}O decay. The efficiency of the detector was calibrated using a ^{228}Th

sealed source. The ^{228}Th source decay chain has a branching ratio of ≈32% to ^{208}Tl which emits a 2.6 MeV gamma ray. The measured amount of ^{14}O released from the target was $2.25 \pm 0.2 \times 10^5$ per second. This corresponded to a release efficiency of approximately 0.02 %. The tantalum is several hundred degrees hotter than the carbon depending on the temperature. At temperatures above approximately 1500 degrees Celsius the tantalum forms a vapor in the vacuum chamber that acts as a getter pump. The CO molecule is pumped onto the fresh surface of tantalum on the vacuum chamber wall. When CO molecules strike the tantalum surface they form TaO and TaC. After the second experimental run there was an observable tantalum layer deposited on the surface of the carbon fiber. This method was then abandoned for the target design discussed in the next section.

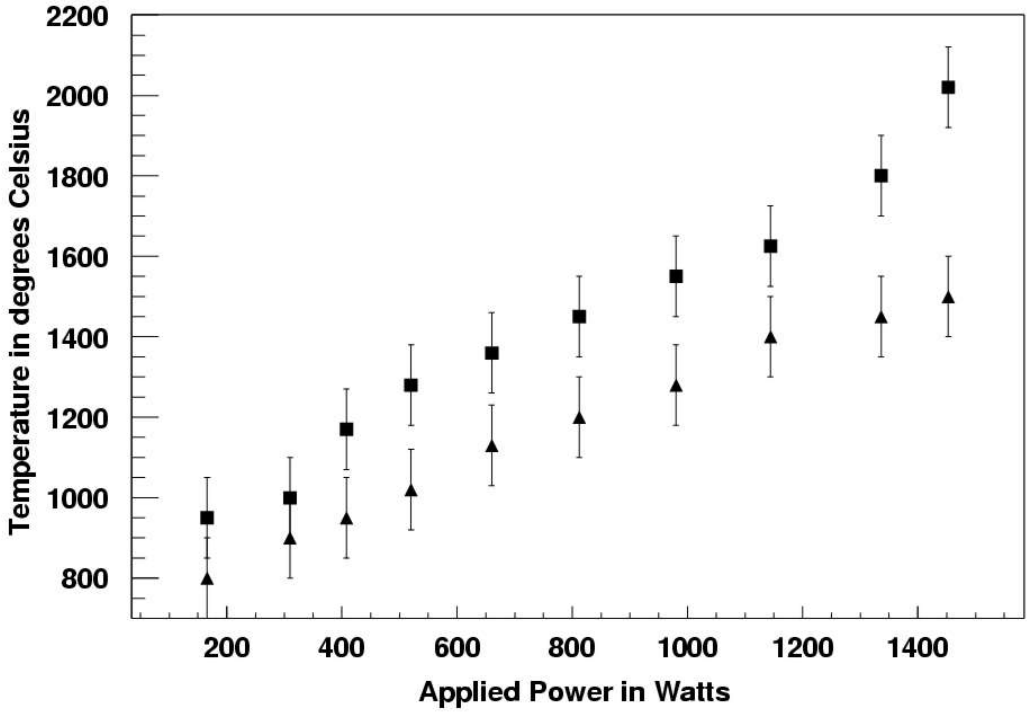

Figure 2.7 Tantalum target temperature versus power. Square markers represent the tantalum filament and the triangle markers represent the carbon fiber.

2.3 Reticulated Vitreous Carbon

In order to avoid chemical reactions at high temperatures a new approach was to use a solid piece of reticulated vitreous carbon (RVC). This self supporting target is heated by passing direct current through it thereby removing the need for any heated metal filaments. RVC is a material used in the aerospace industry for heat shielding or thermal insulation. RVC has a porous structure similar to a sponge with several hundred micron diameter filaments. The microscopic structure of each filament is amorphous graphite. This was determined by taking a few samples to the Center for Electron Microscopy at LBNL and performing transmission electron microscopy. The narrow beam transmission photograph in Figure 2.8 shows symmetric diffraction rings consistent with an amorphous structure.

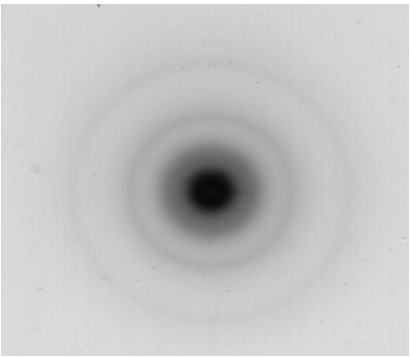

Figure 2.8 Transmission electron micrograph of RVC material.

An old vapor deposition vacuum chamber was refurbished and used to test a sample of the material. This test proved that the RVC could be directly electrically heated in vacuum and reach temperatures exceeding 1500 degrees Celsius. The temperature versus power graph is shown in Figure 2.9 and was determined using the optical pyrometer technique discussed previously.

The target shown in Figure 2.10, was fitted with two concentric graphite heat shields with a hole to allow the beam from the cyclotron to strike the broad side of the RVC. The graphite heat shields are supported by two boron nitride disks which electrically isolate the heat shields. The target is heated with direct current through it via electrical contacts at either end.

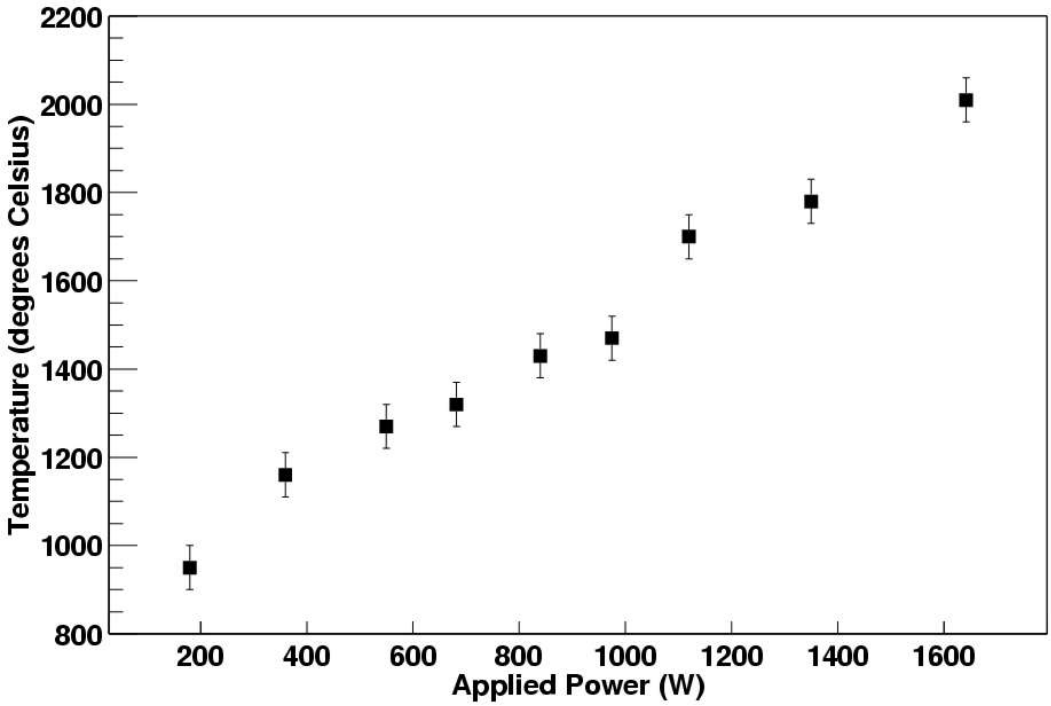

Figure 2.9 RVC target temperature as a function of applied power.

During the second test run with the RVC, the temperature of the target approached 1800 degrees Celsius due to beam heating and power supplied to the target. The vacuum pressure in the target chamber was 4 x 10^{-6} Torr with 2 pμA of beam on target. This was higher than in the previous runs and it was not simply a transient effect due to outgassing. Upon inspection of the target it was apparent that the boron-nitride

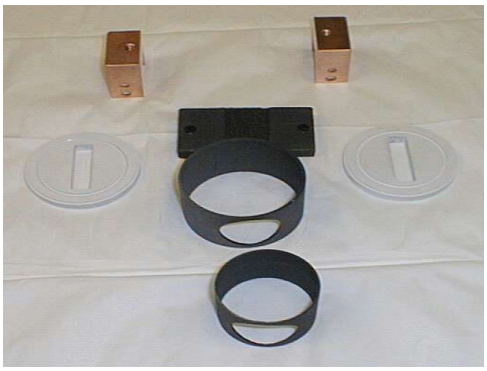

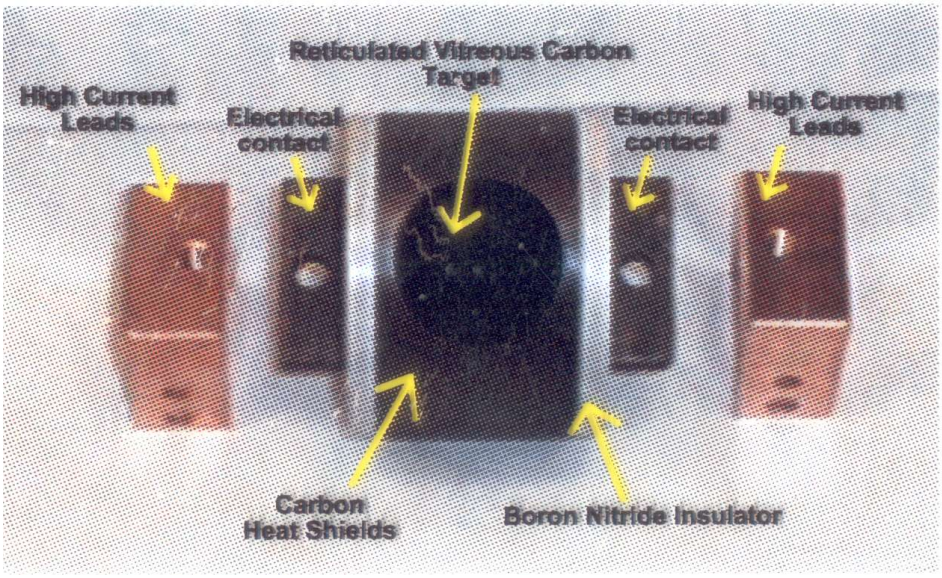

Figure 2.10 Assembled RVC target with heat shields installed

insulator had sublimated where it was in contact with the RVC. The RVC target tested in August 1998 had an improved release rate shown in Figure 2.11. The 2 puA beam on target produced approximately 5.4 x 10^6 ^{14}O atoms per second arriving at the end of the transfer line. This rate was monitored with a pair of NaI detectors detecting the annihilation radiation from the beta decay. A germanium detector monitored the 2.31 MeV gamma ray peak from the ^{14}O decay. The radioactive gas from the output of the turbo molecular pump, just upstream of the ECR, was shunted into a fixed volume for a

specific period of ≈200 seconds. The radioactivity was counted to identify half-lives and to establish the production rate of the radioactive isotopes. The time dependence of the count rate discriminates between ^{11}C, ^{13}N, and ^{14}O with half-lives of 20.4 minutes, 9.96 minutes, and 70.6 seconds respectively. With 2 pμA of ^{3}He bombarding the target at a temperature of 1750 degrees Celsius the ^{14}O rate at the output of the turbo molecular pump was 5.5 x 10^{6} per second. This corresponds to a release efficiency of 1.4 %, an improvement of a factor of 62 over the tantalum filament design.

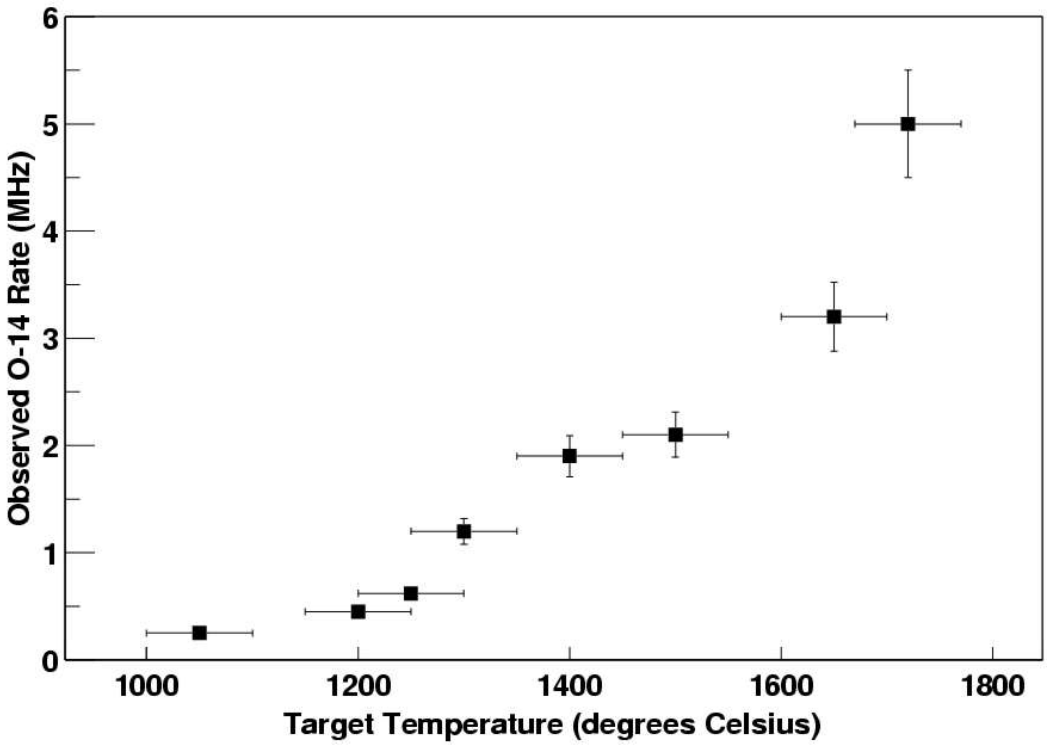

Figure 2.11 RVC target release rate as a function of target temperature.

2.4 RVC and Solid Carbon Heat Shields

In order to eliminate the boron-nitride standoffs an RVC target with an all carbon heat shield design (shown in Figure 2.12) was constructed and put in place in August 1999. The two halves of the heat shield overlap but do not touch. The electrical contact is made by two graphite yokes (shown in Figure 2.13) that mount on the copper electrodes and hold the heat shield and target in place. During the bakeout process, the vacuum pressure was higher than the previous target design. This was due to the larger mass of graphite carbon in the heat shields and supports. Unfortunately while the target was being baked out and calibrated the power supplies failed allowing unregulated 460 volts onto the electrical feedthroughs. The closest surface of the heat shield arced over to the other heat shield and formed a carbon arc plasma which vaporized 30 to 50 percent of the heat shielding and destroyed the target. Target design three never saw beam from the 88" Cyclotron.

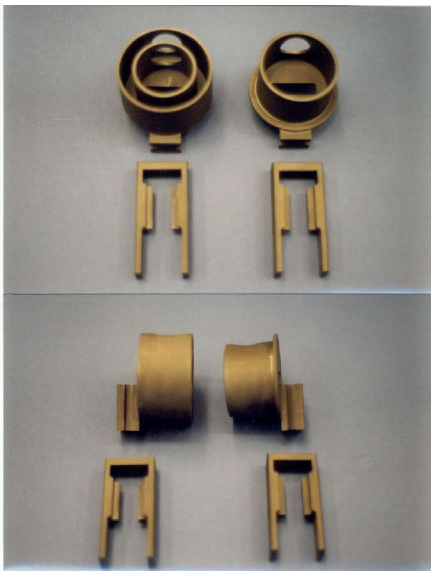

Figure 2.12 Target design two carbon heat shields are shown.

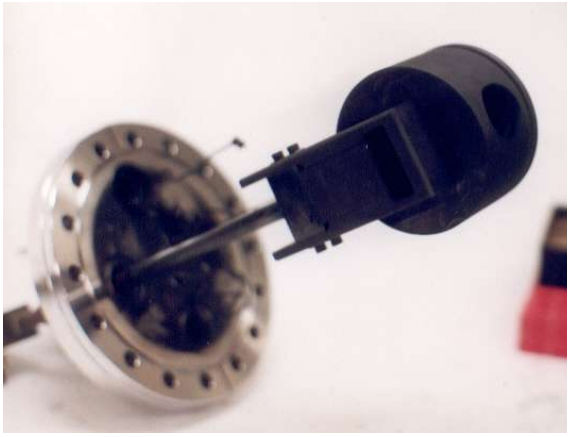

Figure 2.13 Target three design mounted on flange for insertion into target chamber.

2.5 Carbon Aerogel

Larger release efficiency requires a smaller scale microscopic structure. One of the smallest scale micro-structure materials in the world is silica aerogel. A similar process that forms silica aerogel was created to manufacture carbon aerogel. The material created specifically for this experiment was manufactured by Ocellus Inc. A "high density" carbon aerogel was designed which has 100 nanometer filaments (shown in Figure 2.14) and a density of 0.250 grams per cm^3 . The carbon aerogel has an open porosity that is estimated at 10^4 times that of graphite. Open porosity is the internal surface area per unit volume of a solid. During initial testing of the carbon aerogel it was noted that the core of the target had sublimated while the surface temperature had not exceeded 2000 degrees Celsius. Carbon sublimates at a temperature of 3500 degrees Celsius. This indicated that the radiative insulation of the material allowed it to support a temperature gradient of approximately 400 degrees Celsius per mm. The finer

microscopic structure of the aerogel allows only the outside surface to radiate energy. Compare this to the RVC carbon which has many dimples and surface imperfections which effectively increases the radiating surface area. This allows the use of less power to achieve the temperature needed for the experiment. Figure 2.15 illustrates the different power requirements of an RVC target to that of an aerogel target of similar dimensions.

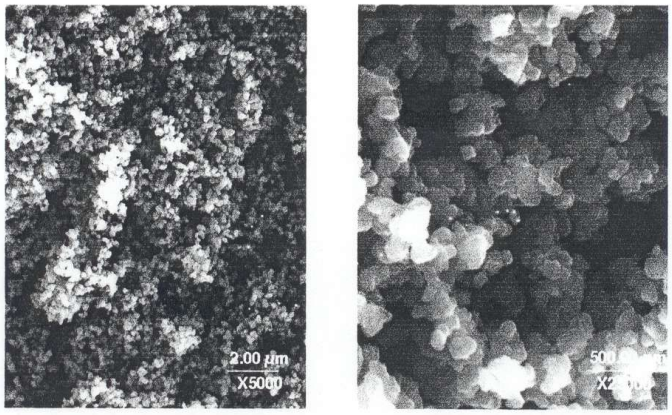

Scanning Electron Microscopy views (2 and 0.5 μ) of the morphology of low-density carbon nanocellular solid

Figure 2.14 Scanning electron microscope photo of carbon aerogel. Courtesy of Ocellus Inc.

The aerogel is manufactured using a process that fixes a large number of carboxyl groups to the carbon lattice, X-COOH. This can be seen when the target is heated above a few hundred degrees Celsius by monitoring the residual gas spectrum. The residual gas analyzer (RGA) attached to the transfer line shows large amounts of water vapor, carbon monoxide, and carbon dioxide. These species decrease in

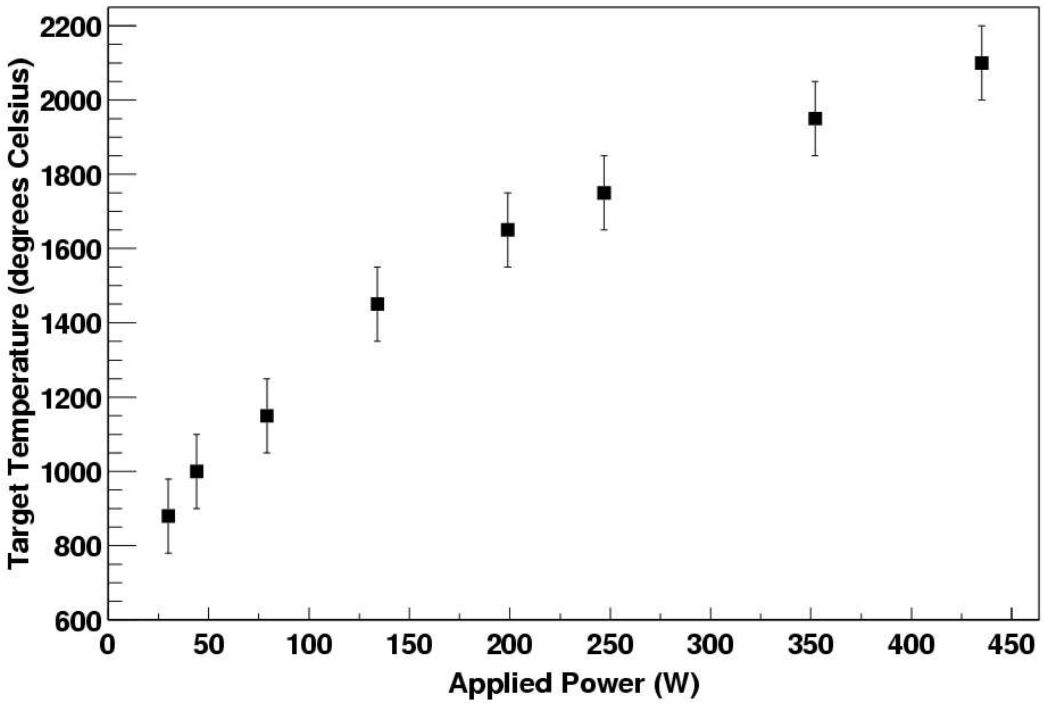

Figure 2.15 Aerogel target temperature as a function of applied power.

abundance as the target is heated until the vacuum pressure approaches the 10^{-7} Torr region after several days. During the bakeout procedure the amount of oxygen present in the target decreases. The oxygen present in the target is the limiting factor in the production and transport of $^{13}N^{16}O$ and $^{11}C^{16}O$ to the ion source. The reduction of ^{11}C and ^{13}N transport is desirable in that they are backgrounds for the half-life experiment which is discussed in chapter 4. The target is conditioned for three or four days before an experiment. The conditioning or bakeout occurs by heating the target to approximately

500 degrees Celsius and holding it at this temperature for several days. The oxygen in the target forms CO and CO_2 and diffuses out of the target. The relative amount of CO and CO_2 present is measured by the RGA located on the gas transfer line shown in Figure 2.2.

Typically the initial pressure in the target vacuum chamber is 1.5×10^{-6} Torr prior to the bakeout. After 4 days at approximately 500 degrees Celsius the pressure has dropped to 1.5×10^{-7} Torr. The CO_2 outgassing rate is approximately 84 times smaller as measured by the RGA peak at mass 28. The CO_2 outgassing rate is approximately 144 times smaller as measured by the RGA peak at mass 44.

More important is the reduction of the outgassing rate by pyrolyzing the target in vacuum. The ionization efficiency of the ion source is negatively correlated with the gas load. As the gas load increases the ionization efficiency decreases. The efficiency of the ECR ion source is discussed in chapter 3.

The release efficiency of ^{14}O is determined by measuring the ^{14}O rate at the output of the turbo molecular pump and dividing by the calculated thick target yield for a given beam intensity. The thick target yield for ^{14}O from the measured cross-section is 2×10^{8} atoms per particle micro ampere of beam. Steady state production is reached after approximately 5 half-lives or 350 s. The ^{14}O rate at the output of the turbo molecular pump (shown in Figure 2.2) is measured by pumping the atoms into a closed volume. The activity of the volume is measured with a germanium detector which monitors the 2.31 MeV gamma ray. The efficiency of the germanium detector is calibrated with a ^{228}Th source as previously discussed. The equation for release efficiency is

$$Release\ Efficiency = \frac{Measured\ Activity(Hz) \times Correction\ for\ Germanium\ Efficiency}{Beam\ current \times Production\ Cross-section} \quad .$$

The carbon aerogel has a measured release efficiency of 45 ± 5 % with 5 pμA on target at a temperature of 2000 degrees Celsius. This is an improvement of approximately 2000 times over the tantalum target design and 32 times better than the RVC target. The overall efficiency, including ionization and extraction discussed in chapter 3, achieved in this system is approximately an order of magnitude better than any system currently available.

There is approximately 12 ± 0.6 mCi of ^{14}O flowing through the transfer line per second and special precautions must taken to avoid exposure to the radiation fields. The 12 mCi of ^{14}O can generate radiation fields up to 1200 mRem/hr if confined to a volume of a few hundred cm^3.

Gradual sublimation of the target by the beam occurs due to local beam heating. However the local heating enhances the release of the CO molecules. The sublimation rate can be reduced by expanding the beam area and reducing the energy deposited per unit volume. Experimental run times exceeding 60 hours have been achieved.

Chapter 3

3 Electron Cyclotron Resonance Ion Source Performance

An ion source is a device that converts a solid or gaseous species into a neutral plasma from which ions can be extracted and accelerated. Two major concerns for producing radioactive beams are the reliability and efficiency of the ion source.

Various ion sources use heated filaments in various arrangements to produce a plasma. Others use a high voltage arc to produce a plasma. These types of ion sources have limited operational lifetimes due to the destructive nature of the arc or filament. An ECR ion source uses microwaves to create a plasma. There is no direct contact of the source for ionization and the plasma, ie: no filament to wear out. ECR ion sources have long operational lifetimes, on the order of years, which creates reliable and repeatable operating conditions.

The ion source efficiency for converting a neutral gas into a specific charge state beam is usually the highest loss mechanism in the ISOL process. Initially a multiple-CUSP ion source was tested for this research. It was abandoned due to its poor ionization efficiency and antenna lifetime which is discussed in section 3.1. ECR source

performance can be tailored to maximize the efficiency for a specific charge state. The CUSP source employed initially (discussed in section 3.1) was replaced with a compact ECR source, more suited to this experiment. The pertinent physics of ECR sources in general and the performance of the IRIS ion source specifically is covered in section 3.2.

3.1 Multiple-CUSP Ion Source

The multiple-CUSP ion source we tested consisted of a small (≈1 liter) cylindrical vacuum chamber surrounded by a sextupole magnetic field, see Figure3.1. The back of the source contains an antenna feedthrough and gas injection ports. The plasma was extracted out the opposite side through a cylindrical hole located on the central axis of the main cylinder. The plasma was produced by feeding 13.56 Mhz radio frequency (RF) power into the chamber via a helical shaped antenna. The electrons in the chamber were accelerated by the RF field near the antenna. The accelerated electrons collided with the neutral gas molecules and ionized them creating a plasma. The resulting plasma was confined by a magnetic field produced by 14 separate lengths of samarium-cobalt permanent magnets located around the circumference of the main vacuum chamber. The multiple-CUSP source operated at a relatively high pressure, in the 10^{-3} Torr range. This is an advantage in that a higher gas load can be tolerated compared to an ECR ion source which operates in the pressure range of 10^{-6} Torr or less. The disadvantage of a CUSP source is the limited antenna lifetime and ionization efficiency.

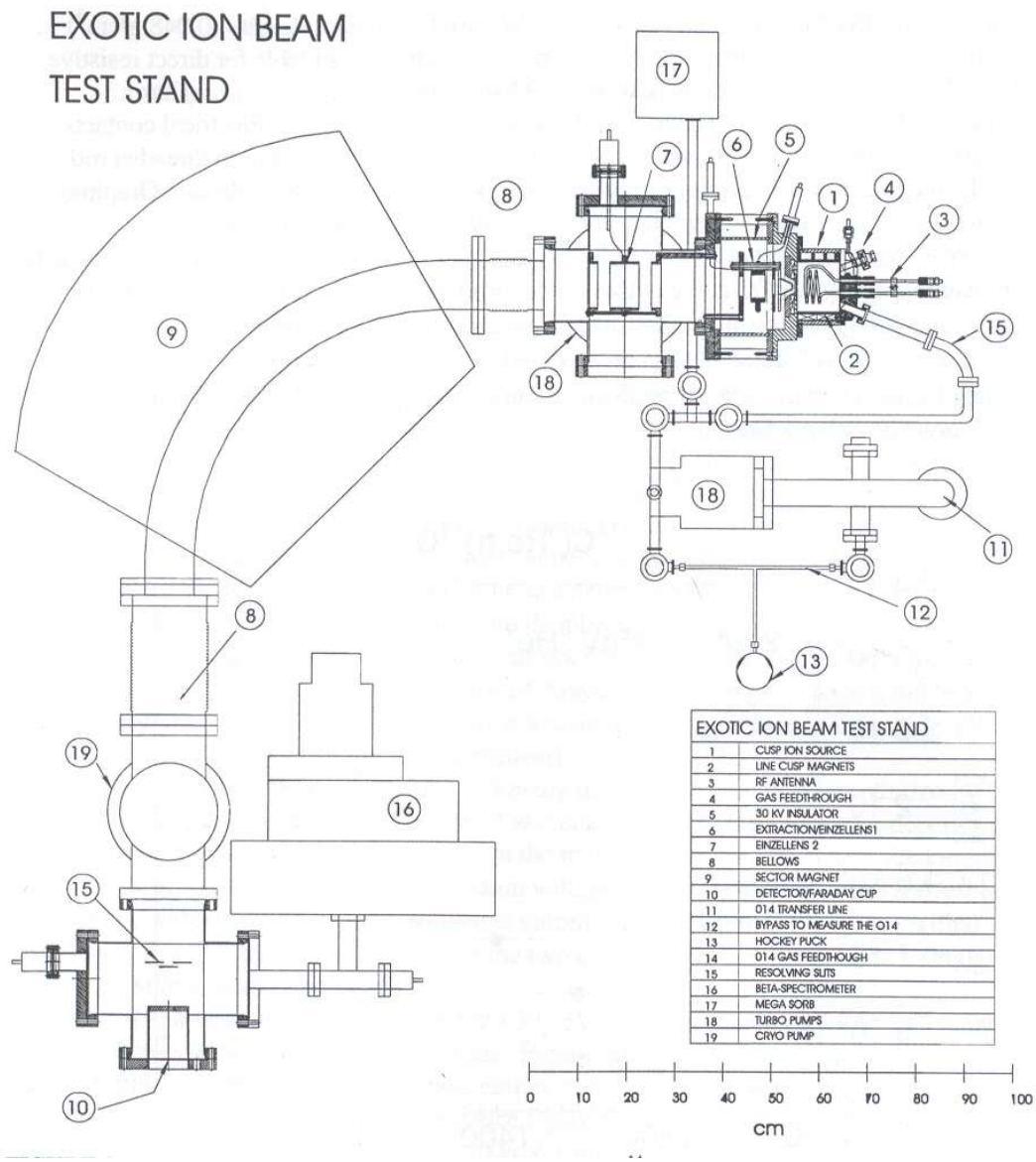

Figure 3.1 Schematic of CUSP source mounted on the test stand. The CUSP source received radioactive gas from the transfer line which connected it to the target. The ions

created in the CUSP source were then extracted at energies on the order of 20 keV and filtered by the analyzing magnet. The resulting ion beams could be measured by the Faraday cup located at the end of the beam line.

3.1.1 Antenna Lifetime

There are several antenna designs for CUSP sources, none to date meet the criteria for this experiment. In order to perform the lifetime experiment the ion source must be able to run continuously for approximately 50 hours. Since the antenna of the CUSP source is in intimate contact with the plasma it gradually erodes.

The first antenna design consisted of a hollow copper tube coated with a layer of porcelain to electrically isolate the antenna from the high voltage applied to bias the plasma. The copper tube was cooled by running chilled water through the hollow core to dissipate the heat due to the RF power. After an operational time of several hours the porcelain was eroded by the plasma and the bias voltage shorted to the antenna.

The second antenna design consisted of a hollow quartz tube through which a thin copper wire was passed. Water flowed through the hollow quartz tube to cool the wire. After several hours the heat stress and plasma erosion on the quartz tubing fractured the tube and allowed water to freely enter the vacuum chamber. Both of these failure modes required removing the antenna from the source and replacing it completely.

3.1.2 Ionization Efficiency

While either antenna was functional, the ionization efficiency of the ion source

was measured using a calibrated CO gas leak. This method involves injecting a known rate of CO molecules via one of the gas injection ports shown in Figure 3.1. The source was optimized to produce an intense oxygen beam and allowed to stabilize. Once stable, the calibrated gas leak was closed off from the source, and the change in ion beam current was measured as a function of time. The difference in oxygen ion current was then divided by the calibrated leak rate and the ionization efficiency was determined. The highest ionization efficiency achieved was 0.7 % for a O^{1+} ion beam [57]. This is 37 times less efficient than the AECR-U ECR ion source used at the 88-Inch Cyclotron that was tested using the same technique. Based on these comparisons it was decided to replace the CUSP source with an ECR ion source.

3.2 IRIS Electron Cyclotron Resonance Ion Source

In general, an ECR ion source consists of a cylindrical vacuum chamber (or plasma chamber) with two solenoid magnets, a sextupole (or higher order) radial magnetic field, a microwave radiation field, a gas injection port, a vacuum pumping port, and an extraction orifice. ECR ion sources dissociate and ionize neutral molecules and atoms by direct electron collisions. Electrons in the chamber are driven in cyclotron orbits by a combination of microwave radiation and externally applied magnetic field. Where the microwave frequency and magnetic field are resonant with the electron cyclotron frequency, a plasma surface is formed. In this region, neutral atoms undergo collisions with energetic electrons and become ionized.

The pertinent characteristics of the Ion Source for Radioactive Isotopes (IRIS) ECR which is shown in Figure 3.2 are discussed below. General information on ECR sources can be found in Brown [58] and Geller [59].

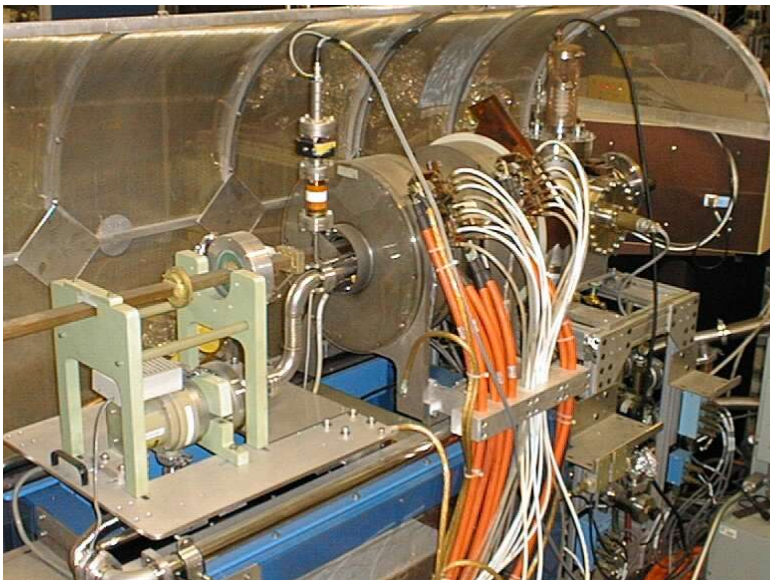

Figure 3.2 IRIS ECR injection side at left and extraction side on the right.

3.2.1 IRIS Plasma Chamber

The IRIS plasma chamber is a 13.5 cm diameter by 28 cm long tube made of aluminum. The total volume of the chamber is approximately 5 liters. The plasma chamber is double walled to allow for cooling water. It is necessary to cool the aluminum chamber due to the heat load from the plasma. The injection side of the chamber has a vacuum flange with ports for a microwave guide, a 3.4 cm diameter vacuum pumping port, and a 0.64 cm and 1.90 cm diameter neutral support gas injection ports and are

shown in Figure 3.3. The chamber is connected to a 110 liter per second turbomolecular pump. The geometry of the vacuum flanges and port size limits the pumping speed at the plasma chamber to approximately 4 liters per second and the residual neutral gas was pumped out every 1.25 seconds on average. The 0.64 cm diameter gas injection port is connected to a gas manifold which allows the introduction of various stable gases. Support gas species and presseure are varied to optimize the ionization efficiency of the radioactive isotopes as discussed in section 3.2.6. The 1.90 cm diameter gas injection port is connected to the radioactive gas transfer line described in section 3.2.5.

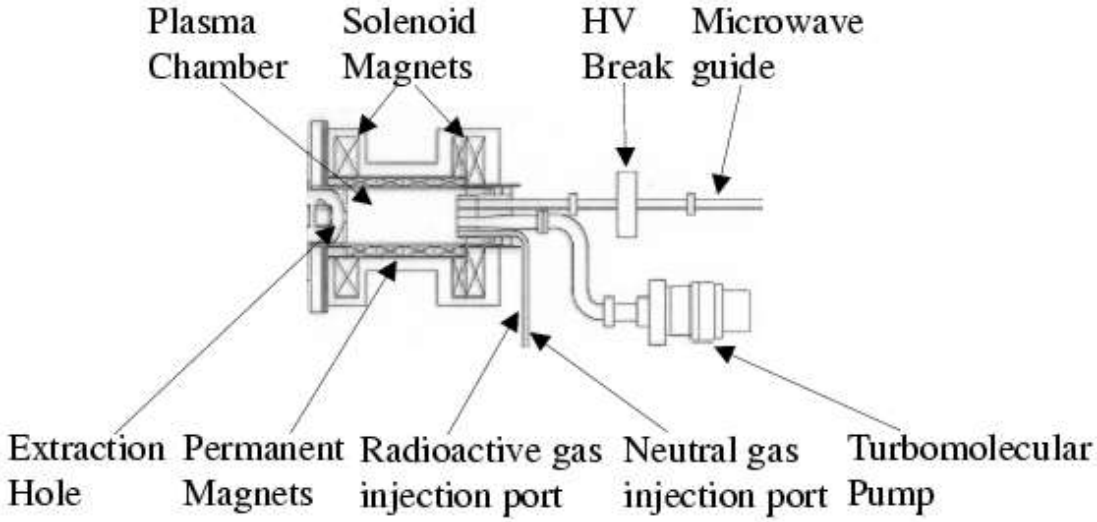

Figure 3.3 Schematic overview of the IRIS ECR plasma chamber.

3.2.2 Solenoid Magnetic Field

The variable solenoid magnetic field serves two purposes: it creates a magnetic bottle for the energetic electrons and defines the plasma surface. The solenoid magnetic

field was generated by two sets of water cooled copper "pancake" coils [60]. The IRIS ECR was originally designed to operate at 2.45 GHz. It was modified after being relocated to the 88-Inch Cyclotron to operate at a frequency of 6.4 Ghz. This frequency was used because a spare microwave klystron was available which operated at 6.4 GHz. The original magnetic field configuration was augmented by adding on another pancake coil and iron to the return yoke which is shown in Figure 3.4. The extraction solenoid consists of four water cooled pancake coils that generate a maximum magnetic field of 0.4 Tesla. The injection solenoid consists of five water cooled pancake coils that generate a maximum field of 0.7 Tesla. Four EMI model number ESS 35-300-2-D power supplies were used to power the solenoid magnets. Figure 3.5 shows how the two power supplies were connected in parallel for each solenoid to provide enough current. The power supplies typically operated at a current of approximately 400 amperes and 22 volts. This corresponds to approximately 9000 watts per solenoid for a total of 18000 watts. The heating due to this load was dissipated by running parallel cooling lines through the pancake coils. A water pressure booster pump was added to the cooling system to increase the cooling water flow rate. The booster pump increased the cooling water supply pressure from 80 psi to 200 psi. Without adequate cooling, the coils overheat. They are interlocked to prevent damage.

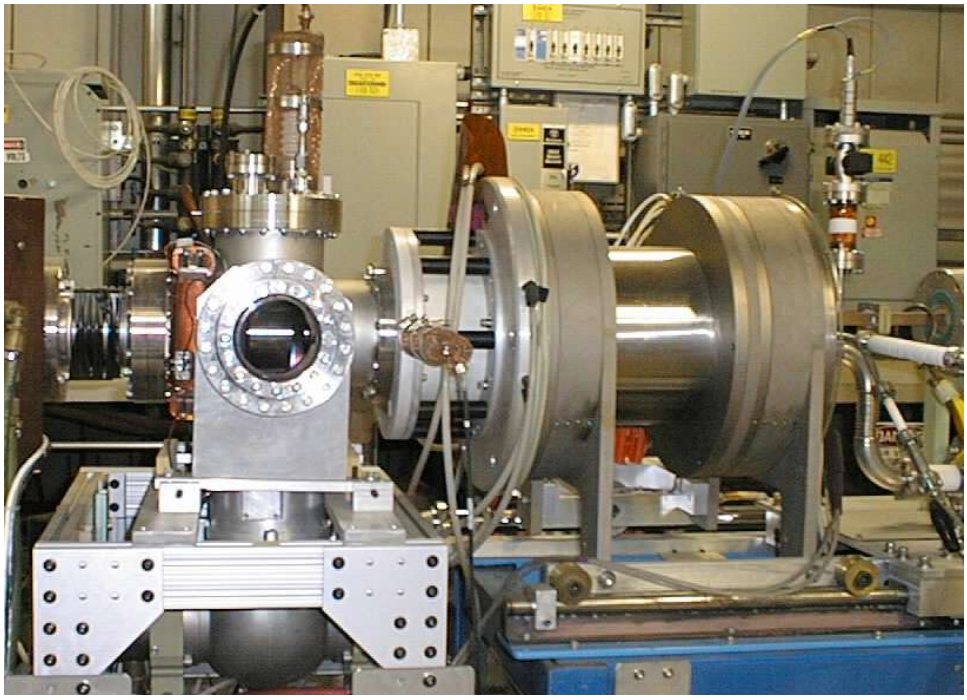

Figure 3.4 IRIS ECR showing the two solenoid pancakes at right

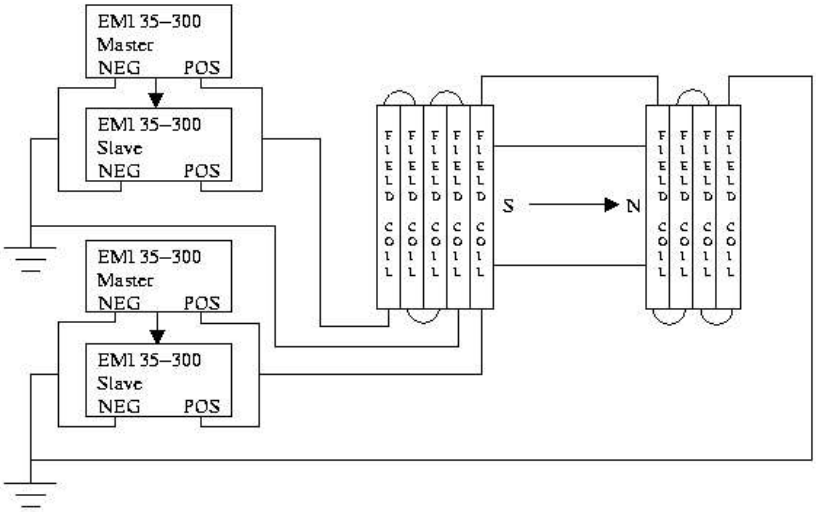

Figure 3.5 Electrical schematic for solenoid magnetic power. The solenoids are powered by four commercially available EMI 35-300 power supplies.

3.2.3 Sextupole Magnetic Field

The sextupole magnetic field radially confines the ions in the plasma chamber. As an ion approaches the wall of the plasma chamber, the field increases and the Lorentz force redirects the ion to the center of the chamber. Figure 3.6 shows the sextupole field confining the plasma which was created by 24 rows of NdFeB permanent magnets. The octagonally shaped magnets are mounted in grooves on the outside of the plasma chamber and then epoxied in place. The magnetic field orientation of the magnets is rotated as they are installed to produce a sextupole field. The measured and calculated field gradient profile of each pole of the sextupole are shown in Figure 3.7. The ECR resonance radial distance corresponding to 6.4 GHz at about 5.5 cm. The continuous line in Figure 3.7 shows the expected field as calculated by solving Poisson's equation [61]. The water cooling supplied to the aluminum vacuum chamber also cools the permanent magnets.

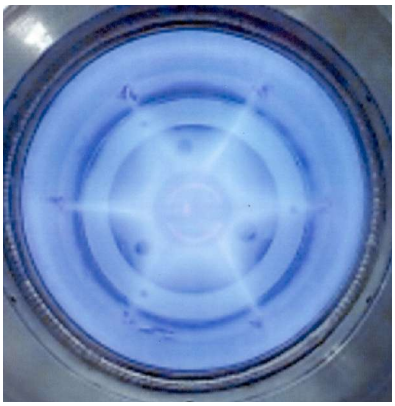

Figure 3.6 Plasma confined radially by the sextupole magnetic field.

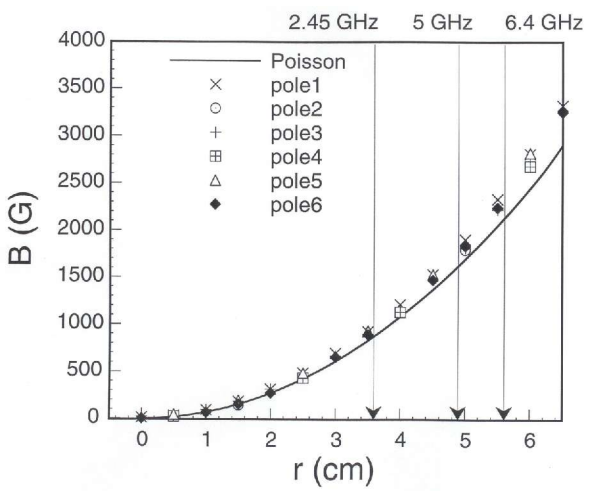

Figure 3.7 Magnetic field gradient in NdFeB sextupole. Courtesy of D. Wutte [61].

3.2.4 Microwave Power Source

The microwave power is generated by a Varian model VA-936L12 C-band transmitter at 6.4 GHz. Microwave power was delivered to the plasma chamber via a vacuum coupled wave guide through a quartz window that is transparent to the 6.4 Ghz microwave frequency. The maximum power available from the microwave transmitter is 3000 W, although an average of only 200 W was used. The microwave power level is controlled by a feedback circuit which samples the output power of the transmitter and compares it to an operator controlled setpoint. Figure 3.8 shows the feedback and control circuit which regulates the output power to within a 0.5 % or 1 watt in 200 watts. Regulating the power to this level keeps the ion source stable and leads to reliable long term operation.

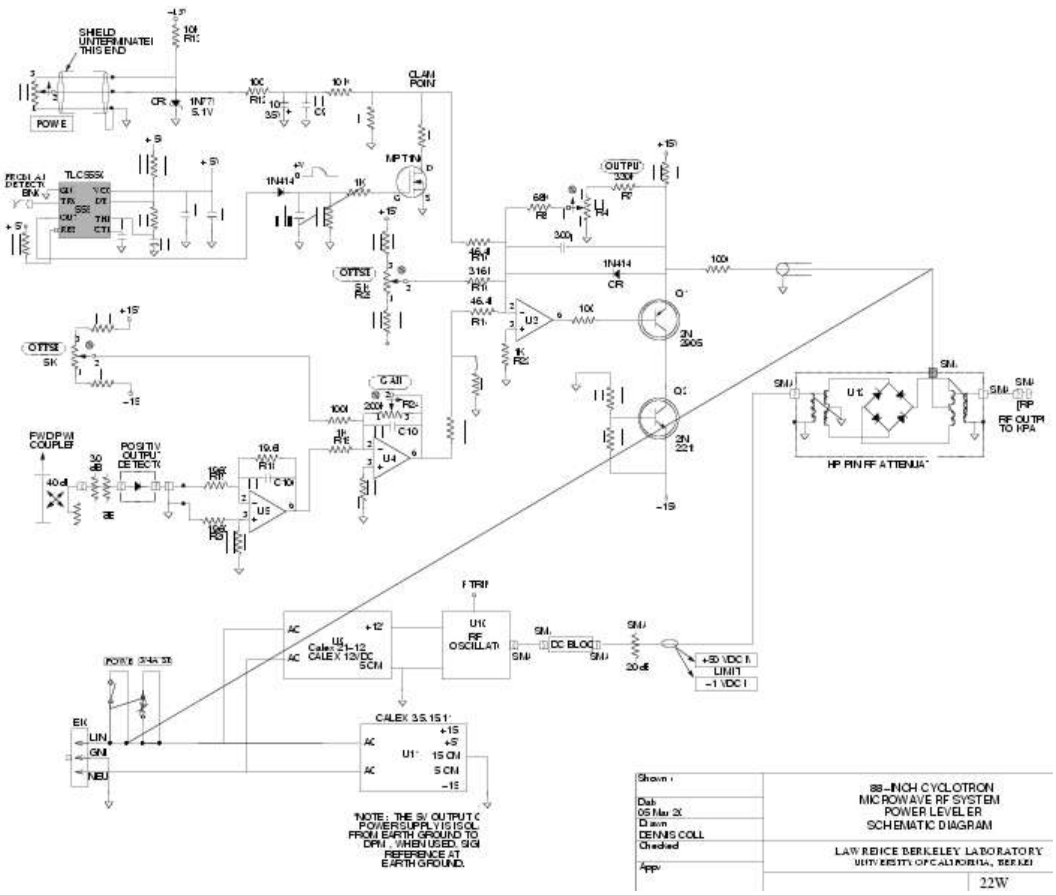

Figure 3.8 Schematic of RF Level Controller. Courtesy of D. Collins from LBNL.

3.2.5 Stable Gas Injection Manifold

The stable gas injection manifold allows up to two support gases to be mixed and injected into the plasma chamber. A third connection to the manifold allows the attachment of a calibrated leak to the system which is shown in Figure 3.9. The manifold takes atmospheric pressure gases and introduces them to the vacuum by throttling the gas

through a Balzers all metal gas dosing valve. The manifold introduces stable support gas to the plasma chamber to maximize the efficiency of the ion source for the production of O^{1+} and O^{2+} beams of stable and radioactive isotopes. To avoid contaminants in the system, the manifold can be pumped independently allowing the connected lines to be purged without contaminating the ion source.

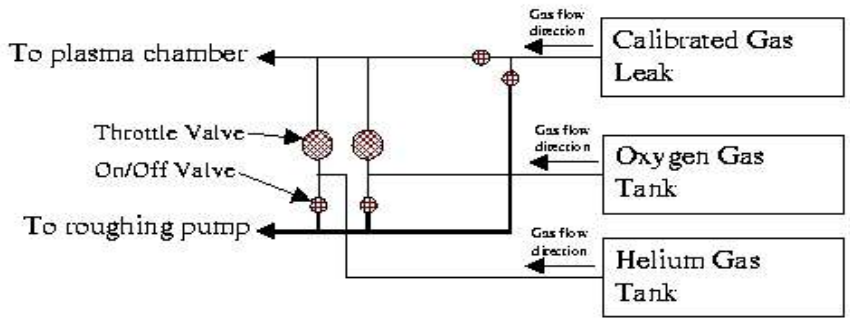

Figure 3.9 Schematic of the stable support gas injection manifold.

3.2.6 Ionization Efficiency and Support Gases

The efficiency is determined as in section 3.1.2 for the CUSP source. During these measurements the importance of proper ratios of helium and oxygen support gases became clear. The oxygen from the CO calibrated leak can bind to the surface of the quartz liner. This chemical reaction can result in long hold up times with respect to the half-life of 70.6 seconds. The addition of helium and oxygen support gases reduced the hold-up time and increased the ionization efficiency. Without adding helium or oxygen,

the sharp change in output when the calibrated leak was closed was not observable. With the addition of approximately equal amounts of helium and oxygen to the source, the ionization efficiency with the CO calibrated leak was 20 % for $^{16}O^{1+}$. The ion source runs with a stable plasma and an ionization efficiency of 20% for stable oxygen under the following conditions:

- extraction voltage 27.2 kV
- extraction current 1.4 mA
- puller voltage -1.4 kV
- extraction magnet current 202 A, injection magnet current 204 A
- bias voltage ranges between 60 V and 3.4 mA to 120 V and 3.0 mA
- microwave power 175 to 185 Watts
- total neutral gas pressure 1.10×10^{-6} to 1.30×10^{-6} Torr

Figure 3.10 is a schematic of these settings and their location. The ionization efficiency with radioactive ^{14}O was only 4%. The lower efficiency was possibly due to the hold-up time of ^{14}O on the walls of the plasma chamber discussed in the following section.

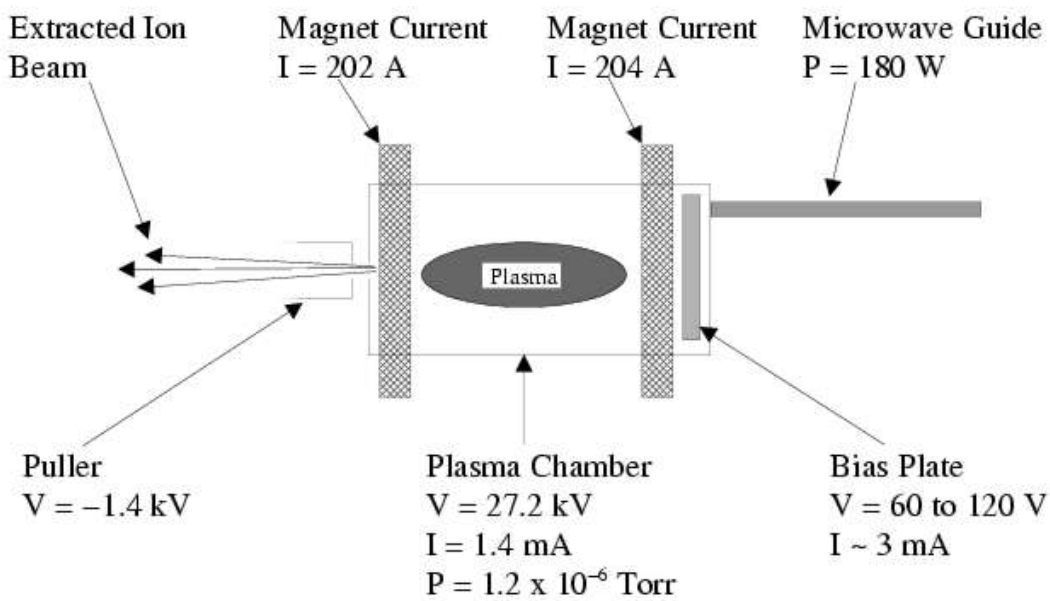

Figure 3.10 Schematic diagram of the IRIS ECR settings.

3.2.7 Gas Hold-Up Time

The gas hold-up time for the system determines the maximum overall efficiency along with the ionization efficiency discussed previously. The radioactive beam rate is the product of the production rate and all the exponential losses due to hold-up times multiplied by the ionization efficiency,

$$\prod_i \epsilon_i = \epsilon_{target}\,\epsilon_{transfer}\,\epsilon_{coldtrap}\,\epsilon_{ECR}\,\epsilon_{ionization}\,\epsilon_{beamoptics} \tag{3.1}$$

The hold-up time was measured by monitoring the ion beam current of a particular ion as a function of time after the closing the calibrated leak valve. Figure 3.11 shows the data that are then fit with a single exponential to determine the effective hold-up time. The hold-up time is found to be 17.3 ± 0.6 s which gives an efficiency of

$$\epsilon_{ECR} = e^{\frac{-\ln(2)\times 17.3\,s}{70.6\,s}} = 0.844 \quad \cdot \tag{3.2}$$

Note that the hold-up time measured is that of stable oxygen which is abundant in the ion source. This hold-up time measurement does not take into account that a fraction of the radioactive ^{14}O may stay on the walls for considerably longer periods of time.

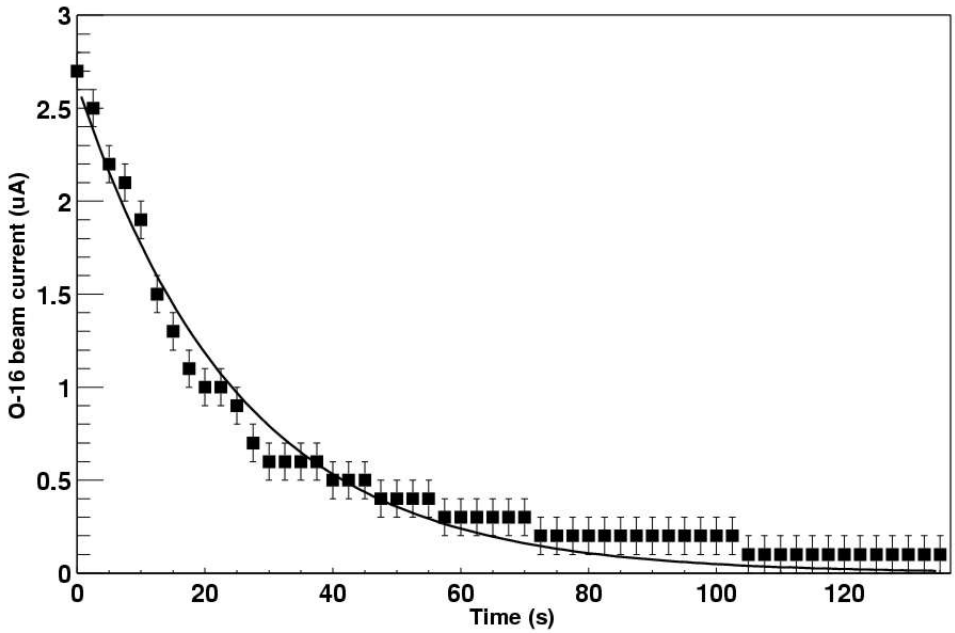

Figure 3.11 Stable oxygen hold-up time measured in IRIS. The calibrated leak was used to establish the efficiency and hold-up time of oxygen in the IRIS ECR. After achieving steady state performance the valve to the calibrated CO leak was closed and the beam current monitored. The plot shows the change in beam current for an $^{16}O^{1+}$ ion beam with a constant offset of 117.5 μA. The decay curve is fit with a single exponential and the characteristic hold-up time is found to be 17.3 ± 0.6 s.

The reduction in ionization efficiency can then be attributed to this hold-up time. Table 3.1 is a summary of hold-up times and efficiencies for the overall system. For processes

that delay the ^{14}O propagation through the system the efficiency is determined by the exponential decay of the ^{14}O. For example, the hold up time in the transfer line is 3 ± 0.3 s the efficiency is

$$\epsilon_{transfer} = e^{\frac{-\ln(2)\times 3s}{70.6s}} = 0.971 \quad . \tag{3.3}$$

Figure 3.12 shows the rate of ^{14}O gas as a function of time. The steady state condition is interrupted by closing the valve to the transfer line near the target, valve V2 in Figure 2.2. A NaI detector located near the transfer line monitors the 2.31 MeV gamma ray rate. This rate was recorded as a function of time during the experiment.

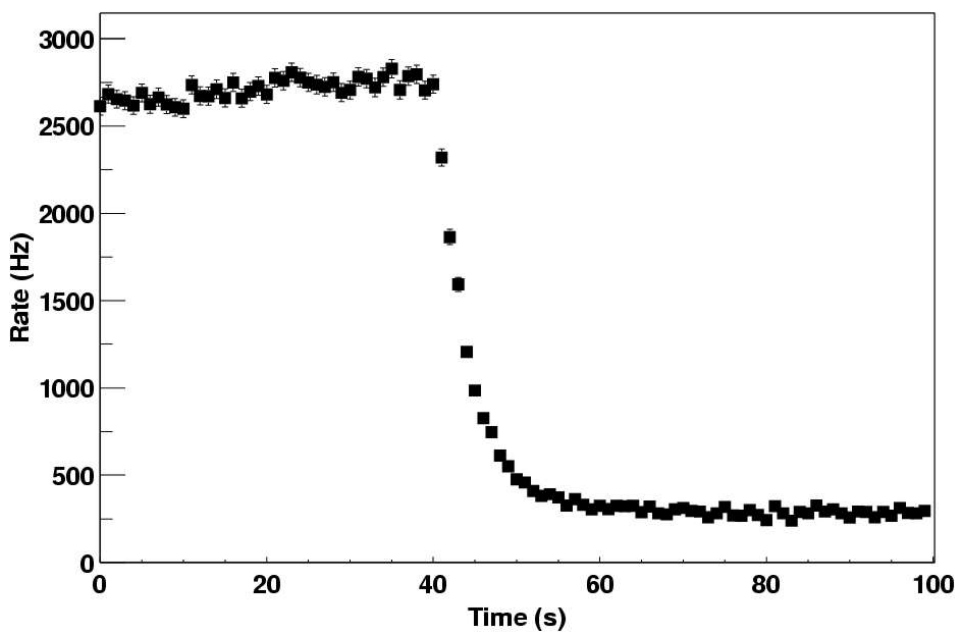

Figure 3.12 Transfer line gas hold-up time. The transfer line rate gas hold-up time found by fitting the exponential decay curve after the target valve has been shut-off. The target valve was closed at approximately 40 s. The characteristic time for the hold-up time in the transfer line is 3 s.

Similarily, the rate of ^{14}O in the cold trap was monitored using a Ge(Li) detector setup to monitor the ^{14}O 2.31 MeV gamma ray. Figure 3.13 shows the rate as a function of time for the steady state and when the valve feeding the cold trap is closed, valve V7 in Figure 2.2. The gas hold-up time is determined by fitting the expontial curve for the characteristic decay time which was 5 ± 0.5 s. The efficiency of the cold trap is then

$$\epsilon_{coldtrap} = e^{\frac{-\ln(2)\times 5s}{70.6s}} = 0.952 \quad . \tag{3.4}$$

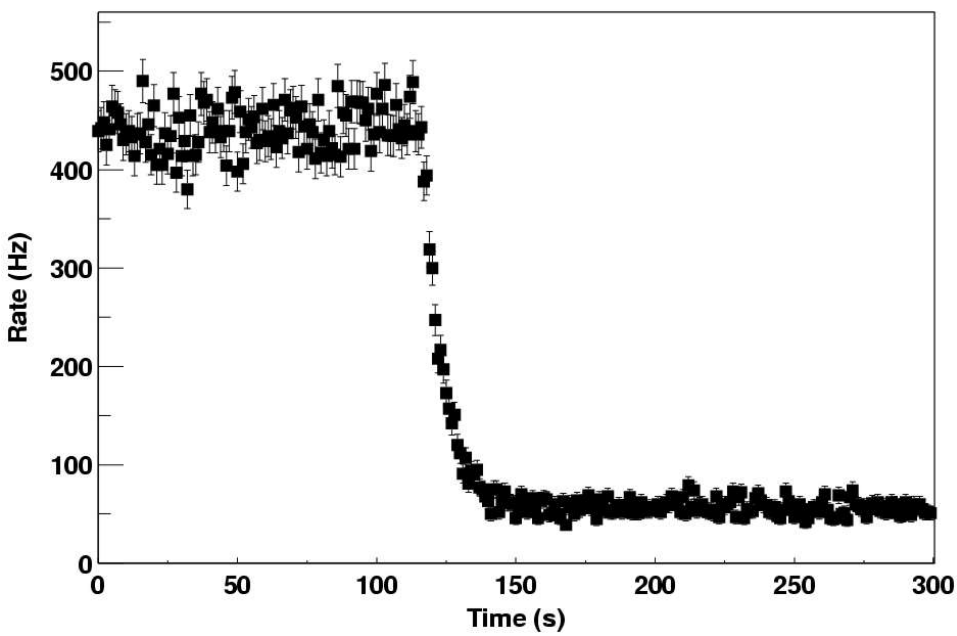

Figure 3.13 Cold trap gas hold-up time. The cold trap gas hold-up time was determined by fitting the exponential decay curve after the cold trap valve was closed. The valve feeding the cold trap and ion source was closed at approximately 110 s. The characteristic time for the hold-up time in the transfer line is 5 s.

The total efficiency is the product of the efficiency of all the component efficiencies. Note that there are two exponential components for the hold-up time of oxygen in the ion source. The fast component represents the plasma hold-up time while the slow component is due to wall sticking effects. Oxygen atoms recombine on the wall of the plasma chamber and form chemically stable compounds. They remain there until they are re-excited into the plasma by interactions with the plasma. The interactions of atoms and molecules with the plasma chamber wall is complicated because of the poorly understood interactions with the high temperature plasma.

The production rate of ^{14}O is 2 x 10^8 ^{14}O/pμA as determined from the thick target yield at 20 MeV as discussed in section 2.1. With a typical beam current of 5 pμA the ^{14}O production rate is 10^9 ^{14}O atoms/s. The radioactive beam rate is determined by multiplying the production rate by the total efficiency from Table 3.1. The expected beam rate is then 10^9 x 0.009 = 9 x 10^6 ^{14}O/s which is consistent with the measured value during a typical experiment.

Component of System	Hold-Up Time (s)	Efficiency (%)	Method of Determination	Reference in Thesis
Target	76 ± 7	47.4 ± 3.0	calc / exp	Sec. 2.5
Transfer Line	3 ± 0.3	97.1 ± 0.3	experiment	Fig. 3.12
Cold Trap	5 ± 0.5	95.2 ± 0.5	experiment	Fig. 3.13
ECR	17.3 ± 0.6	84.4 ± 0.5	experiment	Fig. 3.11
Radiaoctive Gas Ionization	-	4.0 ± 0.4	experiment	Sec. 3.2.7
Beam Optics	-	60.0 ± 6.0	experiment	Sec. 3.5
Total	101 ± 17	0.9 ± 0.25	-	-

Table 3.1 Summary of hold-up times and efficiencies for O-14 beam production. The uncertainties quoted refer to precision of the fits to the data or the uncertainty associated with the measurement performed.

3.3 Ion Beam Extraction

The ion extraction system for the IRIS ECR consists of three elements: an extraction hole in the plasma chamber, a puller electrode, and an Einzel lens are shown in Figure 3.14. Ions are extracted from the plasma through a 0.6 cm diameter hole at the center of the plasma chamber. The neutral plasma is biased to 25 kV to 30 kV by an external high voltage supply connected directly to the plasma chamber. The puller electrode is negatively biased and helps shape the electric field at the extraction hole. An electrostatic Einzel lens is located along the beam axis approximately 30 cm from the

extraction hole. The accelerated ions are focused electrostatically to correct the beam divergence. A photo of the Einzel lens for the IRIS ECR is shown in Figure 3.15.

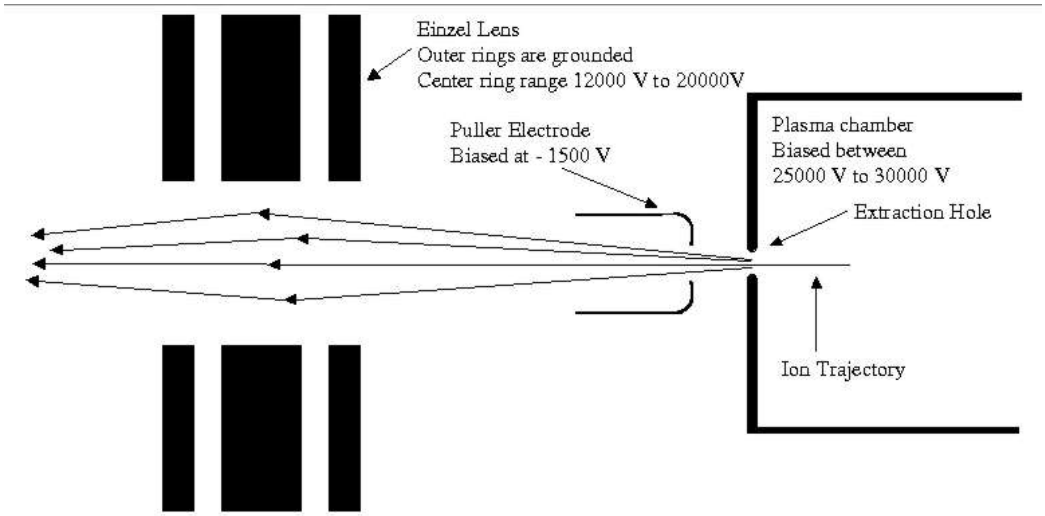

Figure 3.14 Schematic of ion extraction optics.

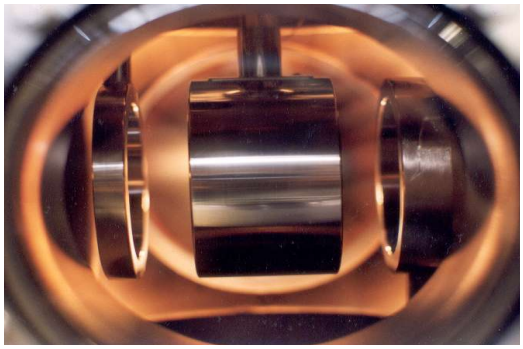

Figure 3.15 Einzel lens used to focus the beam after extraction.

The magnetic field generated by the solenoid magnets allow aluminum ions that sputter from the extraction hole to be deposited on the ceramic insulator. Plasma shields were installed to protect the critical ceramic insulator that isolates the main plasma

chamber from the ground plane. Two concentric aluminum shields allow vacuum pumping, but provide no line of sight for the ions, see Figure 3.16.

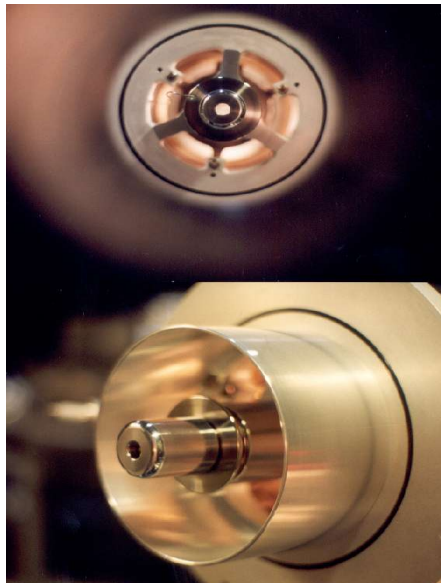

Figure 3.16 The puller used to accelerate the ions from the plasma.

The theoretical maximum number of ions that can extracted from the plasma surface is given by the Childs-Langmuir law,

$$J_{CL} = \frac{4\epsilon_o}{9}\sqrt{\frac{2q}{m_i}}\frac{V^{\frac{3}{2}}}{d^2} \tag{3.5}$$

Here J_{CL} is the current density, q is the charge of the species, m is the mass of the species, V is the applied voltage, and d is the distance from the high voltage surface to ground. A more conventional form of the above equation is

$$J_{CL} = 1.72\sqrt{\frac{\xi}{A}}\frac{V^{\frac{3}{2}}}{d^2} \quad . \tag{3.6}$$

Here J_{CL} is the current density in mA/cm^2, ξ is the charge state of the ion, A is the mass in amu, V is the applied voltage in kV, and d is the distance from the high voltage surface to ground in cm. This formula assumes that the plasma surface, that the ions are being extracted from, is flat. A precise determination of the theoretical current extractable from a plasma requires a more sophisticated treatment which takes into account space charge effects [62]. A rough calculation for $^{14}O^{1+}$ is worked out as follows. An extraction voltage of 30000 volts is typically used during this experiment. The distance from the extraction hole to the puller electrode (the effective ground in this case) is 4.44 cm. The theoretical maximum current density for a singly charged ion beam of $^{14}O^{1+}$ is 3.83 mA/cm^2. The current density is multiplied by the area to obtain the actual ion current. The extraction hole for IRIS is 0.6 cm diameter. The area of the extraction hole is 0.283 cm^2 which allows a current of 1.08 mA to be extracted. This beam current corresponds to a calculated steady state radioactive source of 6.74 x 10^{15} decays per second. The calculated production rate of ^{14}O is 10^9 atoms per second with a 10 pμA beam of ^3He on target. The theoretical upper limit is ≈6 orders of magnitude greater than the ^{14}O supply rate. The extraction hole and voltage do not limit the ^{14}O beam intensity. There are multiple charge species and isotopes in the ion source plasma. The composition can be determined by scanning with the analyzing magnet. For this experiment, the mean ion mass is approximately 8 amu with ^4He and ^{16}O as the support gases. The average charge state of the ions is 1 at the low microwave power level used and the high pressure of 1.5 x 10^{-6} Torr used. With these average values, the calculated maximum extractable current density is 5.05 mA/cm^2, and for a 0.6 cm extraction hole this gives 1.43 mA of beam.

The plasma sheath from which the ions are extracted should be flat in order to maximize the extracted current. If the plasma density is greater than the plasma density calculated with the Childs-Langmuir law, then the extracted beam is expanding. A fraction of the expanding beam will strike the puller electrode and be lost reducing the efficiency. When the plasma density is greater than the optimum value, the extracted beam will be underfocussed and the beam will diverge after the puller electrode. The beam could be recollimated if adequate ion optics are present in the beam line. The ideal extraction conditions allow a flat miniscus to form. This can be achieved by matching the plasma current density to the theoretical current density. In this condition, the extracted beam can be focussed and collimated in the beam line with little loss. The plasma current density, J_{Pl}, is given by the following formula,

$$J_{Pl} = \frac{en}{2}\sqrt{1.602\, x10^{-19}\frac{(T_e + T_i)}{m_i}} \quad . \tag{3.7}$$

Here e is the electron charge in Coulombs, n is the plasma density in particles per m^3, T_e is the electron temperature in eV, T_i is the ion temperature in eV, and m_i is the mass of the ion species in kg. Based on the support gases used in the plasma chamber, the average values used for equation 3.7 are a charge state of 1 and mass of 8 amu. The plasma temperature is estimated to be 0.5 eV for the ions and 3 eV for the electrons. The plasma density at 1.5 x 10^{-6} Torr is 5.30 x 10^{16} particles per m^3. The current density from these parameters is 27.5 A/m^2 or 2.75 mA/cm^2. Figure 3.17 shows a schematic of the beam trajectory for over dense, matching, and under dense plasmas. The above condition of J_{Cl} = 5.05 mA/cm^2 and J_{Pl} = 2.75 mA/cm^2 puts the plasma in the condition of $J_{Pl} < J_{cl}$. In

order to bring the equation into balance, the plasma temperature should be increased to 11.9 eV. This is accomplished by increasing the microwave power supplied to the plasma.

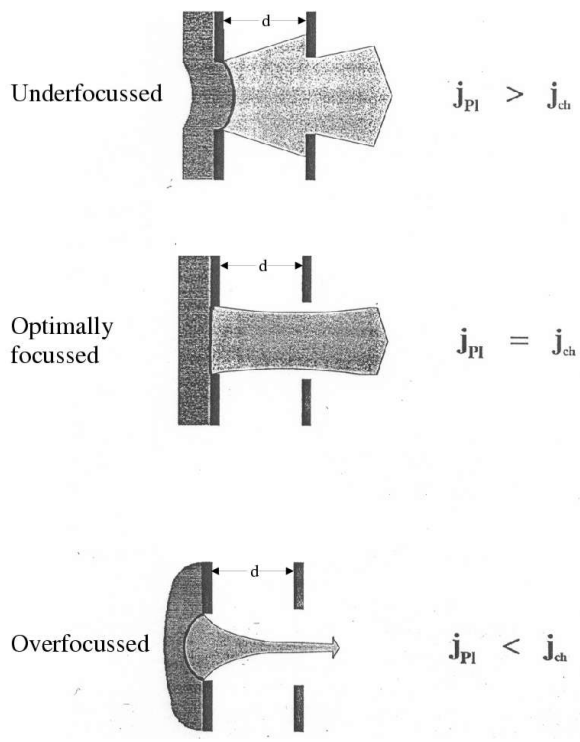

Figure 3.17 Beam extraction shape dependence on plasma conditions. Courtesy of D.Wutte. J_{pl} is the plasma current density and J_{ch} is the theoretical Childs-Langmuir current density both are in units of mA/cm^2.

3.4 Radiation Shielding

The ECR ion source generates radiation well into the x-ray region. The source of photons is the accelerated electrons in the plasma. The plasma chamber is wrapped with

approximately 2.5 cm of lead sheet to absorb the x-ray flux. The highest radiation field produced occurs along the axis of the ion source at either end of the plasma chamber where the shielding is minimal. On axis, the extraction side of the plasma chamber has approximately 1 cm of aluminum to absorb the radation generated inside the chamber. The beam optics and chamber design limit the addition of any further radiation shielding. Similarily, the on axis injection side of the plasma chamber has multiple feedthroughs and vacuum connections which limit the amount of radiation shielding. The largest open angle to the plasma is on the extraction side of the ion source. At a distance of 50 cm from the extraction hole radiation fields at the level of 5 mR/hr are possible. Additional radiation shielding consisting of 2.5 cm thick polyethylene sheets and 0.15 cm tungsten sheets were used to bring the radiation levels down to the background level of approximately 0.1 mR/hr. Polyethylene and tungsten were used due to the availability of the material.

3.5 Analyzing Magnet

The mass analyzing magnet for this experiment is a double focusing 90° sector magnet. The magnet was originally part of the Heavy Ion Linac (HILAC) injection line at LBNL. The horizontal focus is approximately 43 cm down stream from the vertical focus. This distorts the ion beam into an ellipse. The distortion is corrected down stream with an electric quadrupole. The vertical acceptance gap of the magnet is only about 2 cm while the horizontal acceptance is greater than 10 cm. The ion optics and vertical gap

limits the ion beam to approximately 60% beam transmission. The mass resolution of the magnet is $\partial M/M = 0.53$ %. This corresponds to a median to median beam separation of 10 cm, at the end of the beam line, with a measured one sigma beam width of 0.67 cm.

Chapter 4

4 The O-14 Half-Life Experiment

Measurement of the half-life of Fermi transitions allows the determination of the effective vector coupling constant in the weak interaction between leptons and quarks in the nucleus. This can be combined with the effective coupling constant from purely leptonic weak decay to obtain the first element of the CKM matrix. The ^{14}O half-life must be measured to approximately 2 or 3 parts in 10^4 to have an impact on the present result of 70.603 ± 0.018 seconds. The previous experimental techniques for measuring ^{14}O decay and results are discussed in section 4.1. It is important to note that there are several other isotopes that have been measured to this level of precision. The theoretical corrections to the decay have uncertainties on the order of 10^{-4}. In performing a precision half-life measurement on ^{14}O the systematic uncertainties of the detector system must be well characterized. In this chapter the experimental technique, systematic errors, and results for the ^{14}O half-life are discussed.

4.1 Fitting Data

As experimenters have made more statistically precise measurements of the half-life, the analysis techniques used to fit exponential decay data were called into question by Hardy [20]. An important realization was that the least squares minimization routine used was in error. Chi-square minimization does not conserve the area under the curve when the data follow a Poisson distribution [63]. The half-life determined from a chi-square minimization with Poisson distributed data is systematically shorter. The magnitude of the offset depends on the number of bins, initial rate, and ending rate. The data in this experiment were fit using the maximum likelihood method described by Baker and Cousins [64]. The maximum likelihood minimization

$$Maximum\ Likelihood\ \Xi^2 = \sum_i y_i - n_i + n_i \ln\left(\frac{y_i}{n_i}\right) \quad , \tag{4.1}$$

conserves the area under the curve during the fit. This means that the sum of the number of events in the fit is equal to the number of events in the data, within the uncertainty of the fit. In equation 4.1, y_i is the predicted number of counts from the theoretical fit function and n_i are the data in a particular interval or bin. Problems arise with Neyman's chi-square

$$Neyman's\ \chi^2 = \sum_i \frac{(y_i - n_i)^2}{y_i} \tag{4.2}$$

or Pearson's chi-square

$$Pearson's\ \chi^2 = \sum_i \frac{(y_i - n_i)^2}{n_i} \tag{4.3}$$

minimization when the data become Poisson distributed, as in the tail of a half-life fit. In equation 4.2 and 4.3, y_i is the predicted number of counts from the theoretical fit

function and n_i is the data in a given interval or bin. The chi-square minimization under estimates the area in the tail of the half-life distribution which results in a systematically shorter half-life. Monte Carlo simulations show this effect as a function of rate in Figure 4.1 for a nominal half-life of 70.600 seconds with a background rate of 1 Hz. The offset in the half-life between the chi-square and maximum likelihood fits also depends on the final rate of the fit. Early experiments did not use long runs. In most cases, an average background was assigned to the set of data and assumed to be constant for the duration of the experiment.

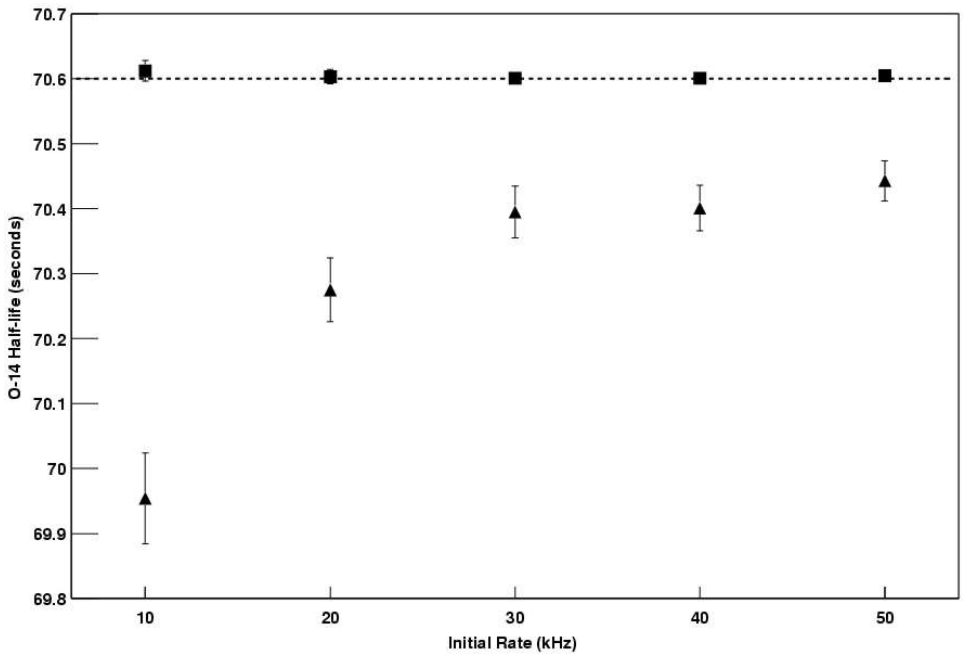

Figure 4.1 Chi-square minimization versus maximum likelihood minimization from a simulation. The square points indicate data fit with maximum likelihood minimization. The triangular points are data fit with the chi-square minimization. The dashed line is the nominal half-life of 70.600 s. The results show how the Chi-square minimization

systematically skews the half-life lower as a function of the initial rate chosen for the fit. The maximum likelihood minimization shows no signs of this systematic behavior.

4.2 Previous Experiments

The half-life of ^{14}O has been measured fourteen times. Experimenters produced ^{14}O by bombarding a natural carbon target with a ^{3}He beam or a ^{14}N target with a proton beam. The nuclear reaction products are ^{11}C, ^{13}N, ^{14}O, and ^{15}O. These isotopes are all positron emitters and have different half-lives shown in Table 4.1.

Isotope	β^+ ***Branching Ratio (%)***	***Beta Endpoint Energy (MeV)***	γ***'s Emitted (MeV)***	***Half-Life (seconds)***
^{11}C	100	0.96	0.511	1222.8
^{13}N	100	1.19	0.511	597.6
^{14}O	99.4 0.6	1.81 4.12	2.31 / 0.511 0.511	70.6
^{15}O	99.89	1.72	0.511	122.2

Table 4.1 Summary of nuclear reaction products. The data above is from the Table of Isotopes [65].

The unique feature of ^{14}O decay compared to ^{11}C, ^{13}N, and ^{15}O decay is the 2.31 MeV gamma ray, and previous experiments observed the 2.31 MeV gamma ray to measure the ^{14}O half-life. The gamma ray was detected with NaI, CsI, Ge(Li), or plastic

scintillation detectors. The detectors were positioned a short distance from the solid target after it had been removed from the beam line. These detectors all have intrinsic deadtimes on the order of several microseconds with the exception of the plastic scintillator. At a rate of 10 kHz, with a deadtime of 5 μs, a count loss correction of ≈500 Hz or ≈5 % is necessary. This is limited primarily by the scintillation time of the detection element which are summarized later in Table 4.3. It is desirable to minimize this correction term by using faster detectors.

The uncertainty of the half-life is limited by the statistical precision of the data as well as the systematics of the experimental apparatus. The statistical precision of the half-life depend on the initial rate of ^{14}O as can be seen in Table 4.2. An initial rate of 10 kHz leads to an observed total of 1.02 million events in approximately 1200 s. The precision of the result relative to the half-life is 9.9 parts in 10^4 or 0.070 seconds for a half-life of 70.6 seconds. To increase the statistical precision an experimenter either increases the initial rate or needs to repeat the experiment multiple times. In the past, experiments have been limited by the deadtime of the detector to initial rates of approximately 10 kHz or less. This required repeating the data taking procedure for many cycles, in some cases up to 100 data cycles were required.

Initial Rate of ^{14}O (Hz)	***Total Number of Events Observed (in millions)***	***Statistical Precision of Half-life (parts in 10^{-4})***	***Uncertainty in Half-life (ms)***
10000	1.02	9.9	70
20000	2.04	7.0	49

Initial Rate of ^{14}O (Hz)	*Total Number of Events Observed (in millions)*	*Statistical Precision of Half-life (parts in 10^{-4})*	*Uncertainty in Half-life (ms)*
30000	3.06	5.7	40
40000	4.07	5.0	35
50000	5.09	4.4	31
60000	6.11	4.1	29
70000	7.13	3.8	26
80000	8.15	3.5	25
90000	9.17	3.3	23
100000	10.19	3.1	22

Table 4.2 Statistical uncertainty as a function of initial rate.

The 0.511 MeV positron annhilation gamma ray produced by ^{14}O and contaminating activities creates two different backgrounds in the detector. A detected event can be generated when the 0.511 MeV and 2.31 MeV gamma ray arrive at the same time in the detector. The 0.511 MeV and 2.31 MeV events can be real coincidence events or accidental coincidence events. The real coincidence events occur from the same decaying nucleus. The accidental coincidence events are from two distinct nuclei which happen to decay within the observation time (T). In either case, the coincident events effectively remove the 2.31 MeV event from the acceptance window and produce a 2.82 MeV event as shown in Figure 4.2. The loss rate is the product of the 0.511 MeV rate and the 2.31 MeV rate multiplied by the observation time (T)

$$Loss\,Rate = T \times R_{0.511} e^{\left(\frac{-\ln(2)t}{\tau_{long}}\right)} \times R_{2.31} e^{\left(\frac{-\ln(2)t}{\tau_{O14}}\right)} \quad . \tag{4.4}$$

The 0.511 MeV rate ($R_{0.511}$) is approximately an order of magnitude larger than the 2.31 MeV rate ($R_{2.31}$) due to the production cross section and detector efficiency. The result is that events are lost as a function of rate modulated by the contaminant half-life. To reduce this effect in the experiment of Clark [48] lead brick was placed between the detector and the source to preferentially attenuate the 0.511 MeV gamma rays.

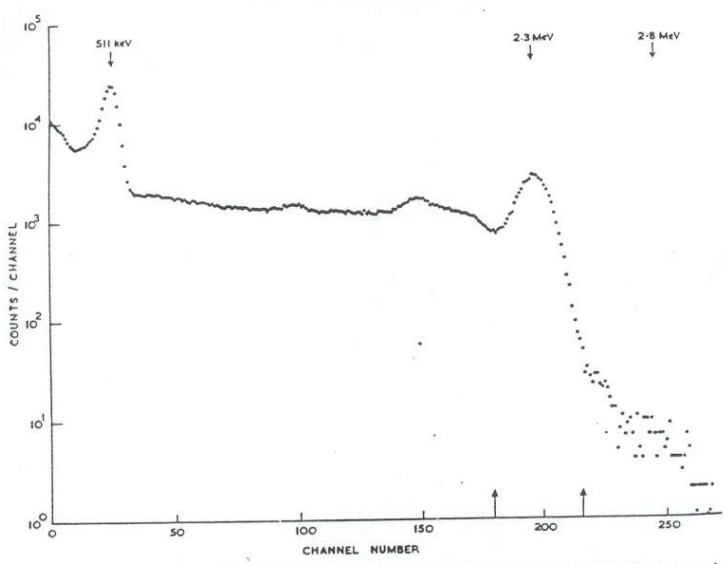

Fig. 2. A γ-ray spectrum obtained with a NaI detector and with 2.5 cm of lead between target and detector. Arrows indicate a typical range chosen for the single-channel analyser.

Figure 4.2 NaI gamma ray spectrum of O-14 decay from Clark [46].

Similarly, accidental pile-up of events in the Compton continuum can produce events that fall above the discriminator threshold. These accidental coincidences produce events which have half the original half-life, because the accidental rate is the product of the singles rates times the observation time,

$$R_{acc} = T \times A_o e^{\frac{-\ln(2)t}{t_{1/2}}} \times A_o e^{\frac{-\ln(2)t}{t_{1/2}}} = B_o e^{\frac{-\ln(2)t}{\frac{t_{1/2}}{2}}} \quad . \tag{4.5}$$

With one exception, Becker et al. [50], none of the previous experiments discuss this possibility or take it into account in the analysis. A new experiment should try to minimize or avoid these two background effects. Figure 4.2 shows a typical gamma ray spectrum from an ^{14}O half-life experiment. The area under the 2.31 MeV peak represents approximately 10% of the total events. The summing effect is estimated with an overlap time of 5 μs and the relative areas from Figure 4.2. The half-life in the Monte Carlo simulation of this effect is set at 70.600 seconds. The summing effect creates an offset in the fitted half-life which depends on the initial rate of the ^{14}O. The offset of the summing effect on the ^{14}O half-life is shown in Figure 4.3. At an initial rate of 2500 Hz the half-life is offset by approximately 110 ms.

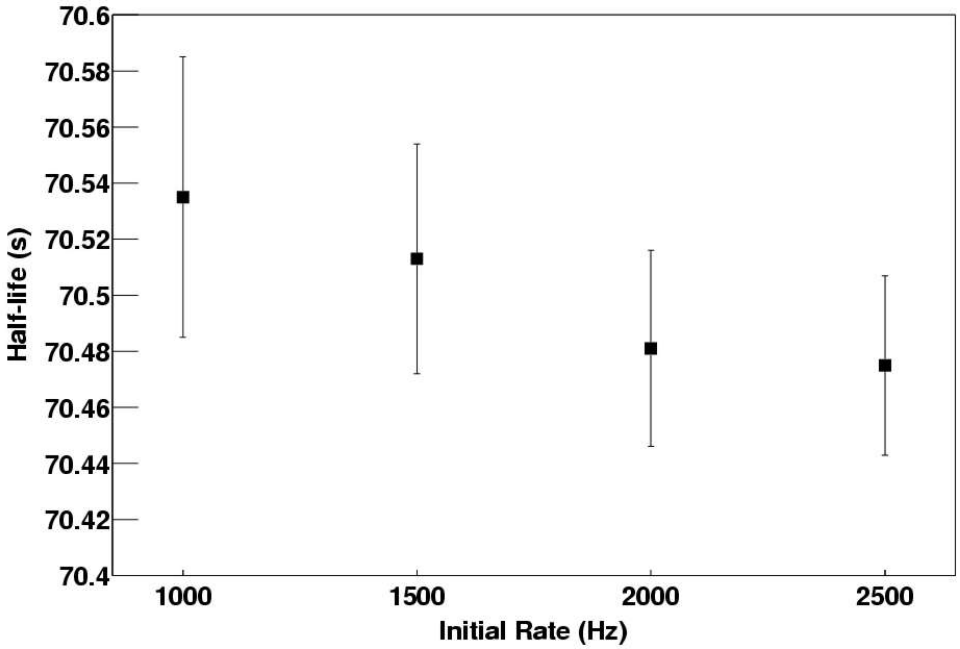

Figure 4.3 Summing effect on ^{14}O half-life. The summing effect on the ^{14}O half-life is determined from Monte Carlo simulations which incorporate an overlap time of 5 μs and the relative gamma ray probabilities from Figure 4.2. The nominal half-life used in the Monte Carlo simulated data is 70.600 s.

4.3 Deadtime

The deadtime of the system is dominated by the time required to integrate the pulse shape and/or reading out the actual event. There are two distinct forms of deadtime: extending or non-extending. Extending deadtime is also referred to as paralyzable deadtime or updating deadtime. Similarily, non-extending deadtime is also known as non-paralyzable or non-updating deadtime. The type of deadtime has quantitatively different behavior and formulae. The deadtime is actually the length of time during which

the output pulse occurs and the acquisition system can not record a new event. The type of deadtime is determined by the electronic element used, in this experiment a discriminator. The discriminator is either an extending or non-extending device. In this thesis, the term extending deadtime is synonymous with extending discriminator. An extending deadtime allows the response of the detecting element to be lengthened in time. When a new event occurs within the preset deadtime, the pulse is extended from the arrival time of the second pulse as shown in Figure 4.4. Non-extending deadtime does not allow the output pulse width to be extended. If a new event arrives within the preset deadtime the event is ignored. The effect the types of deadtime have on the measurement process are discussed in the following section.

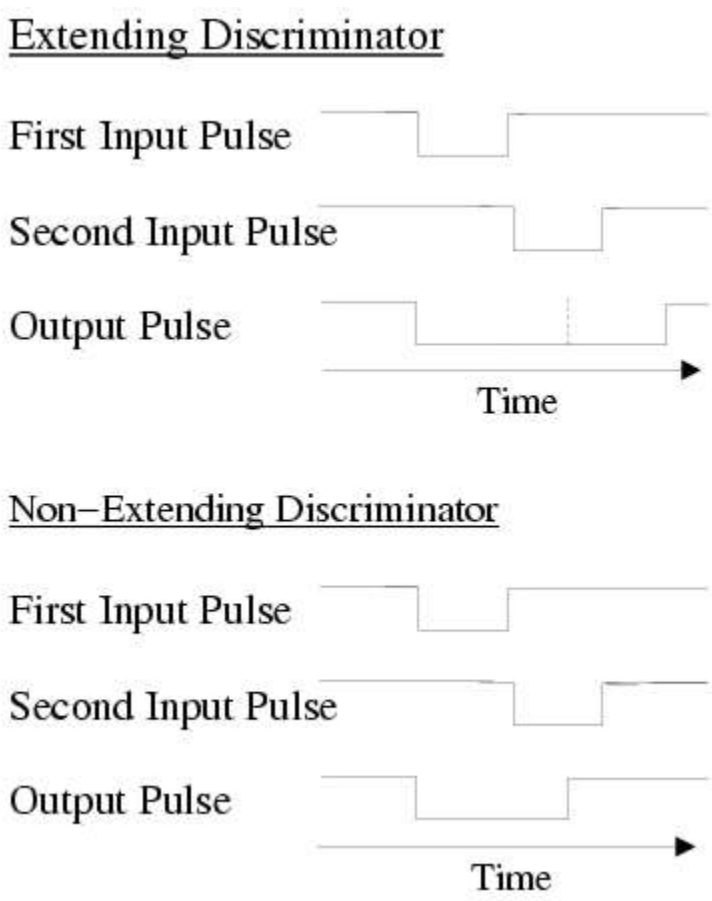

Figure 4.4 Extending and non-extending discriminator diagrams.

4.3.1 Extending Deadtime Distributions

The extending deadtime distribution follows Poisson statistics and has the form,

$$P_{ext}(n,\tau)=e^{-n\tau} \quad . \tag{4.6}$$

Here $P_{ext}(n,\tau)$ is the probability that true events (n) in time τ (the deadtime) will be observed. The observed counting rate (n') using the above probability is

$$n'=n\,P_{ext}(n,\tau)=n\,e^{-n\tau} \quad . \tag{4.7}$$

In a half-life experiment, the source is decaying during the observation time, and the time

dependence of the real rate must be included in the above equation,

$$n' = (A_o \exp(\frac{-\ln(2)t}{\tau_{1/2}}) + B_o) * \exp(-\tau * (A_o \exp(\frac{-\ln(2)t}{\tau_{1/2}}) + B_o)) \quad . \tag{4.8}$$

Here A_o is the true initial rate, B_o is the true background rate, t is the time, τ is the deadtime, and $\tau_{1/2}$ is the half-life.

The live time fraction (LTF) is the fraction of observation time during which the system can respond to new events. For the extending distribution the live time fraction is

$$LTF = e^{-n\tau} \quad . \tag{4.9}$$

At a rate of 100 kHz with a deadtime of 400 ns the LTF is 0.96 . The system is able to respond to new events at this rate and deadtime 96% of the time.

4.3.2 Non-Extending Deadtime Distributions

The non-extending deadtime follows a slightly different distribution again using Poisson statistics given by

$$P_{nonext}(x) = \frac{(n\tau)^x e^{-n\tau}}{x!} \quad . \tag{4.10}$$

$P_{nonext}(x)$ is the probability of x events occurring in time τ and n is the true event rate. In order to determine the number of events missed during a period τ, we multiply the event rate by the probability of an event occurring during that time summed over all possible number of events

$$\sum_1^{\infty} x P(x) \quad . \tag{4.11}$$

The true event rate can be determined by writing

$$n'_t \sum_1^{\infty} x P(x) = n'_t n_t \tau \quad , \tag{4.12}$$

where n_t' is the observed rate and n_t is the true event rate without deadtime.

The observed rate is simply the true rate minus the number of events lost, so we write

$$n'_t = n_t - n_t n'_t \tau = \frac{n_t}{1+\tau n_t} \quad . \tag{4.13}$$

Taking into account the decay rate of the source, we find

$$n'_t = \frac{A_o e^{\frac{-\ln(2)t}{\tau_{1/2}}} + B_o}{1+\tau\left(A_o e^{\frac{-\ln(2)t}{\tau_{1/2}}} + B_o\right)} \quad . \tag{4.14}$$

4.3.3 Effective Deadtime

In any system there will usually be a mixture of deadtimes as a signal is processed. Consider a detector that has a finite pulse width of 10 ns, is followed by a simple level discriminator with a non-extending deadtime of 15 ns. The detector is an analog device and multiple events could pileup on each other within the 10 ns pulse width. This effectively behaves as an extending deadtime. The discriminator will only output a pulse every time the input level passes from zero to above threshold. Now the event chain consists of an extending 10 ns deadtime followed by a 15 ns non-extending deadtime. If a second pulse arrives 8 ns after the first pulse, it will render the detector inoperable for another 10 ns, which gives a total deadtime of 18 ns. Which model is appropriate to account for the deadtime losses in the data? One way to resolve this situation is to make the final stage in the signal processing the dominant deadtime. A rule

of thumb is that the final deadtime should be on the order of 5 to 10 times larger than the next longest deadtime in the chain of events. The deadtime of the system is then determined by the final output stage. This ensures that the data follows either the extending or non-extending probability distribution. Appropriate formula can then be applied to fit the data. The effect of any deadtime chain should be verified by Monte Carlo methods to ensure it works properly. Figure 4.5 shows the effect of the first 40 ns extending deadtime has on the half-life [66-67].

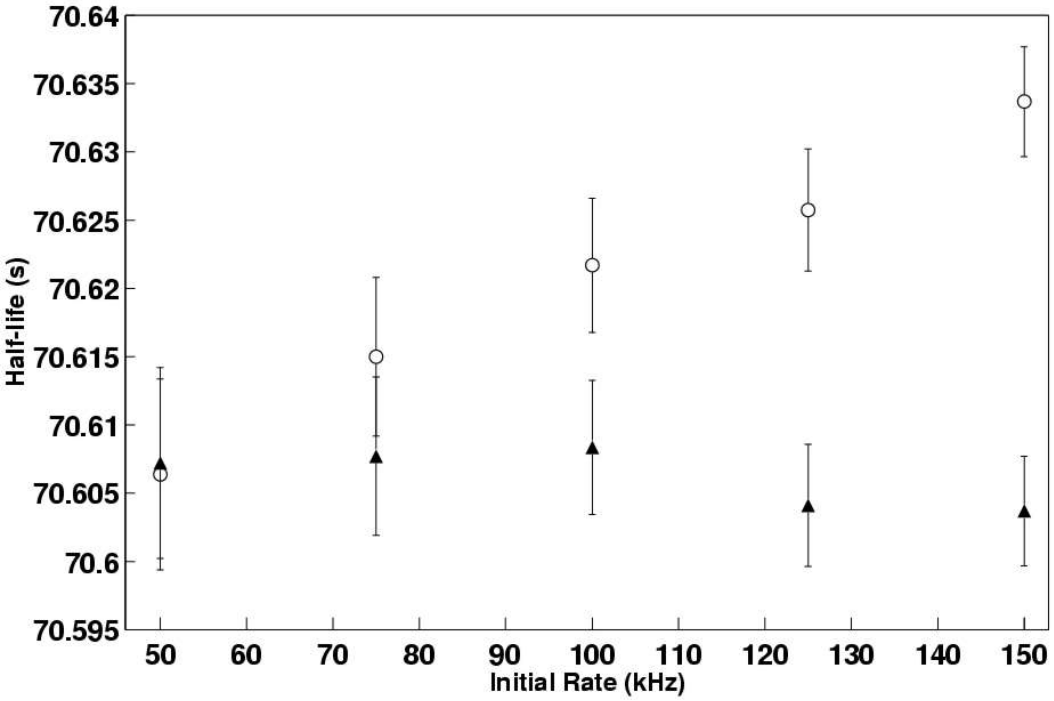

Figure 4.5 Half-life effect of the first deadtime on the second deadtime. The solid circles are the resulting half-life from a Monte Carlo simulation consisting of a 40 ns extending deadtime followed by a 400 ns non-extending deadtime. The open circles are the resulting half-life from a Monte Carlo simulation with a 400 ns extending deadtime

followed by a 400 ns non-extending deadtime. Both sets of data are fit assuming only a 400 ns extending deadtime starting at various initial rates.

4.3.4 Data Readout Deadtime

There is a final deadtime associated with the recording of data. During an experiment, events are usually recorded by an electronic scaler. The scaler is a simple counter which is incremented with each logic pulse. The scaler must be read and zeroed at some periodic interval to give the data time structure. During the read process, the scaler input is inhibited from recording any events. The data acquisition system should also measure the time during which the data is not being collected. This deadtime is then corrected for during the fit. In this experiment, the scaler data are recorded in bins of 0.4995 seconds. The data acquisition system is inhibited for 0.0005 seconds to allow the data to be recorded. During this 0.0005 second interval another scaler records the clock cycles to ensure that the readout time was only 0.0005 seconds long. The scaler with the data readout time is readout during the next data acquisition cycle of 0.4995 seconds. This creates a closed time line in which the data acquisition time and data readout time are both recorded.

4.4 Gamma-Ray Detector Design

To prevent the potential errors of previous experiments, a new detection material was researched. The ideal detector for this experiment would have a short scintillation

decay time, a low intrinsic background, and a high efficiency for 2.31 MeV gamma rays. The efficiency of the scintillator relies on: the amount of light output per unit energy absorbed and the energy absorbed per unit volume of the detector. A gamma ray deposits energy in matter via: the photoelectric effect, Compton scattering, and pair production. These effects scale with the number of protons in the nucleus (Z) roughly as Z^5, Z, and Z^2. Higher Z materials are generally more efficient at detecting gamma rays. The ideal detector for gamma rays for a half-life experiment would be a high Z material with efficient light output and a short scintillation time. A summary of currently available materials are summarized in Table 4.3.

In particular YAP:Ce, with a scintillation half-life of 27 ns, holds the most promise for fast gamma ray detection. Large sizes of YAP:Ce are not currently available. An efficient detector volume could not be produced for this experiment. The next material investigated was BaF_2 which can be produced in large volumes to make an efficient detector. BaF_2 has two distinct scintillation times 0.7 ns and 630 ns. The longer time could render this detector useless for this experiment, but the scintillation light spectrum is well separated as shown in Figure 4.6.

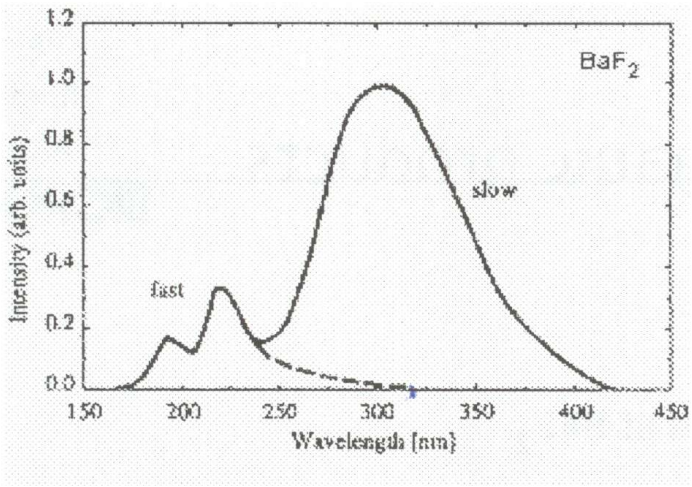

Figure 4.6 BaF_2 fluorescence spectrum. The part of the spectrum labelled as fast has a scintillation half-life of 0.7 ns and the slow part of the spectrum is 630 ns. Flourescence spectrum courtesy Dr. D. Morrissey from M.S.U.

An optical filter and a wavelength shifter design was investigated in order to take advantage of the short scintillation time of the BaF_2 crystal. Figure 4.7 is a photo of two large (12.7 cm diameter by 15.2 cm length) BaF_2 crystals which were obtained from the Michigan State University Cyclotron Facility for experimentation. Upon performing some basic spectral measurements it was discovered that the BaF_2 crystals were radioactive. In the manufacturing process, naturally occurring radium, chemically similar to barium, is incorporated into the crystal lattice as it grows. The decay energy spectrum of the radium overlaps the energy spectrum of a 2.31 MeV gamma ray. The crystals obtained for the experiments each had a radium count rate of 300 to 400 Hz. The discovery of this high background ruled out the use of this material for the experiment.

Figure 4.7 BaF_2 crystal from M.S.U. with pen shown for scale.

Scintillator Material	***Density (g/cm^3)***	***Light Output efficiency (% of Anthracene)***	***Primary Decay Time (ns)***
Anthracene	1.25	100	30
Stilbene	1.16	50	4.5
YAP:Ce	4.57	35	27
NaI(pure)	3.67	440 at 77K	60
NaI(Tl)	3.67	230	230
BGO	7.13	35	300
CsI(Tl)	4.51	95	1000
CsI(Na)	4.51	150	630
CsI(pure)	4.51	500 at 77K	16
CaF_2 (Eu)	3.17	110	940
$CaWO_4$	6.1	36	6000
BaF_2	4.89	12 and 46	0.7 and 630

Scintillator Material	*Density (g/cm^3)*	*Light Output efficiency (% of Anthracene)*	*Primary Decay Time (ns)*
LiI(Eu)	4.06	75	1200
ZnS(Ag)	4.09	300	200 (polycrystalline)
ZnO(Ga)	5.61	90	1.48 (polycrystalline)
EJ204 Plastic	1.03	68	1.8

Table 4.3 Summary of scintillation material and decay times.

4.5 Beta Particle Detector Design

With a pure source of ^{14}O, direct detection of the beta particles for a half-life measurement becomes attractive. The mass separated beam minimizes the temporal contamination from ^{11}C, ^{13}N, and ^{15}O. An efficient fast detector for detecting beta particles was made from plastic scintillator, light guide, and photomultiplier tube. Plastic scintillator from Eljen Technology, EJ-204, was used to detect the beta particles. It has a scintillation half-life of 1.8 ns as described in Table 4.3. The scintillators were 0.1 cm thick by 2.54 cm wide by 2.54 cm long. Four beta detectors using plastic scintillator attached edge on to a 3.8 cm adiabatic light guide mounted to the photomultiplier tube were made as shown in Figure 4.8.

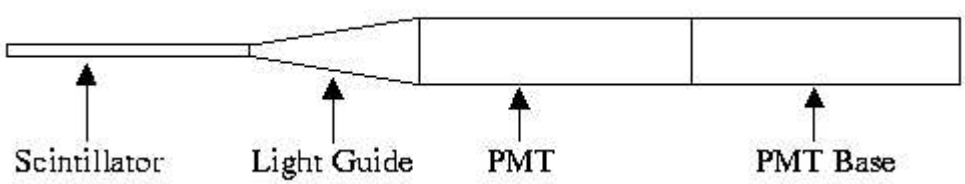

Figure 4.8 Schematic of beta detector.

The beta particles are energetic enough to pass directly through the thin scintillator. Relativistic beta particles deposit only a fraction of the total energy in the plastic scintillator. The spectrum they produce is called a minimum ionizing spectrum as shown in Figure 4.9. The characteristic shape of the minimum ionizing particle is described by Vavilov's theory for electrons interacting with thin absorbers [68]. The efficiency of measuring a beta particle is approximately 100%. The beta particle deposits approximately 200 keV in the 0.1 cm scintillator. The scintillation yield for this scintillator is 10400 photons per 1 MeV of energy deposited. On average a beta particle produces approximately 2100 photons in the scintillator. The scintillator has a measured cross section of 0.77% for 0.662 MeV gamma rays, see section 4.12. The detectors are essentially decoupled from the environmental backgrounds. The backgrounds considered here are gamma rays from the room in which the experiment is carried out, naturally occurring isotopes (U, K, Ra), and cosmic ray showers. Cosmic ray muons are detected with approximately 100% efficiency. High energy muons produce the same minimum ionizing signal in the scintillator as the beta particles.

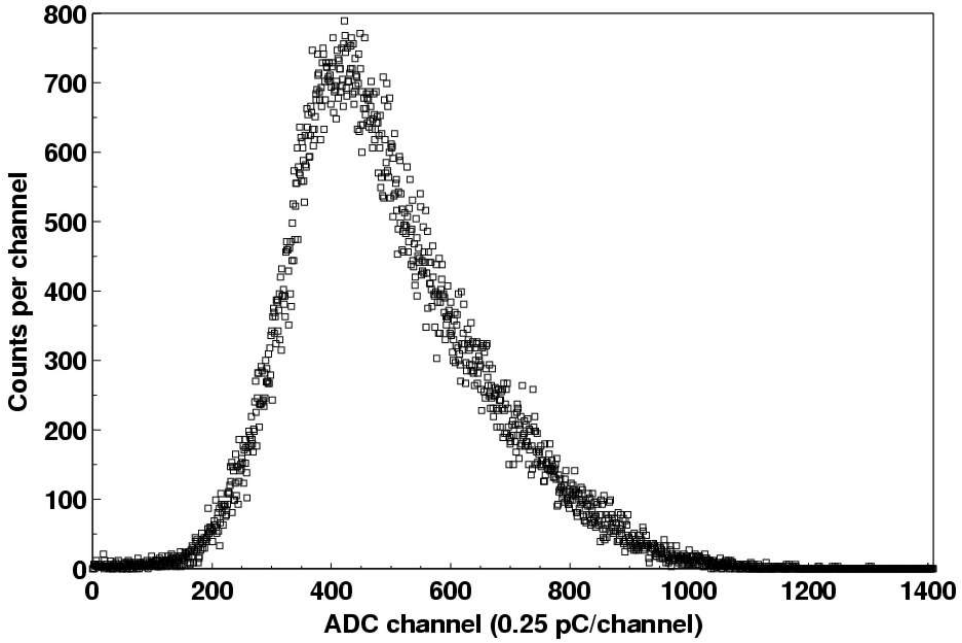

Figure 4.9 Typical beta particle spectrum from ^{14}O source during the experiment.

4.6 Photomultiplier Tube

The beta detector photomultiplier tubes were Hamamatsu model R647 designed for high speed timing and particle identification. The PMTs were powered by Ortec model 456 high voltage supplies. They draw a nominal operating current of 1 mA at 1200 Volts DC. The PMTs have a maximum rated operating voltage of 1250 volts. The complete technical specifications can be found in appendix B.

The entire pulse width of any of the four PMTs used was less than 30 ns from rising edge to trailing edge. Figure 4.10 shows an oscilloscope trace of 14 pulses averaged together from beta particle events in the scintillator. The rising edge of the signal is on the order of 5 ns. The falling edge of the signal returns to background levels after approximately 20 ns. The discriminators used for this experiments were triggered on

the negative leading edge of the PMT signal. The discriminator threshold was set in the range of 20 mV to 25 mV depending on the PMT gain.

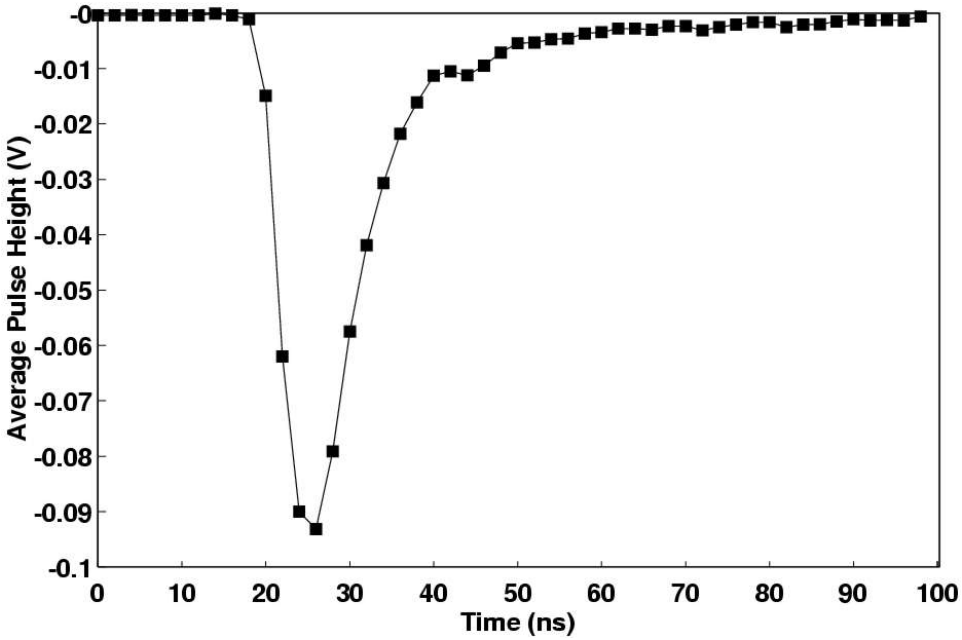

Figure 4.10 Photomultiplier pulse shape and timing. The pulse height spectrum shows the average pulse height of 14 beta events. The average pulse duration is less than 40 ns.

4.6.1 Photomultiplier Tube Afterpulsing

Afterpulsing in a PMT could lead to correlated events that would add non-statistically to the total count rate. There are two distinct sources of after pulsing in a PMT: luminous reactions and ionization of residual gas [69]. Luminous reactions occur when electrons strike the dynode surface and emit photons. It is possible for these photons to be reflected back towards the photocathode and generate another pulse. These events are characterized by having a short 20 ns to 100 ns delay time between the initial

pulse and the secondary pulse. After pulsing due to residual gas occurs when the electrons in the PMT ionize He, H, or some hydrocarbon e.g.: CH_4. The ions travel backwards in the PMT along the electric field lines and strike the photocathode, liberating electrons and generating a secondary pulse. The characteristic time for these events is on the order of 300 ns to 1 μs, depending on the ion mass and the PMT geometry.

The PMTs were checked for afterpulsing by using a LeCroy 2228A time to digital converter (TDC). Figure 4.11 shows the TDC start pulse was triggered by delayed beta particle event. The stop pulse was generated by the same electronic circuit without a delay. This circuit triggers the TDC start channel every time an event occurs. If no afterpulsing is present, then the time distribution of stop pulse events is expected to be flat, consistent with a random distribution of pulses coming from the PMT. However if afterpulsing is present, the TDC spectrum would show a peak at a time characteristic of the afterpulsing.

Figure 4.11 Afterpulsing electronic circuit.

The TDC spectrum showed no discernible peak after collecting approximately 150000 start events for detector A, C, and D. Detector B showed afterpulsing occurring at

approximately 300 ns after the initial event. The position of detectors A, B, C, and D are discussed in section 4.10. The afterpulsing fraction was determined by dividing the number of afterpulse events by the number of triggers. For detector B, there were 150581 trigger events with 102 after pulse events in the peak shown in Figure 4.12. The average rate of 0.636 events per channel was subtracted from the afterpulse peak. The afterpulse occurs with a probability of $(6.8 \pm 0.7) \times 10^{-5}$ per pulse approximately 300 ns after the initial pulse.

The shortest deadtime for this experiment was set at 400 ns to minimize the effect of afterpulsing. If afterpulsing occurred, it would be omitted by the non-extending deadtime. If a true pulse occurred within the 400 ns window its after pulse could occur after the deadtime window was over. The probability of a pulse arriving in the 400 ns deadtime window at 100 kHz is 0.039. The after pulse effect is the product of the two probabilities which gives a probability of 2.65×10^{-5}. This would lead to an additional count rate of 2.65 Hz compared to a statistical variation of ± 316 Hz. The afterpulsing effect varies as the rate changes and has the same effect as a rate dependent gain shift discussed in section 4.13.9. The after pulsing effect of 6.8×10^{-4}, adding 2.65Hz at 100 kHz, will affect the lifetime at the level of ± 0.25 ms. This is a negligible systematic uncertainty for this experiment.

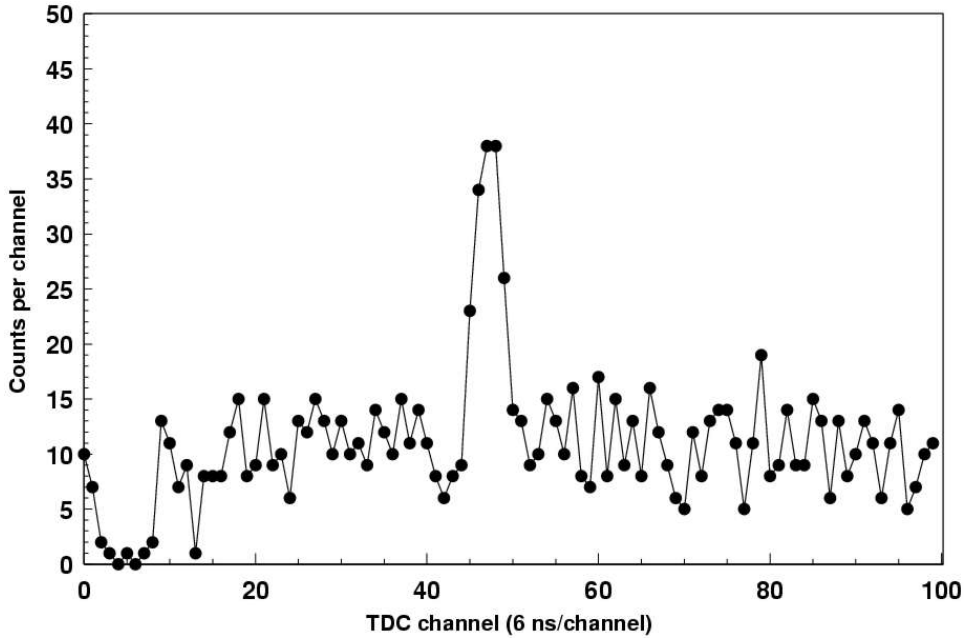

Figure 4.12 TDC spectrum with afterpulsing occurring at 300 ns. The TDC scale is 6 ns per channel and the data has been binned together by a factor of 20. The spectrum shows events that triggered the TDC after a true beta particle event was used to start the TDC. Random events would create a flat spectrum. Correlated events from afterpulsing would create a peak. These events can be seen centered around channel 47 in the spectrum.

4.7 Signal Processing Electronics

The half-life measurment is a precise event counting experiment. The experiment measures the number of events that occur in a given amount of time. A total of 33 channels of data were read out. There are 3 channels for the clocks, 28 channels for the detectors, and 2 channels for monitoring rates in the beam line and transfer line. The

beam line rate is the the number of events observed by a NaI detector located at the end of the beam line. The transfer line rate is the the number of events observed by a NaI detector located in the middle of the transfer line. The schematic of the electronics used to collect the data are shown in Figure 4.13.

An event begins when a beta particle produces a minimum ionizing pulse in the beta detector. The PMT output pulse triggers the LBL model 21x4141 P-1 discriminator whose output was a NIM level logic pulse of ≈40 ns duration. The discriminator output was fanned out to three separate gate generators. The gate generators were EG&G model

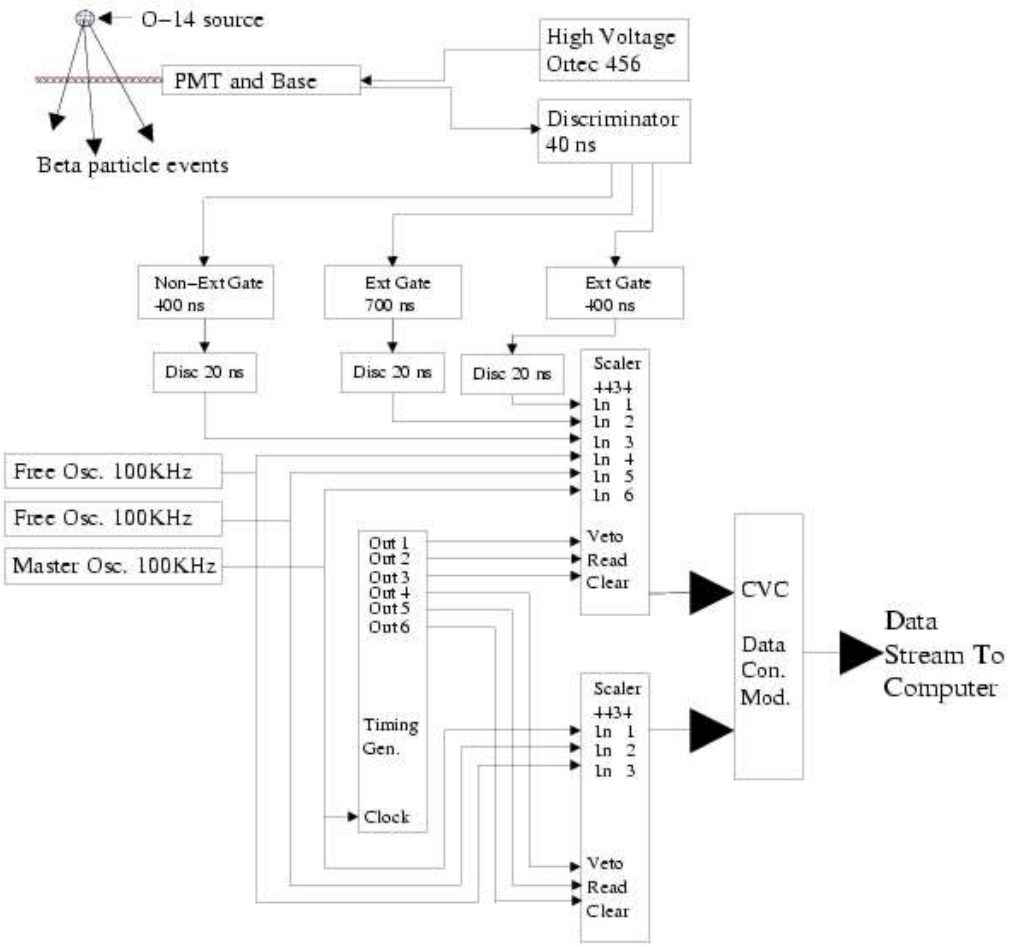

Figure 4.13 Schematic of data acquisition electronics.

GG8000. Each gate generator has either an extending or a non-extending output NIM logic pulse. The gate generator outputs for one channel of data consisted of one 400 ns non-extending gate, one 700 ns extending gate, and one 400 ns extending gate. The output of each gate generator went into a discriminator that generates a ≈20 ns wide NIM logic pulse. The output of the discriminator then went into a LeCroy 4434 latching scaler. This step was necessary to avoid a small deficiency of the LeCroy 4434 scaler. The

double pulse resolution is ≈30 ns, creating an artificial deadtime at the end of the logic pulse of ≈30 ns. The 20 ns discriminator pulse eliminated this problem by allowing the scaler to recover while the gate pulse controls the deadtime of the data stream. Finally the latching scaler is controlled by the timing generator. Figure 4.14 shows a timing diagram of the above discussion.

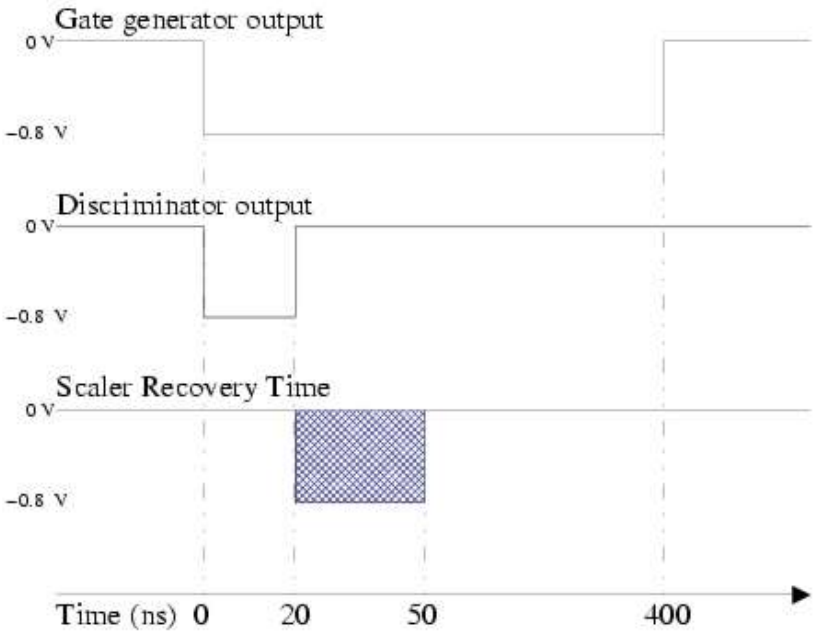

Figure 4.14 Timing diagram of LeCroy 4434 scaler recovery time. The LeCroy scaler requires approximately 30 ns to recover before it can be triggered again. To avoid any problems associated with this deadtime the gate generator output triggers a discriminator with a 20 ns output pulse. The discriminator pulse is then used to increment the scaler. The gate generator pulse inhibits any other pulses from triggering the discriminator while the 20 ns discriminator pulses allows the scaler to recover for the next event.

4.8 Data Acquisition Timing

The scaler data were read out by a CAMAC to VSB crate Controller (CVC) developed at the GSI research institute in Darmstadt, Germany. The read out timing sequence was controlled by a Kinetic Systems Corporation model 3655-L1A timing pulse generator. The pulse generator uses a calibrated external clock reference running at 100 kHz which is discussed in section 4.13. The timing generator output pulse sequence is shown in Figure 4.15 and Figure 4.16.The timing generator controlled the veto, load, and clear commands issued to the two 4434 scalers. The data were recorded in 0.4995 second long bins and read out every 0.5 seconds.

The data scaler recorded the number of clock cycles and the number of events that occur in the 0.4995 second window. The scaler was vetoed (inhibited) when the load trigger was initiated. The data from the scaler were loaded into the memory buffer in 220 ns. After 220 ns, the scaler was ready to start recording data. The CVC control module was triggered to read out the data in the memory buffer. The scaler used for this experiment took approximately 1 μs to read out a word of data. The data stream consisted of 30 words readout from one scaler module. The scaler was inhibited for at least 30 μs for each read out cycle. While the CVC control module was reading the memory buffer, the scaler value was zeroed by a clear signal from the timing generator. The clear action on the 4434 scaler took 100 ns to execute. After 50 clock cycles (500 μs), the veto was removed and the scalers began recording events again. To establish a continuous time

line, a second scaler was used which compliments the data scaler. While the data scaler was inhibited for read out, the second scaler was inhibited and recorded clock cycles. In this way, the data can be reconstructed with every clock cycle recorded.

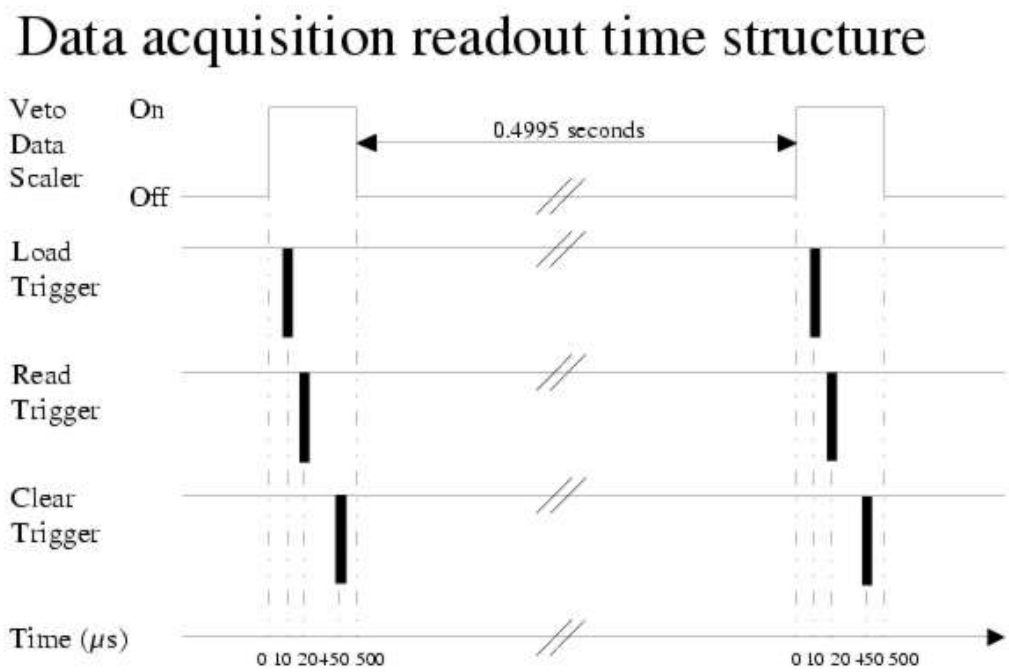

Figure 4.15 Data acquisition readout time structure. The data are acquired by the scaler for 0.4995 s when the VETO is OFF. Each readout cycle consists of a load event, read event, and a clear event. The data scalers are read out during the veto interval of 500 clock cycles. The clock is running at a frequency of 100000 Hz therefore scaler readout occurs within 50 cyc x 10^{-5} s/cyc = 500 μs. The time scale shows when the various triggers are fired by the Kinetic Systems model 3655-L1A timing generators. The cycle is repeated indefinitely.

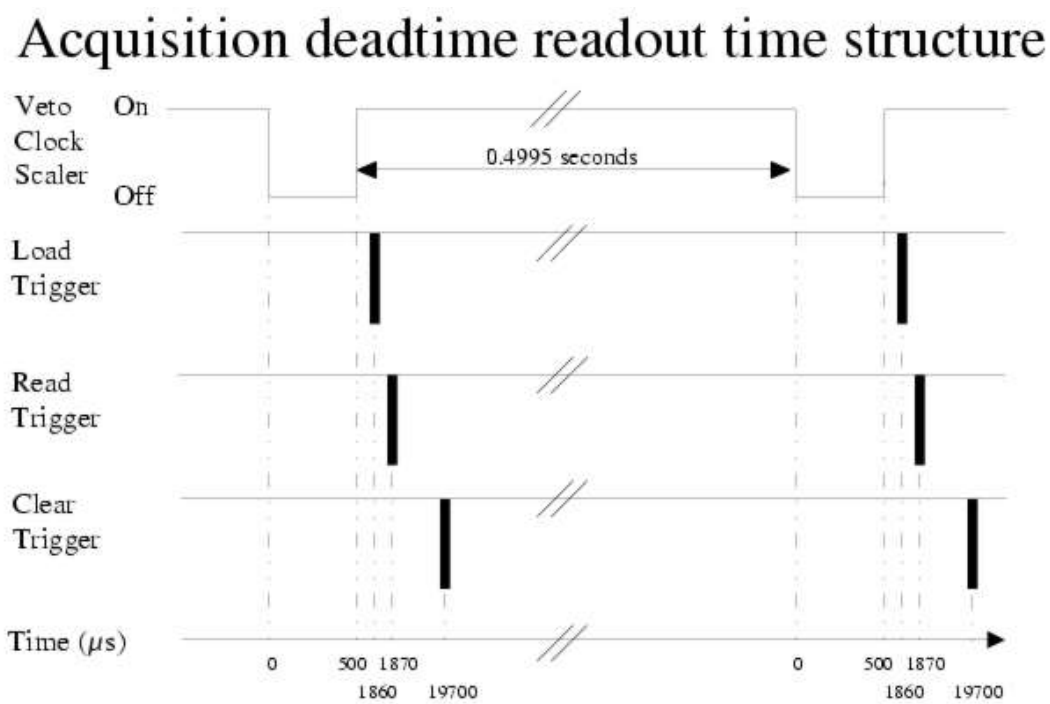

Figure 4.16 Acquisition deadtime readout time structure. The deadtime associated with the data acquisition system readout is recorded by a complementary scaler. The scaler records the 100000 Hz clock cycles during the data readout time of 500 μs. The time scale shows when the various triggers are fired by the Kinetic Systems model 3655-L1A timing generators. For example: the load trigger is fired at clock cycle 1860 which is 1860 cyc x10^{-5} s/cyc = 0.0186 s after the complementary scaler began recording data. The cycle is repeated indefinitely.

4.9 Monte Carlo Simulations

Monte Carlo simulations of the ^{14}O half-life decay are used to check the fitting algorithm and examine the systematic effects. The simulation includes deadtime and the data acquisition timing to reproduce the experimental conditions. The simulation creates

a decay time spectrum based on a nominal half-life of 70.600 seconds. In the simulation, an extending 40 ns deadtime is followed by a non-extending 400 ns deadtime as in the actual experiment. To begin the Monte Carlo simulation, random points in time are generated, weighted by the exponential decay probability function for a 70.600 second half-life isotope. A uniform background is then added to the same time interval. This is done on a time scale from 0 to 4000 seconds. The linear time scale is further divided into 8000 bins of 0.50000 seconds. Within the bins, only events that fall within the acquisition time from 0 to 0.49950 seconds are used to increment the number of counts within a bin. The next section of the simulation accounts for the deadtime associated with each event.

Only events which generate a non-updating deadtime pulse are counted by the program, just as these are the only events included by the electronics in the actual experiment. The program searches for the first event in time (t1) and the bin is incremented by one count. This time starts two deadtime routines, the first routine tracks the updating deadtime (40 ns) and the second the non-updating deadtime (400 ns). The program checks to when the next event arrives. If the next event (t2) arrives within 40 ns of the original pulse (t1), then the deadtime is extended again from that point in time. In effect, t2 now becomes t1 and the program searches for the subsequent arrival time. All events arriving with the non-updating deadtime are not counted; they are losses due to the deadtime. The algorithm only allows events that occur outside of the 400 ns non-extending deadtime to trigger the 400 ns deadtime. Consider an event that arrives at the first discriminator at 390 ns into the non-extending deadtime. The algorithm tracks the 30 ns of deadtime past the end of the 400ns deadtime. Any events arriving within this

window are also omitted. Should another event arrive within this 40 ns extending window, it will extend the deadtime as described above. This slight complication is due to the two deadtimes in series. The probability of an event arriving within a 40 ns window at 100 kHz is 0.4 % and at 10 kHz it is 0.04 %. The program continues to search for the next event that arrives after the non-updating deadtime. Once found, the above process is repeated until all events have been processed and recorded to a data file. Only events that fall within the 4000 second acquisition time of the cycle are recorded.

As a double check on the exponential decay distribution, the raw events (with no deadtime present) are also recorded in the data file. The simulated decay spectrum can also be modified by adding contaminants with various half-lives, gain shifts, or deadtime variations. For example, changing the gain of the detector as a function of rate can be used to modulate the original decay spectrum. The new modified decay spectrum is then fit with the routine used for the half-life analysis. The results from various gain changes are shown in Figure 4.17. From these results, the systematic uncertainties associated with such a gain change can be studied. The Monte Carlo simulations allow the systematic effects to be isolated and studied.

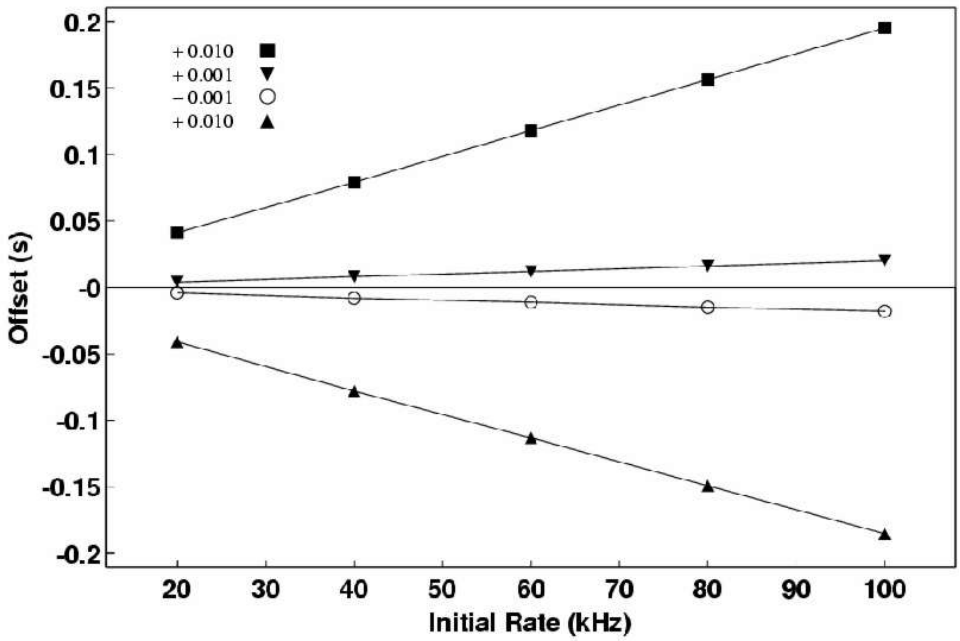

Figure 4.17 Effect of rate dependent gain shift on half-life. The Monte Carlo data have been modified by adding or subtracting events proportional to the rate as they would occur due to a gain shift in the photomultiplier tube. The data are then fit with the maximum likelihood method to determine the half-life. The offset from the nominal half-life of 70.600 s is plotted for various gain shifts.

4.10 O-14 Source Enclosure

The detectors are positioned on either side of the target vacuum enclosure as closely as possible to maximize the solid angle for beta detection. Figure 4.18 is a schematic which shows the location of the detectors with respect to the vacuum chamber. Figure 4.19 shows the scintillators, light guide, and photomultiplier tubes in the plastic

light tight enclosure that secures them in place for the measurement. The vacuum enclosure that contains the source of ^{14}O is visible to the left in Figure 4.19. The bottom of this enclosure is made of a 2.5 cm by 2.5 cm by 2.0 cm aluminum cube which has been machined out to act as a frame to support 0.005 cm thin mylar windows shown in Figure 4.18.

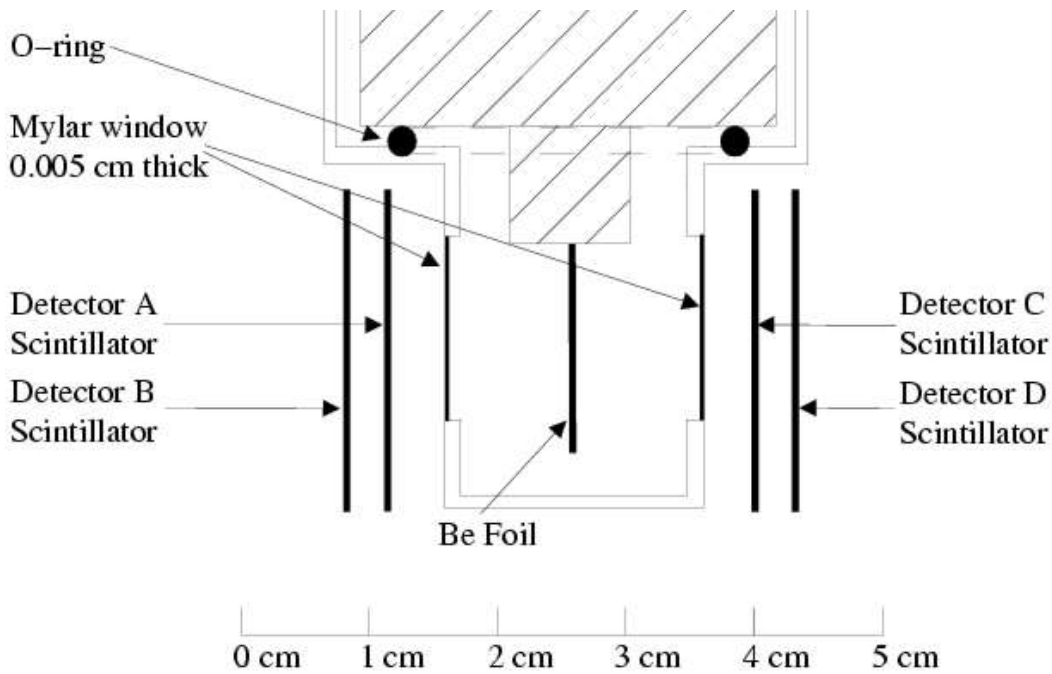

Figure 4.18 Scale drawing of the beta detectors located around the ^{14}O source. The ^{14}O is implanted in the Be foil for the half-life experiment. The beta particles travel through the mylar vacuum window and then pass through the beta detectors located on either side.

The mylar window allows the beta particles to exit the vacuum while losing 10 keV of energy on average. The mylar window can be seen bowing in towards the vacuum in Figure 4.20. The circular hole that is visible behind the mylar window is 1.5 cm in

diameter. The plastic scintillator is positioned within a 0.5 cm of the front surface of the mylar. The geometric solid angle for a beta particle, is approximately 12 percent.

Figure 4.19 Scintillators mounted on PMTs in plastic enclosure.

Figure 4.20 Mylar vacuum window mounted on beam line.

4.11 Radiation Shielding

In order to minimize any backgrounds from the environment approximately 1500 pounds of low radioactivity lead bricks were stacked around the detectors. Figure 4.21 shows the lead shielding which was 10 cm thick, at its thinnest point, and up to 25 cm thick in the direction of any potential external point source. The absorption length (1/e attenuation length) for a 2.31 MeV gamma ray is 22 g/cm^2 and 5.5 g/cm^2 for a 0.511 MeV gamma. The density of the lead bricks lead is 11.35 g/cm^3. The survival probability of a 2.31 MeV gamma ray passing through 10 cm of lead is 0.006 and for 25 cm of lead is 3×10^{-6} . The survival probability of a 0.511 MeV gamma ray passing through 10 cm of lead is 10^{-9} and for 25 cm of lead is essentially zero. For each run performed in the experiment, data were taken to monitor the room background.

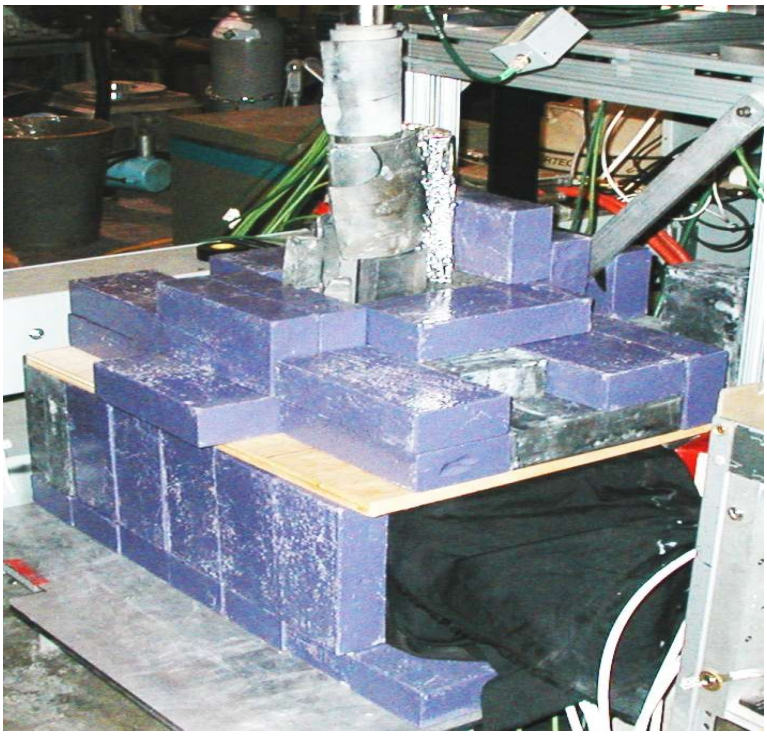

Figure 4.21 Photograph of lead shielding surrounding the beta detectors.

4.12 Sensitivity to Gamma Ray Backgrounds

The room background is predominantly due to β^+ annihilation photons and γ rays from ^{14}O decays in the ECR and associated vacuum equipment. In this experiment, it is desirable to decouple the detectors from any potential fluctuations in room background that could affect the half-life measurement. A ^{137}Cs source was used to establish a baseline for expected backgrounds without any shielding around the detectors. The probability of detecting a gamma ray with the β detector was determined by counting the event rate produced by an 898 μCi ^{137}Cs source placed a distance of 16.5 cm in front of the scintillator. A visual scaler was used to count the number of events that arrive in a period of 500 seconds. The background was determined by repeating the process without the source then subtracted from the signal. The probability of detecting a γ ray of energy equal to 0.66 MeV is $0.77 \pm 0.01\%$. The probability increases at lower energies and decreases at higher energies as the cross-section for photon interaction with matter changes.

4.13 Calibrated Frequency Standard

All the deadtimes discussed above were measured absolutely by a time to digital converter (TDC) which was calibrated by a frequency generator. The frequency generator was calibrated by two frequency counters which were calibrated by the NIST broadcast frequency standard at 1 Mhz, 2.5MHz, 5 Mhz, and 10Mhz. The frequency counter calibration results are shown in Table 4.4.

The timing reference for this experiment is based on three independent free running oscillators. The frequency generators are set to run at 100 kHz each by adjusting their frequency while watching the calibrated frequency counters. Each oscillator signal is logged by the scalers during the acquisition and readout time. The frequency generators used for the master clock and the two free running oscillators were an HP3325A (master), an HP3336C (free running #1), and an HP3336C (free running #2). The frequency counters used for this experiment were an HP5386A (counter A) and another HP5386A (counter B).

Proper Frequency (Hz)	***HP5386A counter A reads***	***HP5386A counter B reads***
1000000.0	1000000.6	1000000.2
2500000.0	2500001.6	2500001.2
5000000.0	5000003.2	5000002.4
10000000.0	10000006.0	10000004.0

Table 4.4 Calibration data for the Hewlett Packard frequency counters.

4.14 Deadtime Measurement

The deadtime of an event was dominated by the width of the gate generator output. This pulse width must be well measured against a traceable time standard. Traceability was established from the frequency counters, which were used to set the signal generator frequency. The signal generator frequency was then used to calibrate the TDC. The TDC was calibrated over a range from 300 ns to 714 ns which is discussed in section 4.14.1. Once the TDC was calibrated, the gate widths of the individual channels were measured and are discussed in section 4.14.2.

4.14.1 Calibration of the TDC

A LeCroy 2228A time to digital converter was used to measure the deadtime. The TDC has a resolution of 11 bits (2048 channels) or 0.25 ns per channel with a full scale time period of 500 ns. The TDC was calibrated by measuring the time between pulses of a known frequency. A Hewlett Packard HP5386A frequency counter measures the signal generator frequency. A Hewlett Packard HP3325A level generator was used to calibrate the TDC. The TDC was calibrated at the six different frequencies listed in Table 4.5 and plotted in Figure 4.22.

Frequency (MHz)	***Corresponding Time (ns)***	***Measured TDC channel***	***Uncertainty (channel)***	***Corresponding Uncertainty in Time (ns)***
1.4000	714.29	1812.46	1.02	0.40
1.6660	600.24	1338.37	0.86	0.39
2.0000	500.00	922.30	0.73	0.39

Frequency (MHz)	***Corresponding Time (ns)***	***Measured TDC channel***	***Uncertainty (channel)***	***Corresponding Uncertainty in Time (ns)***
2.5000	400.00	507.65	0.60	0.47
3.0000	333.33	231.35	0.52	0.75
3.3330	300.00	93.60	0.48	1.54

Table 4.5 TDC calibration times. The frequency was determined using a calibrated HP5386A frequency counter. The frequency determines the deadtime which is then measured by the TDC. The TDC channels are calibrated at several points as shown.

The frequency of the signal was determined with a fractional uncertainty of 10^{-5}. The uncertainty of the calibration time was on the order of a nanosecond. The LeCroy 2228A TDC requires a start pulse, stop pulse, and approximately 100 μs to digitize the time. The electronic schematic for this circuit is shown in Figure 4.23. The timing diagram of the pulses is shown in Figure 4.24.

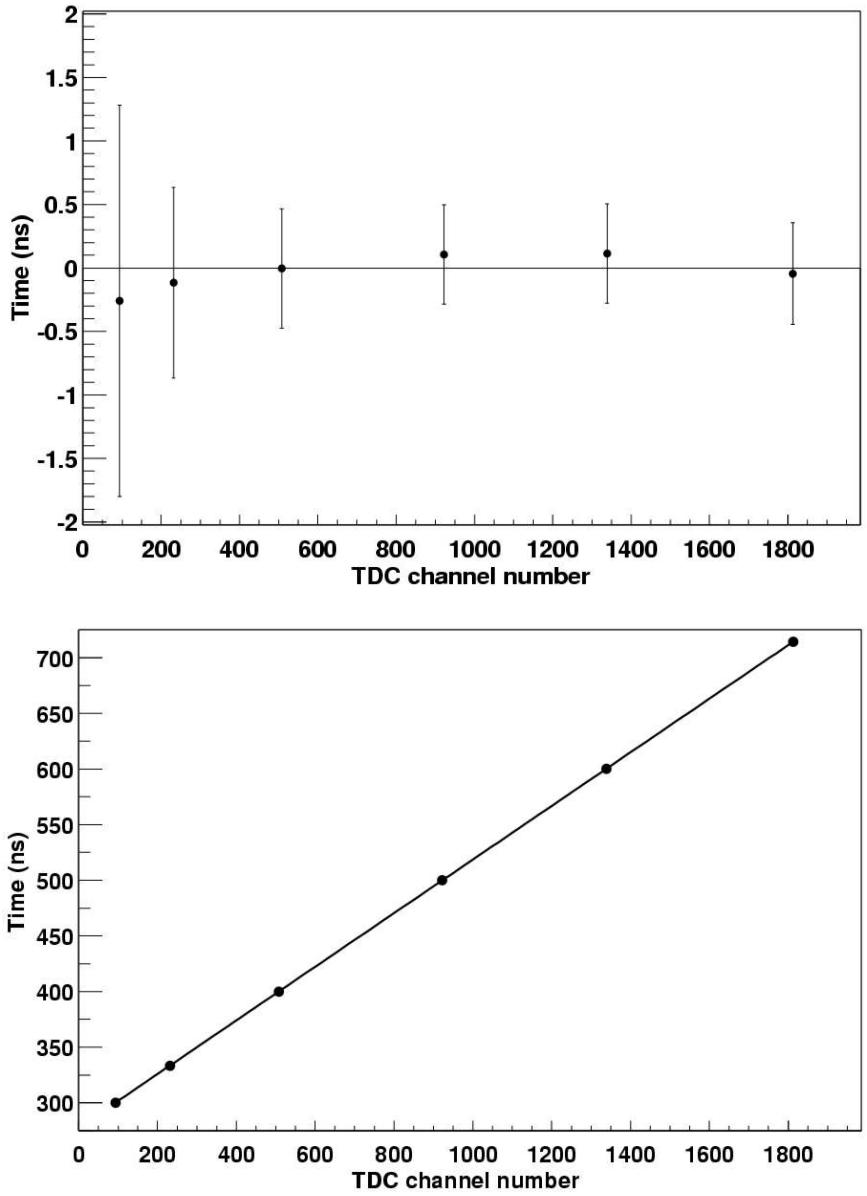

Figure 4.22 TDC calibration data. The TDC was calibrated with the frequency counter as discussed and the data from Table 4.5 are plotted in the lower graph. The data wer then fit to a straight line to check for linearity. The residuals with the uncertainty of each point in time is plotted in the upper graph. The TDC is linear within the precision measured.

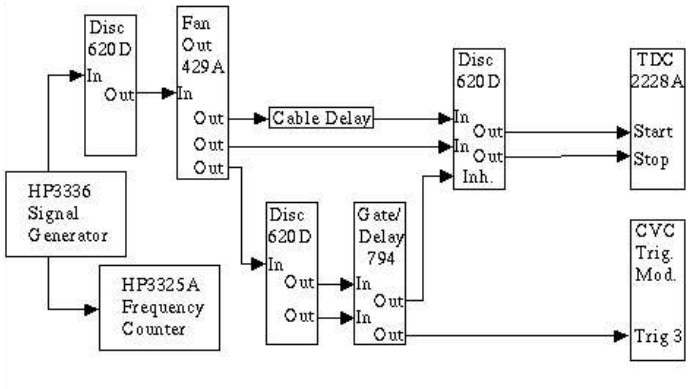

Figure 4.23 TDC calibration electronics. The signal generator produced a sine wave whose frequency was precisely measured by the frequency counter. The fan-out circuit and associated electronics started the 2228A TDC. The cable delay allowed the time difference between two subsequent pulses to be measured. The frequency was scanned from 1.4 Mhz to 3.3 Mhz which correspond to approximately 715 ns and 300 ns respectively.

A sine wave is generated by a frequency generator and input to a level discriminator. The discriminator output pulse of ≈20 ns width was fed into a LeCroy 429A logic fan-out. One fan-out output was delayed and then fed into a LeCroy 620D level discriminator. The output of this discriminator channel was the start pulse for the TDC. The second fan-out output was directly connected to a LeCroy 620D level discriminator. The output of this discriminator channel is the stop pulse for the TDC. The delay shifted the calibration range of the TDC by approximately 280 ns. This allowed the TDC to be calibrated up to times of approximately 775 ns. The TDC does not start its clock until the arrival of a start pulse. The stop pulse that arrived before the start pulse

was ignored. The next stop pulse stops the TDC clock and the digitization process begins. Any further start pulses are inhibited by the inhibit signal applied to the 620D discriminator.

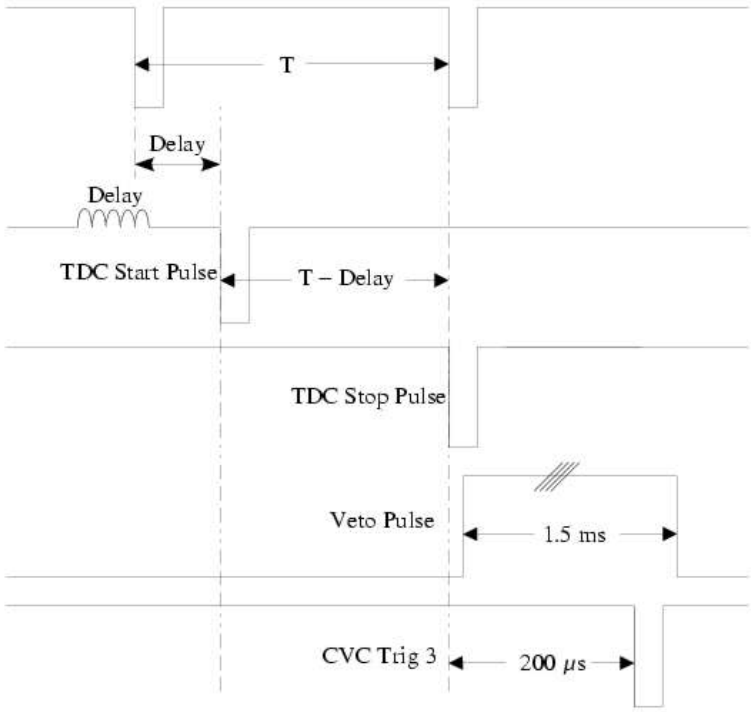

Figure 4.24 TDC calibration timing diagram. The timing diagram illustrates the order of the TDC start and stop pulses. The TDC data is read out after a delay of 200 μs from the stop pulse. During the data read out cycle the signal is inhibited by a veto pulse for 1.5 ms.

The final output from the 429A fan-out was buffered through another 620D discriminator to split the signal. Both outputs go to the Philips Scientific 794 gate and delay generator. One of the PS794 outputs was delayed and sent to the inhibit input of the

620D which controlled the start and stop pulses. This inhibit signal lasted for approximately 1.5 ms and allowed time for the TDC to digitize the signal and proper readout of the TDC by the CVC control module. The second output of the PS794 was delayed for approximately 200 μs, to allow for the TDC digitization, it then triggered the readout of the TDC module via the CVC trigger module. All TDC values are measured this way and the results are listed in Table 4.6.

Each data point in Table 4.6 consists of approximately 5 x 10^4 measurements of the TDC channel. Figure 4.25 shows a typical channel fitted with a gaussian using maximum likelihood minimization. The results from these fits and the one sigma uncertainty can be found in Table 4.6.

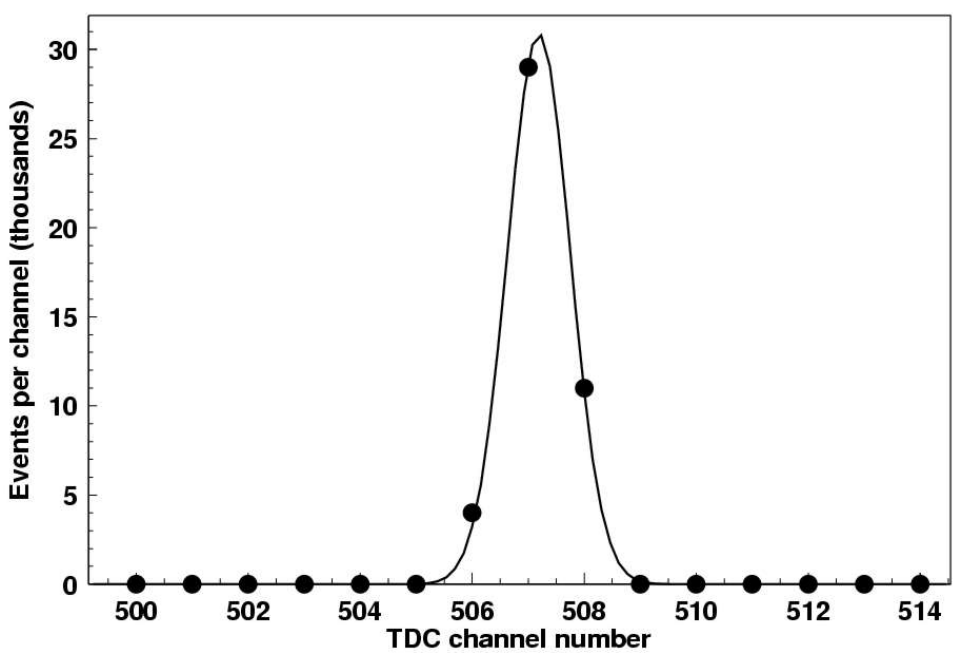

Figure 4.25 Typical TDC data points. The TDC data are fit with a gaussian to determine the TDC channel number and the uncertainty for a known pulse duration. The example

shows the TDC response to a 400 ns pulse width. The time and uncertainty are found to be 400.0 ± 0.47 ns.

4.14.2 Calibration of the Deadtime

The deadtime was calibrated with the same electronics used for the TDC calibration with one minor change. The output pulse from the gate generator only triggers a discriminator on its leading edge. In order to produce a pulse corresponding to the tailing edge the inverted output of the gate generator is fed into a discriminator shown in Figure 4.26. Figure 4.27 shows the timing diagram for the deadtime calibration measurement. The LeCroy 620D discriminator was checked to see if the channels produced any offset in output timing. This could happen if the slew rate of the discriminator electronics varied. The offset was examined on a Tektronix 2247A 100 MHz oscilloscope and the output difference was found to be less than 0.25 ns. The data was acquired the same way the TDC was calibrated. Each channel was fit with a gaussian using maximum likelihood minimization.

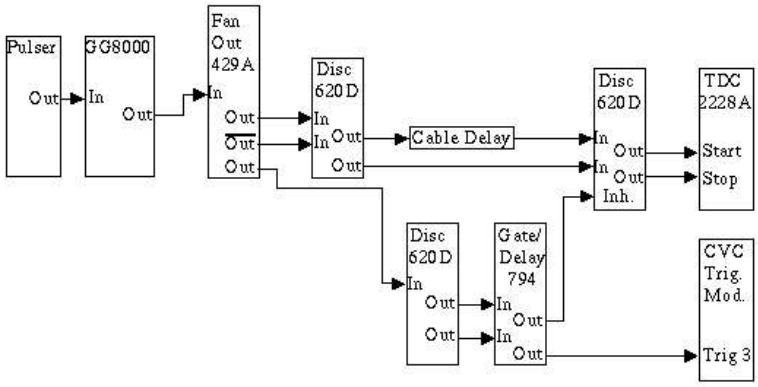

Figure 4.26 Deadtime calibration electronics. The pulse width (deadtime) of each channel was calibrated using the same circuit as the TDC calibration. The one change is that the input from the signal generator has been replaced by the pulse width generator (GG8000) used for the experiment.

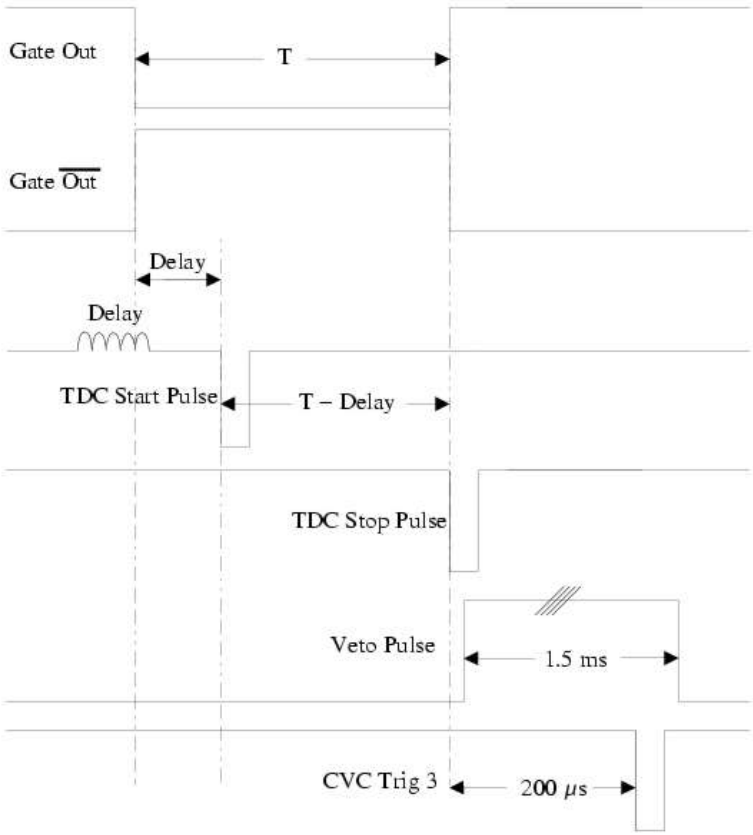

Figure 4.27 Deadtime calibration timing diagram. The timing diagram illustrates the order of the TDC start and stop pulses. The TDC data was read out after a delay of 200 μs from the stop pulse. During the data read out cycle the signal is inhibited by a veto pulse for 1.5 ms. The timing diagram is the same as used for calibrating the TDC. The only difference is that the pulse widths are obtained from the gate generator.

Channel	Nominal Deadtime (ns)	Type of Deadtime	Measured Deadtime (ns +/- 1 ns)
A	400	Non-Ext	400.4
B	400	Non-Ext	399.4
C	400	Non-Ext	401.1
D	400	Non-Ext	397.3
AB coincidence	400	Non-Ext	397.0
A delay B	400	Non-Ext	396.5
CD coincidence	400	Non-Ext	401.2
C delay D	400	Non-Ext	461.3
A	700	Ext	695.1
B	700	Ext	695.1
C	700	Ext	695.8
D	700	Ext	698.0
A singles	400	Ext	398.5
B singles	400	Ext	399.9
As delay Bs	400	Ext	396.8
Cs delay Ds	400	Ext	395.1
A	400	Ext	402.1
B	400	Ext	398.2
C	400	Ext	399.1
D	400	Ext	402.1
AB coincidence	400	Ext	398.7
CD coincidence	400	Ext	400.0
A delay B	400	Ext	399.4

Channel	Nominal Deadtime (ns)	Type of Deadtime	Measured Deadtime (ns +/- 1 ns)
C delay D	400	Ext	399.4

Table 4.6 Summary of deadtime for each channel. The deadtime of the 24 channels corresponding to the ^{14}O events have been measured. The nominal deadtime was set by adjusting the output pulse width while monitoring the pulse on an oscilloscope. The type of deadtime indicates either non-extending (Non-Ext) or extending (Ext).

4.15 Beta Detector Systematics Effects

A precise half-life experiment requires a detector system which has a constant efficiency for a period of time at least as long as a measurement cycle. Ideally the detector system response to a decay event should not depend on any extrinsic or intrinsic parameters e.g.: PMT temperature, discriminator temperature, high voltage temperature, rate dependent gain shift, high voltage fluctuations, gain shifts, or AC line voltage changes. If the detector response is sensitive to any of these parameters, then the measured half-life can be modulated. The effect can either shorten or lengthen the measured half-life depending on the trend in the parameter during the measurement cycle. Extensive testing of the detectors was performed using a sealed source before and after the experiment. The possible systematic effects on the half-life measurement from detector stability issues are discussed in the following sections.

4.15.1 ^{90}Sr Sealed Source for Stability Tests

A thin window ^{90}Sr sealed source was used as a source of beta particles. The ^{90}Sr sealed source had an activity of 75 microcuries or 2.7 x 10^6 decays per second. ^{90}Sr decay contains two beta decay branches shown in Figure 4.28. The endpoint energies of the branches are 0.546 MeV and 2.28 MeV. This source was used to simulate the ^{14}O beta spectrum that would occur during the experiment. The intensity of the source allowed testing of the detectors up to event rates of 100 kHz.

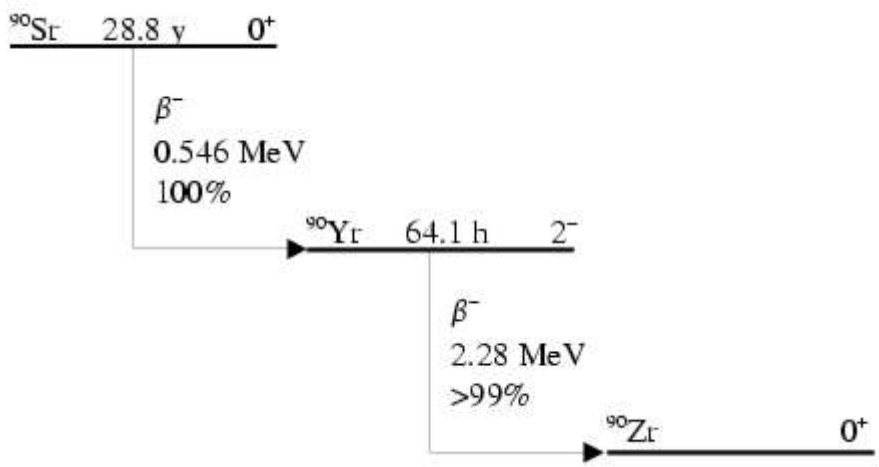

Figure 4.28 Sr-90 decay scheme. The data were taken from the Table of Isotopes[86].

4.15.2 High Voltage Supply Temperature Stability

Each detector had an Ortec 456 high voltage power supply (HVPS) connected to its base. The temperature of the power supply was varied in order to determine the effect that temperature changes have on the count rate. The temperature of the HVPS was

varied by blowing hot air on it with a heat gun. Simultaneously, the HVPS temperature was monitored with a thermocouple probe connected to a digital readout display. The count rate of the ^{90}Sr source was monitored continuously by the data acquisition system throughout the measurement. The temperature was increased from 26.7 ºC to 37.7 ºC the count rate increased for each detector as the HVPS temperature increased as shown in Figure 4.29. The relative count rate change was used to calculate the temperature stability and is summarized Table 4.7.

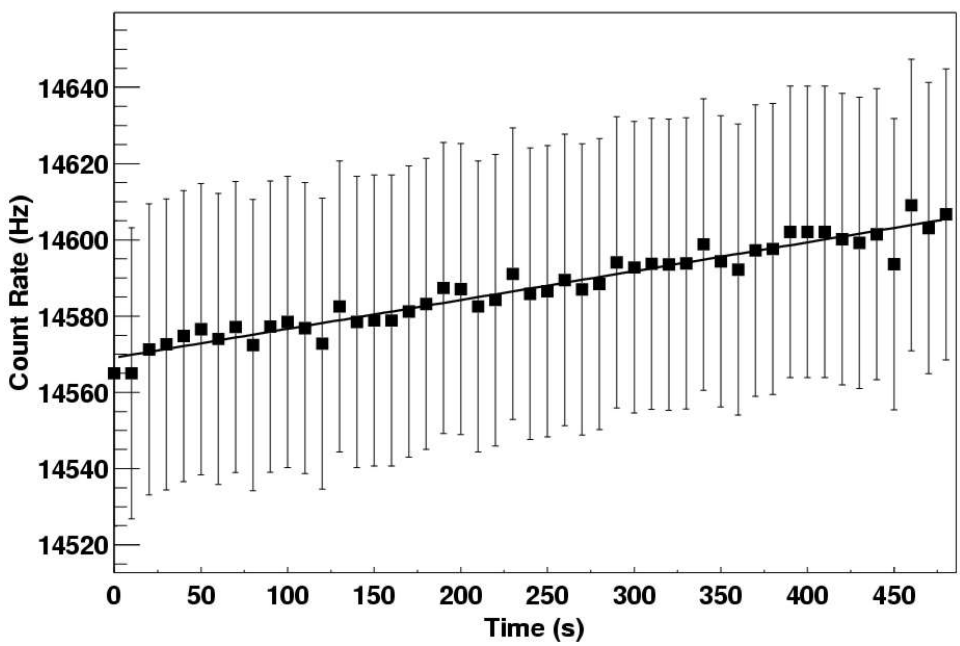

Figure 4.29 Temperature effect on high voltage supply. The graph shows the dependence the rate has on the temperature of the high voltage supply. The data shown here was averaged over 10 s intervals. The temperature of the high voltage supply was raised from

26.7 ºC to 27.7 ºC over the time interval.

The temperature of the HVPS was measured with a thermocouple during the run. The temperature output of the thermocouple was recorded on a linear chart recorder and is plotted in Figure 4.30. The largest temperature variation was 2.4 ºC in 5 hours which corresponds to a slope of 0.48 ºC per hour. The effect on the half-life depends on the initial count rate. An average value is 1.8 ms at 60 kHz and specific cases are listed in Table 4.8 and plotted in Figure 4.31. The effect this slope has on the half-life is determined by Monte Carlo methods discussed in section 4.9.

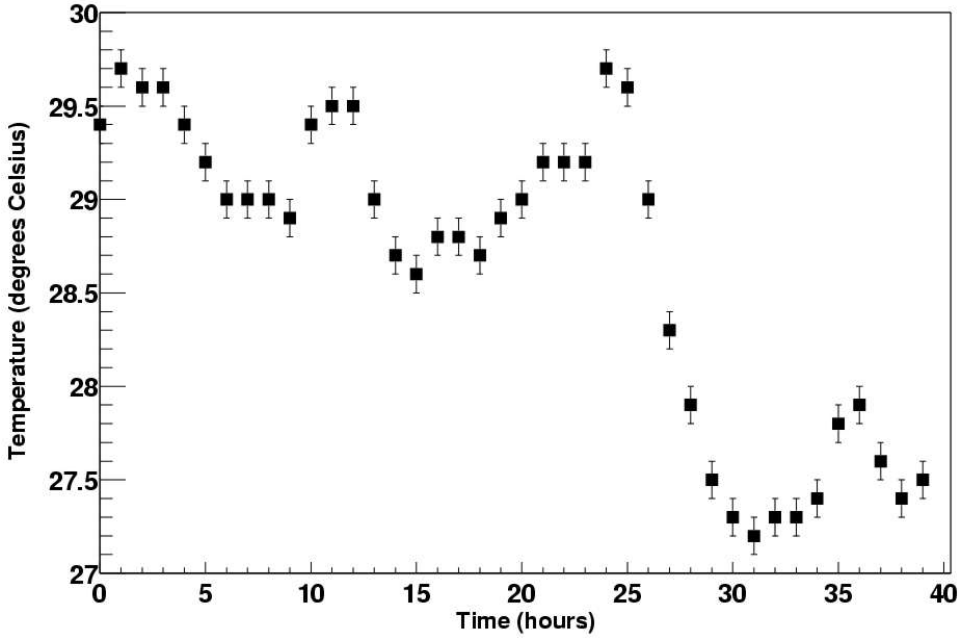

Figure 4.30 Temperature of high voltage supplies versus time. The temperature of the high voltage power supplies was monitored during ther experiment. The uncertainty

arises from the uncertainty associated with reading the temperature from the chart recorder data.

High Voltage Supply for Detector	***Relative Rate Change in % / °C***	***Largest Slope in % / hour***
A	0.038	0.018
B	0.026	0.013
C	0.032	0.015
D	0.014	0.007

Table 4.7 Summary of temperature effects of high voltage power supply.

Initial Count Rate for Fit in Hz	***Shift in the lifetime in ms with a slope of 0.015 % / hour***
20000	1.00
40000	1.20
60000	1.80
80000	2.40
100000	3.00

Table 4.8 Summary of high voltage temperature effect on half-life.

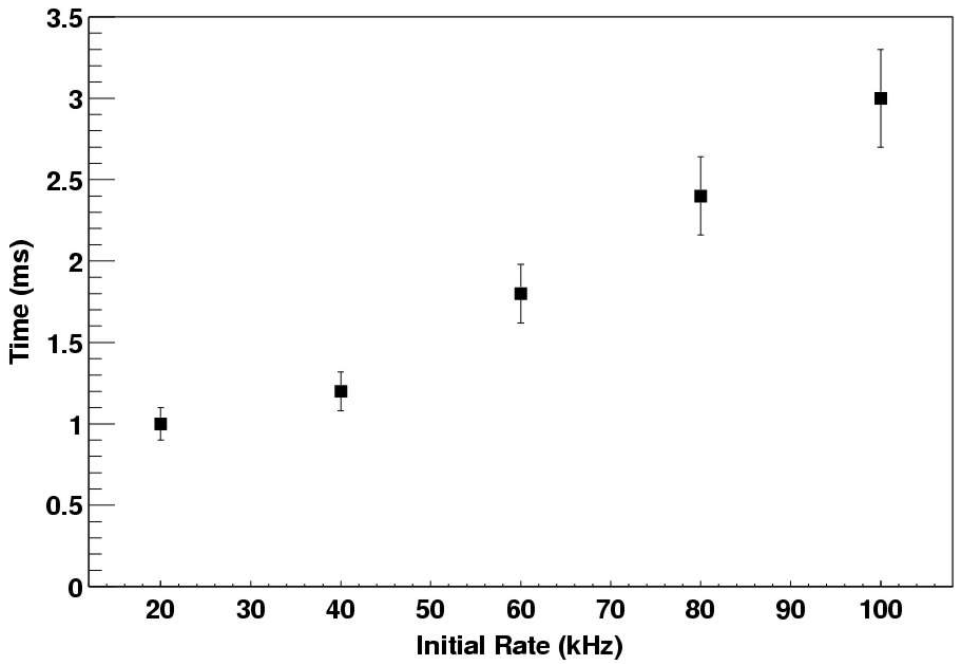

Figure 4.31 Systematic offset due to temperature change of high voltage supply. The data from Table 4.9 are plotted in the graph above. The time in ms above shows the offset to the half-life due to the slope introduced by the temperature dependence of the high voltage supply.

4.15.3 High Voltage Power Supply Voltage Stability

The voltage of the PMT power supply affects the gain of the PMT. This can change its response to the beta particle events. The voltage stability of the power supply was measured using a voltage sensitive LeCroy 8232 ADC. The 8232 ADC has a resolution of 4096 channels and a DC voltage range of 0 to 10 volts. The high voltage output of the power supply was divided by a voltage divider 138.75 times from 1250 volts to 9.009 volts. The voltage was recorded every second for approximately 10000

seconds. All events during this measurement arrived at channel 3690. The sensitivity of the ADC was calibrated by varying the input voltage by 100 volts from 1250 V to 1150 V and recording the channel number of the ADC. At 1250 V channel 3690 acquired all events and a 1150 V channel 3395 acquired all the events. All events acquired during the measurement and calibration fell within a single channel. The sensitivity of the ADC is 0.339 V/channel. The voltage from the power supply is stable at the level of 0.00027 or 1 part in 3687 for a period of 10000 seconds. The effect on the lifetime can be inferred by assuming a monotonic drift of the voltage of the measurement period which gives a slope of approximately 0.122 V/hr.

To determine the effect a change in voltage has on the count rate a direct measurement was performed. The ^{90}Sr source produced beta events while a scaler recorded events for period of 5 seconds. The voltage was then varied from 1250 V to 1225 V. The count rate changed from 115463 Hz to 112559 Hz for a difference of 2903 Hz or 116Hz/V. The magnitude of this effect is then 0.1 %/V which becomes 0.034 %/hr. This is the worst case scenario for a voltage variation in the high voltage supply. The maximum effect this could have on the half-life is summarized in Table 4.9 and plotted in Figure 4.32.

Initial Count Rate for Fit in Hz	***Shift in the lifetime in ms with a slope of 0.034 % / hour***
20000	2.26
40000	2.72
60000	4.08

Initial Count Rate for Fit in Hz	*Shift in the lifetime in ms with a slope of 0.034 % / hour*
80000	5.44
100000	6.80

Table 4.9 Summary of voltage variation effect on half-life.

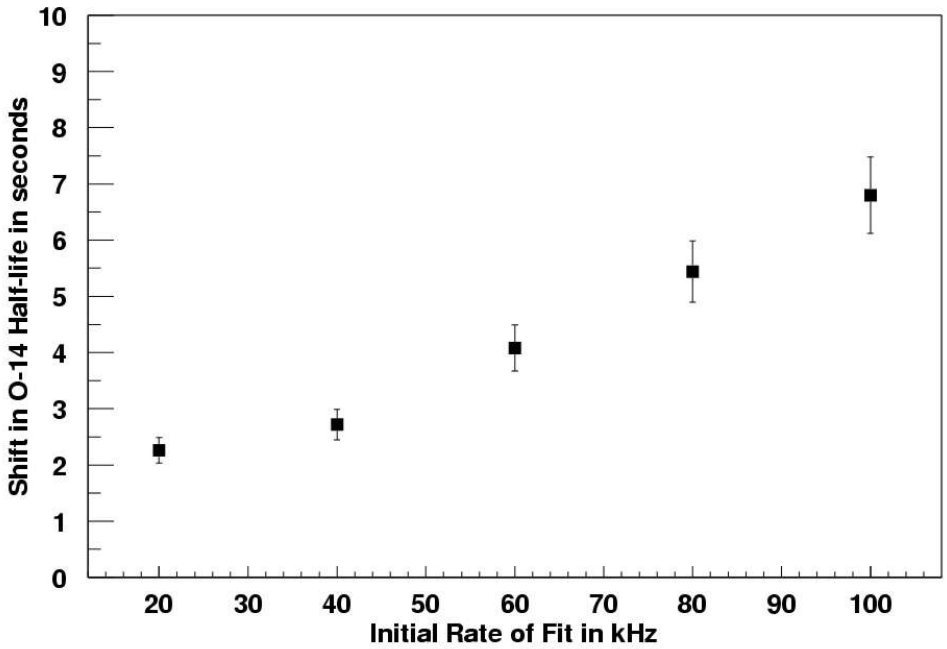

Figure 4.32 High voltage variation effect on half-life.

4.15.4 PMT Temperature Stability

Each detector is made of a Hamamatsu R647 photomultiplier tube and base. The temperature of the PMT and base were varied in order to determine the effect on the count rate. The temperature of the PMT and base was changed by blowing heated air into the PMT support stand with a heat gun. Simultaneously the PMT and base temperature

were monitored with a thermocouple probe connected to a digital readout display. The count rate of the ^{90}Sr source was monitored continuously by the data acquisition system throughout the measurement. The temperature was increased from 20.3 ^{o}C to 39.2 ^{o}C over a period of approximately 8100 seconds. The count rate increased for each detector as the temperature increased. The relative count rate change was used to calculate the temperature effect which is summarized in Table 4.10.

Photomultiplier Tube	***Relative Rate Change in % / ^{o}C***
A	0.0050
B	0.0035
C	0.0056
D	0.0039

Table 4.10 Photomultiplier tube temperature stability.

Following this test, the bases of the photomultiplier tubes were connected to copper heat sinks cooled by the 88-Inch Cyclotron low pressure cooling water supply. The temperature of the PMTs was monitored after the run under the same conditions as the run. A thermocouple was placed inside the enclosure near the PMT and base while the temperature was recorded on a linear chart recorder. The temperature varied by ± 0.15 ^{o}C over a period of 140 hours as shown in Figure 4.33. The steepest slope during the observation time was 0.05 ^{o}C/hour. Using a relative rate change of 0.0056 %/^{o}C, the largest dependence of the detectors, the slope would be 0.00028 %/hour. This would have

an effect on the lifetime at the level of 0.011 ms at an initial rate of 10 kHz and 0.056 ms at an initial count rate of 100 kHz. This effect contributes negligibly to the systematic uncertainty of the result.

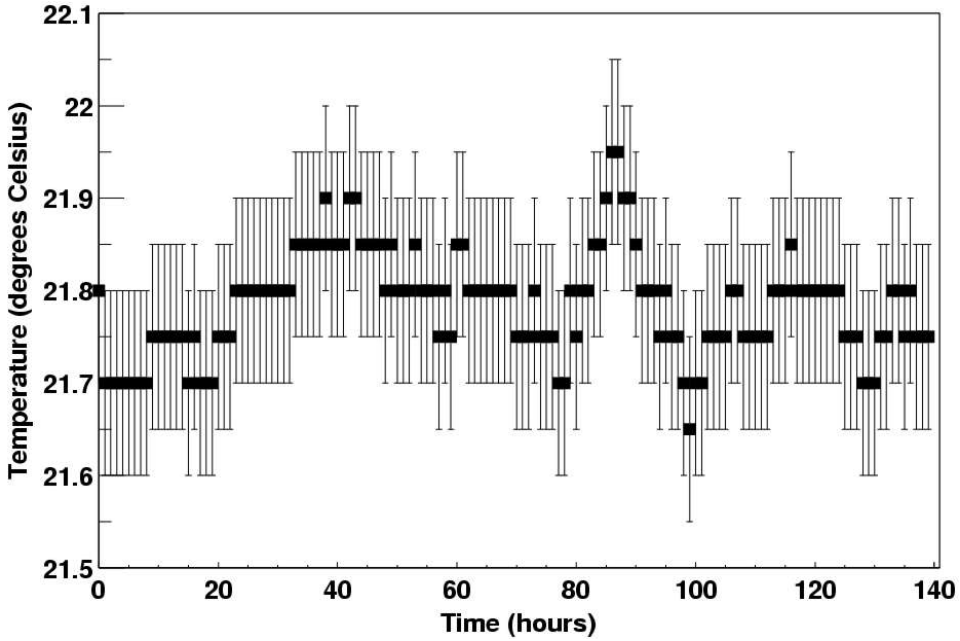

Figure 4.33 Temperature of PMTs used for the half-life experiment. The temperature of the PMTs was monitored with a thermocouple and a chart recorder for 140 hours following the experiment. The temperature recorded here establishes that the PMT temperature variation influences the half-life at the level of only 0.05 ms and is a negligible effect.

4.15.5 Discriminator Voltage Stability

The discriminator stability was monitored directly via the comparator monitor voltage on the front of the 11x2121 discriminator module. The output voltage was

connected to a linear chart recorder with a sensitivity of 2.5 mV per cm and recorded at a rate of 5 cm/hr for 13 hours. The discriminator was set at 20.6 mV and the voltage varied by < ± 0.03 mV over the observation time. An overall systematic uncertainty of ± 0.03 mV is assigned to the discriminator voltage due to the uncertainty in measuring the small variations. An uncertainty of ± 0.03 mV introducesd a maximum systematic effect of ± 3.0 ms at 100 kHz.

The effect of the discriminator voltage on the count rate was determined directly by varying the discriminator voltage from 20 mV to 100 mV in 1 mV steps. At each step the change in count rate from a ^{90}Sr source was recorded as shown in Figure 4.34. At 25 mV, a typical value for the experiment, a change of ± 0.03 mV produces a change of ± 0.017% in the count rate. This would affect the lifetime value at the level of ± 0.6 ms at 20 kHz and ± 3.0 ms at 100 kHz if the effect were not randomly distributed. The drift in the discriminator value has a characteristic period of several hours so the values stated above are extreme values resulting from a coherent monotonic drift.

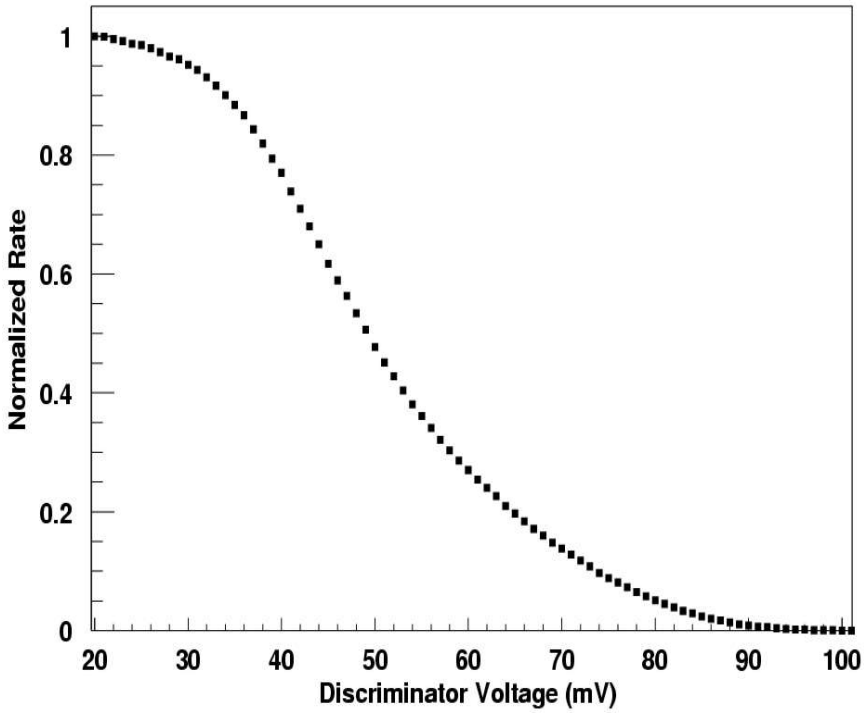

Figure 4.34 Discriminator response versus discriminator voltage.

4.15.6 Deadtime Uncertainty

The uncertainty associated with measuring the longer non-extending deadtime also contributes to the systematic uncertainty of the half-life. The nominal uncertainty in measuring the deadtime is ± 1.0 ns. This corresponding uncertainty in the half-life depends on the initial count rate. The effect the deadtime has on the half-life is examined using Monte Carlo methods discussed in section 4.9. An uncertainty of ± 1.0 ns with a 400 ns deadtime produces a systematic uncertainty of ± 0.2 ms per 10 kHz of initial start rate. For example, an initial count rate of 20 kHz and 400 ns deadtime with a ± 1.0 ns

uncertainty produces a systematic uncertainty of ± 0.4 ms in the half-life. Similarly an initial count rate of 50 kHz and a 400 ns deadtime with a ± 1.0 ns uncertainty produces a systematic uncertainty of ± 1.0 ms in the half-life. The uncertainty due to deadtime is one of the smaller systematic effects in this experiment. The systematic uncertainties are summarized later in Table 4.13 for easy comparison. Figure 4.35 is a plot of the deadtime offset effect for initial rates of 20 kHz and 50 kHz. In this figure the data is fit with nominal deadtime of 400 ns - 50 ns, 400 ns, 400 ns + 50 ns.

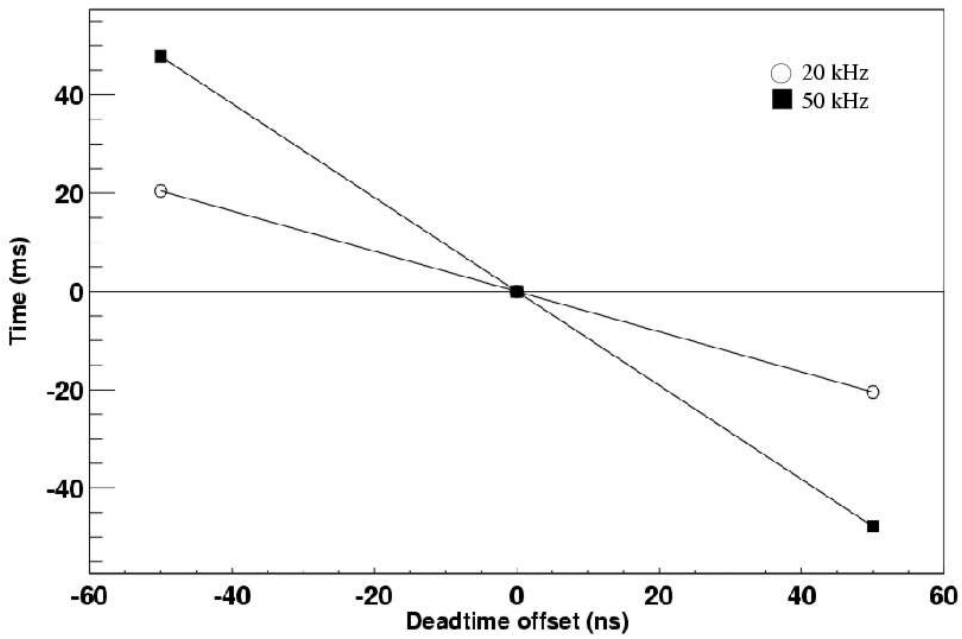

Figure 4.35 Half-life offset due to deadtime offset. The half-life is systematically shifted when the incorrect deadtime is used to fit the data. The Monte Carlo simulated data used here had a deadtime of 400 ns. The Monte Carlo data was fit with deadtime offset of -50 ns, 0 ns, and +50 ns. The magnitude of the shift depends on the initial rate of the fit as can be seen from the data fit at an initial rate of 20 kHz and 50 kHz.

4.15.7 PMT Noise

The background rate of the detectors must also be stable in time to make a precise half-life experiment. Drift in the background can skew the half-life value and lead to erroneous determination of any other time dependent components. The background is monitored for each set of data acquired out to a time of 4000 seconds. The background after the experiment was also observed to verify that the rate agreed with rate during the experiment.

During and after the experiment, the background count rate showed 25%to 50% deviations from average values. This is due to dark counts, leakage currents, and electronic noise associated with PMTs [70]. At some times, the background in the four separate detectors appeared correlated and at others uncorrelated. In order to characterize the effect this fluctuation could have on the half-life, an artificial shift in the background was inserted into the data analysis fitting routine. For each detector ± 50% constant offsets from the average background were used to determine the offset these deviations could produce in the half-life. The data for each detector was fit without any offset in the background, with a 50% increase, and with a 50% decrease. The resulting offset of the half-life from the unperturbed values are shown in Table 4.11 at two different initial rates. It was found that the background has a larger effect on the half-life at low initial count rates than at larger initial count rates. This is simply due to the statistical

importance of the background relative to the statistical importance of the ^{14}O data.

Detector	*Average Background in Hz*	*Offset of Half-life at 20 kHz in ms*	*Offset of Half-life at 100 kHz in ms*
B	0.1056	1.60	1.00
C	0.5583	8.50	4.80
D	0.1890	2.90	1.60

Table 4.11 Summary of background uncertainty effect on half-life.

4.15.8 Gain Shift versus Count Rate

The gain of the PMT can change as a function of the event rate. This can be measured by examining the pulse height spectrum of the PMT at various rates. The beta events were generated by an uncollimated ^{90}Sr beta source. The beta particle event rate was varied by moving the source away from the detector which reduced the solid angle. The pulse height spectrum was measured with a LeCroy 2259W ADC at event rates of 10 kHz and 100 kHz as shown in Figure 4.36. These rates represent the two extreme initial rates used for fitting the data. At 10 kHz the mean of the pulse height spectrum was 60.83 and at 100 kHz the mean was 57.38. The difference indicates a shift of 3.45 channels in the ADC spectrum. The fractional change in the count rate was determined by integrating the total area under the pulse height spectrum and dividing it by the area of a channel at the threshold. The fractional change in the count rate for a shift in the spectrum at the discriminator set point by 1 channel is 0.000164 at 10 kHz and 0.00012 at 100 kHz. A

shift of 3.45 channels results in a relative count rate change of 0.000566 at 10 kHz and 0.000414 at 100 kHz. This shift is proportional to the rate and affects the half-life by increasing it by 2.26 ms at 10 kHz and 8.28 ms at 100 kHz. This linear shift with rate is discussed in the Monte Carlo section 4.9.

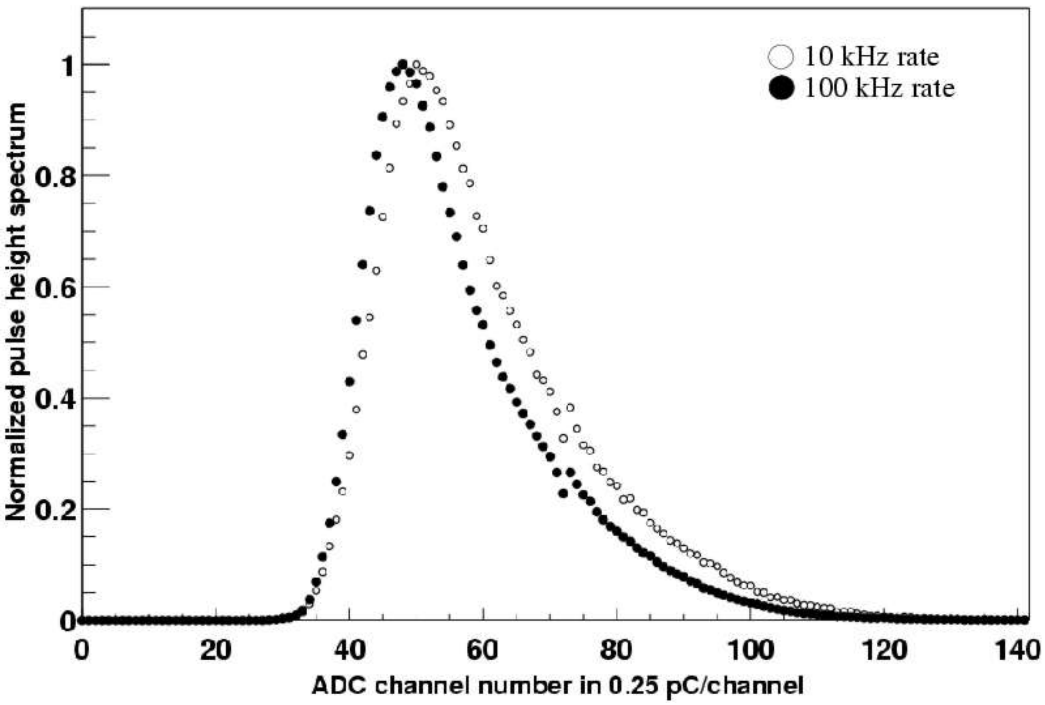

Figure 4.36 Detector spectra at 10 kHz to 100 kHz rate. The gain of the photomultiplier decreases as the rate increases. This can be seen by examining the shift of the mean of the spectrum from ADC channel 60.83 at 10 kHz to ADC channel 57.38 at 100 kHz.

4.15.9 Summary of Systematic Effects on Half-life

The overall systematic uncertainty varies from detector to detector and is also rate dependent. The systematic effects discussed above are summarized in Table 4.13. The

total uncertainty for each detector as a function of initial rate is plotted in Figure 4.37.

Systematic Effect	***10 kHz***	***20 kHz***	***30 kHz***	***40 kHz***	***50 kHz***
HVPS temperature	0.90	1.00	1.10	1.20	1.50
HVPS voltage	2.15	2.26	2.49	2.72	3.40
PMT temperature	0.01	0.02	0.02	0.03	0.03
Discriminator	0.30	0.60	0.90	1.20	1.50
Deadtime	0.20	0.40	0.60	0.80	1.00
After Pulse	0.50	0.49	0.48	0.47	0.46
Gain Shift	2.00	2.67	3.33	4.00	4.67
Bgnd Detector B	1.80	1.60	1.40	1.20	1.00
Bgnd Detector C	9.73	8.50	7.27	6.03	4.80
Bgnd Detector D	3.33	2.90	2.47	2.03	1.60
Total for Detector B	5	6	6	7	7
Total for Detector C	13	13	12	11	11
Total for Detector D	7	7	7	7	8

Table 4.12 Summary of systematic uncertainty as a function of initial rate.

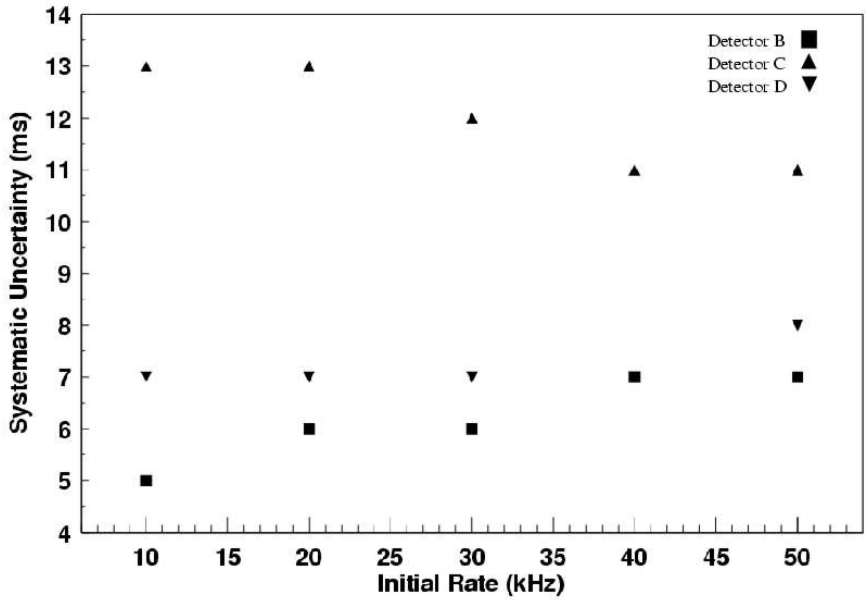

Figure 4.37 Summary of systematic uncertainty as a function of rate.

4.16 Contamination by Other Half-Life Components

The nuclear reaction used for this experiment produces ^{11}C, ^{13}N, ^{15}O, and ^{14}O. Some of the molecules that can be formed in the carbon target are: $^{11}C^{16}O$, $^{13}N^{16}O$, $^{12}C^{15}O$, and $^{12}C^{14}O$. These isotopes diffuse out of the target as described in section 2.1. Approximately 50% of these radioactive molecules end up in the vacuum chamber attached to the IRIS ECR. The molecules can then diffuse throughout the vacuum chamber. The end-point energies of these isotopes is similar to that of ^{14}O. The efficiency of each detector to these isotopes is equal to that of ^{14}O. There are two vacuum pumps on the IRIS beam line that remove molecules from the chamber. The first one is a 500 liter per second turbomolecular pump which is backed by a Megasorb zeolite pump. Molecules that enter the turbomolecular pump are removed from the system. The second

vacuum pump is a Cryo-Torr 7 cryogenic pump with a pumping speed of approximately 1000 liters per second. The cryogenic pump uses activated charcoal on a cold head array to effectively trap molecules that enter the pump. Even with this pumping capacity there are still a small fraction of radioactive molecules which are not removed from the system by either of these pumps. These radioactive molecules can then be trapped in the observation volume once the foil holder has been lowered into place for a counting cycle. Figure 4.38 shows the observation chamber which is approximately 10^{-5} the volume of the vacuum chamber after the ion source.

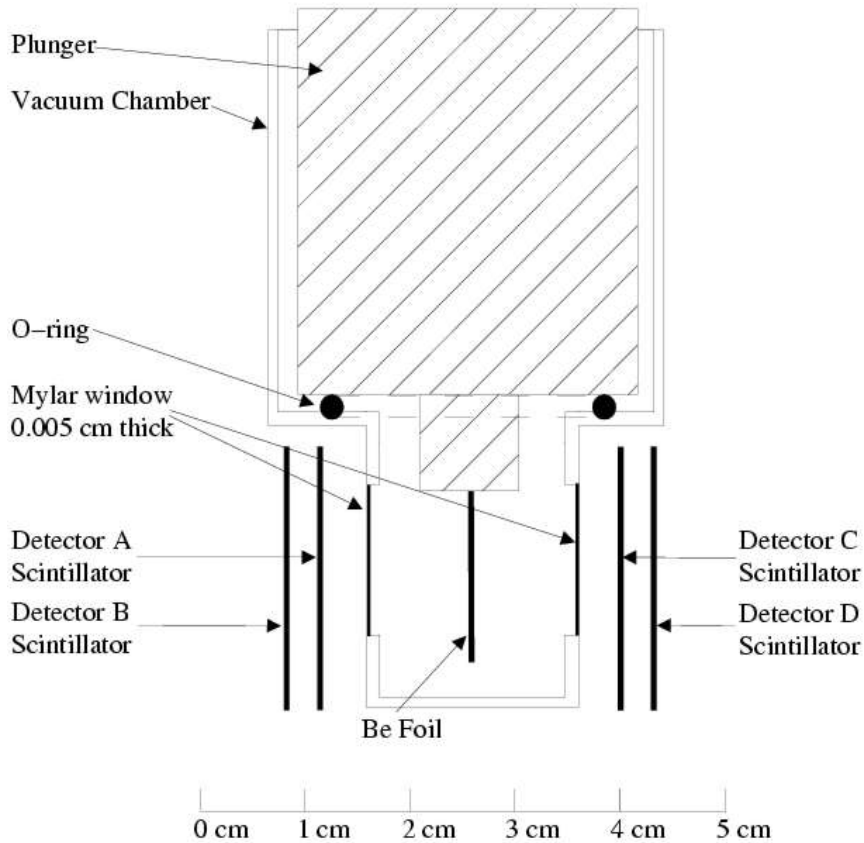

Figure 4.38 Observation chamber for the half-life experiment. The Be foil, with the ^{14}O implanted on it, is located in the center of the vacuum chamber. The beta particles from ^{14}O decay lose 10 keV of energy on average traversing the mylar vacuum window. The active scintillator of each detector is placed as close as possible to the vacuum window to maximize the solid angle with respect to the source.

These radioactive isotopes all have longer half-lives than the ^{14}O isotope. If they are not included in the data analysis, they skew the ^{14}O half-life towards a longer half-life. The size of the offset depends on the initial rate used for the fit. At lower initial rates, ie 10 kHz, the longer half-life components have a larger effect on the half-life than at higher

initial rates, ie 60 kHz. The relative size of these effects is tabulated in Table 4.13 for each isotope separately. The effect of each isotope on the half-life is determined using the Monte Carlo technique discussed in section 4.9. This was accomplished by adding 100 Hz of the contaminant at the initial rate of 60 kHz to a pure ^{14}O decay spectrum with a 0.5 Hz background and not including the contaminant as a fit parameter. The nominal ^{14}O half-life for the Monte Carlo is 70.600 seconds. In Table 4.13 the fitted ^{14}O half-life is shown along with the offset from the expectation value. In each case the contaminant increases the ^{14}O half-life and causes the ^{14}O half-life to change with initial rate. Figure 4.39 is a plot of the offset in the ^{14}O half-life due to the contaminants. A typical amount of ^{15}O trapped in the detection volume at the start of a half-life experiment is approximately 15 Hz. This was determined from the summed data analysis discussed in section 4.19. Given the production cross section of 3.4 x 10^6 ^{15}O/pμA, a release efficiency of approximately 50% for $^{12}C^{15}O$ molecules, and an observation volume of 10^{-5}, with 5 pμA on target one would expect approximately 75 Hz of ^{15}O to be trapped in the observation volume. This amount will be reduced by the vacuum pumping of the beam line. The observed rate of 15 Hz is within a factor of 5 of the expected rate without losses due to pumping. The amount of ^{11}C observed under the same conditions was found to be approximately 0.4 Hz. This rate is reduced due to the lack of free oxygen in the target which limits the $^{11}C^{16}O$ molecule formation rate.

Initial Rate (kHz)	*O-15 $T_{½}$ = ^{14}O in seconds*	*N-13 $T_{½}$ = ^{14}O in seconds*	*C-11 $T_{½}$ = ^{14}O in seconds*	*O-15 offset in seconds*	*N-13 offset in seconds*	*C-11 offset in seconds*
10	70.692	71.093	71.024	0.092	0.493	0.524
20	70.642	70.877	70.843	0.042	0.277	0.243
30	70.629	70.792	70.773	0.029	0.192	0.173
40	70.621	70.751	70.737	0.021	0.151	0.137
50	70.619	70.726	70.718	0.019	0.126	0.118
60	70.619	70.712	70.704	0.019	0.112	0.104

Table 4.13 Summary of contaminant effects on half-life.

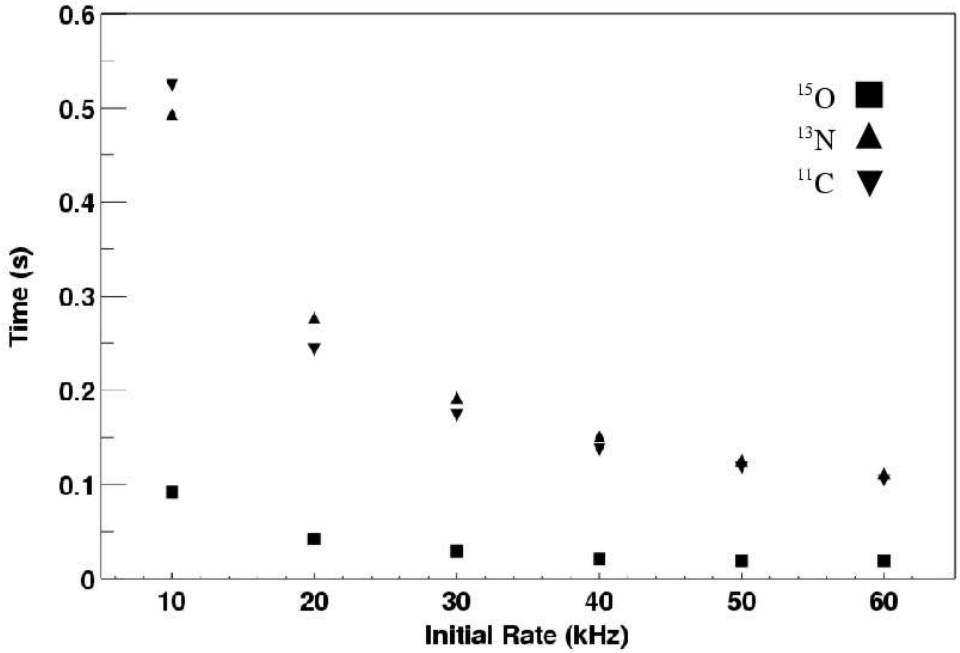

Figure 4.39 Half-life offset due to unaccounted contaminants. The half-life can be offset due to the presence of a radioactive contaminant (^{15}O, ^{13}N, ^{11}C) that is not included in the

fit. The offset in the half-life is plotted as a function of the initial rate of the fit. The offset decreases with increasing initial rate due to the dominance of the ^{14}O signal compared to the contaminant. The amount of contaminant is estimated from the production rate and the volume of the observation chamber as discussed in the text.

4.17 Implantation of ^{14}O

A fixed source of ^{14}O is produced by implanting the $^{14}O^{2+}$ ion beam into a 152 μm thick solid beryllium foil. The ion beam acceleration voltage is 28 kV so the ions have an energy of 54 keV. The ion beam is focused and collimated by a 0.6 cm diameter aperture approximately 1.5 cm upstream of the beryllium foil. The implantation depth was determined using the SRIM 2003 simulation program from IBM labs and is plotted in Figure 4.40. The average depth of the ^{14}O in the beryllium is approximately 136 nm. The beryllium foil is electrically grounded to avoid charging up to a voltage comparable to the beam energy. Once the ions impact the beryllium, they form one of two possible chemical bonds. The first bond is Be=O which forms at the interstitial grain boundaries in the solid and has a binding energy of 4.6 eV. The second bond is Be=O=Be and forms in the bulk of the beryllium lattice and has a bond strength of 14.4 eV. Both compounds are solids at room temperature and they do not diffuse out of the foil [71-73]. The distribution has only 2 out of 10^4 events implanted at less than 10 nm.

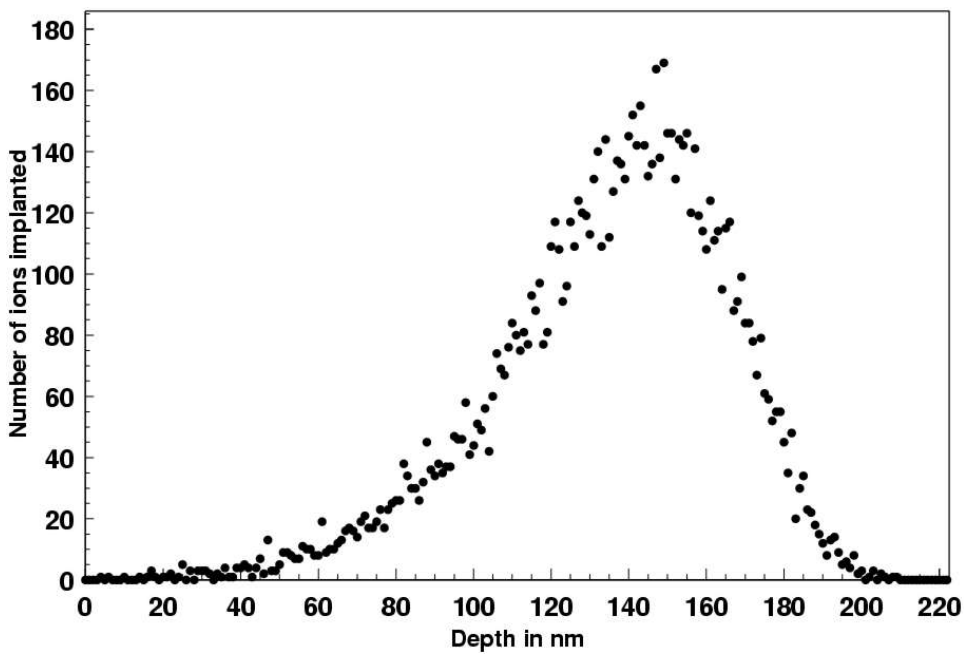

Figure 4.40 Ion implantation profile from SRIM 2003 software. The $^{14}O^{2+}$ ion beam was implanted into a Be foil during the experiment. The SRIM 2003 edition ion transport software was used to model the $^{14}O^{2+}$ ion interaction with the Be foil. The $^{14}O^{2+}$ ion beam was implanted at an energy of 54 keV in the simulation. This average implantation depth was found to be 136 nm.

The beam heating due to the presence of stable $^{14}N^{2+}$ is negligible. During the run up to 2 eμA of nitrogen are present which could deliver 54 mW of power to the foil. The beam is present for approximately 200 seconds for each load cycle depositing a total of 10.8 J. The fraction of the beam striking the aperture is reduced by approximately one half. This limits the energy delivered to the foil to approximately 6 J. The foil dimensions are 1.0 cm wide by 1.5 cm long by 0.0152 cm thick. The density of beryllium is 1.848 g/cm^3 with a specific heat of 1.825 J/g^{o}K at 300 ^{o}K. The thermal conductivity of

beryllium is one half that of copper, it is reasonable to assume the heat is distributed over the volume of the foil during the beam exposure. The calculated temperature rise of the foil is approximately 80 ^{o}K above the ambient temperature.

4.18 Fitting Data

The Minuit minimization software routine is used to fit the data [74]. The actual routine used to minimize the data is MINOS. MINOS uses the MIGRAD routine to minimize the function. If the MIGRAD routine has any trouble the program reverts to the SIMPLEX routine until a proper minimum is obtained then MIGRAD is called again. MINOS correctly calculates the uncertainty in the final parameters and takes into account any non-linearities in the function and parameter correlations. In operating the software, care must be taken to avoid having Minuit enter an unphysical region in parameter space. Should this occur, the fitting routine fails to find a minimum and the program terminates. This is overcome by setting limits on the parameters. For instance the background is only allowed to vary between 0.001 and 1000. This avoids having a negative background which the routine does not recover from. The minimization routine was extensively tested with the Monte Carlo simulation data. The Minuit minimization routine using the maximum likelihood method finds the correct half-life within uncertainty. Figure 4.41 shows the half-life results of the Monte Carlo simulations from an initial rate of 10 kHz to 50 kHz. Each data point is the weighted average of 20 separate runs summed together. The results are summarized in Table 4.14 along with the chi-square and confidence level

of the distribution. In each of these fits, the same data is being fit, only the initial rate of the fit is changing. The nominal half-life used for these simulations is 70.600 seconds.

Initial Rate (kHz)	***Half-life (s)***	***Statistical Uncertainty (s)***	***Reduced Chi-Square***	***Confidence Level (%)***
10	70.612	0.016	1.46	12
20	70.603	0.011	0.87	68
30	70.601	0.009	1.14	36
40	70.601	0.008	1.29	22
50	70.605	0.007	1.34	18

Table 4.14 Summary of Monte Carlo results for maximum likelihood fit.

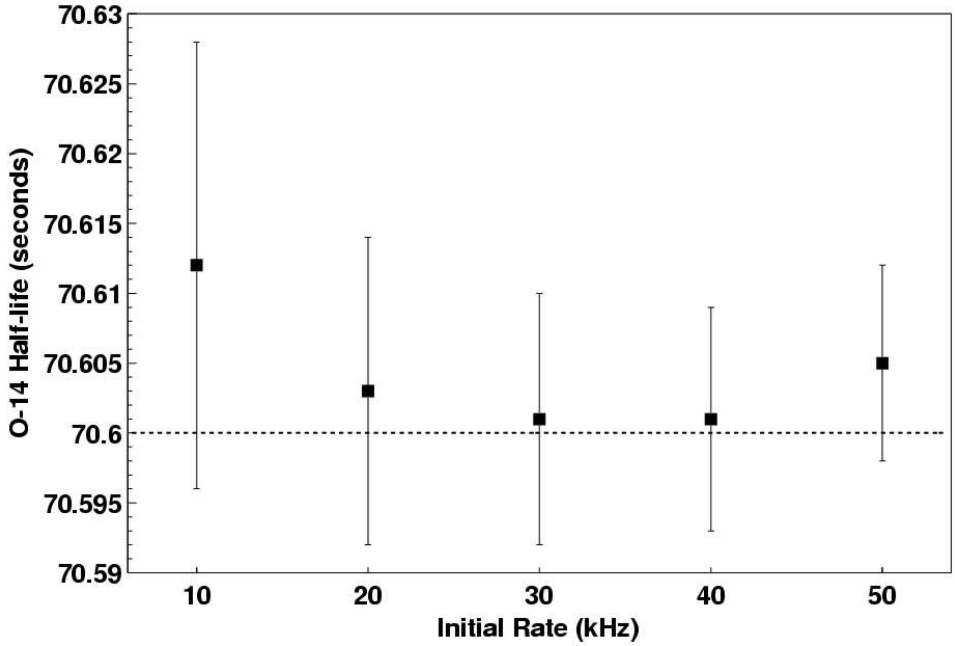

Figure 4.41 Monte Carlo simulated data fit with Minuit. Twenty separate Monte Carlo simulations of ^{14}O decay, including the series deadtimes, were fit using the Maximum

Likelihood method which was minimized by Minuit. The weighted average of the results of the twenty runs are plotted as a function of the initial rate of the fit. The results are consistent with the nominal half-life of 70.600 s shown by the dashed line.

4.19 Half-life Results

The data was analyzed two different ways. The first method used the sum of the data from a detector. The second method fit each run at a time and then combined the results. The half-life of ^{14}O was measured with three separate detectors surrounding a common source of activity. The fourth detector, detector A, had a failure during the experiment. The base connected to the PMT had a faulty contact which caused the applied high voltage to be intermittently interrupted. The high voltage variations affected the gain of the PMT rendering the data unusable. The data from the other three detectors were deadtime corrected and summed together. The deadtime correction is performed using equation 4.14 for each of the 8000 time bins of 0.4995 second duration. The corresponding time bins of each run are then summed together. The process is performed for each detector individually.

$$R_{Tj} = \sum_{i=1}^{27} \frac{R_{Ei}}{1 - \tau R_{Ei}} \tag{4.15}$$

Upon examination of the decay spectrum, it was determined that ^{15}O and ^{11}C were present in the spectrum. The ^{11}C decay was evident in the tail of the decay distribution once the average background was subtracted. The ^{15}O decay was observed by subtracting the average background, ^{11}C decay curve, and an approximate ^{14}O decay curve. The resulting

spectrum was rebinned approximately 10 times to improve the statistics and fit to an single exponential. The half-life of this fit was approximately 122 seconds indicating the presence of ^{15}O. The data was then fit with equation 4.15, a five parameter fit consisting of the ^{15}O amplitude, ^{11}C amplitude, ^{14}O amplitude, ^{14}O half-life, and a flat background.

$$R = R_{o14} e^{\frac{-\ln(2)T}{\tau_{o14}}} + R_{c11} e^{\frac{-\ln(2)T}{1223.4s}} + R_{o15} e^{\frac{-\ln(2)T}{122.4s}} + B_o \tag{4.16}$$

Here R is the fit value, T is time in seconds, R_{o14} is the initial rate of ^{14}O, R_{c11} is the initial rate of ^{11}C, R_{o15} is the initial rate of ^{15}O, τ_{o14} is the ^{14}O half-life, and B_o is the background. The function was minimized using the maximum likelihood method described in section 4.1 and 4.18. The initial rate of each fit was varied to look for rate dependent effects. None were found at the level of precision of the experiment. A typical plot of the summed data and corresponding fit are shown in Figure 4.42, Figure 4.43, and Figure 4.44. The fit for each of these results is shown as a solid continuous line in each plot.

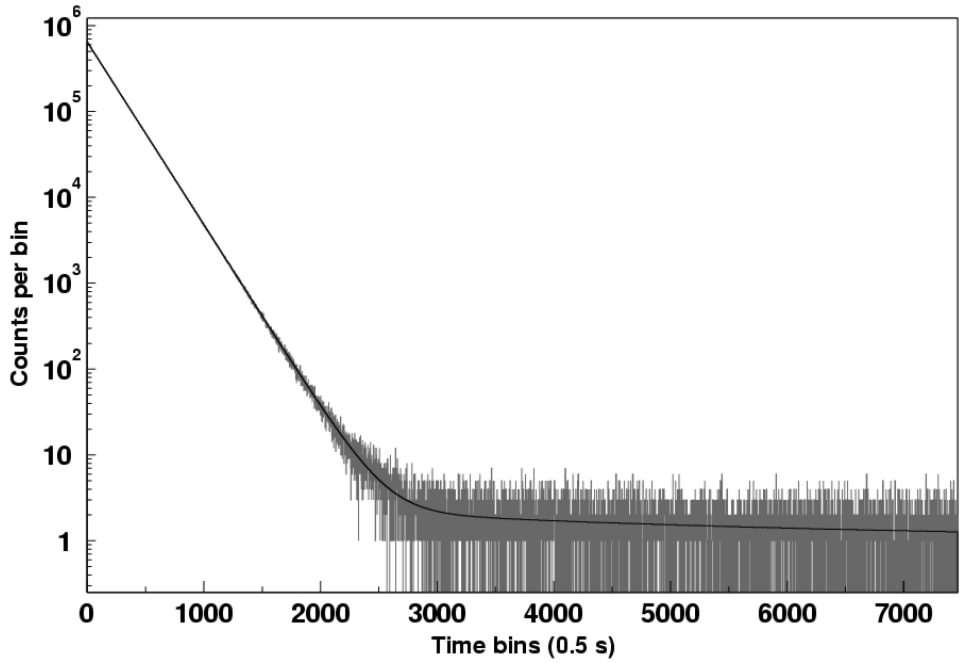

Figure 4.42 Detector B summed data with fit. The deadtime corrected data from 27 runs was summed together and fit. The resulting half-life from the chi-square minimization is t = 70.678 ± 0.006 s and from maximum likelihood is t = 70.680 ± 0.006 s.

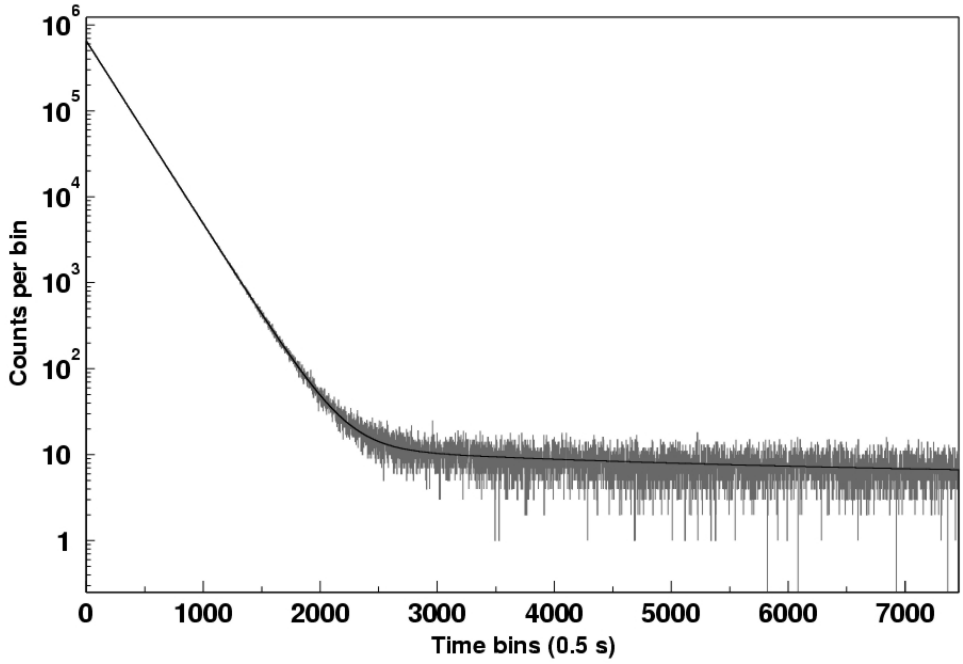

Figure 4.43 Detector C summed data with fit. The deadtime corrected data from 27 runs

was summed together and fit. The resulting half-life from the chi-square minimization is t = 70.658 ± 0.012 s and from maximum likelihood is t = 70.669 ± 0.012 s.

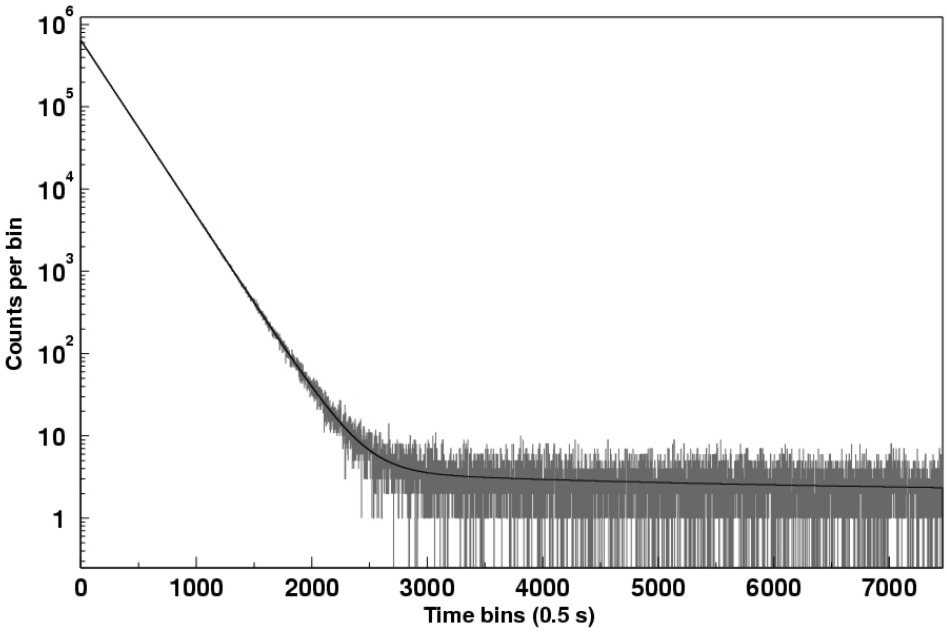

Figure 4.44 Detector D summed data with fit. The deadtime corrected data from 27 runs was summed together and fit. The resulting half-life from the chi-square minimization is t = 70.687 ± 0.011 s and from maximum likelihood is t = 70.680 ± 0.011 s.

These results are summarized in Table 4.15, 4.16, and 4.17 and are plotted in Figure 4.45. Each table of data includes the systematic uncertainty associated with the initial rate. The systematic uncertainties quoted are the extreme values as determined in section 4.15 and are summarized in Table 4.12. The statistical uncertainties quoted are determined by Minuit from the fit parameters.

Initial Rate (kHz)	***Half-life (s)***	***Systematic (ms)***	***Statistical (ms)***	***Total Uncertainty (ms)***
10	70.689	5	14	15
20	70.701	6	10	11
30	70.695	6	8	10
40	70.689	7	7	10
50	70.687	7	6	9

Table 4.15 Detector B results from analysis of 27 runs summed together and fit.

Initial Rate (kHz)	***Half-life (s)***	***Systematic (ms)***	***Statistical (ms)***	***Total Uncertainty (ms)***
10	70.682	13	29	32
20	70.679	13	20	24
30	70.688	12	16	20
40	70.679	11	13	17
50	70.669	11	12	16

Table 4.16 Detector C results from analysis of 27 runs summed together and fit.

Initial Rate (kHz)	***Half-life (s)***	***Systematic (ms)***	***Statistical (ms)***	***Total Uncertainty (ms)***
10	70.707	7	28	29
20	70.712	7	19	20
30	70.678	7	15	17
40	70.683	7	12	14
50	70.676	8	11	14

Table 4.17 Detector D results from analysis of 27 runs summed together and fit.

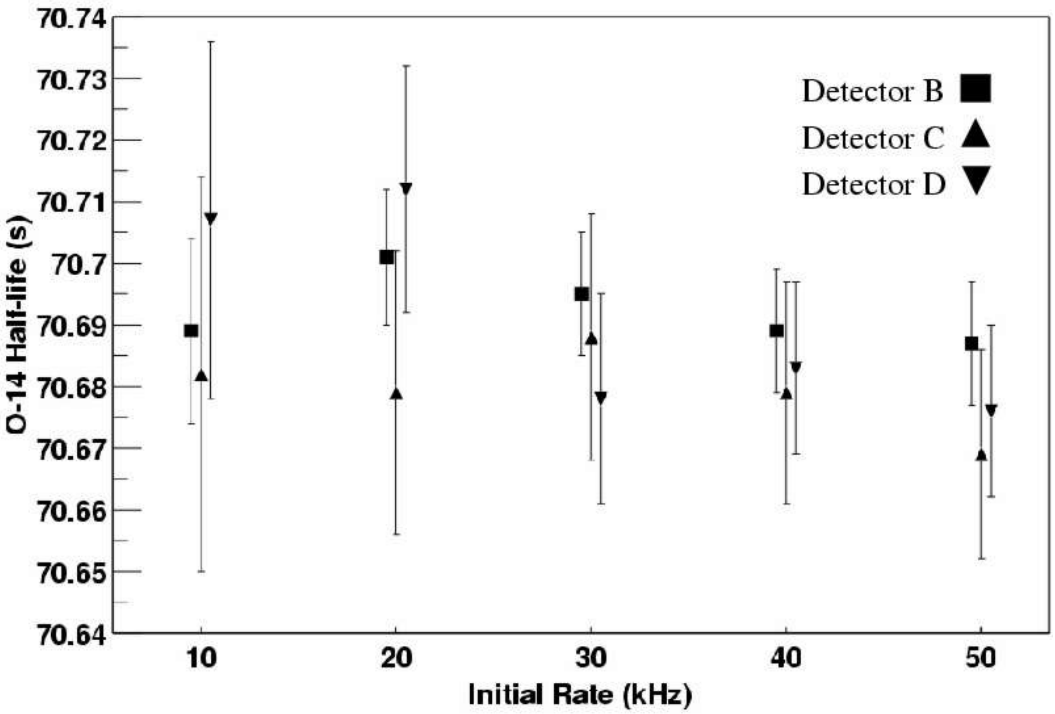

Figure 4.45 Summed Half-life results. The weighted half-life of the summed data of the 27 runs for each detector is plotted as a function of the initial rate used to fit the data.

In the second method, all 27 runs were fit individually. The results were averaged together, taking into account the uncertainty from each result. These results are summarized in Tables 4.18, 4.19, and 4.20. The result for each of the 27 runs is plotted in Figure 4.46, Figure 4.47, and Figure 4.48. Along with the systematic uncertainties, the calculated statistical uncertainty is quoted. The variance of the mean and reduced chi-squared values are also given for 26 degrees of freedom. Figure 4.49 is the summary of the results of all 27 runs for each detector at various intial rates from 10 kHz to 50 kHz.

Initial Rate (kHz)	*Half-life (s)*	*Systematic (ms)*	*Statistical (ms)*	*Total Uncertainty (ms)*	*Variance (ms)*	*Reduced Chi Square*	*CF (%)*
10	70.678	5	16	17	16	1.004	46
20	70.685	5	13	15	12	0.782	78
30	70.694	6	12	13	12	1.009	45
40	70.699	7	11	12	12	1.302	14
50	70.695	7	9	12	10	1.245	18

Table 4.18 Detector B results from analysis of 27 individual runs.

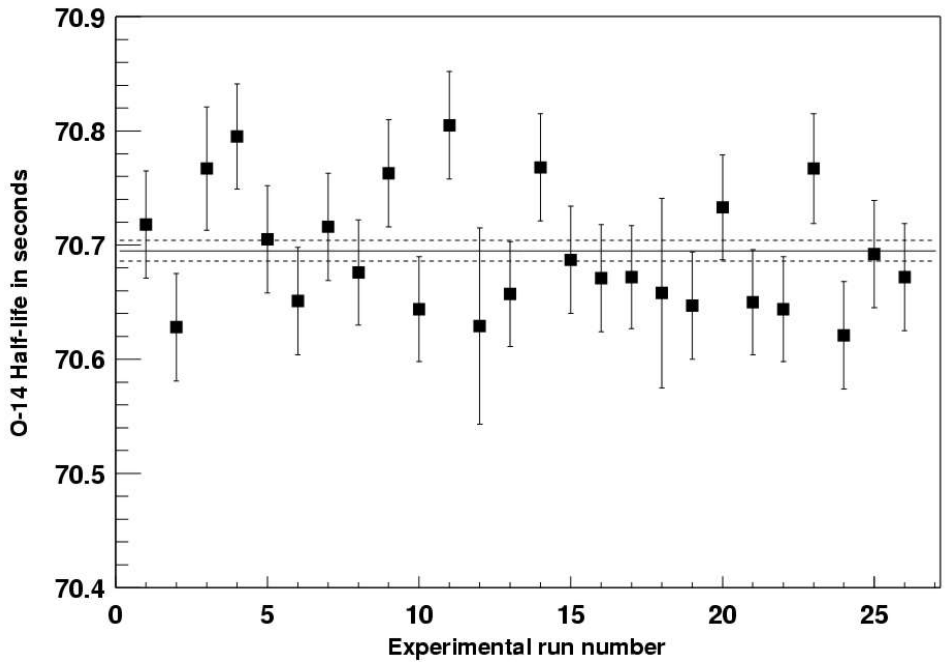

Figure 4.46 Detector B half-life results plotted with average.

Initial Rate (kHz)	*Half-life (s)*	*Systematic (ms)*	*Statistical (ms)*	*Total Uncertainty (ms)*	*Variance (ms)*	*Reduced Chi Square*	*CF (%)*
10	70.680	13	18	22	11	0.903	61
20	70.687	13	13	18	10	0.712	86
30	70.676	12	12	17	10	1.114	31
40	70.666	11	11	16	10	1.299	14
50	70.663	11	10	15	9	1.097	33

Table 4.19 Detector C results from analysis of 27 individual runs.

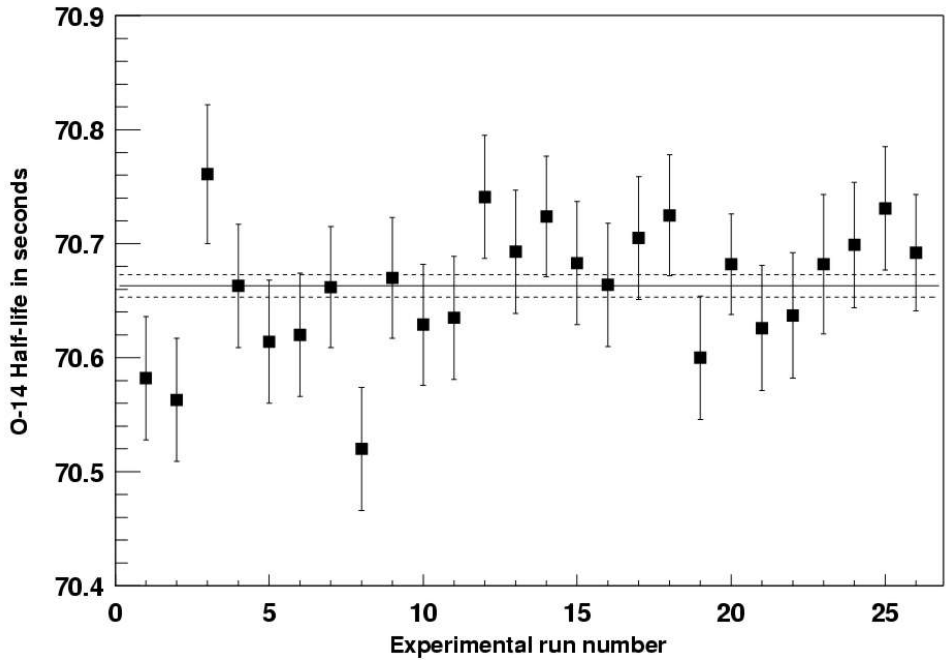

Figure 4.47 Detector C half-life results plotted with average.

Initial Rate (kHz)	*Half-life (s)*	*Systematic (ms)*	*Statistical (ms)*	*Total Uncertainty (ms)*	*Variance (ms)*	*Reduced Chi Square*	*CF (%)*
10	70.678	7	19	20	13	1.030	42
20	70.697	7	15	17	11	0.969	51
30	70.694	7	14	15	11	1.042	40
40	70.684	7	13	15	9	0.744	83
50	70.684	8	12	14	9	0.728	84

Table 4.20 Detector D results from analysis of 27 individual runs.

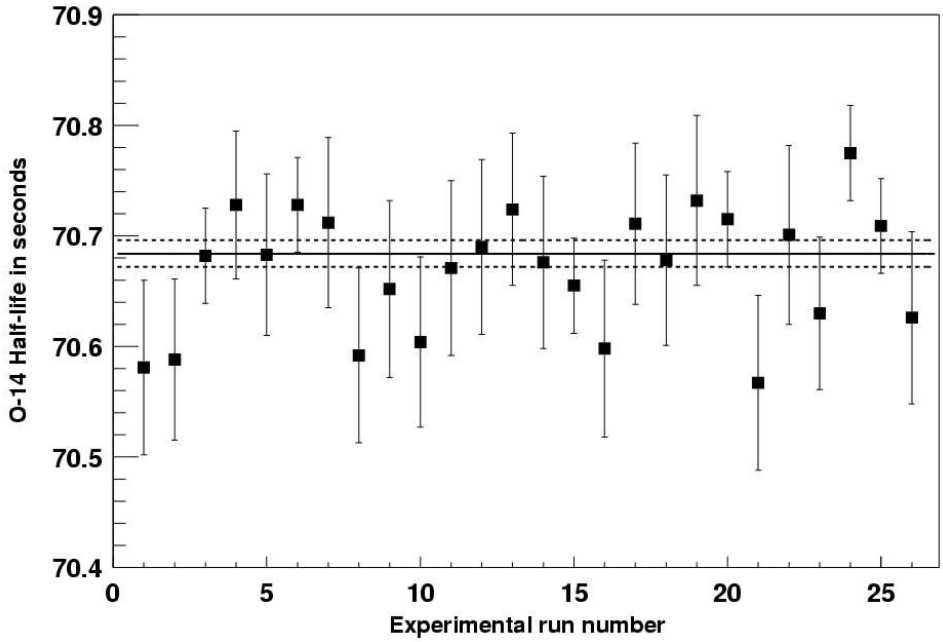

Figure 4.48 Detector D half-life results plotted with average.

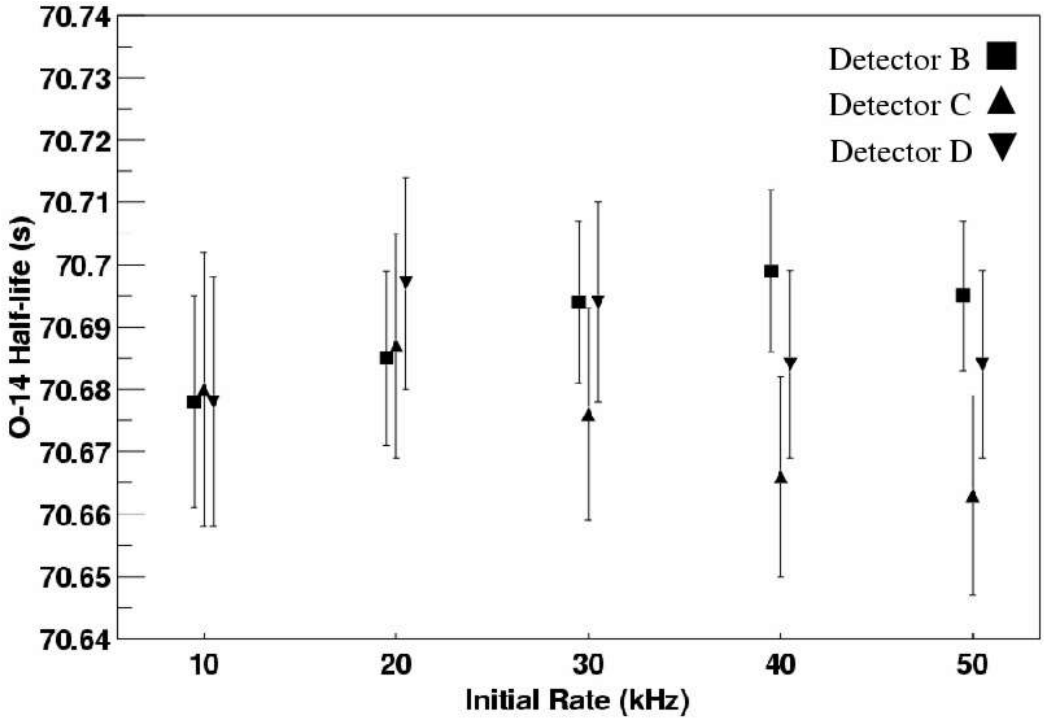

Figure 4.49 Summary of individual runs. The weighted half-life of the individually fit 27 runs for each detector is plotted as a function of the initial rate used to fit the data.

The variance of the individual runs is equal to or less than the statistical error derived from the sum of the 27 runs. This implies that there are no large unaccounted for systematic errors in the data.

The geometry of the detectors with respect to the source was such that detector C and D count a large fraction of the same particles. To avoid double counting, the results

for detector C and D should not be combined together. The half-life results for various combinations of detectors B, C and D are presented in Table 4.21 through 4.26. The results in Table 4.21 and 4.22 are presented for completeness only.

Initial Rate (Hz)	***Half-life (s)***	***Systematic (ms)***	***Statistical (ms)***	***Total (ms)***
10000	70.691	14	12	18
20000	70.700	15	8	17
30000	70.690	15	7	16
40000	70.686	15	6	16
50000	70.681	16	5	16

Table 4.21 Summary of half-life values for detectors B, C, and D summed runs.

Initial Rate (Hz)	***Half-life (s)***	***Systematic (ms)***	***Statistical (ms)***	***Total (ms)***
10000	70.678	14	10	18
20000	70.689	15	8	17
30000	70.689	15	7	16
40000	70.686	16	7	16
50000	70.683	16	6	17

Table 4.22 Summary of half-life values for detectors B, C, and D individual runs.

Initial Rate (Hz)	***Half-life (s)***	***Systematic (ms)***	***Statistical (ms)***	***Total (ms)***
10000	70.688	13	13	18

Initial Rate (Hz)	*Half-life (s)*	*Systematic (ms)*	*Statistical (ms)*	*Total (ms)*
20000	70.697	13	9	16
30000	70.694	13	7	15
40000	70.687	13	6	14
50000	70.682	13	6	14

Table 4.23 Summary of half-life values for detectors B and C for summed runs.

Initial Rate (Hz)	*Half-life (s)*	*Systematic (ms)*	*Statistical (ms)*	*Total (ms)*
10000	70.679	13	12	18
20000	70.686	13	9	16
30000	70.687	13	9	16
40000	70.686	13	8	15
50000	70.683	13	7	15

Table 4.24 Summary of half-life values for detectors B and C for individual runs.

Initial Rate (Hz)	*Half-life (s)*	*Systematic (ms)*	*Statistical (ms)*	*Total (ms)*
10000	70.693	7	13	15
20000	70.704	8	9	12
30000	70.690	9	7	12
40000	70.687	9	6	11
50000	70.683	11	5	12

Table 4.25 Summary of half-life values for detectors B and D for summed runs.

Initial Rate (Hz)	*Half-life (s)*	*Systematic (ms)*	*Statistical (ms)*	*Total (ms)*
10000	70.678	7	12	14
20000	70.690	8	10	13
30000	70.694	9	9	13
40000	70.693	9	8	13
50000	70.690	11	7	13

Table 4.26 Summary of half-life for detectors B and D for individual runs.

The results from the initial rate of 50 kHz have the least effect due to background fluctuations. This is the largest systematic uncertainty to the half-life. Using the results from 50 kHz initial rates, the half-life of ^{14}O from the individual runs from detector B and C analysis is 70.683 ± 0.015 seconds. This result is compared to the previous experimental results in Figure 4.50 and summarized in Table 4.27. The implications of this result are discussed in the following section. The most recent ^{14}O half-life measurement published by Gaelens [52] is questionable in that the result in the thesis (70.504 ± 0.040 s) [74] and the published result (70.560 ± 0.049 s) differ by 0.054 seconds. This change in value was due to a re-analysis of the systematic effects post-experiment. This was complicated by the fact that the electronics for the experiment had been dissassembled before the systematics were re-examined [75].

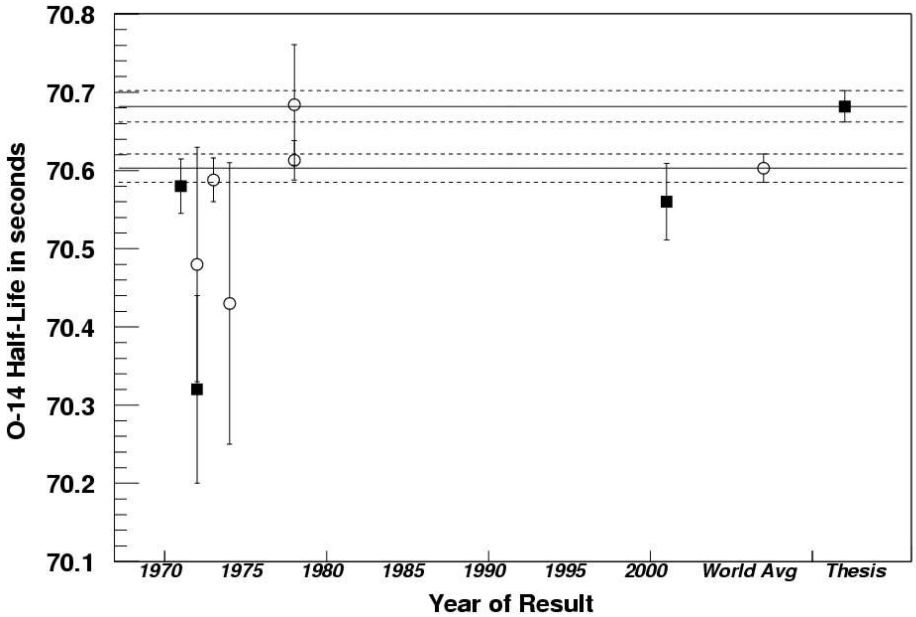

Figure 4.50 Summary plot of half-life measurements. The open circles represent the currently accepted world average values. The square marker on the right is the result from this work with a value of 70.683 ± 0.015.

Year and Reference	*Lifetime (seconds)*	*Error (seconds)*
1971 [45]	70.580	0.035
1972 [46]	70.480	0.150
1972 [47]	70.320	0.120
1973 [48]	70.588	0.028
1974 [49]	70.430	0.180
1978 [50]	70.613	0.025
1978 [51]	70.684	0.077
2001 [52]	70.560	0.049
World average	70.603	0.018
Thesis result 2004	70.683	0.015

Table 4.27 Summary of modern ^{14}O half-life results.

4.20 Impact on Physics

The ^{14}O half-life can now be used to determine the V_{ud} coupling constant and test the unitarity of the CKM matrix. The ^{14}O half-life needs to be combined with the Q-value and branching ratio to calculate the Ft and V_{ud} values. The old V_{ud} value from ^{14}O was 0.9740 ± 0.0005 and the V_{ud} value with the ^{14}O half-life from this thesis is 0.9738 ± 0.0005. The summary of the current and past values are in Table 4.28 below. The ft-values of several Fermi beta decaying nuclei are summarized in Table 4.29 and plotted in Figure 4.51. The reduced chi-square for these ft-values is 1.1 which yields a 35% confidence level. The 50% confidence level error for this average is 1.09 seconds. The agreement between ft-values indicates that there are no major problems with experiments and/or the theory used to compute the ft-values.

Measured Parameter	***Old values (2002)***	***New Q-value (2003)***	***Old Q-value new ^{14}O half-life***	***New Q-value new ^{14}O half-life***
Q-value (keV)	2830.40 ± 0.19	2831.47 ± 0 .14	2830.40 ± 0 .19	2831.47 ± 0 .14
Half-life (s)	70.603 ± 0.18	70.603 ± 0.18	70.683 ± 0.15	70.683 ± 0.15
Fermi BR (%)	99.33 ± 0.01	99.33 ± 0.01	99.33 ± 0.01	99.33 ± 0.01
Ft-value (s)	3069.7 ± 2.6	3076.1 ± 2.3	3073.18 ± 2.3	3079.59 ± 2.3
V_{ud} from ^{14}O	0.9740±0.0005	0.9734±0.0005	0.9738±0.0005	0.9728±0.0005

Table 4.28 Summary of ft-values for ^{14}O.

The unitarity of the Cabibbo-Kobayashi-Maskawa mixing matrix can now be

computed using V_{ud}, V_{us}, and V_{ub}. For completeness, the squared sum (total) of the first line of the CKM matrix is tabulated for various results. The Hyperon decay analysis and the E865 branching ratio measurements are given as well as the currently accepted PDG values for V_{us}. The conclusion from this experiment combined with the recent measurements (described in section 1.2) is that the CKM matrix is consistent with unitarity. An upper limit on the magnitude of a fourth generation coupling constant is

Nucleus	***Ft-value (s)***	***Uncertainty (s)***	V_{ud}	***Uncertainty***
^{10}C	3072.90	4.8	0.9739	0.0015
^{26m}Al	3070.00	2.1	0.9743	0.0007
^{34}Cl	3070.10	2.4	0.9743	0.0008
^{38m}K	3071.10	2.7	0.9742	0.0009
^{42}Sc	3077.30	2.3	0.9732	0.0007
^{46}V	3074.40	2.7	0.9736	0.0009
^{50}Mn	3073.80	2.7	0.9737	0.0009
^{54}Co	3072.30	2.7	0.9740	0.0009
Average	3072.62	0.9	0.9739	0.0005

Table 4.29 Summary of ft-values of Fermi transitions.

given in Table 4.30. For example the data from the E865 experiment and the ^{14}O half-life from this experiment sets an upper limit of 0.009 on the magnitude of a fourth generation coupling constant. The formula for unitarity with four generations of quarks can be written as

$$|V_{ud}|^2+|V_{us}|^2+|V_{ub}|^2+|V_{uX}|^2=1.0 \quad . \tag{4.17}$$

The limit on the magnitude for the V_{uX} term can be determined from the above formula as

$$|V_{uX}|\leqslant\sqrt{(1.0-(|V_{ud}|^2+|V_{us}|^2+|V_{ub}|^2))} \tag{4.18}$$

The previous limit on the magnitude of a fourth generation coupling constant was < 0.07 [20].

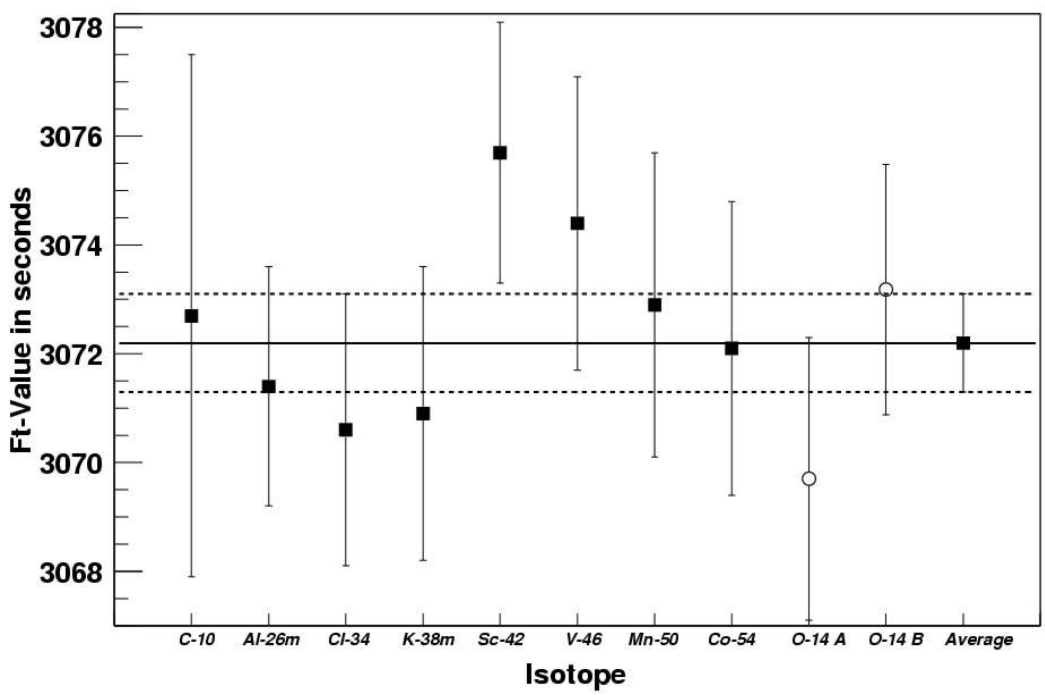

Figure 4.51 Summary of Ft-values. O-14 A is the old half-life ft-value and O-14 B is the new half-life ft-value from Table 4.28. The O-14 values do not use the new Q-value.

CKM Values	***Measurement***	V_{ud}	V_{us}	V_{ub}	$V_{ud}^2+V_{us}^2+V_{ub}^2=$	***Max*** V_{uX}
PDG values	Old Values	0.9740 (5)	0.2196 (26)	0.0035 (15)	0.9969 (15)	0.056
	New ^{14}O Q-value	0.9734 (5)	0.2196 (26)	0.0035 (15)	0.9957 (15)	0.065
	New ^{14}O half-life	0.9738 (5)	0.2196 (26)	0.0035 (15)	0.9965 (15)	0.059
	New ^{14}O half-life new Q-value	0.9728 (5)	0.2196 (26)	0.0035 (15)	0.9946 (15)	0.074
Hyperon Data	Old Values	0.9740 (5)	0.2250 (27)	0.0035 (15)	0.9993 (16)	0.026
	New ^{14}O half-life Q-value	0.9734 (5)	0.2250 (27)	0.0035 (15)	0.9981 (16)	0.043
	New ^{14}O half-life	0.9738 (5)	0.2250 (27)	0.0035 (15)	0.9989 (16)	0.033
	New ^{14}O half-life new Q-value	0.9728 (5)	0.2250 (27)	0.0035 (15)	0.9970 (16)	0.055

CKM Values	***Measurement***	V_{ud}	V_{us}	V_{ub}	$V_{ud}^2+V_{us}^2+V_{ub}^2=$	***Max*** V_{uX}
E865 Data	Old Values	0.9740 (5)	0.2272 (30)	0.0035 (15)	1.0003 (17)	0.000
	New ^{14}O Q-value	0.9734 (5)	0.2272 (30)	0.0035 (15)	0.9991 (17)	0.029
	New ^{14}O half-life	0.9738 (5)	0.2272 (30)	0.0035 (15)	0.9999 (17)	0.009
	New ^{14}O half-life new Q-value	0.9728 (5)	0.2272 (30)	0.0035 (15)	0.9980 (17)	0.045

Table 4.30 Summary of CKM parameters and unitarity.

Chapter 5

5 The Branching Ratio Experiment

This experiment measures the ^{14}O allowed Gamow-Teller branching ratio. This is accomplished by simultaneously measuring the allowed Fermi and Gamow-Teller beta spectra with a magnetic spectrometer. The resulting spectra were then fit to determine the Gamow-Teller branching ratio. The Fermi and Gamow-Teller branching ratios are inputs for the ft-value as discussed in section 1.3. The Gamow-Teller branching ratio was measured with a 180 degree flat field magnetic spectrometer described in section 5.4. The beta particles were detected with a multiple wire proportional chamber (MWPC). The ^{14}O source was prepared in a similar manner as the ^{14}O source used for the half-life experiment. The following chapter discusses the previous branching ratio experiments, ^{14}O allowed Fermi and Gamow-Teller spectra, and the MWPC detector system. Finally, the analysis and results are presented.

5.1 Previous Experiments

The ^{14}O branching ratio has been measured three times since the discovery of the ^{14}O nucleus in 1949. The first measurement was performed in 1955 using a magnetic lens spectrometer [76]. The spectrometer focused the beta particles onto a thin window geiger counter backed by an anthracene crystal. To reduce the background associated with the 2.31 MeV gamma ray from ^{14}O decay, the geiger counter gated the anthracene crystal. The branching ratio result for this experiment was determined to be 0.60 ± 0.10 %. There is no discussion of the systematic errors associated with the apparatus.

The second measurement was performed in 1963 with a Siegbahn-Slatis intermediate image focusing spectrometer [77]. The spectrometer had an acceptance of 5% of 4π which yielded a 4% energy resolution. The spectrometer focused the beta particles onto a thin window Geiger-Muller counter. A gamma ray detector located near the source monitored the 0.511 MeV positron annhilation radiation in order to normalize the production rate. The spectrometer was scanned over the Fermi and Gamow-Teller spectra. The ^{14}O branching ratio from this experiment was found to be 0.65 ± 0.05 %.

The most recent branching ratio experiment was performed in 1966 using an iron free solenoidal spectrometer by Sidhu and Gerhart [78]. The spectrometer acceptance was 3.3% with a momentum resolution of $\Delta p/p = 1\%$. This experiment only measures the Gamow-Teller branch of the spectrum by examining the high energy beta events. The branching ratio is inferred from the ft-value as 0.61 ± 0.01 %. The results of these branching ratio experiments are summarized in Table 5.1.

Year of Experiment	*Branching Ratio (%)*
1955 [76]	0.6 ± 0.1
1963 [77]	0.65 ± 0.05
1966 [78]	0.61 ± 0.01

Table 5.1 Summary of previous branching ratio measurements

5.1.1 Comment on Sidhu and Gerhart Branching Ratio Experiment

In this experiment [78], the ft-value is obtained directly from the beta spectrum as $2.14 \pm 0.03 \times 10^7$ seconds. They calculate the statistical rate function (f) and from the information in their paper we find f is 1861 for the Gamow-Teller branch. This is inconsistent with the values from Wilkinson and Macefield who calculate f as 1656.3 ± 1.6 [79]. The Wilkinson and Macefield value does not include the shape factor term of -5.2 %/MeV from Holstein and Calaprice [80]. The statistical rate function was re-calculated here with and including the order alpha radiative corrections from Sirlin [24] and including the -5.2 %/MeV shape factor. The result without the shape factor is f = 1659.3 and with the shape factor f = 1243.5. The Sidhu and Gerhart value is 50 % larger than the value calculated here.

Sidhu and Gerhart use the weighted average total half-life result from Bardin [41] and Hendrie and Gerhart [42] of 71.36 ± 0.09 seconds to obtain the branching ratio. The

Gamow-Teller total half-life is determined by dividing the measured ft-value by the

$$t = \frac{ft}{f} = \frac{2.14\,x\,10^7\,s}{1861} = 11500\,s \tag{5.1}$$

calculated f value and they find t = 11500 ± 100 seconds. The branching ratio is determined by dividing the Fermi total half-life by the Gamow-Teller total half-life to obtain 0.61 ± 0.01%. An error was made in the Sidhu and Gerhart paper, the branching ratio with the half-lives quoted is 0.62 ± 0.01%.

5.2 The O-14 Beta Spectrum

The ^{14}O nucleus beta decays via three branches to various states of ^{14}N. The beta decays are allowed Fermi and Gamow-Teller transitions as shown in Figure5.1 and summarized in Table 5.2. The endpoint energy of the ^{14}O Gamow-Teller branch with a branching ratio of 0.6% is 4.63 MeV. The allowed Fermi branch endpoint energy is 2.32 MeV with a branching ratio of 99.3%. The allowed Gamow-Teller 0.06% branch endpoint energy is 0.69 MeV. The 0^+ excited state of ^{14}N decays to the ground state emitting a 2.31 MeV gamma ray. The 1^+ excited state of ^{14}N decays to the 0^+ excited state 96.1% of the time via M1 gamma emission. Finally the 1^+ excited state of ^{14}N decays to the 1^+ ground state 3.9% of the time via E2 gamma emission.

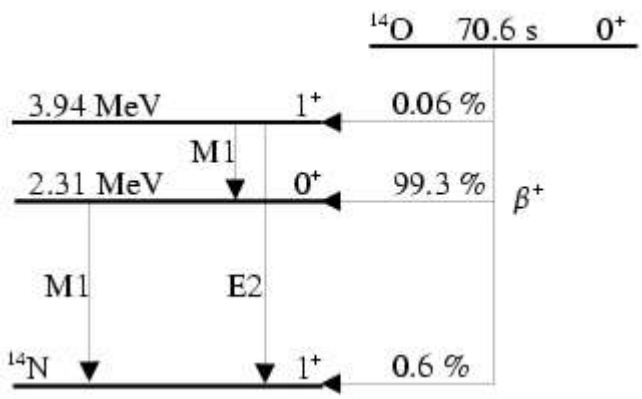

Figure 5.1 O-14 decay scheme. The data for the decay scheme is taken from the Table of Isotopes [86].

Transition	***Branching Ratio (%)***	***Endpoint Energy (MeV)***	***Initial State J^P***	***Final State J^P***
Fermi	99.3	2.32	0^+	1^+
Gamow-Teller	0.6	4.63	0^+	0^+
Gamow-Teller	0.06	0.69	0^+	1^+

Table 5.2 Summary of beta endpoint energies and branching ratios.

5.2.1 The Allowed Fermi Beta Spectrum

The Fermi transition in ^{14}O beta decay occurs between the 0^+ ground state of ^{14}O

and the 0^+ first excited state of ^{14}N as shown in Figure 5.1. The total energy available for the decay is 2.32 MeV. The beta spectrum is given by Fermi's theory of beta decay described in chapter 1.

$$\frac{dP}{dE} = \frac{G_V^2}{2\pi^3} C(E) R(\alpha) F(Z,E) \left|\int 1\right|^2 pE(E-E_o)^2$$

(5.2)

Here dP/dE is the probability per unit energy of a beta decay, p is the momentum of the beta particle, E is the total energy of the beta particle, and E_o is the endpoint energy of the beta particle. G_V is the effective vector coupling constant and the integral $\left|\int 1\right|^2$ for ^{14}O Fermi decay is equal to 2. The F(Z,E) term is the Fermi function which corrects for the effects of the nuclear Coulomb field. The Fermi function takes into account the nuclear Coulomb field, finite deBroglie wavelength, finite nuclear size, and electron screening of the nuclear field. The values of the Fermi function have been calculated and tabulated by Behrens and Janecke [15]. The F(Z,E) values including all screening effects for ^{14}O decay are shown in Figure 5.2.

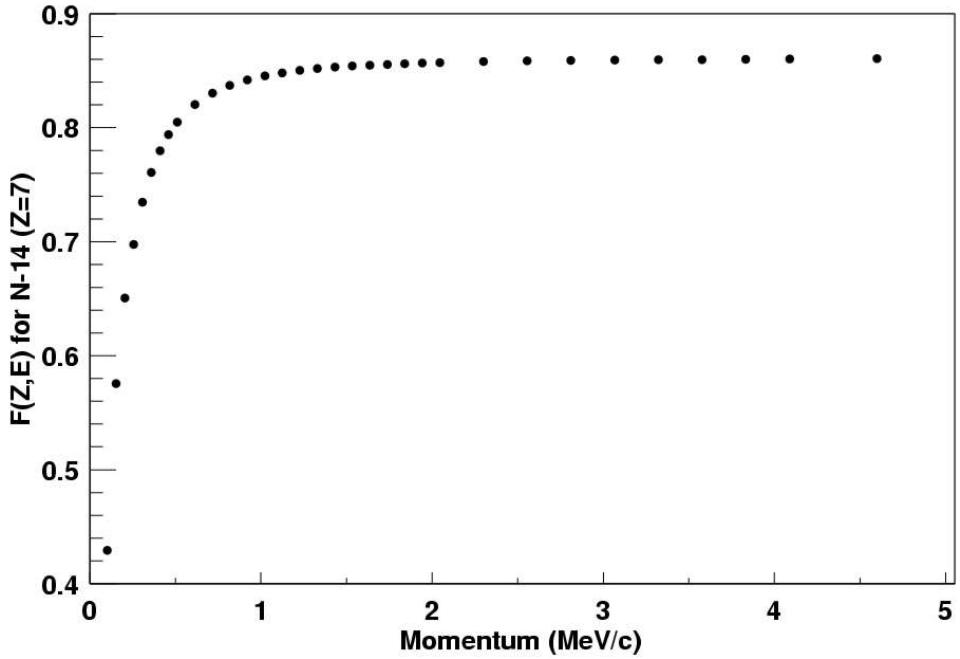

Figure 5.2 Fermi function for ^{14}O beta decay. The Fermi function for 14O is plotted with the radiative corrections from Behrens and Janecke [15].

The C(E) term is the spectral shape factor,

$$C(E)=1+aE+\frac{b}{E}+... \quad . \tag{5.3}$$

The spectral shape factor depends on the weak magnetism (a) and Fierz interference (b) terms. The weak magnetism term for Fermi decay is consistent with zero. The Fierz interference term is also consistent with zero for Fermi decay.

The R(α) term is the radiative correction term which accounts for the effect that real and virtual photon exchanges have on the beta particle. The radiative correction is given by Sirlin [25] as

$$R(\alpha)=1+\frac{\alpha}{2\pi}g(E,E_m,m) \quad . \tag{5.4}$$

Where α is the fine structure constant and g(E, E_m, m) is

$$g(E,E_m,m)=3\ln(\frac{m_p}{M})-\frac{3}{4}+4\left[\frac{\tanh^{-1}\beta}{\beta}-1\right]\left[\frac{(E_m-E)}{3E}-\frac{3}{2}+\ln\left(\frac{2(E_m-E)}{m}\right)\right]add$$

$$\frac{4}{\beta}L\left(\frac{2\beta}{1+\beta}\right)add\frac{1}{\beta}\tanh^{-1}\beta\left[2(1+\beta^2)+\frac{(E_m-E)^2}{6E^2}-4\tanh^{-1}\beta\right] \tag{5.5}$$

Where E is the total energy of the beta particle, E_m is the Q-value of the decay, β is p/E, m_p is the mass of the proton, M is the mass of the nucleus, and L(x) is the Spence function. The Spence function is given as

$$L(x)=\int_0^x\frac{\ln(1-t)}{t}dt \quad . \tag{5.6}$$

The radiative correction for ^{14}O Fermi decay is plotted in Figure 5.3.

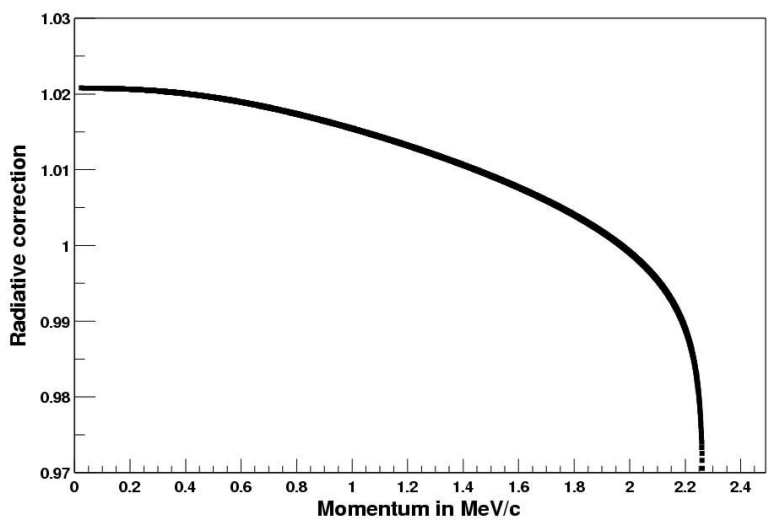

Figure 5.3 Order alpha radiative correction term for the Fermi branch. The radiative corrections to the Fermi branch are taken from Sirlin [25].

The net effect of the spectral shape factor, the Fermi function, and the radiative corrections on the Fermi beta decay spectrum are shown in Figure 5.4.

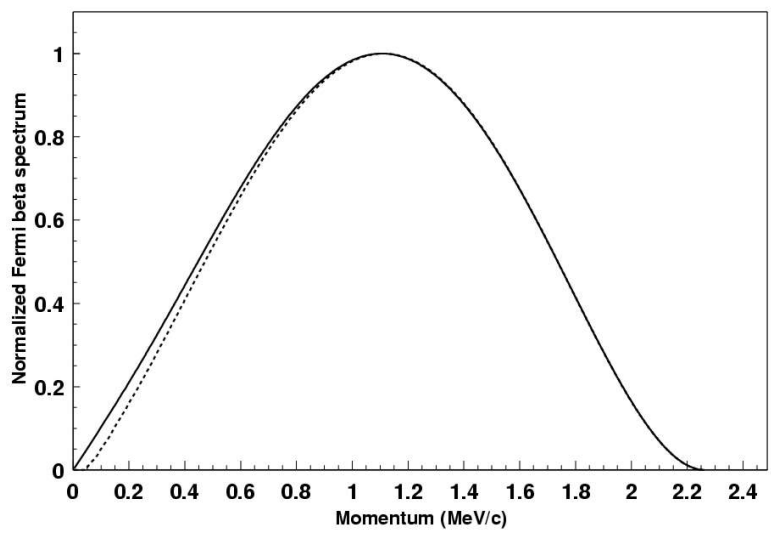

Figure 5.4 Fermi spectrum with correction terms. The solid black line is the original Fermi spectrum. The dashed line is the Fermi spectrum including the correction terms.

5.2.2 The Allowed Gamow-Teller Beta Spectrum

The Gamow-Teller transition in ^{14}O beta decay occurs between the 0^+ ground state of ^{14}O and the 1^+ ground state of ^{14}N shown in Figure 5.1.

$$\frac{dP}{dE} = \frac{G_A^2}{2\pi^3} C(E) R(\alpha) F(Z,E) \left| \int \sigma \right|^2 pE(E-E_o)^2$$

(5.7)

Here dP/dE is the probability per unit energy of a beta decay, p is the momentum of the beta particle, E is the total energy of the beta particle, R(α) is the radiative correction

term, and E_o is the endpoint energy of the beta particle. G_A is the effective axial vector coupling constant and the integral $|\int \sigma|^2$ for ^{14}O Gamow-Teller decay is equal to 5/3. The C(E) term is the spectral shape factor,

$$C(E) = 1 + aE + \frac{b}{E} + \ldots \quad . \tag{5.8}$$

The spectral shape factor depends on the weak magnetism (a) and Fierz interference (b) terms. Following the treatment of Holstein and Calaprice [80], the weak magnetism term is determined from the magnetic form factor (B) , the structure function (C) and the mass of the nucleus (M) in MeV as

$$a \approx \frac{2}{3M}\left(5\, pm \frac{2B}{C}\right) \quad . \tag{5.9}$$

The magnetic form factor is related to the width of the analog M1 gamma transition 0^+ to 1^+ in ^{14}N given by

$$\Gamma_{M1} = \frac{\alpha E_\gamma^3 B_\gamma^2}{6M^2} \quad . \tag{5.10}$$

Where Γ_{M1} is the width of the M1 gamma ray transition, α is the fine structure constant, E_γ is the energy of the M1 gamma ray (2.31 MeV), and M is the mass of the nucleus in MeV. Solving equation 5.9 we find B_γ is 9.25. The structure function (C) is determined from the ratio of the Fermi ft-value to the ft-value of the transition. In the case of ^{14}O the structure function is

$$C \approx \sqrt{\frac{2\, Ft_{Fermi}}{Ft_{Gamow\,Teller}}} = \sqrt{\frac{3069.7}{1.9\, x\, 10^7}} = 0.018 \quad . \tag{5.11}$$

The weak magnetism term is calculated to be -5.2 % per MeV by Calaprice for ^{14}O

Gamow-Teller decay [80]. Using the updated values of Ft_{Fermi} from chapter 4 and the corrected value of $Ft_{Gamow\text{-}Teller}$ with the shape factor we find

$$C \approx \sqrt{\frac{2\,Ft_{Fermi}}{Ft_{Gamow\,Teller}}} = \sqrt{\frac{2\,(3073.2)}{1.9\,x\,10^{7}}} = 0.018 \quad . \tag{5.12}$$

The shape factor is unchanged and remains -0.052 %/MeV. The Fierz interference term is consistent with zero for Gamow-Teller decay. The radiative correction, as described in section 5.2.1, for ^{14}O Gamow-Teller decay is plotted in Figure 5.5. The Gamow-Teller spectrum is shown in Figure 5.6 with the spectral shape factor, radiative correction, and the Fermi function correction terms.

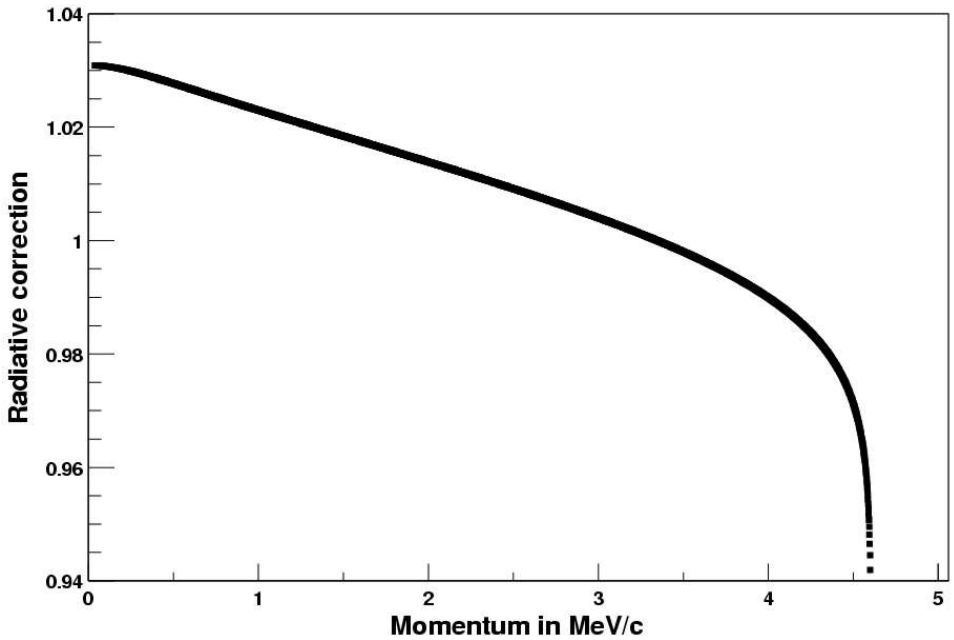

Figure 5.5 Order alpha radiative correction term for the branch. The radiative corrections to the Gamow-Teller branch are taken from Sirlin [25].

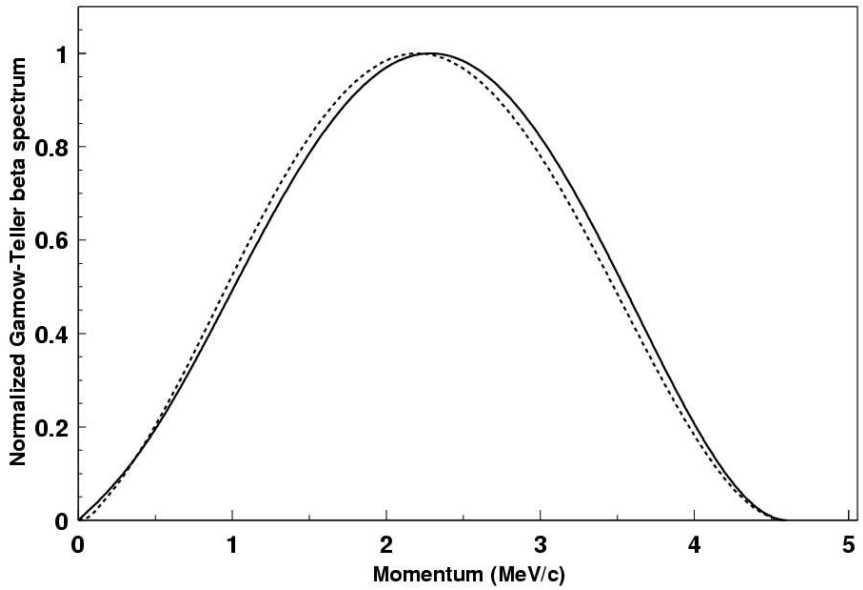

Figure 5.6 Gamow-Teller spectrum with correction terms. The solid black line is the original Gamow-Teller spectrum. The dashed line is the Gamow-Teller spectrum

including the correction terms.

5.3 O-14 Source for the Branching Ratio Experiment

The ^{14}O source was formed in the same manner as described for the half-life experiment. Up to 300 μCi of $^{14}O^{1+}$ was implanted in a 0.0013 cm thick beryllium foil at appproximately 27 keV. The beam was rastered by varying the analyzing magnet field over a collimator with a 0.55 ± 0.05 cm diameter aperture. Systematic effects of the source size are discussed in section 5.10.1. It is possible to form $^{13}NH^{1+}$ in the ion source which has an M/Q value of 14. The deposited source could contain ^{14}O and ^{13}N isotopes. ^{13}N beta decay has an endpoint energy of 1.190 MeV and the highest momentum beta particle is 1.62 MeV/c. The momentum range measured for this experiment was 1.71 MeV/c to 3.64 MeV/c. Contamination of the spectrum due to ^{13}N was not an issue.

To reduce backgrounds associated with the beam line, the beryllium foil containing the ^{14}O was shuttled between the beam line and the spectrometer. The small branching ratio of the Gamow-Teller branch (≈0.6%) and the limited spectrometer acceptance (10^{-4}) made the acquisition of statistics in the Gamow-Teller branch difficult. The highest average decay rate of the source is desired to maximize the signal to noise. With a source foil transfer time from the beamline to the spectrometer of approximately 10 seconds the optimal loading and decay time was determined to be approximately 80 seconds. The ^{14}O beam flux during the experiment was approximately 10^7 ^{14}O atoms per second. This beam flux yields a steady state decay rate of approximately 4 x 10^6 decays

per second with the source foil in front of the spectrometer. The accepted beta particle event rate in the spectrometer was approximately 40 Hz.

5.4 The Beta Spectrometer

A flat field 180 degree magnetic beta spectrometer enclosed in a vacuum chamber was used as shown in Figure 5.7. The source was positioned 25.0 cm away from a 0.55 cm diameter active collimator located at the top of the spectrometer. A source distance of 25.0 cm was chosen as a compromise between the necessary radiation shielding and geometrical acceptance of the spectrometer. The source and collimator are centered on the plane perpendicular the magnetic field. Beta particles follow a circular path in the magnetic field and exit the spectrometer through a 0.005 cm thick mylar vacuum window. Magnetic pole faces are separated by a 2.009 ± 0.005 cm gap. If the opening angle formed by the source and the collimator was too large, the beta particles could scatter off the pole face of the spectrometer. The beta particle position at the exit of the spectrometer was detected by a multiple wire proportional chamber (MWPC) which was attached directly to the face of the spectrometer and is described in section 5.6. The tungsten shielding mounted between the ^{14}O source and the MWPC attenuates the 2.31 MeV and 0.511 MeV gamma rays from the nucleus and positron annhilation. Tungsten shielding has a density of 17.2 g/cm^3 and is approximately 15 cm thick at the thinnest point. This provides an attenuation factor of approximately 10^{-16} for 0.511 MeV gamma rays and 3 x 10^{-5} for 2.31 MeV gamma rays.

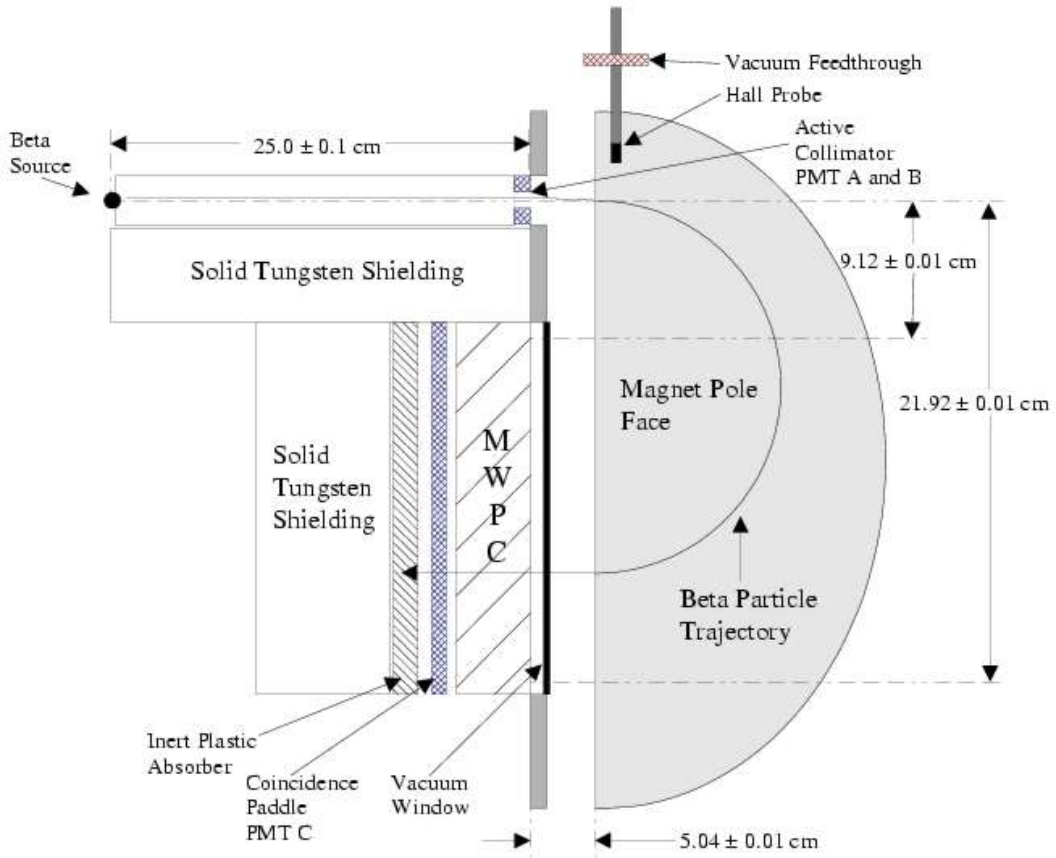

Figure 5.7 Schematic diagram of the spectrometer, source, and wire chamber. Note that the spectrometer pole face is contained in a vacuum chamber which is connected to the beam line vacuum system. The beta particles travel from the source to the exit window of the spectrometer in a vacuum at a pressure of approximately 10^{-6} Torr.

5.4.1 The Spectrometer Magnetic Field Profile

A Bell model HTj8-0618 hall probe was used to measure the magnetic field of the spectrometer. The hall probe controller was a Bell model 8860 with a calibration constant of 0.8937. Figure 5.8 shows the magnetic fringe field that extends several centimeters out from the front face of the spectrometer. Fringe fields effectively increase the average radius of curvature for a beta particle. The offset of the beta particle from its true value for a flat magnetic field, as a function of p, is shown in Figure 5.9 and Figure 5.10. Note that the lower energy (momentum) beta particles are deflected more than the higher energy (momentum) beta particles. The shift is calculated by numerically integrating the equation of motion of the beta particle as it travels through the magnetic field. Position of the beta particle was tracked from the source to the detection surface of the MWPC.

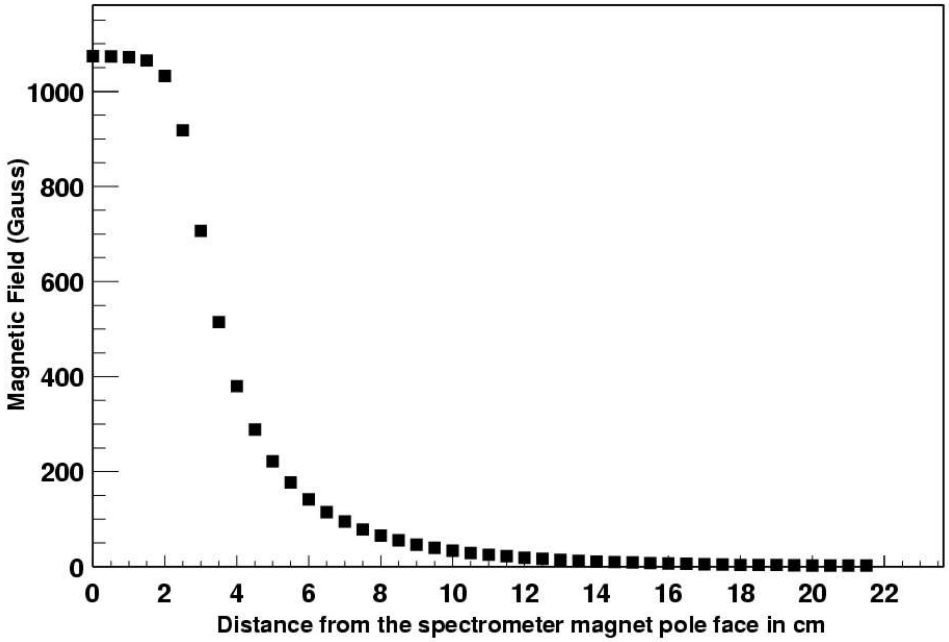

Figure 5.8 Magnetic fringe field of the spectrometer. The magnetic field was measured using the Bell Hall probe to monitor the magnetic field during the experiment. The field

was measured from the edge of the pole face to the source position with the spectrometer steel vacuum flange in place.

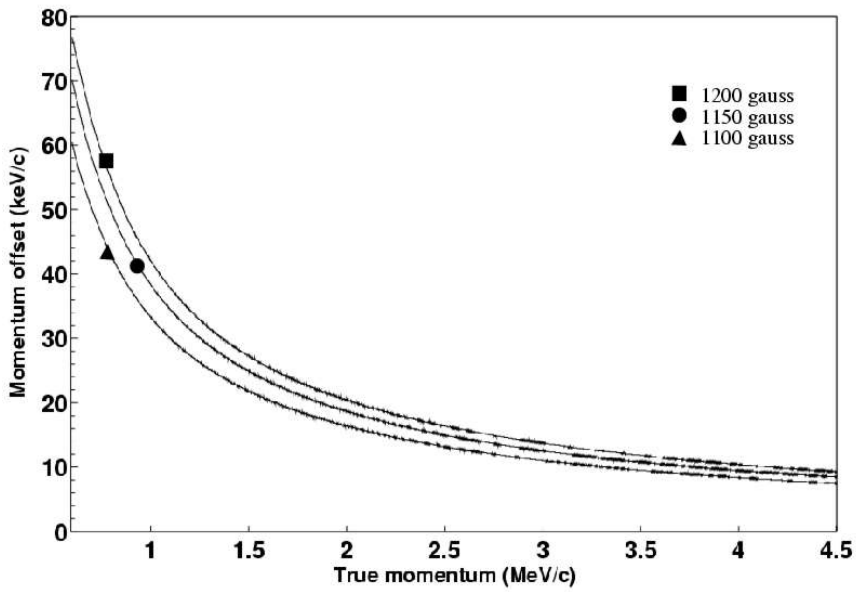

Figure 5.9 Magnetic fringe field offset in momentum. The beta particles are deflected by the fringe field and have an apparent momentum that is greater than their true momentum. The offset of the beta particle momentum is plotted with respect to the true momentum.

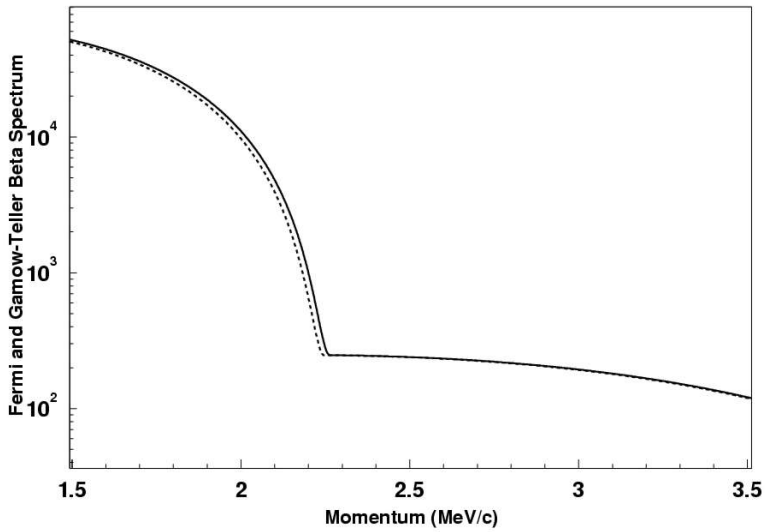

Figure 5.10 The momentum shift due to fringe field. The dashed line is the spectrum for a flat field geometry and the solid line includes the fringe field effect.

5.4.2 Magnetic Field Stability

During the experiment, the magnetic field was measured using a Hall probe inserted into the field through a vacuum feedthrough at the top of the magnet shown in Figure 5.7. The Hall probe measured the magnetic field for the duration of the experiment. The magnetic field was set to 1158 gauss and drifted by 2 gauss to 1160 gauss over a period of 30.75 hours. This corresponds to a change of 0.003 MeV/c at a momentum of 1.71 MeV/c and 0.006 MeV/c at a momentum of 3.64 MeV/c. The branching ratio is determined by dividing the observed Gamow-Teller events by the observed Fermi events. At a magnetic field setting of 1158 gauss the wire chamber measures approximately 9 % of the Fermi spectrum and approximately 64 % of the Gamow-Teller branch. Systematic uncertainty associated with the magnetic field is

discussed in section 5.11.7.

5.5 Multiple Wire Proportional Chamber

The beta particles are detected by a multiple wire proportional chamber (MWPC) filled with a 50% argon and 50% ethane gas mixture at atmospheric pressure. The MWPC detects the spatial information necessary to re-construct the momentum spectrum. Figure 5.11 is a schematic of the MWPC which consists of two sense planes sandwiched between three high voltage planes. A beta particle traveling through the gas in the chamber ionizes the atoms and molecules along its path. Electrons and ions are accelerated by the high voltage field which create secondary ions and electrons producing an amplification of the original ionization path. Electrons are collected on the sense wires and the corresponding electronic pulse is amplified and sent to a discriminator. When the pulse is above the discriminator threshold, the discriminator produces an ECL level pulse. Each element of the MWPC is described in detail in the following subsections.

5.5.1 Mechanical Construction of the MWPC

The MWPC consists of five parallel planes of gold coated tungsten wire, two are sense planes and three are high voltage planes. The sequence (starting from the spectrometer face) is high voltage, vertical sense plane, high voltage, horizontal sense plane, and high voltage as shown in Figure 5.11. The MWPC horizontal sense plane has 64 wires spaced at 0.2 cm intervals in the horizontal direction. This first wire is

positioned 9.12 cm below the center of the active collimator and the last wire is at a distance of 21.92 cm. The MWPC vertical sense plane consists of 16 wires spaced at 0.2 cm. The vertical sense plane is centered on the magnetic pole face gap of the spectrometer. The geometry of the MWPC and spectrometer allow a maximum of approximately 60% of a momentum spectrum to be measured for a given magnetic field setting.

The high voltage planes are all connected to a common high voltage supply and are at the same potential. The applied high voltage can be varied between 0 and -3200 volts. The high voltage supply is a Bertran model 375N current limited power supply. The high voltage planes extend past the sense planes on either side by 0.5 cm to minimize any electric fringing fields. The high voltage supply is current limited to less than 8 μA. This is done to avoid a spark that could vaporize a high voltage wire and ruin the wire chamber. The high voltage supply is internally regulated to within 0.005 %. This ensures that the gain does not vary with time. Refer to section 5.8.3 for a discussion of the plateau curve of the wire chamber.

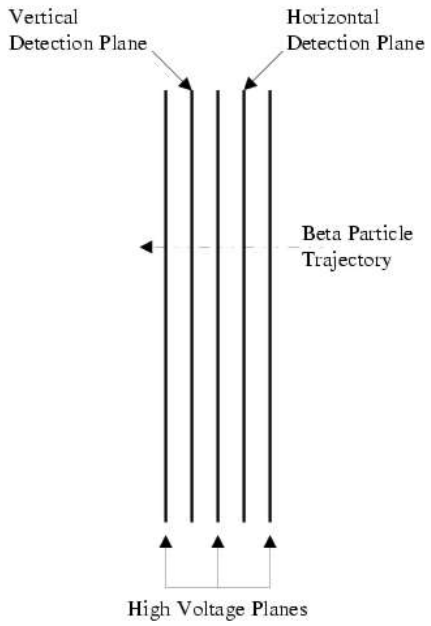

Figure 5.11 Schematic of MWPC sense and high voltage planes. The beta particles travel from the spectrometer through the planes and out from right to left as indicated. Each plane is 0.3 cm thick and the high voltage planes had 2500 V applied to them during the experiment.

5.5.2 Argon Ethane Fill Gas

The gas in the chamber is of particular importance as it responsible for the gain of the chamber along with the applied high voltage. Gain is defined as the ratio of the number of electrons collected to the number of initial electrons created by the ionization along the path length. A relativistic beta particle travelling through a gas loses approximately 26 eV per ion pair created [81]. In the mixture of 50% argon and 50% ethane at atmospheric pressure the beta particle loses approximately 3000 eV/cm. Beta particles create approximately 120 electron ion pairs per cm travelled in the gas. The

measured pulse heights from beta particles in the gas are on the order of 100 mV after the pre-amplifier. The pre-amplifier gain is approximately 2μV per electron collected therefore the number of electrons collected is approximately 50000. Gain of the gas and wire geometry used for this experiment is approximately 4000.

Gain increases exponentially with applied voltage as can be seen from the plateau curve of the chamber in section 5.8.3. Exponential growth of the gain region is due to the geometry of the wire and the strength of the electric field near the surface of the wire [82]. As the electric field surpasses 10^6 V/m the ion pairs that are formed by the beta particle cannot recombine.

5.5.3 Pre-Amplifier Electronics

The 80 readout channels for the wire chamber are grouped into 5 sets of 16 channel readout electronics. A schematic of the electronics used to readout the horizontal channels is shown in Figure 5.12 and the vertical channels are shown in Figure 5.13.

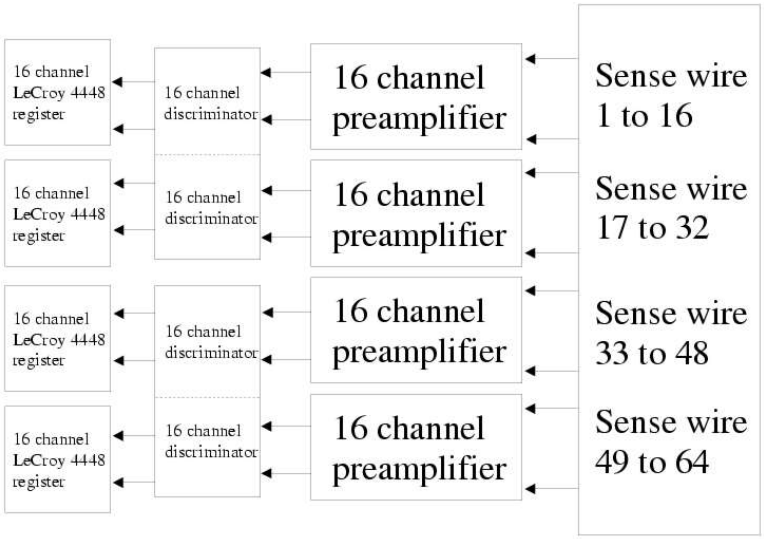

Figure 5.12 Schematic layout of the horizontal sense plane and supporting electronics.

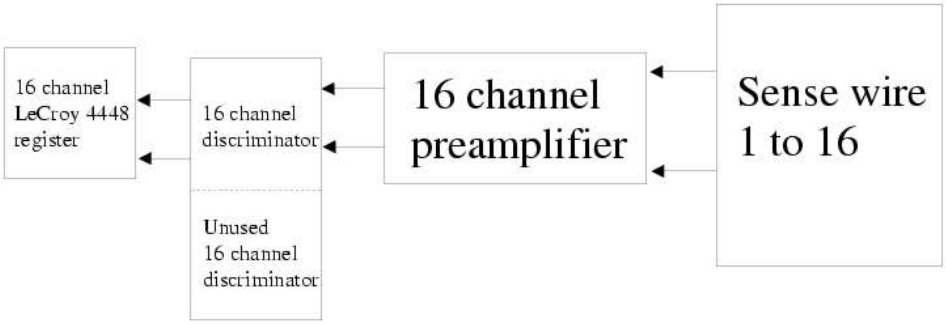

Figure 5.13 Schematic layout of the vertical sense plane and supporting electronics.

A LeCroy MQS104 chip was used as a pre-amplifier which contained 4 differential inputs per chip. The input impedance is 230 ohms and the gain is approximately 2 μV per electron. The electronic circuit for a single sense wire is shown in Figure 5.14. Transistors after the MQS104 chip provide the current amplification needed to drive the input stage of the discriminator circuit. Figure 5.15 is a photograph of

one of the five sixteen channel preamplifier boards attached to the sense planes.

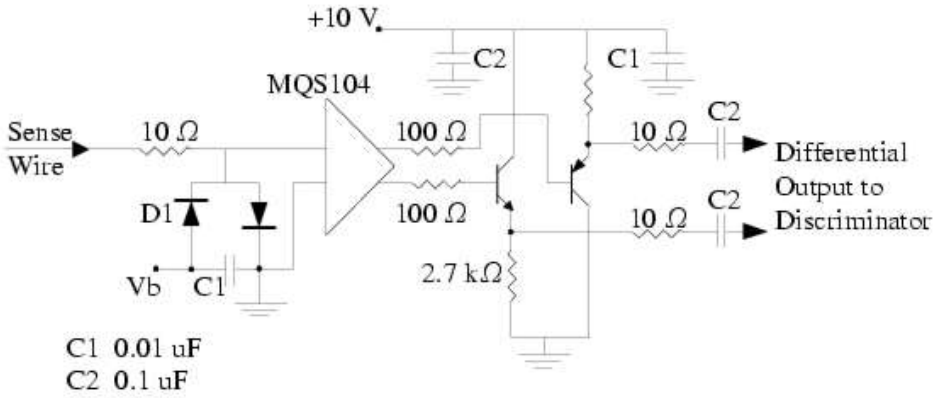

Figure 5.14 pre-amplifier electronics overview

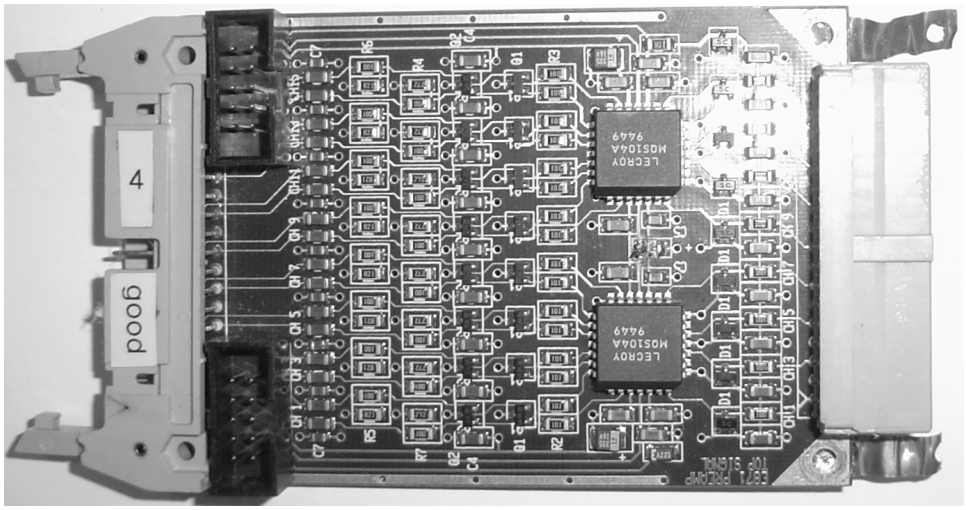

Figure 5.15 Sixteen channel preamplifier board for MWPC.

5.5.4 Discriminator Electronics

The discriminator circuit consists of five chips in series as shown in Figure 5.16. Differential input signal from the pre-amplifier was connected to the MVL 407

discriminator. The reference voltage (threshold) was externally controlled by an adjustable power supply. A common threshold voltage was used for all 80 channels and could be varied between 0 to 50 mV. The MC10H115 differentiator chip creates an ECL pulse which was the output logic level of the discriminator. The MC10H101 pulse stretcher allowed the output pulse width to be varied. Output width was controlled by applying an external voltage to the pulse stretcher. The output width was common for all 80 channels and was continuously adjustable from 25 ns to 110 ns. The pulse stretcher chip contained an auxiliary output channel for each 4 channel chip. Auxillary output provided a prompt signal before the 100 ns delay line. The prompt signal was used to generate the coincidence trigger condition. Sixteen auxiliary channels for the horizontal sense plane and the four auxillary channels for the vertical sense plane were summed together in an operational amplifier and used to trigger the data acquisition system. The summed signal pulse height was proportional to the number of wires that passed the discriminator threshold. From the pulse stretcher each channel went through a 100 ns delay line before entering the output buffer. The MC10H116 output buffer chips were connected with a 32 wire ribbon cable to a LeCroy 4616 ECL to NIM converter. NIM output from this converter was connected to a LeCroy 4448 16 channel gated register. The register recorded the hit pattern of the wire chamber and stored the data for readout as discussed in section 5.5.5. Figure 5.17 is a photograph of one of the three discriminator boards used for the MWPC.

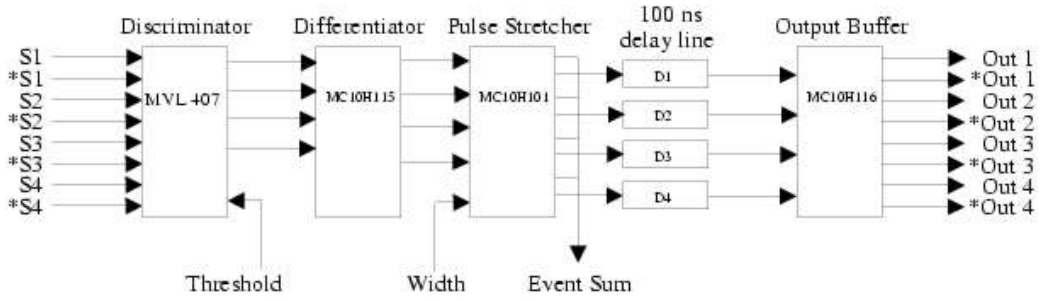

Figure 5.16 MWPC discrimintor discrete electronics overview. The signals from the pre-amplifiers arrive at the discriminator on the left side of the figure. The signal threshold and output pulse width are controlled by externally applied voltages. A fast output is produced by the event sum line prior to the 100 ns delay line. The output buffer passes the ECL level signal onto the registers for later data readout.

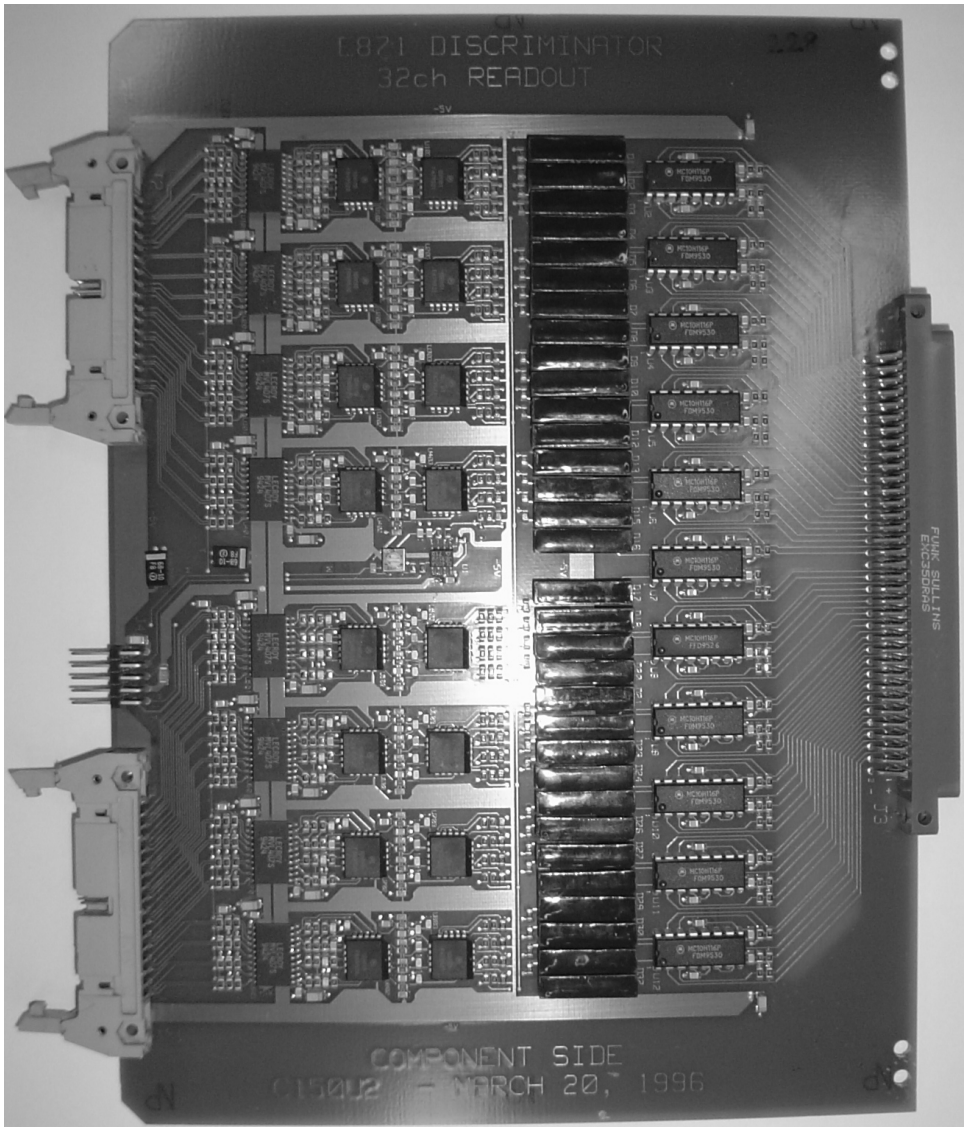

Figure 5.17 32 channel MWPC discriminator board.

5.5.5 Data Acquisition Electronics

The data acquisition system recorded data from the active collimator, coincidence paddle, and the wire chamber for each event. Six data channels acquired were the pulse height from the two anti-coincidence PMTs and one coincidence PMT, the timing of the

events from the two anti-coincidence PMTs and one coincidence PMT, and the horizontal and vertical wires which triggered the MWPC. A trigger event consists of any coincidence hit of at least one wire in the vertical and horizontal planes of the wire chamber. The coincidence circuit used the sum output from the vertical and horizontal discriminator board after it had been conditioned as shown in Figure 5.18. Sum output of the vertical and horizontal discriminator was conditioned in order to prevent multiple triggering of the detector. Multiple triggering could occur when multiple wires were triggered in the wire chamber, the resulting sum pulse was large enough to cause electronic ringing in the sum output line. The sum pulse was amplified by a factor of ten by a Philips 776 ten channel amplifier. The amplified signal was fed into a discriminator with a threshold of 100 mV. The discriminator output was connected to a gate and delay generator and a Phillips Scientific 756 coincidence module.

Gate and delay generators produced an 11 μs and 13 μs veto signal that arrives after the direct pulse from the discriminator. This permitted only a single logic pulse to be produced for each horizontal or vertical sum pulse. Output of the vetoed AND gates were each passed through a discriminator which produced a 170 ns output pulse. The 170 ns output pulses were fed into the horizontal and vertical coincidence AND gate. The 170 ns width compensates for the different propagation delay times between the wire chamber board sum pulses. When the vertical and horizontal pulses overlap they produce a coincidence event which triggered the CVC trigger module.

The CVC trigger module was triggered by one of the outputs from the coincidence AND gate. Output from the AND gate passed through a discriminator which

split the signal. One branch was fed into a LeCroy 222 gate and delay generator. The delay was set to 211 μs to allow for digitization of all the signals being processed. A final discriminator ensured a clean and consistent trigger pulse of 20 ns duration. A second output of the discriminator located directly after the AND coincidence gate triggered another LeCroy 222 gate and delay generator. This second gate and delay pulse provided a 335 μs veto signal to the coincidence AND gate. The veto stopped any further triggering of the system until all the data channels had been digitized and read out by the CVC acquisition module.

A coincidence AND gate also provided a third output which was split into four more logic pulses to gate the ADC, the wire chamber registers, and start the TDC. The wire chamber vertical and horizontal registers were gated open for 192 ns to record the wire chamber data. A LeCroy 2249A ADC was used to record the pulse height from the active collimator PMTs and the coincidence paddle PMT. The ADC gate was opened for 114 ns. A LeCroy 2228A TDC was gated open for 267 ns and recorded the arrival time of the PMT signals mentioned previously. Data channels were digitized and read out by the CVC crate control module. All analysis such as cuts in ADC spectra or TDC timing were performed off-line after the experiment.

Deadtime of the acquisition system was limited by the 335 μs veto applied to the coincidence AND gate. The highest acquisition rate achieved was approximately 40 Hz. The maximum count loss due to deadtime is approximately 1 %. The deadtime affects the entire spectrum uniformly so there was no systematic error introduced to the spectrum due to deadtime.

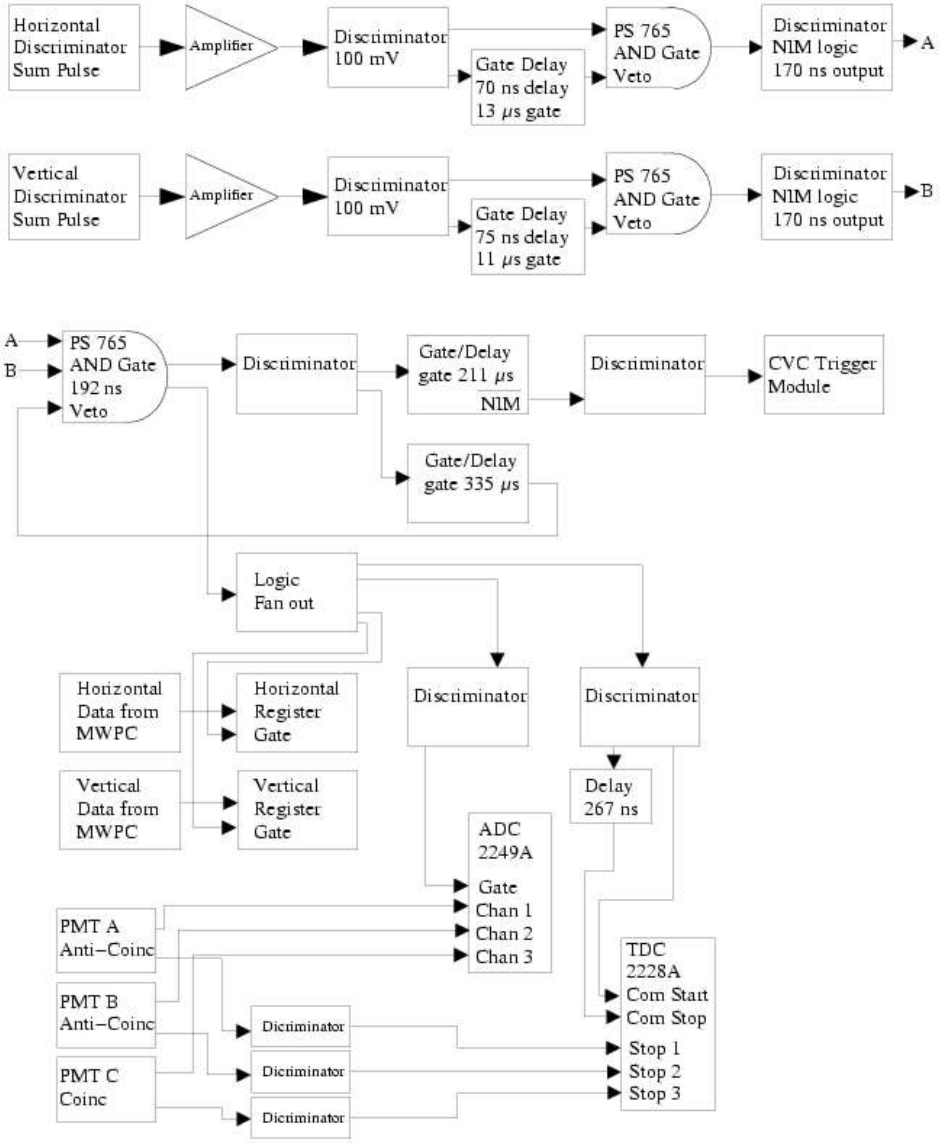

Figure 5.18 MWPC data acquisition electronics. These electronics form the coincidence trigger circuit for recording an event. To trigger the readout module, at least one event in the horizontal and vertical sense planes must occur in coincidence. The acquisition system records the wire hit pattern, the PMTs pulse heights, and the TDC times for each event.

5.6 The Anti-Coincidence Active Collimator

An active collimator defined the entrance aperture for the beta particles into the spectrometer. The active collimator was designed and constructed to measure the scattering of beta particles from the collimator. Eljen-204 plastic scintillator was used to make the active collimator. A 0.1 cm thick piece of scintillator was made into an annular ring with an inner diameter of 0.55 cm and an outer diameter of 1.52 cm.. The scintillator was held in a cylindrical depression in a piece of lucite that was coated with 0.0006 cm thick aluminized mylar foil shown in Figure 5.19. A PMT was attached via a light guide on either side of the lucite holder. Hamamatsu model R647 PMTs were used, the same as those used in the half-life experiment. The lucite holder (with aluminized mylar attached) was placed between two mating blocks with O-rings in order to produce a vacuum seal. All beta particles that entered the spectrometer either passed through the 0.55 cm diameter aperture or interacted with the scintillator material. Beta particles that interacted with the active collimator and triggered the wire chamber were recorded. The corresponding scintillation light from the interaction was collected by the two PMTs (labelled PMT A and PMT B). ADC spectra of PMT A and PMT B were recorded for each beta event and are shown in Figure 5.20 and Figure 5.21.

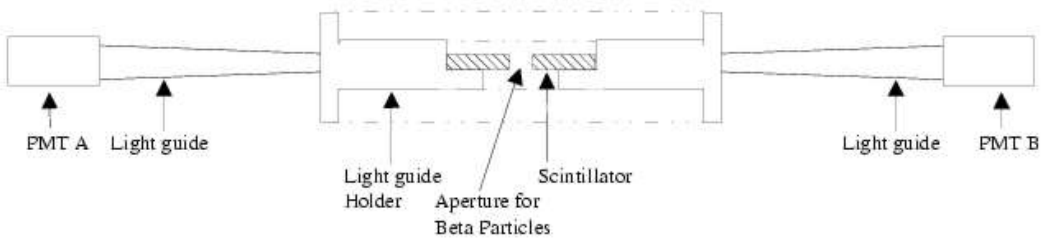

Figure 5.19 Schematic of the active collimator (side view). The beta particles are incident on the active collimator from the top of the page. The scintillation light is collected by the PMT A and PMT B located on either side.

The sensitivity of the active collimator was measured during the experiment. The beta particles passing through the scintillator deposited on average 175 keV of energy. This peak appeared at channel 800 on the LeCroy 2249A ADC as can be seen in Figure 5.22. The energy scale of the ADC was 0.25 keV per channel. The ADC threshold used in the analysis was set at channel 200 which corresponds to an energy of 18 keV.

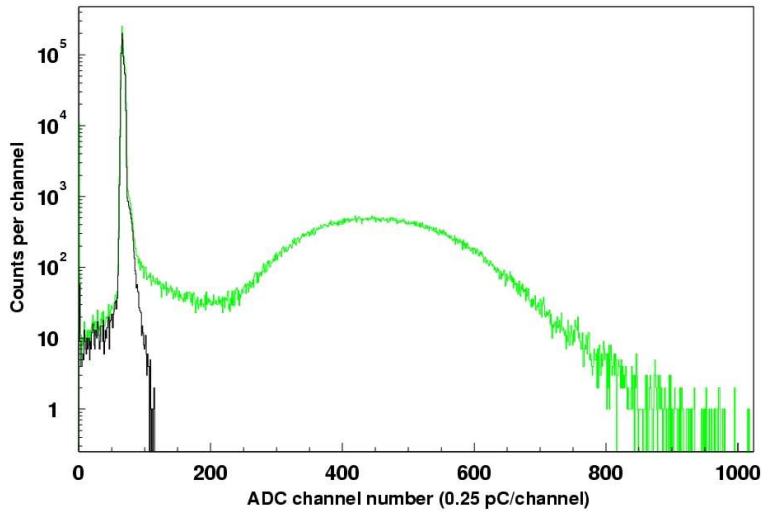

Figure 5.20 ADC spectrum anti-coincidence collimator detector A. The black line shows

the accepted events with the ADC cut. The grey curve shows all the events.

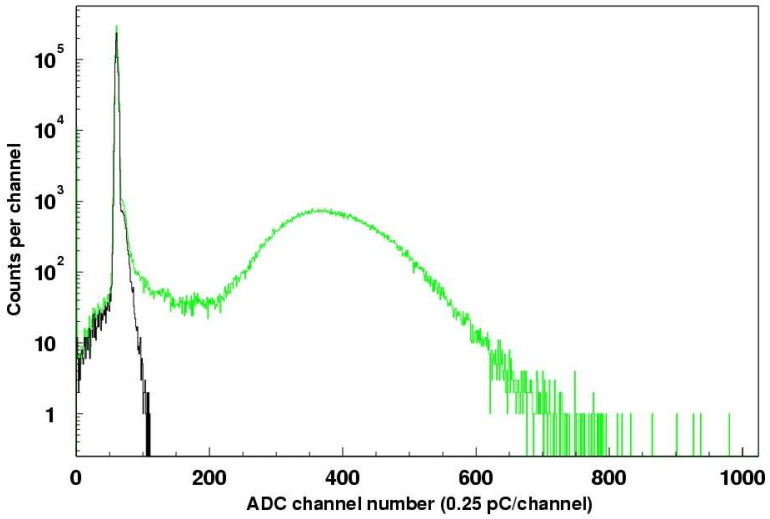

Figure 5.21 ADC spectrum anti-coincidence collimator detector B. The black line shows the accepted events with the ADC cut. The grey curve shows all the events.

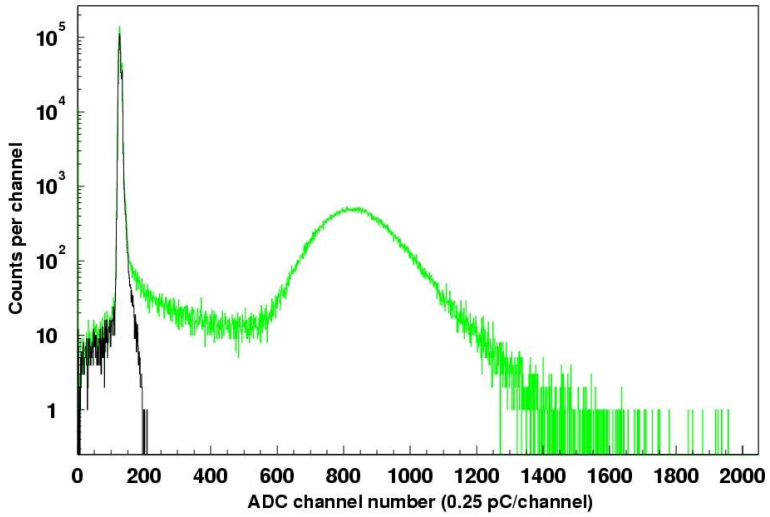

Figure 5.22 Summed ADC spectrum anti-coincidence collimator detector A and B. The black line shows the accepted events with the ADC cut. The grey curve shows all the

events. ADC channel 200 corresponds to 18 keV of energy.

Time spectrum of the of the PMT pulses relative to the wire chamber were also recorded and are shown in Figure 5.23 and Figure 5.24. Accepted events all timed out on the TDC at channel 1024. The timing spectrum was also recorded to help discriminate against electronic noise or pick-up. Electronic noise was present in early testing due to sparking of one of the PMT bases. The arrival time of the pulses due to electrical noise was shifted earlier than a true beta particle event. Sparking did not occur during the experiment.

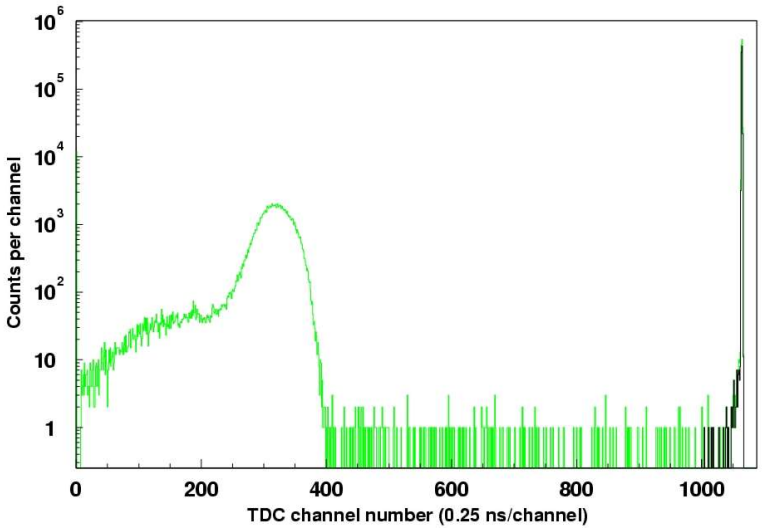

Figure 5.23 TDC spectrum of the anti-coincdence collimator detector A. The black line shows the accepted events with the TDC cut. The grey curve shows all the events.

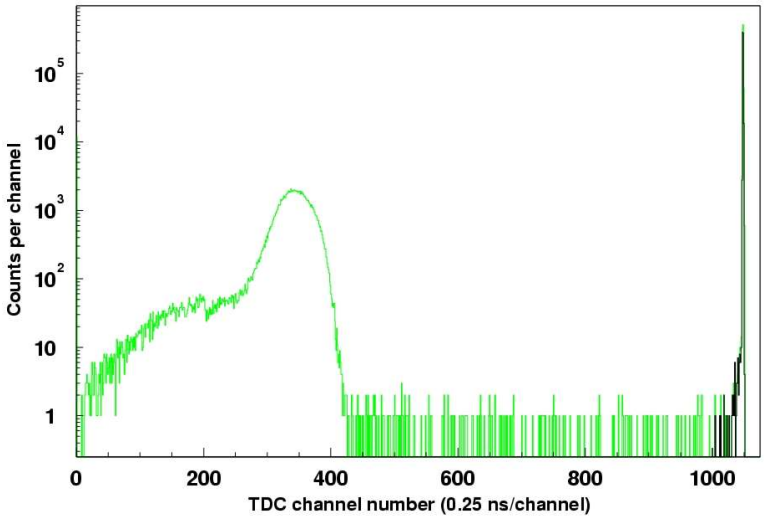

Figure 5.24 TDC spectrum of the anti-coincdence collimator detector B. The black line shows the accepted events with the TDC cut. The grey curve shows all the events.

5.7 The Coincidence Beta Paddle

The coincidence paddle was a 0.2 cm thick piece of Eljen-204 plastic scintillator. A plastic scintillator with dimensions of 15.24 cm long by 3.81 cm wide was mounted to a light guide which channelled the light to an RCA 8850 PMT. The coincidence paddle helped eliminate random noise from the wire chamber due to sparking and transients in the electrical ground. Figure 5.25 shows the ADC spectrum of the paddle which was recorded for each event. The average energy deposited in the scintillator for a minimum ionizing particle was 350 keV. The energy scale of the coincidence paddle ADC was determined to be approximately 1 keV per channel. Threshold for the analysis of the coincidence paddle was set at channel 100 which corresponded to an energy threshold of 100 keV. The probability that a beta particle deposited less than this amount of energy

was 0.001. It was possible for the beta particle to backscatter from the plastic scintillator and deposit less than 100 keV of energy. Figure 5.26 is the TDC spectrum which provides a double check of the event type as previously mentioned.

During the analysis it was determined that beta particles could scatter at large angles while traversing the wire chamber. The scattered beta particles could also miss the coincidence beta paddle. This was demonstrated using the data taken at a magnetic field setting of 728 gauss. The the ratio of coincident events between the wire chamber and the coincidence paddle varies from the center of the chamber to the edge of the chamber.

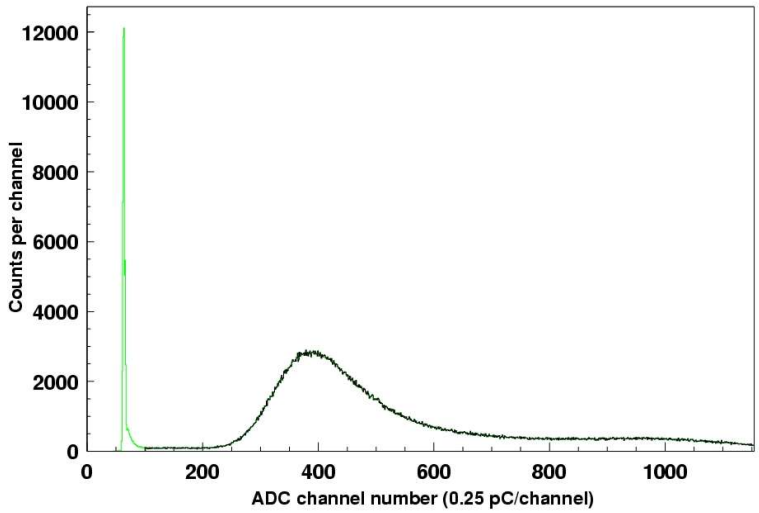

Figure 5.25 Coincidence paddle ADC histogram. The grey curve shows all events. The black curve shows the coincident event spectrum.

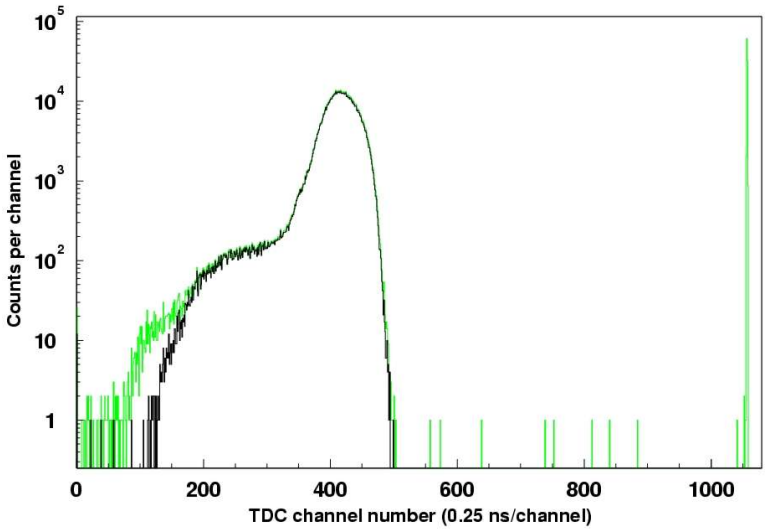

Figure 5.26 Coincidence paddle TDC histogram. The black curve shows coincident events. The grey curve shows all events.

Figure 5.27 shows a plot of the wire chamber events that triggered the center vertical wire (channel 7) divided by the number of events that trigger the center vertical wire and the coincidence paddle. Figure 5.28 shows a plot of the wire chamber events that trigger one of the off center vertical wires (channel 3) divided by the number of events that trigger the off center vertical wire and the coincidence paddle. Due to this scattering effect the coincidence requirement of the beta paddle was not used to analyze the data.

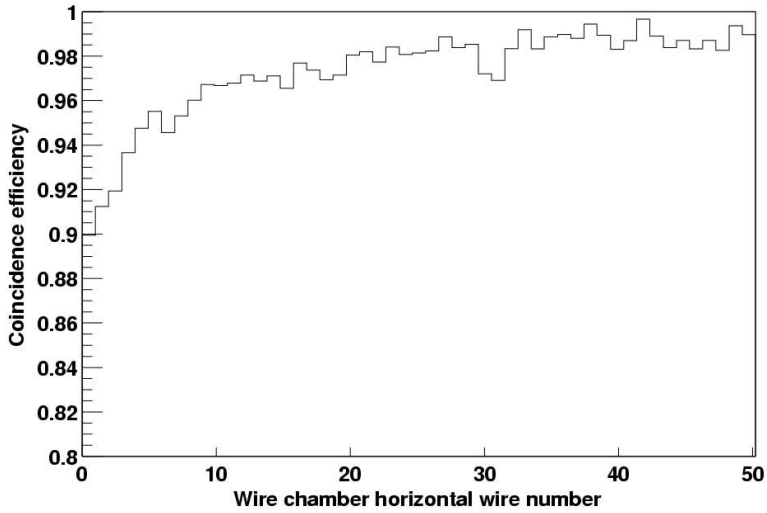

Figure 5.27 Coincidence efficiency for vertical wire 7 in the center. The coincidence efficiency is the ratio of paddle and wire chamber events over only wire chamber events. The coincidence efficiency increases as the momentum of the beta particle increases.

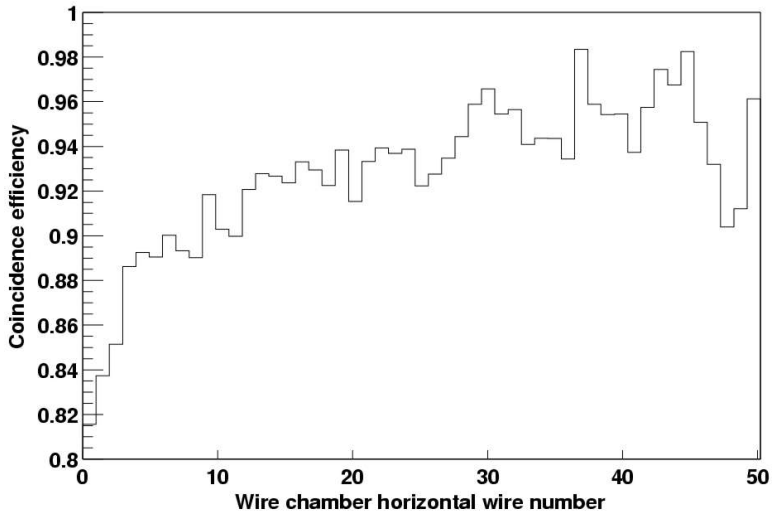

Figure 5.28 Coincidence efficiency for vertical wire 3 at the edge. The coincidence efficiency is the ratio of paddle and wire chamber events over only wire chamber events.

The coincidence efficiency increases as the momentum of the beta particle increases.

5.8 Characterization of the MWPC

The characterization of the wire chamber falls into four categories; electronic noise, background events, beta particle response, and gamma ray response. Electronic noise is defined as the intrinsic noise associated with the preamplifier electronics. Background events are due to naturally occurring high energy muons that traverse the wire chamber volume. Beta particle response efficiency was determined from a plateau curve of the entire chamber. Finally, the gamma ray response was tested to ensure the radiation shielding was adequate for the experiment.

5.8.1 High Voltage Conditioning of the MWPC

The applied high voltage can cause electrical breakdown of the fill gas. This can produce false coincidence events in the MWPC. Microscopic imperfections on the wires and the presence of minute amounts of dust cause local electric fields exceeding the breakdown limit of the fill gas. Electrical discharge in the fill gas triggers many wires in the chamber simultaneously. Noise associated with the high voltage decreases over time with a period of several hours.

High voltage conditioning of the MWPC increases the reliability and performance of the MWPC. The MWPC is conditioned by gradually increasing the high voltage and burn away microscopic imperfections and dust particles from the wires. The high voltage

is held at a given voltage (e.g. 2000 V) until the current drawn decreases to nA levels. High voltage was increased to the next stable point (e.g. 2400 V) and held for several hours until the current drawn decreases to the nA level again. This process was repeated until the MWPC could hold a voltage of 3000 V without tripping the current limit of the power supply set at 80 nA for at least 12 hours.

Typically, high voltage breakdown events trigger more than 10 wires in the vertical and horizontal plane in coincidence. This type of event was selected out in the analysis. The rate for these events was on the order of 0.1 Hz or less depending on the condition of the chamber. These events do not disrupt the basic operation of the chamber in any way. After the MWPC was conditioned for the experiment, the leakage current was 6.5 nA at 3000 V and the high voltage noise rate was 0.0635 Hz.

5.8.2 Intrinsic Electronic Noise

Electronic noise was due to the intrinsic noise of the MQS104A chips and the noise on the ground plane due to external sources. Intrinsic noise of the MQS104A chips was stated to be less than 3000 electrons per channel. This corresponded to an output voltage, with a gain of 4.2 μV per channel, of 12.6 mV. Work done by Professor Kam-Biu Luk and colleagues have found this level rather difficult to achieve [83]. The average value was found to be approximately 2 times higher when several channels were assembled on the same circuit board. The electronic noise spectrum was measured for this MWPC by varying the discriminator threshold with the high voltage off and is shown in Figure 5.29. The sharp knee shows the average roll-off of the noise over all the wires

in the chamber.

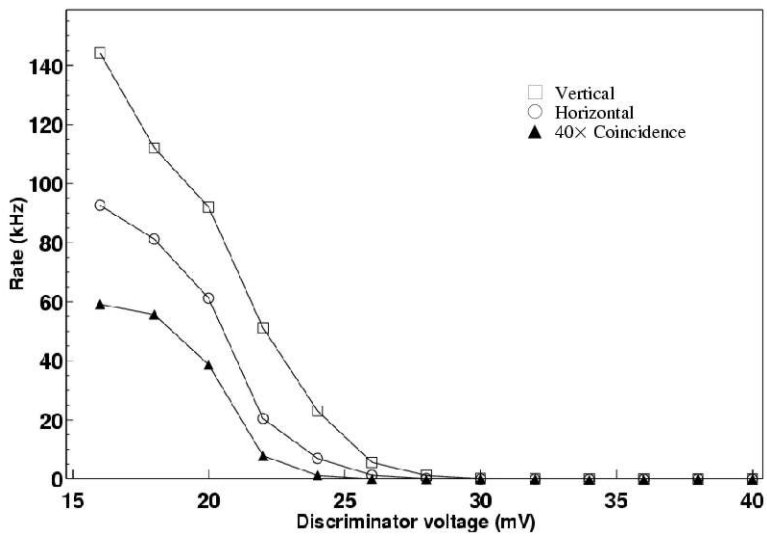

Figure 5.29 Electronic noise rate as a function of the discriminator threshold. Noise associated with the electronics was measured relative to the discriminator threshold voltage. The vertical and horizontal rates are measured independently. Note that the coincidence rate is approximately 40 times less than singles rate in either sense plane.

The most critical component in reducing the electronic noise of the system was to ensure proper grounding of the pre-amplifiers. This was achieved by using a 0.64 cm thick copper plate was the mounting surface for the wire planes and the pre-amplifiers. The copper plate was electrically isolated from the spectrometer by insulated stand-offs.

The wire chamber was mounted directly to the copper plate by steel screws. The chamber was enclosed by a copper sheet which was 0.16 cm thick in order to shield the inputs to the pre-amplifiers from the environment. This ensured a common low impedance ground for the wires and helped eliminate pick-up from the environment.

Environmental noise originated from many sources. The most common source was noise from electrical motors, vacuum pumps, computers, and switching power supplies in the building. Sources external to the building include the KPFA transmitter at 90.1 Mhz and various other broadcast signals.

5.8.3 The Plateau Curve

The plateau curve of the wire chamber is a measure of the beta particle response and efficiency. Due to intrinsic variations in the performance of the MQS104 chip, the gain varies from channel to channel. It is important to make sure that the gain is sufficiently high so that the pulses are all above the discriminator threshold. This ensures uniform response over the wire chamber for minimum ionizing particles. The wire chamber plateau curve was measured with the above electronics in place and a discriminator threshold of 40 mV. With the discriminator set point fixed the high voltage applied to the wire chamber was increased in steps of 50 V starting from 1400 V. The signal was generated by a ^{90}Sr beta source which was placed in the same position as the ^{14}O source for the branching ratio experiment. The magnetic field of the spectrometer was reversed so the beta minus particles travel through the spectrometer and enter the wire chamber as they would during the experiment. At each voltage the beta particle rate for

the horizontal, vertical, and coincidence conditions was acquired for 10 s. The average rate over 10 seconds is plotted in Figure 5.30. This curve represents the integral of the pulse height distribution. Above 2800 volts the singles rates begin to increase and the wire chamber high voltage supply can occasionally trip off. The wire chamber was run at a voltage of 2500 V approximately the middle of the plateau curve.

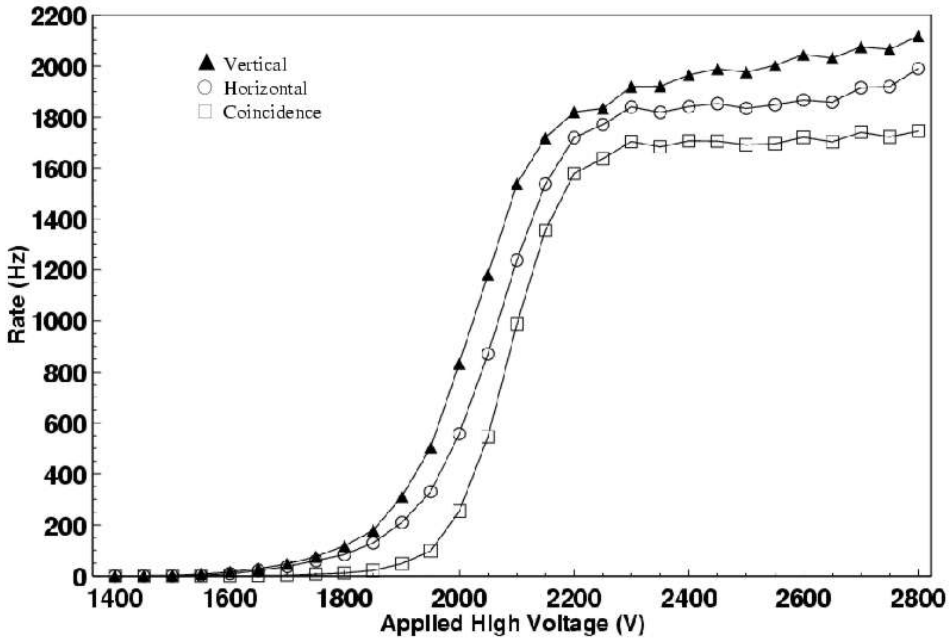

Figure 5.30 MWPC plateau curve. The plateau curve was obtained using a ^{90}Sr beta source which irradiated the MWPC causing the wire chamber to trigger. At 25 V intervals a 10 s average of the MWPC rates were recorded. Above 2800 V the MWPC rate increased sharply and would not hold voltage reliably with the ^{90}Sr source in place. The MWPC was set at 2500 V for the experiment in the middle of the plateau curve.

5.8.4 The Cosmic Ray Muon Background Rate

The MWPC detects muons as well as beta particles. High energy cosmic rays striking the upper atmosphere of the earth produce charged mesons. These mesons decay into energetic muons which penetrate the atmosphere and produce an average flux of 1 muon/(cm^2-minute) at sea level for a horizontal detector. Background noise due to the cosmic ray flux can be calculated from the muon flux at sea level. Geometry of the wire chamber and the angular distribution of the muons needs to be included to obtain an accurate result. Active area of the wire chamber was 12.8 cm by 3.2 cm which gives 41 cm^2. The muon distribution with respect to the horizon angle is $\cos^{1.8}\theta$. Theta is zero looking directly up from the earth and approaches 90° at the horizon of the earth. Theta ranges between 31° to 90° due to the geometry of the wire chamber. The integrated rate of muons for this area and angular distribution 0.34 Hz. The spectrometer opening angle limits the phi acceptance to approximately 30°. The approximate rate expected for muons triggering the chamber is reduced to 0.17 Hz.

A cosmic ray background was measured over a 400 hour period after the experiment and recorded a total of 209370 events which yields a background rate of 0.14 Hz. The cosmic ray background rate agrees with the estimate above. The cosmic ray background with the same cuts as the data from section 5.10 registered 81491 events with a rate of 0.057 Hz. Figure 5.31 is the muon spectrum taken over the 400 hour period after the experiment. The cosmic rate event rate for a horizontal wire is approximately 0.001 Hz.

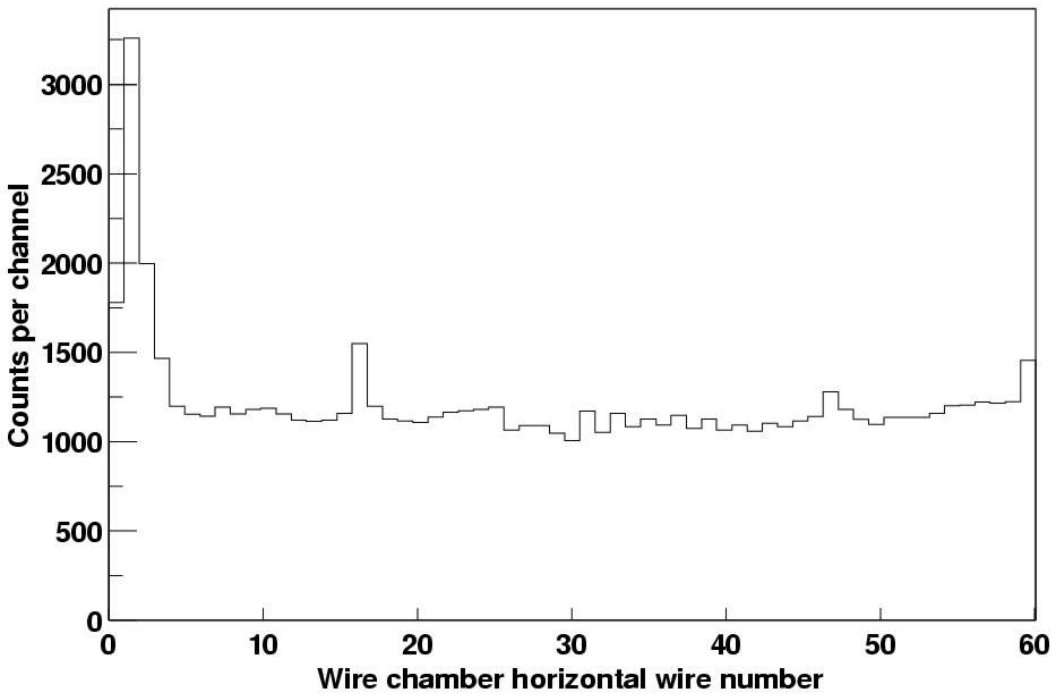

Figure 5.31 Cosmic ray background spectrum. The cosmic ray background shown here has the same cuts as applied to the data.

5.8.5 The ^{14}O Source Background

The ^{14}O source background was measured during the run by closing a 2 mm thick tantalum flap in front of the active collimator. This prevented the beta particles from entering the spectrometer while allowing the ^{14}O source to decay in the same manner as during data acquisition. The 2.31 MeV gamma ray from ^{14}O decay can pair produce in the tantalum and is discussed below. Source background was acquired for a period of 9406 s during the experimental run under the same conditions as the data was acquired. A total of 8434 events were registered with the same cuts applied as the data in section 5.10. The beam line rate and source intensity were also monitored during the background

measurement with an average rate of 7597 Hz and 1041 Hz respectively. The source and beam line rates measure the 2.31 MeV gamma ray with a NaI detector located at each position. Output of the NaI detector was sent to a discriminator which only recorded the 2.31 MeV gamma rays. Figure 5.32 shows the resulting source background spectrum. Note that the source is closer to wire one and the rate is correspondingly larger.

The 2.31 MeV gamma ray can produce positrons when it interacts with the tantalum. The probability of creating a electron positron pair with a 2.31 MeV gamma ray in a 0.2 cm thick piece of tanatalum is approximately 17 % [84]. The energy used to create the positron electron pair is equal to the rest mass energy of each particle.

$$E_{creation} = m_{e\,sub} c^2 + m_{e\,add} c^2 = 0.511\,MeV + 0.511\,MeV = 1.022\,MeV$$

(5.13)

The remaining kinetic energy available to the positron electron pair is 1.288 MeV. If all the energy was carried away by the positron, leaving the electron at rest, it would have a momentum of 1.72 MeV/c. This momentum is too low to be measured for the magnetic field setting of 1158 gauss. The 2.31 MeV gamma ray does not artificially increase the background measurement of the ^{14}O source via pair production in the tantalum beta absorber.

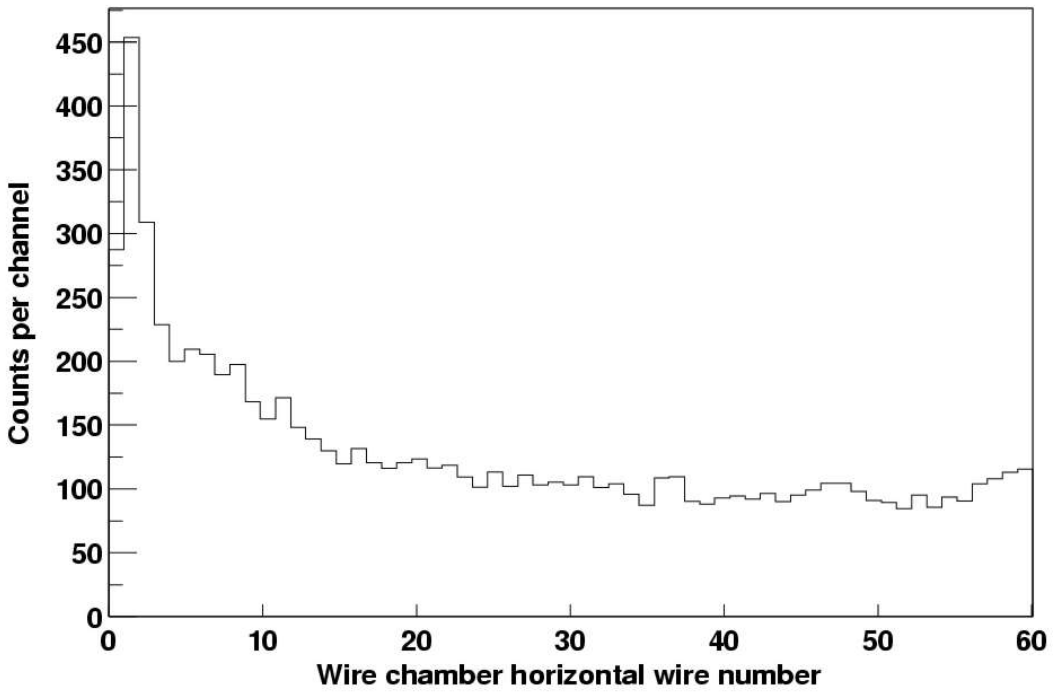

Figure 5.32 Background due to the ^{14}O source. The ^{14}O source background was recorded during the experiment by closing a tantalum flap located in front of the active collimator. A 0.2 cm tantalum flap stopped the beta particles from entering the spectrometer.

5.8.6 The Beam Line Background

Beam line background was measured during the experiment during the load cycle of the ^{14}O source. The beam line background was measured for 21842 s during the experiment. A total of 12201 events were recorded with the same cuts as applied to the data. Beam line radiation produced an average rate of 0.559 Hz in the MWPC. The beam

line rate was also monitored and had an average rate of 17406 Hz. Background in the MWPC due to the beam line is plotted in Figure 5.33.

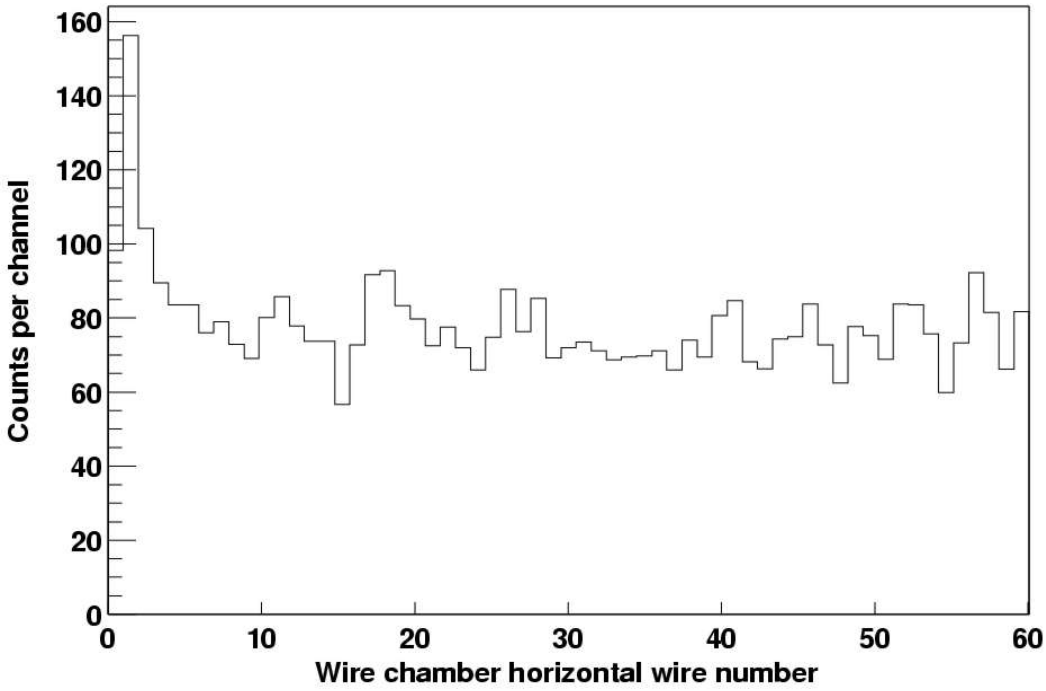

Figure 5.33 The background due to O-14 in the beam line. The ^{14}O beam line background was recorded during the experiment during the load cycle of the ^{14}O. During the load part of the cycle the Be foil containing the ^{14}O and the ^{14}O beam are located at the beam line.

5.9 Monte Carlo Simulations

Monte Carlo simulations of the beta spectrum were used to determine the effect on the beta spectrum due to the finite source size, source distance, collimator size, magnetic field, wire chamber position, and wire chamber response. A simulation models the Fermi and Gamow-Teller ^{14}O beta decay spectrum as shown in Figure 5.4 and Figure

5.6. The ^{14}O source is a finite diameter disk of zero thickness whose radius can be varied. Beta particles are emitted isotropically from the surface of the source. Beta particles are projected forward onto the collimator aperture. Only beta particles that fall within the collimator aperture are allowed to continue in the simulation. Beta particles that pass the collimator acceptance are transported through the magnetic field. The beta particle position is recorded into two arrays: a 2 dimensional array representing the MWPC and a linear sum of the 16 vertical wires which forms a 64 bin horizontal array. The finite size of the source and aperture allow the beta particles to spread in the vertical direction as they travel through the spectrometer. Width of the actual distribution is limited by the source size and the collimator aperture.

5.9.1 Finite Source Spectrum

The ^{14}O beta spectrum was distorted by the finite size of the implanted source. The size of this effect was determined using the Monte Carlo simulation described previously. The size of the effect was determined for various momenta and source diameters. Results are plotted in Figure 5.34 over the momentum range of interest. Source size distorts the spectrum at the few keV/c level and does not contribute significantly as a systematic effect on the branching ratio.

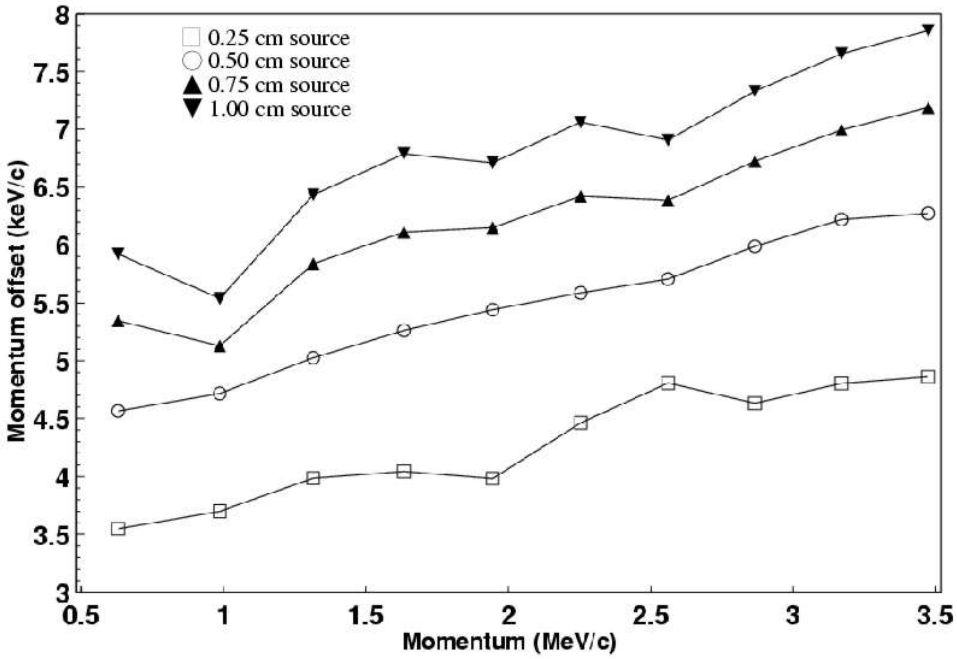

Figure 5.34 Momentum offset due to finite source distribution. The momentum shift is determined using a Monte Carlo simulation of the beta particles and spectrometer. Momentum of the beta particle is shifted slightly due to the finite size of the source. The shift in momentum depends on the source size as shown in the figure.

5.9.2 Collimator Aperture Effect

The ^{14}O beta spectrum was distorted by the finite size of the collimator aperture. This size of this effect was determined using the Monte Carlo simulation described

previously. The size of the effect was determined for various momenta and collimator diameters. Results are plotted in Figure 5.35 over the momentum range of interest. The collimator aperture distorts the spectrum at the few keV/c level and does not contribute significantly as a systematic effect on the branching ratio.

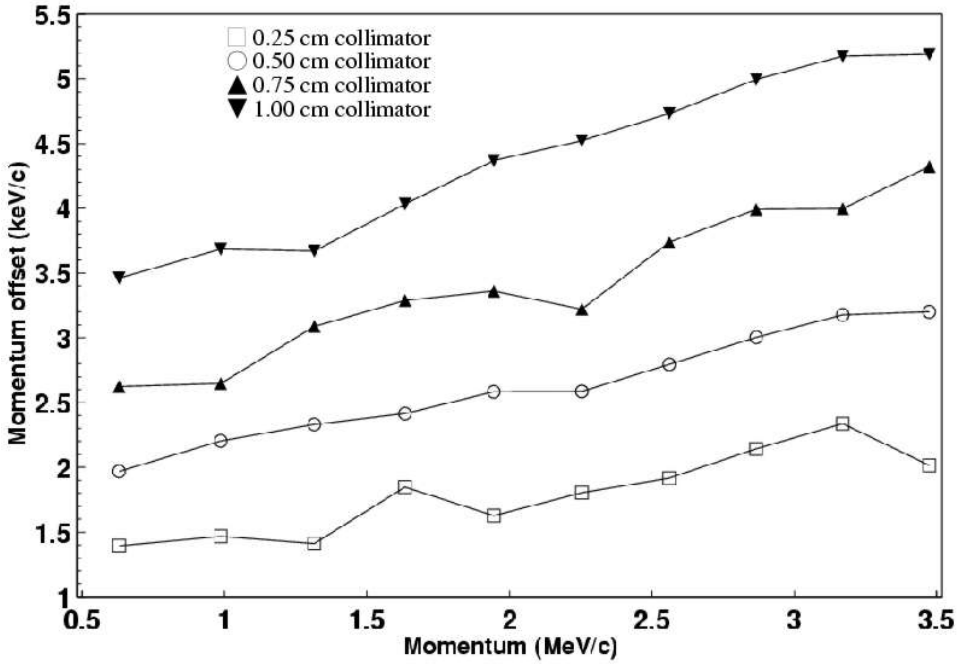

Figure 5.35 Momentum spread due to finite collimator size. The momentum shift is determined using a Monte Carlo simulation of the beta particles and spectrometer. Momentum of the beta particle is shifted slightly due to the finite size of the collimator. The shift in momentum depends on the collimator size as shown in the figure.

5.10 Data Analysis

The branching ratio was measured during a 48 hour run at the 88 Inch Cyclotron.

The ^{14}O was loaded on the foil for 80 s and observed for 80 s per cycle. Background from the ^{14}O source was also measured during the run as discussed in section 5.8. The branching ratio was measured for a total of 23840 s. Data cuts used for analysis can be found in Table 5.3.

Parameter	***Threshold Value***
Horizontal Wire Number	<= 3
Vertical Wire Number	<= 3
Anti-coincidence paddle ADC channel	< 200
PMT A and B TDC	> 1000 & < 1100

Table 5.3 Summary of data cuts used for analysis.

The branching ratio is determined by fitting the background subtracted data to the Fermi and Gamow-Teller spectra. The fitting routine also corrects the spectrum for the offset in momentum due to the finite source size, finite collimator size, and the magnetic fringing field. The fit also convolutes the gaussian wire hit distribution into the spectrum. The sum of the resulting Gamow-Teller spectrum is then divided by the sum of the resulting Fermi spectrum to determine the Gamow-Teller branching ratio.

$$BR = \frac{Gamow-Teller\ total}{Fermi\ total} = \frac{G_t}{F_t} \quad . \tag{5.14}$$

Systematics associated with the wire hit multiplicity, MWPC offset, shape factor uncertainty, gaussian wire response uncertainty, fringe field shift uncertainty, and the

active collimator scattering uncertainty are discussed in the following sections.

5.10.1 Weighted Background Subtraction

Background subtraction was weighted by the duration and rate of the appropriate background with respect to the data acquisition beam line rate and source rate. Cosmic ray background was subtracted directly proportional to the time over which the data and backgrounds were acquired. The data was acquired for 23840 s with a beam line rate of 5700 Hz and a source rate of 1232 Hz. The backgrounds are calculated here using the average MWPC event rates to demonstrate the calculation. The fit was performed with the data corrected for each wire.

The beam line background was acquired for 21842 s with 12201 events. The cosmic ray background must be subtracted as

$$N_{net\,beam\,line} = N_{beam\,line} - N_{cosmic\,ray} \times \frac{T_{beam\,line}}{T_{cosmic\,ray}} = 12201 - 81491 \times \frac{21842\,s}{1437083\,s}$$

$$N_{net\,beam\,line} = 12201 - 81491 \times 0.0152 = 10962\,events \quad . \tag{5.15}$$

Similarily the source background was acquired for 21842 s with 8434 events. The cosmic ray background is then subtracted as

$$N_{net\,beam\,line} = N_{beam\,line} - N_{cosmic\,ray} \times \frac{T_{beam\,line}}{T_{cosmic\,ray}} = 8434 - 81491 \times \frac{9406\,s}{1437083\,s}$$

$$N_{net\,beam\,line} = 8434 - 81491 \times 0.0065 = 7900\,events \quad . \tag{5.16}$$

These net backgrounds can then be used to correct the data as follows

$$N_{data} = N_{data}\, sub\, N_{net\,beam\,line} \times \frac{T_{data}}{T_{beam\,line}} \times \frac{R_{beam\,line\,data}}{R_{beam\,line}}$$

$$sub\, N_{net\,source} \times \frac{T_{data}}{T_{source}} \times \frac{R_{source\,data}}{R_{source}}\, sub\, N_{cosmic\,ray} \times \frac{T_{data}}{T_{cosmic\,ray}} \quad . \tag{5.17}$$

Here T_{data} is the acquisition time for the data, $T_{beam\ line}$ is the acquisition time for the beam line background, $R_{beam\ line\ data}$ is the beam line rate during the data acquisition, $R_{beam\ line}$ is the beam line rate during the background acquisition, T_{source} is the acquisition time for the source background, $R_{source\ data}$ is the beam line rate during the data acquisition, R_{source} is the beam line rate during the source background acquisition, and $T_{cosmic\ ray}$ is the acquisition time for the cosmic ray background. The events are annotated as N_{data} for the data, $N_{netbeamline}$ is the net number of beam line background events as described above, $N_{net\ source}$ is the net number of source background events as described above, and $N_{cosmic\ ray}$ is the number of cosmic ray events. The monitored rates, average number of events, and acquisition time are summarized in Table 5.4.

Background	***Time (s)***	***Monitor Rate (Hz)***	***Total Events***	***Net Events***	***Average Event Rate (Hz)***
Beam Line	21842	17406	12201	10962	0.502
Source	9406	1041	8434	7901	0.840
Cosmic Rays	1437083	N/A	81491	81491	0.057

Table 5.4 Summary of acquisition times and background rates.

5.11.1 Multiplicity Effect on the Branching Ratio

The ^{14}O beta particles have a wire hit multiplicity distribution as shown in Figure 5.36. Multiplicity drops off rapidly with increasing momentum. Data analysis was performed with a vertical and horizontal cut of multiplicity three and less. This includes 96.5 % of the data.

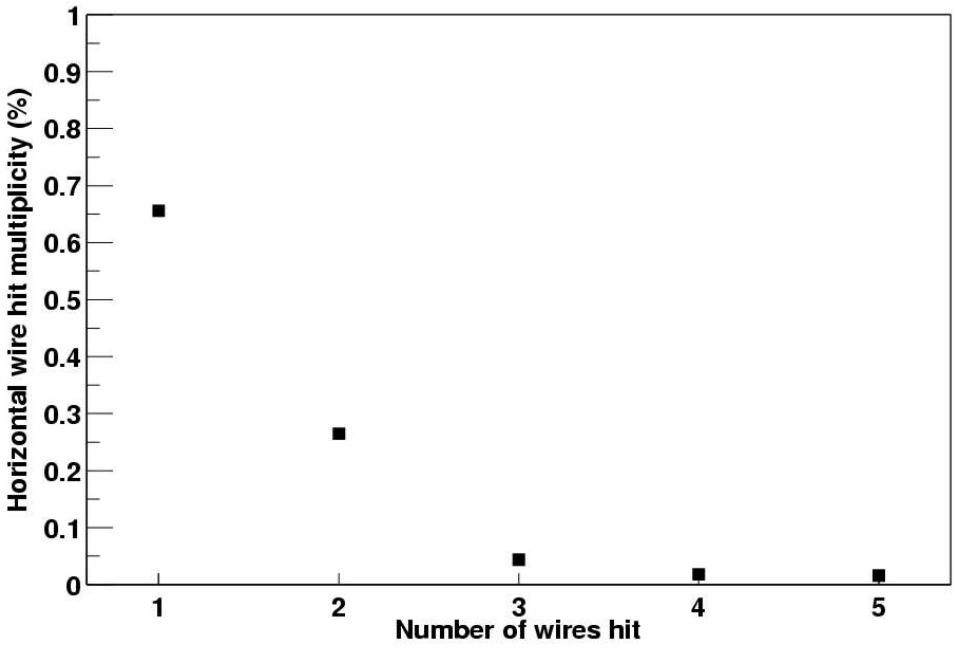

Figure 5.36 Horizontal wire hit multiplicity. Note: 5 wires hit includes all wire multiplicities greater than and including 5.

5.11.2 MWPC Offset Uncertainty

The offset is the distance between the center of the active collimator and the first wire of the wire chamber. This distance was 9.12 ± 0.01 cm. Uncertainty of this measurement can affect the branching ratio as it causes a shift in the apparent momentum. The branching ratio was fit with various offset distances and the results are shown in Figure 5.37. The uncertainty of 0.01 cm produces an uncertainty of 0.001 % in the branching ratio.

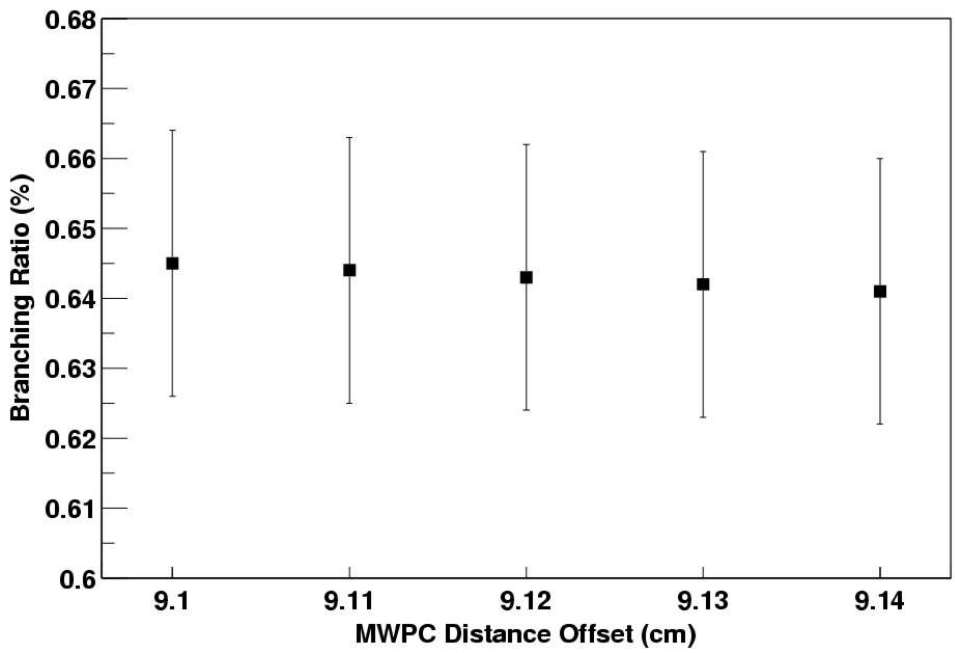

Figure 5.37 Effect of the offset uncertainty on the branching ratio. The branching ratio was fit with various MWPC offset values centered around the measured offset value. The

measured MWPC offset is 9.12 cm ± 0.01 cm.

5.11.3 Shape Factor Uncertainty

The shape factor as determined by Garcia and Brown [85] has a relative uncertainty of 10% or 0.005 %/MeV. This introduces an uncertainty into the fit for the branching ratio. A plot of the branching ratio versus the shape factor value is shown in Figure 5.38. The uncertainty of the branching ratio due to the uncertainty in the shape factor is found to be 0.002 %.

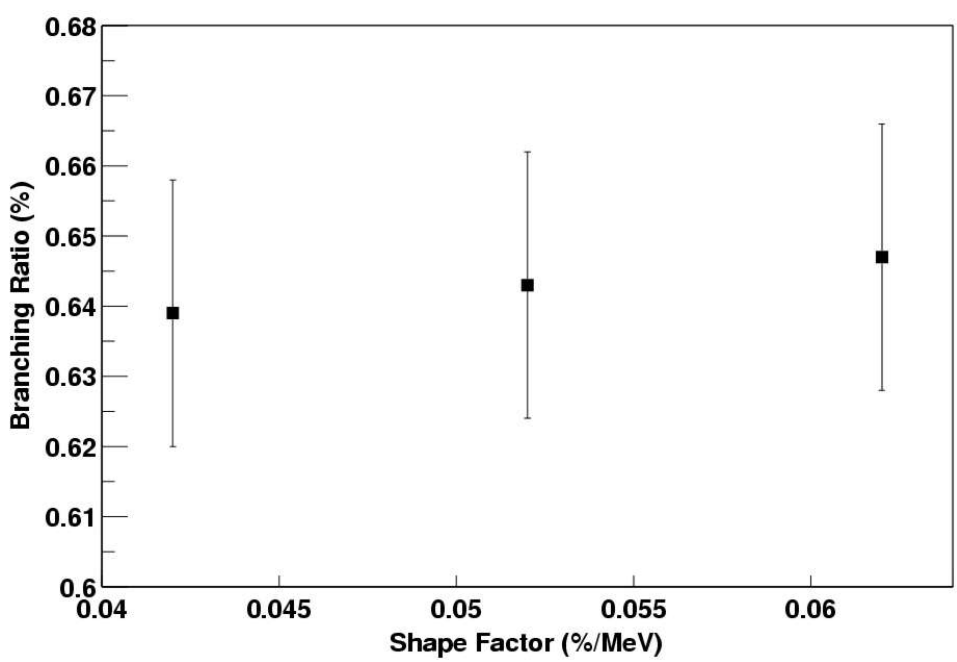

Figure 5.38 The shape factor effect on the branching ratio. The branching ratio was fit

with various shape factor values for the Gamow-Teller branch. The shape factor relative uncertainty was approximately 10% or 0.052 ± 0.005 %. As the shape factor was increased so too was the branching ratio result.

5.11.4 Gaussian Wire Reponse Uncertainty

The beta particle interaction with the wire chamber creates a gaussian response curve. This can be seen by histogramming the events surrounding and including a particular wire when it is triggered. For example, when wire number 10 is triggered the analysis routine adds a hit to each wire that is triggered around wire 10. The result is a gaussian distribution of events that are related to the selected wire. A gaussian width (sigma) was used to convolute the spectra in the fit procedure. Figure 5.39 shows the Fermi spectrum measurement with wires 5, 15, 25, 35, 45, and 55 as selected trigger wires. The Fermi spectrum has a signal to noise ratio on the order of 1000 to 1. The average sigma was found to be 0.646 wire spaces with a variance of 0.019 wire spaces. In the fit routine this becomes a momentum sigma of 0.022 MeV/c with which the Fermi and Gamow-Teller spectra are convoluted. Figure 5.40 shows the effect that the gaussian width uncertainty introduces to the branching ratio. Uncertainty introduced to the branching by the uncertainty in the width of the gaussian convolution is 0.001 %.

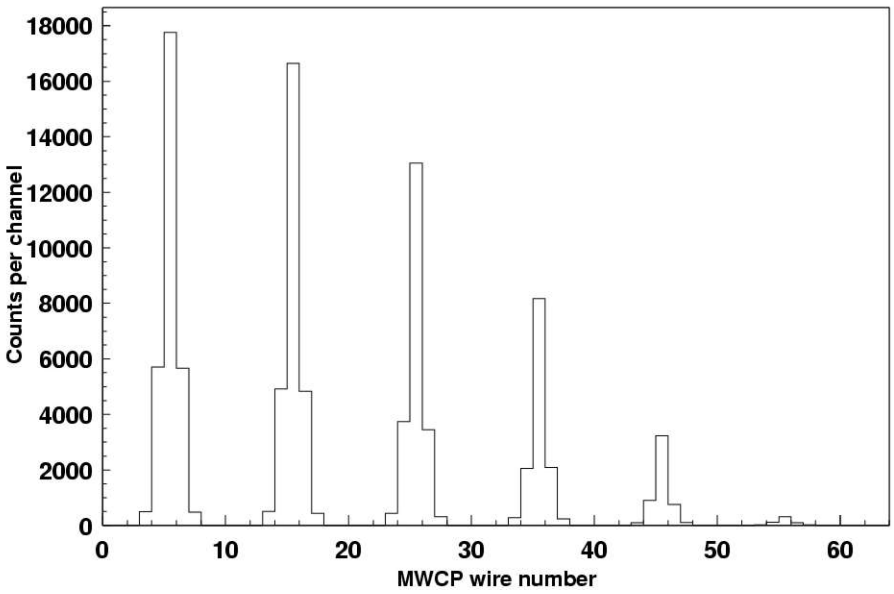

Figure 5.39 The wire hit gaussian distribution versus MWPC wire number. The gaussian response of the MWPC was determined using the data from the Fermi branch measurement. The signal to noise in this branch was better than 1000 to 1 except in the tail of the beta spectrum located above channel 50 in the MWPC.

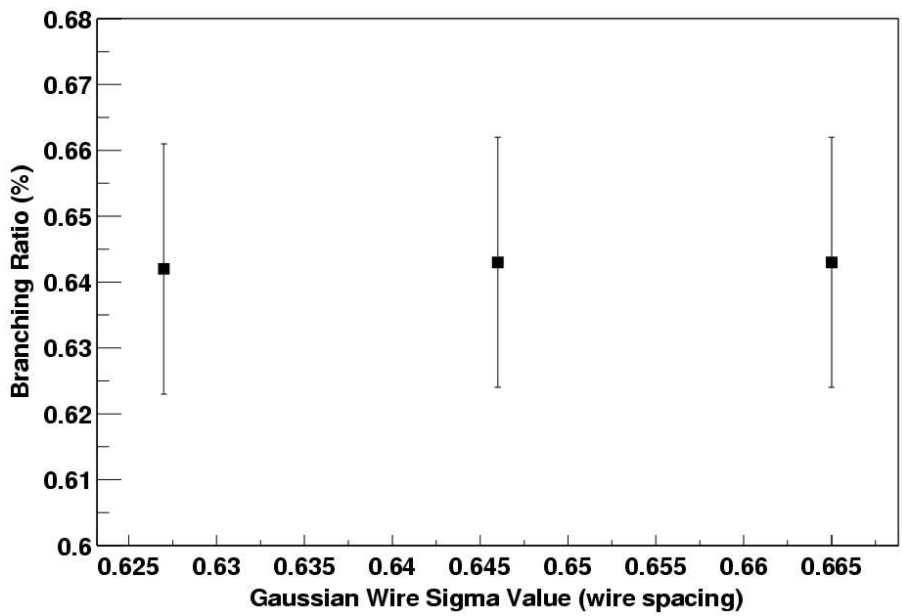

Figure 5.40 Effect of momentum spread on branching ratio. The branching ratio was fit while the gaussian width (sigma value) was varied around the mean value of 0.646 as determined from the Figure 5.39.

5.11.5 Fringe Field Shift Uncertainty

A magnetic fringe field shifts the beta particle trajectory. The measured beta particle momentum was larger than it should be due to the fringing field. The net effect was that the branching ratio was shifted 0.020 % smaller if the fringing field was not incorporated into the fit. The effect the fringing field has on the branching ratio is plotted in Figure 5.41. Branching ratio offset does not change rapidly as the offset nears its full effect. This is due to the size of the momentum binning of the data which is approximately 0.03 MeV/c per bin. Magnetic fringe field was measured with an uncertainty of approximately 10 %. This corresponds to an uncertainty of approximately

0.001 % in the branching ratio.

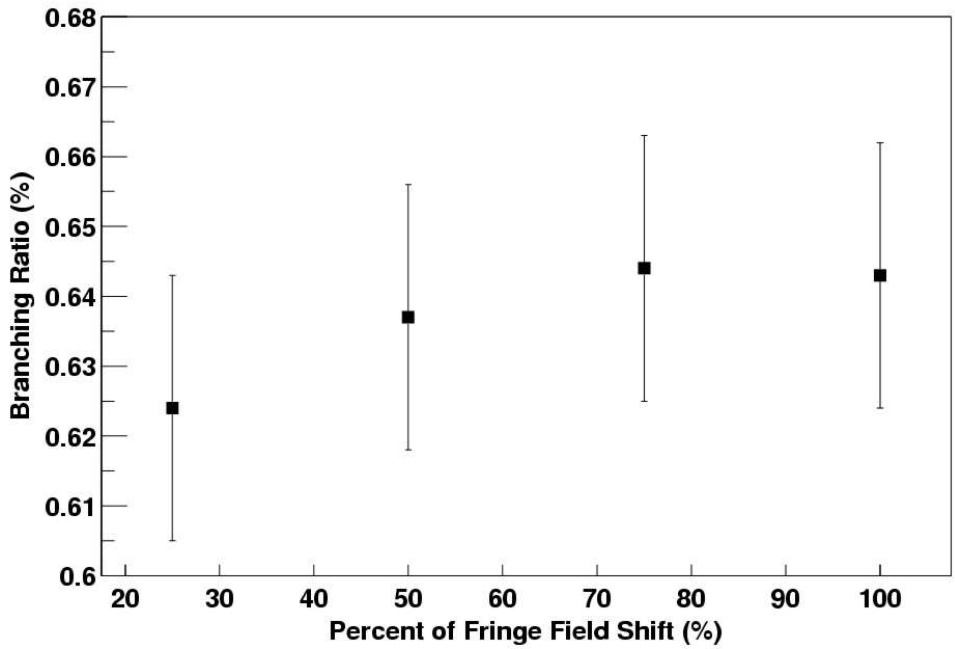

Figure 5.41 Dependence of the branching ratio on the fringe field. The net effect of the fringing field is to increase the branching ratio. Data was fit with 25 %, 50 %, 75 %, and 100 % of the momentum shift. A fringing field effect increases the branching ratio initially and once the momentum is shifted by 75 % or more the branching ratio levels out to its final value of 0.643 %.

5.11.6 Collimator Scattering Uncertainty

The scattering of beta particles from the edge of the active collimator. The scattering effect is proportional to the ratio of the area of the aperture to the solid angle of the edge visible to the ^{14}O source. From a distance of 25.0 cm the source sees an area of

approximately 0.0019 cm^2 due to the thickness of the collimator. The ratio the scattering surface to the open aperture was 1 to 125. One beta particle in 125 could hit the edge of the collimator and scatter into the spectrometer. The maximum energy loss associated with these scattered events could be 18 keV or 19 keV/c and still be included in the data cuts. A spectrum with 1 scattered event in 125 was generated with an energy loss of 18 keV per scattered event. Spectrum with the scattered events and without the scattered events was fit. The difference in the branching ratio was found to be 0.001 %. Figure 5.42 shows the Fermi and Gamow-Teller beta spectra over the momentum range measured in the experiment with and without the scattered beta particles. Figure 5.42 actually shows a 10% scattering probability to better illustrate the size of the effect. The error bars in the spectrum are due to the statistics at each data point. Even with a 10 % fraction of scattered beta particles the shifted spectrum falls within the statistical uncertainty at each point. The cumulative effect is what shifts the branching ratio by 0.001 %.

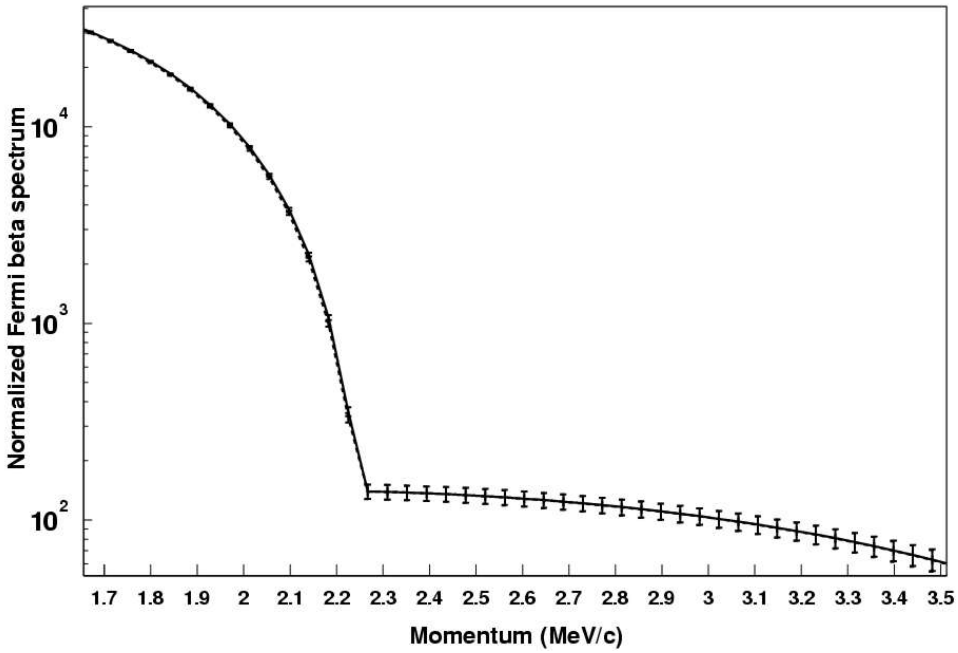

Figure 5.42 Beta spectrum with active collimator scattered events. The solid line in the plot represents the unshifted spectrum. The dashed line represents the beta spectrum with 10% scattering from the active collimator. The error bars are statistical.

5.11.7 Uncertainty Due to the Magnetic Field Drift

The uncertainty due to the magnetic field shift is determined by fitting the data with an offset from the true magnetic field setting. Figure 5.43 shows the branching ratio for various magnetic field offsets. The maximum uncertainty in the branch due to the 2 gauss magnetic field drift is found to be 0.005 %.

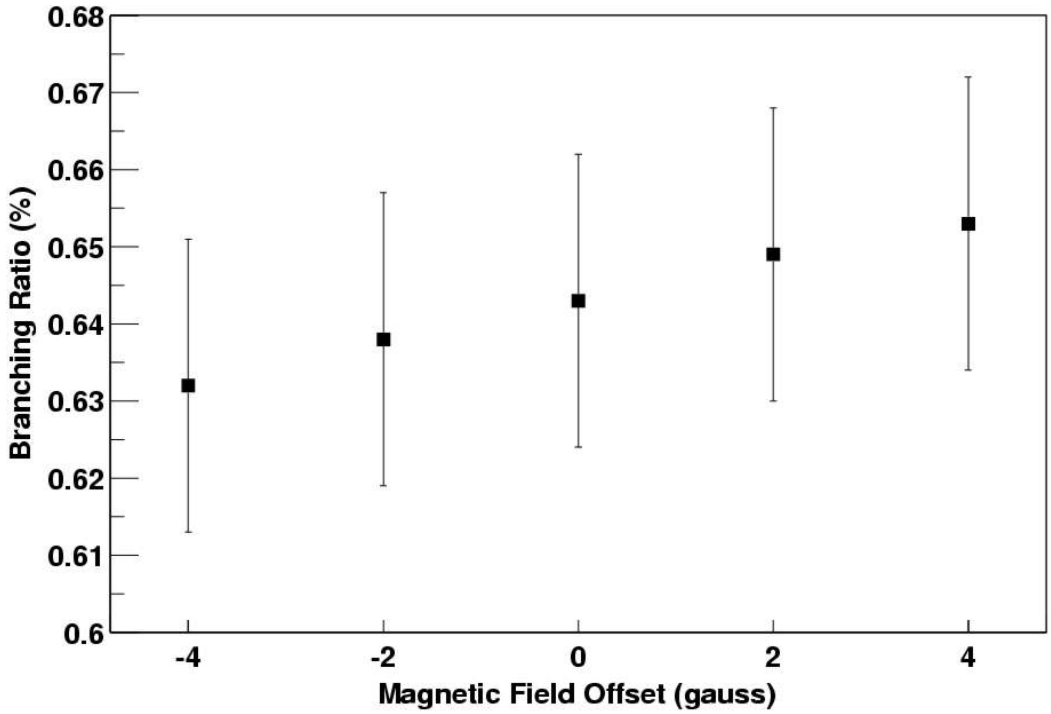

Figure 5.43 Branching ratio shift due to the magnetic field drift. The branching ratio data was fit with the magnetic field offset from its nominal value of 1158 gauss to determine the effect on the branching ratio. When the magnetic field is underestimated the branching ratio decreases and vice-versa.

5.11.8 Summary of Systematic and Statistical Uncertainties

The systematic uncertainties are summarized in Table 5.5. The systematic uncertainties added in quadrature total ± 0.006 %. The statistical uncertainty from the fit is ± 0.019 % for a total uncertainty of ± 0.020 %. The branching ratio is 0.643 ± 0.020 %. Figure 5.44 shows the beta spectra data with the fit.

Effect	***Size of Effect***	***Uncertainty (%)***
Statistics		0.019
Offset	0.01 cm	0.001
Shape Factor	10% of 0.052 %/MeV	0.002
Gaussian Wire Distribution	0.019 on 0.646	0.001
Fringe Shift	10% uncertainty	0.001
Magnetic Field Shift	2 in 1158 Gauss	0.005
Collimator Scattering	1% of betas scatter	0.001
Total Systematic		0.006
Total Uncertainty		0.020

Table 5.5 Summary of statistical and systematic uncertainties.

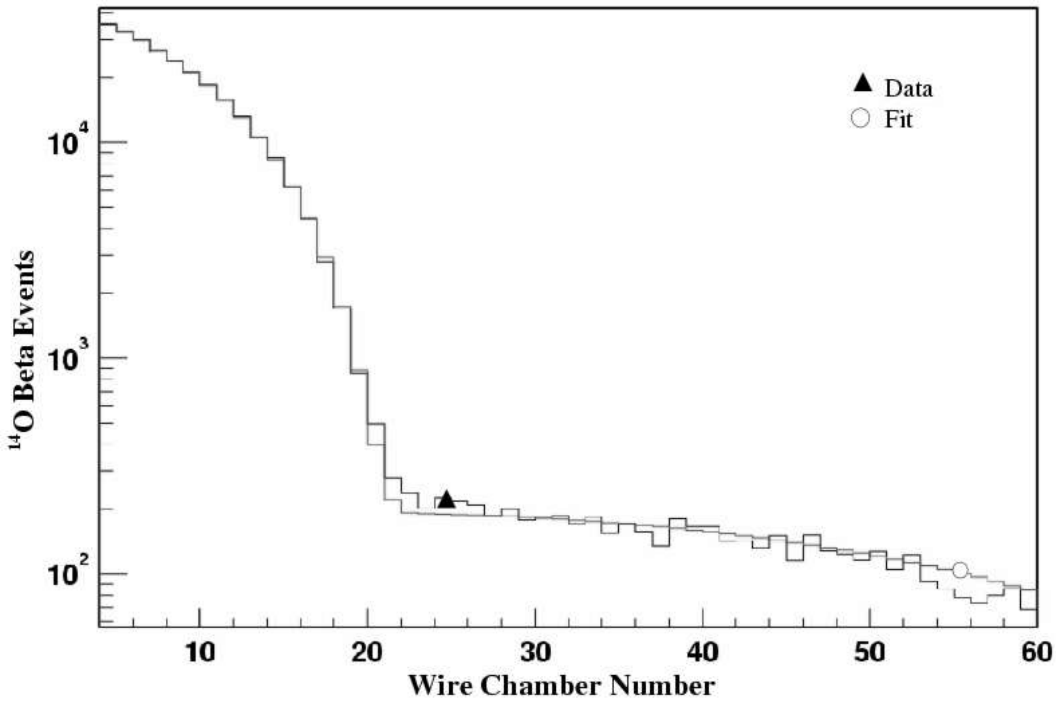

Figure 5.44 Beta spectrum with fit to determine branching ratio. The background subtracted data is plotted with the branching ratio fit. The Gamow-Teller branching ratio was found to be 0.643 ± 0.020 % including systematic uncertainties.

5.13 Final Result and Impact on Physics

The branching ratio can now be used to determine the V_{ud} coupling constant and test the unitarity of the CKM matrix. The branching ratio result of 0.643 ± 0.020 % agrees with the previous results as shown in Table 5.6. The relative uncertainty of the branching ratio is 3 %. The weighted average of the results is 0.618 ± 0.009 % with a chi-square of 0.88 for 3 degrees of freedom gives a confidence level of 45%. This result does not change the conclusions of chapter 4. Figure 5.45 shows the previous results with their respective weighted average as a solid line along with the current branching ratio result

from this chapter.

Year of Experiment	*Branching Ratio (%)*	*Uncertainty (%)*
1955 [76]	0.600	0.100
1963 [77]	0.650	0.050
1966 [78]	0.610	0.010
2004 Thesis	0.643	0.020
Average	0.618	0.009

Table 5.6 Summary of Gamow-Teller branching ratio.

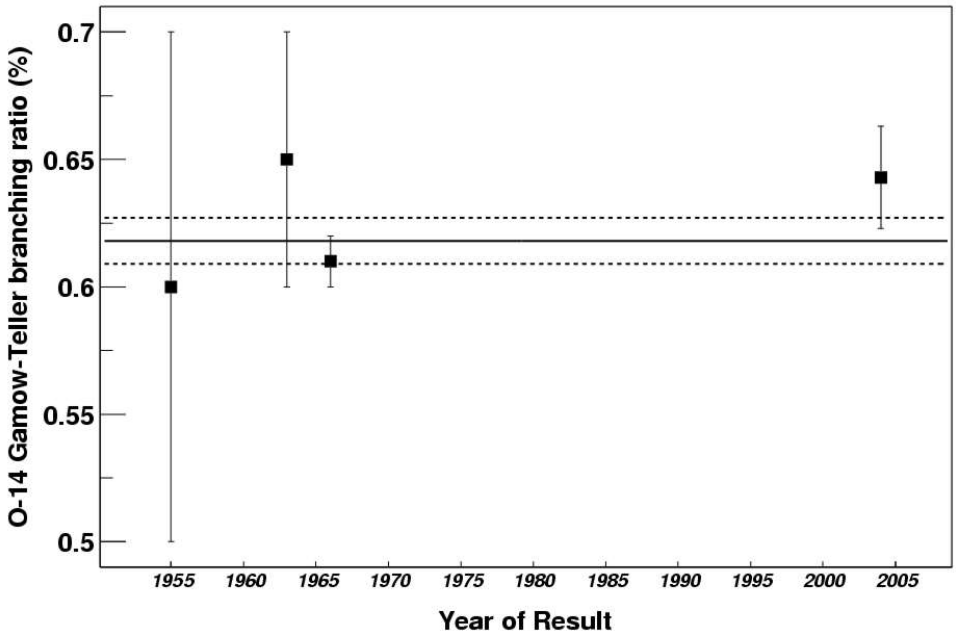

Figure 5.45 Summary of Gamow-Teller branching ratio measurements. The solid line represents the branching ratio average with the one sigma uncertainty represented by the dashed lines.

Conclusions

Development of a radioactive beam of ^{14}O with a flux of 10^7 ^{14}O atoms per second enabled the half-life and branching ratio experiments to be performed. In this experiment, the ^{14}O half-life was measured to a precision of 2 parts in 10000. The ^{14}O half-life was found to be 70.683 ± 0.015 seconds. In a separate experiment, the Gamow-Teller branching ratio was measured with to a relative uncertainty of 4 %. A Gamow-Teller transition to the ground state of ^{14}N branching ratio was determined to be 0.643 ± 0.020 %. The Gamow-Teller transition to the second excited state of ^{14}N branching ratio is 0.0545 ± 0.021 %. The new Fermi branching ratio is 0.9930 ± 0.020 %. Using these results we can calculate the ^{14}O ft-value and the CKM matrix element V_{ud}. The ^{14}O ft-value is now 3073.69 ± 2.6 seconds. The V_{ud} CKM matrix element is 0.9737 ± 0.0010. The weighted average of the current V_{us} results 0.2250 ± 0.0027 and 0.2272 ± 0.0030 gives 0.2260 ± 0.0015. Incorporating the value of V_{ub} 0.0035 ± 0.0015 gives a value of 0.9990 ± 0.0021 for the unitarity of the first row of the CKM matrix. The CKM matrix is unitary with a confidence level of 65 %. A fourth generation of quarks would have to have a coupling constant $V_{ux} < 0.032$ to exist in the current model.

Bibliography

1. M.E. Peskin and D.V. Schroeder, *Introduction to Quantum Field Theory*, Reading, MA: Perseus Books, 1995.
2. K. Hagiwara *et al*. *Phys. Rev. D*, vol. 66, p. 103, 2002.
3. N. Cabibbo, *Phys. Rev. Lett.*, vol. 10, p. 531, 1963.
4. M. Kobayashi and T. Maskawa, *Prog. Theor. Phys.*, vol. 49, p. 652, 1973.
5. P. Langacker and M. Luo, *Phys. Rev. D*, vol. 45, p. 278, 1992.
6. P. Langacker and D. London, *Phys. Rev. D*, vol. 38, p. 886, 1988.
7. B.R. Holstein and S.B. Treiman, *Phys. Rev. D*, vol. 16, p. 2369.
8. K. Hagiwara *et al*. *Phys. Rev. D*, vol. 66, p. 113, 2002.
9. A. Sher *et al.*, *HEP archive*, [arXiv:hep-ex/0305042], 24 june 2003.
10. A. Aloisio *et al.*, *HEP archive*, [arXiv:hep-ex/0307016], 8 July 2003.
11. V. Cirigliano *et al.*, *Eur. Phys. J. C*, vol. 23, p. 122, 2002.
12. N. Cabibbo *et al.*, to be published.
13. K. Hagiwara *et al*. *Phys. Rev. D*, vol. 66, p. 1, 2002.
14. M. Ademollo and R. Gatto, *Phys. Rev. Lett.*, vol. 13, p. 264, 1964.
15. H. Behrens and J. Janecke, *Numerical Tables for Beta-Decay and Electron Capture*,

New York: Springer-Verlag, 1969.

16. M. Morita, *Beta Decay and Muon Capture*, Appendix A.8, Reading, MA: W. A. Benjamin, Inc., 1973.

17. M. Morita, *Beta Decay and Muon Capture*, p. 114, eqn. 5.13, Reading, MA: W. A. Benjamin, Inc., 1973.

18. M. Morita, *Beta Decay and Muon Capture*, p. 114, eqn. 5.15, Reading, MA: W. A. Benjamin, Inc., 1973.

19. W. Bambynek *et al.*, *Rev. Mod. Phys.*, vol. 49, p. 77, 1977.

20. J.C. Hardy *et al.*, *Nucl. Phys. A*, vol. 509, p. 429, 1990.

21. I.S. Towner and J.C. Hardy, *Nucl. Phys. A*, vol. 205, p. 33, 1973.

22. W.E. Ormand and B.A. Brown, *Nucl. Phys. A*, vol. 440, p. 274, 1985.

23. A. Sirlin and R. Zucchini, *Phys. Rev. Lett.*, vol. 57, p. 1994, 1986.

24. A. Sirlin, *Rev. Mod. Phys.*, vol. 50, p. 573, 1978.

25. A. Sirlin, *Phys. Rev.*, vol. 164, p. 1767, 1967.

26.W.J. Marciano and A. Sirlin, *Phys. Rev. Lett.*, vol. 61, p. 1815, 1988.

27. J.C. Hardy and I.S. Towner, , *Nucl. Theory archive*, [arXiv:nucl-th/9812036], 14 Dec 1998.

28. N.R. Tolich, P.H. Barker, and P.D. Harty, *Phys. Rev. C*, vol. 67, p. 1, 2003.

29. J.W. Butler and R.O. Bondelid, *Phys. Rev.*, vol. 121, p. 1770, 1961.

30. R.K. Barden *et al.*, *Phys. Rev.*, vol. 127, p. 583, 1962.

31. M.L. Roush, L.A. West, and J.B. Marion, *Nucl. Phys. A*, vol. 147, p. 235, 1970.

32. R.E. White and H. Naylor, *Nucl. Phys. A*, vol. 276, p. 333, 1977.

33. H. Vonach *et al.*, *Nucl. Phys. A*, vol. 278, p. 189, 1977.

34. R.E. White *et al.*, *Phys. Lett. B*, vol. 105, p. 116, 1981.

35. G.S. Sidhu and J.B. Gerhart, *Phys. Rev.*, vol. 148, p. 1024, 1966.

36. R.W. Kavanagh, *Nucl. Phys. A*, vol. 129, p. 172, 1969.

37. H.S. Wilson, R.W. Kavanaugh, and F.M. Mann, *Phys. Rev. C*, vol. 22, p. 1696, 1980.

38. A.M. Hernandez and W.W. Daehnick, *Phys. Rev. C*, vol. 24, p. 2235, 1981.

39. R. Sherr, H.R. Muether, and M.G. White, *Phys. Rev.*, vol. 75, p. 282, 1949.

40. R.K. Bardin, C.A. Barnes, W.A. Fowler, and P.A. Seeger, *Phys. Rev. Lett.*, vol. 5, p. 323, 1960.

41. D.L. Hendrie and J.B. Gerhart, *Phys. Rev.*, vol. 121, p. 846, 1961.

42. R.K. Bardin *et al.*, *Phys. Rev.*, vol. 127, p. 583, 1962.

43. G. Frick *et al.*, *Phys. Rev.*, vol. 132, p. 2169, 1963.

44. G.J. Clark *et al.*, *Phys. Lett.*, vol. 35B, p. 503, 1971.

45. D.E. Alburger, *Phys. Rev. C*, vol. 5, p. 274, 1972.

46. J. Singh, *Indian J. Pure Appl. Phys.*, vol. 10, p. 289, 1972.

47. G.J. Clark *et al.*, *Nucl. Phys. A*, vol. 215, p. 429, 1973.

48. G. Azuelos, J.E. Crawford, and J.E. Kitching, *Phys. Rev. C*, vol. 9, p. 1213, 1974.

49. D.H. Wilkinson, A. Gallmann, and D.E. Alburger, *Phys. Rev. C*, vol. 18, p. 401, 1978.

50. J.A. Becker, R.A. Chalmers, B.A. Watson, and D.H. Wilkinson, *Nucl. Inst. Meth.*, vol. 155, p. 211, 1978.

51. M. Gaelens *et al.*, *Eur. Phys. J. A*, vol. 11, p. 413, 2001.

52. E.D. Commins and D. A. Dobson, *Phys. Rev. Lett.*, vol. 10, p. 347, 1963.

53. H.C. Bryant *et al.*, *Nucl. Phys.*, vol. 53, p. 97, 1964.

54. M. Gaelens, Ph.D. Thesis - *Production and Use of Intense Radioactive Ion Beams : ^{14}O as a Case Study*, Katholieke Universiteit Leuven, 1996.

55. M. A. Rowe *et al.*, *Phys. Rev. A*, vol. 59, p. 1869, 1999.

56. D. Wutte *et al.*, *Nucl. Instrum. and Meth. Phys. Res. B*, vol. 142, p. 409, 1998.

57. D. Wutte *et al.*, *Development of a radioactive ion beam test stand at LBNL,* LBNL internal report LBNL-42389, October 1998.

58. D. Wutte *et al.*, *Rev. Sci. Instr.*, vol. 69, p. 712, 1998.

59. I.A. Brown, *The Physics and Technology of Ion Sources*, Wiley-Interscience Publication, NewYork, 1989.

60. R. Geller, *Electron Cyclotron Resonance Ion Source and ECR Plasmas*, Bristol, Institute for Physics Publishing, 1996.

61. D. Wutte *et al.*, presented at Heavy Ion Accelerator Technology Conference (HIAT'98), Argonne National Laboratory, Illinois, 1998.

62. D. Wutte *et al.*, *Design and Study of the Extraction System of the 3rd Generation ECR Ion Source*, LBNL internal report LBNL-42388, October 1998.

63. P.R. Bevington and D.K. Robinson, *Data Reduction and Error Analysis for the Physical Sciences 2nd Edition*, Section 9.2, p. 171, New York: NY, McGraw-Hill Inc., 1992.

64. S. Baker and R.D. Cousins, *Nucl. Instrum. and Meth. Phys. Res.*, vol. 221, p. 437, 1984.

65. E.J. Axton and T. B. Ryves, *International Journal of Applied Radiation and Isotopes*, vol. 14, p. 159, 1963.

66. J. W. Muller, *Nucl. Instrum. and Meth.*, vol. 112, p. 47, 1973.

67. J. W. Muller, *Nucl. Instrum. and Meth. Phys. Res. A*, vol. 301, p. 543, 1991.

68. W. R. Leo, *Techniques for Nuclear and Particle Physics Experiments*, p. 50, New York: NY, Springer-Verlag, 1994.

69. W. R. Leo, *Techniques for Nuclear and Particle Physics Experiments*, p. 192, New York: NY, Springer-Verlag, 1994.

70. W. R. Leo, *Techniques for Nuclear and Particle Physics Experiments*, p. 193, New York: NY, Springer-Verlag, 1994.

71. R.G. Musket, C.W. Price, and J.C. Norberg, *Nucl. Instrum. and Meth. Phys. Res. B*, vol. 42, p. 245, 1989.

72. R. Stumpf, C. L. Liu, and C. Tracy, *Appl. Phys. Lett.*, vol. 75, p. 1389, 1999.

73. R.G. Musket, *Nucl. Instrum. and Meth. Phys. Res. B*, vol. 24, p. 698, 1987.

74. F. James, *Minuit -Minimization Package Reference Manual version 94.1*, CERN Program Library Writeup D506, CERN Geneva, Switzerland, 1994.

75.M. Gaelens, Lovain-La-Neuve, (private communcation).

76. R. Sherr, J.B. Gerhart, H. Horie, and W.F. Hornyak, *Phys. Rev.*, vol. 100, p. 945, 1955.

77. G. Frick *et al.*, *Phys. Rev.*, vol. 132, p. 2169, 1963.

78. G.S. Sidhu and J.B. Gerhart, *Phys. Rev.*, vol. 148, p. 1024, 1966.

79. D.H. Wilkinson and B.E.F. Macefield, *Nucl. Phys. A*, vol. 232, p. 58, 1974.

80. F.P. Calaprice and B.R. Holstein, *Nucl. Phys. A*, vol. 273, p. 301, 1976.

81. W. R. Leo, *Techniques for Nuclear and Particle Physics Experiments*, p. 131, New York: NY, Springer-Verlag, 1994.

82. W. R. Leo, *Techniques for Nuclear and Particle Physics Experiments*, p. 142, New York: NY, Springer-Verlag, 1994.

83. Professor Kam-Biu Luk, Lawrence Berkeley National Laboratory, (private communication).

84. K. Hagiwara *et al*. *Phys. Rev. D*, vol. 66, p. 201, 2002.

85. A. Garcia and B.A. Brown, *Phys. Rev. C*, vol. 52, p. 52, 1995.

86. C. M. Lederer *et al.*, *Table of Isotopes 7th Edition*, New York: NY, John Wiley and Sons Inc., 1978.